TECHNISCHE UNIVERSITÄT MÜNCHEN

Lehrstuhl für Numerische Mechanik

Multi-dimensional Coupled Computational Modeling in Respiratory Biomechanics

Christian J. Roth

Vollständiger Abdruck der von der Fakultät für Maschinenwesen der Technischen Universität München zur Erlangung des akademischen Grades eines

Doktor-Ingenieurs (Dr.-Ing.)

genehmigten Dissertation.

Vorsitzender: Prof. Dr. phil. Klaus Bengler

Prüfer der Dissertation:

1. Prof. Dr.-Ing. Wolfgang A. Wall
2. Prof. Marcel Filoche, Ph.D.
   École Polytechnique, Palaiseau / Frankreich

Die Dissertation wurde am 22.12.2016 bei der Technischen Universität München eingereicht und durch die Fakultät für Maschinenwesen am 03.07.2017 angenommen.

Abstract

Pure mechanical or assisted mechanical ventilation are life-saving treatments necessary in many scenarios in modern medicine. However, if conducted improperly, artificial ventilation can cause deleterious side effects for the patient, exacerbate prevailing respiratory disease, and ultimately trigger multi-organ failure. Still, clinically used ventilatory settings are primarily based on large clinical trials conducted for patient groups suffering from certain respiratory diseases. Recent studies have shown that so-called "lung-protective" ventilation strategies can considerably improve patient outcomes, and they provide recommendations for realisation of such protective ventilation protocols. However, individual patients may show differences in their anatomy or (patho-)physiology which limits the effectiveness of the derived generalised guidelines in ventilating a specific patient.

Therefore, in this work advanced modelling and numerical simulation techniques are developed to build a patient-specific imaging-based respiratory model taking into account individual patient anatomy and (patho-)physiology. All modelling approaches developed in this work (Part I) are based on the underlying physics of airflow dynamics and tissue mechanics and thus are more powerful than a pure black-box parametrisation of global lung function measurements. For their derivation, previously reported approaches in advanced respiratory modelling are carefully evaluated and extended towards four coupled computational lung models. The four models operate at different levels of resolution ranging from highly resolved three-dimensional to extremely fast reduced-dimensional representations. They include all effects that are necessary to accurately describe the behaviour of the lung such as airflow-tissue interaction, lung interdependence as well as recruitment and derecruitment dynamics in an imaging-based patient-specific geometry. Further, for the first time they incorporate an approach to validate computationally predicted regional mechanical strains against electrical impedance tomography measurements in a patient-specific setting.

Next to derivation of these models, their applicability in several clinically relevant settings is presented in this work (Part II). The applications include investigations in 4D-CT motion tracking and fully resolved three-dimensional fluid-structure interaction simulations that reveal the differences between healthy spontaneous breathing and pressure- and volume-controlled mechanical ventilation. Further, performed computations using an efficient reduced-dimensional lung model illuminate the stress distribution in a patient suffering from Acute Respiratory Distress Syndrome and allow predictions of required pressures to treat the diagnosed atelectasis. Finally, the models are applied to a scenario where their use is most promising - in understanding the complex airflow phenomena that govern the efficient oxygen transport during High Frequency Oscillatory Ventilation in neonates.

This work contains significant steps from the underlying mathematical equations towards clinical application of respiratory modelling. An inclusion of modern medical imaging techniques is presented as well as a novel validation method that allows to directly visualise simulated data in the electrical impedance tomography data format and to compare them to bedside measurements. The arising possibility to test individualised ventilatory strategies *in silico* before applying them to the real patient is an important step towards personalised intensive care medicine without any risk for the patient but with the potential to significantly improve long-term outcome.

Zusammenfassung

Rein künstliche oder assistierte künstliche Beatmung sind lebensrettende Maßnahmen, die in zahlreichen Gebieten der modernen Medizin Anwendung finden. Falls diese Maßnahmen jedoch nicht optimal auf den Patienten angepasst werden, können diese zu verheerenden Nebenwirkungen führen, welche von der Verschlimmerung einer vorliegenden respiratorischen Erkrankung bis hin zum Multi-Organ Versagen reichen können. Daher werden Richtlinien zur Beatmung von Patienten in groß angelegten klinischen Studien für unterschiedliche Patientengruppen und respiratorische Vorerkrankungen untersucht. Diese Studien haben gezeigt, dass sogenannte „Lungenprotektive" Beatmungsstrategien einen verbesserten Therapieerfolg liefern, und geben Empfehlungen für protektive Beatmungsmuster. Allerdings ist die zugrunde liegende Anatomie und (Patho-)Physiologie für jeden Patienten individuell, sodass die Effizienz einzelner Maßnahmen nicht in jedem Falle gewährleistet werden kann.

Daher werden in dieser Arbeit moderne Modellierungs- und Simulationsansätze entwickelt, die eine patientenspezifische und bilddatenbasierte Modellierung der Lunge unter Berücksichtigung der individuellen Anatomie und (Patho-)Physiologie ermöglichen. Alle Modellierungsansätze, die in Teil I dieser Arbeit entwickelt werden, basieren auf der Physik von Luftströmung und Gewebemechanik und sind daher leistungsfähiger als reine Black-Box Parametrisierungen globaler Lungenfunktion. Für die Entwicklung leistungsfähiger Modelle wird der momentane Stand der Technik im Bereich Lungenmodellierung kritisch ausgewertet und um vier neuartige gekoppelte Lungenmodelle erweitert. Diese vier Modelle besitzen einen unterschliedlichen Detailgrad von hochaufgelösten dreidimensionalen bis hin zu effizienten dimensionsreduzierten Ansätzen. Sie beinhalten außerdem alle Effekte, die notwenig sind, um das Verhalten der Lunge realitätsnah abzubilden. Dazu gehören die Interaktion zwischen Strömung und Gewebe, Wechselwirkungen benachbarter Alveolen sowie Rekrutierung und Derekrutierung. Weiterhin wird der erste bekannte Ansatz zur Validierung simulierter regionaler mechanischer Dehnungen mittels Elektrischer Impedanz-Tomographie präsentiert.

Neben der Herleitung der Modelle, wird deren Anwendbarkeit für klinische Fragestellungen in Teil II dieser Arbeit diskutiert. Die Anwendungen beinhalten 4D-CT Bildregistrierungs- und Fluid-Struktur-Interaktions- Berechnungen zur Untersuchung der Unterschiede zwischen natürlicher Atmung und künstlicher Beatmung. Außerdem geben Berechnungen mit einem effizienten dimensionsreduzierten Lungenmodell einen Einblick in die Spannungsverteilung in der Lunge eines Patienten mit Akutem Atemnotsyndrom, und erlauben Vorhersagen zur Behandlung der vorliegenden Atelektase. Schließlich werden die Modelle auf ein Szenario angewandt, in dem ihr Nutzen am vielversprechendsten ist - in der Hochfrequenzbeatmung von Neugeborenen.

Diese Arbeit enthält entscheidende Schritte ausgehend von den grundlegenden Gleichungen bis hin zur klinischen Anwendung numerischer Lungenmodelle. Die Integration moderner medizinischer Bildgebung wird ebenso präsentiert wie eine neuartige Validierungsmethode basierend auf Elektrischer Impedanz-Tomographie. Die sich daraus ergebende Möglichkeit, individualisierte Beatmungsmuster zunächst im Rechenmodell zu prüfen und nur im Falle einer Verbeserung im Patienten anzuwenden, birgt kein zusätzliches Risiko für die klinische Behandlung, aber die Chance auf eine signifikante Verbesserung des langfristigen Therapieerfolgs.

Acknowledgements

First, I would like to thank Professor Wolfgang A. Wall for offering me this wonderful opportunity and for being a great and inspiring supervisor throughout the entire thesis. Also, I would like to thank Professor Marcel Filoche for reviewing this work and for all corrections and ideas especially on gas transport in the lung.

My sincere gratitude goes to all clinical partners who supported the single topics in this work. A special thanks to Professor Inéz Frerichs and Dr. Tobias Becher from the Department of Anesthesiology and Intensive Care Medicine at Christian Albrechts University, Kiel for sharing their data and especially their wealth of knowledge on Electrical Impedance Tomography. I am also indebted to Professor Christian Martin (Institute of Pharmacology and Toxicology, RWTH Aachen) for his helpful advice on airway wall experiments and to Professor Johannes Schittny (Institute of Anatomy, University of Bern) for providing his imaging data of the alveolar microstructure. A special thanks, finally, goes to Professor Andreas W. Flemmer and Dr. Kai M. Förster from the Division of Neonatology at Dr. von Hauner Children's Hospital, Ludwig-Maximilian-University, Munich for sharing their enormous experience in neonatal ventilation and for their time and interest in this research.

Finally, I would like to thank my colleagues at the Institute for Computational Mechanics for the many discussions, all friends and my parents for their company in the past five years.

Munich, September 2017

To Romy

For Manchester, for London and for the Shetland Isles

Contents

Nomenclature

Representation of scalars, tensors and other quantities

q, Q	Scalar quantity
$\mathbf{q}$	Vector quantity
$\mathbf{Q}$	Tensor/Matrix quantity

Operators and symbols

$(\cdot)^T$	Transpose of a matrix
$(\cdot)^{-1}$	Inverse of a matrix or mapping
$(\cdot)^{-T}$	Transpose of the inverse of a matrix
$\hat{(\cdot)}$	Prescribed quantity
$\dot{(\cdot)}$	Time derivative at fixed reference position
$(\cdot,\cdot)_{\Omega,\Gamma}$	Weak form
$\|\| \cdot \|\|$	L2 norm
$Re\{\}$	Real part
det	Determinant
tr	Trace
∇	Spatial gradient operator
$\nabla\cdot$	Spatial divergence operator
$\mathbf{I}$	Identity matrix
$\mathbf{0}$	Zero matrix
$\mathbf{F}(\cdot)$	Fully resolved fluid operator
$\mathbf{S}(\cdot)$	Fully resolved structural operator
$\mathbf{A}(\cdot)$	Fully resolved ALE operator

Subscripts and superscripts

$(\cdot)^{\mathrm{A}}$	ALE field
$(\cdot)^{\mathrm{C}}$	Constraint
$(\cdot)^{\mathrm{E}}$	Electrical field
$(\cdot)^{\mathrm{F}}$	Fluid field
$(\cdot)^{\mathrm{FSI}}$	Fluid-structure interaction (FSI)
$(\cdot)^{\mathcal{T}}$	Image registration
$(\cdot)_{\mathrm{el}}$	Element

$(\cdot)_{\mathrm{I}}$	Inner domain
$(\cdot)_{\Gamma}$	Boundary/Interface

Domains and boundaries

Ω	Spatial domain
Γ	Boundary/ FSI interface in spatial configuration
Γ_{D}	Dirichlet partition of boundary in spatial configuration
$\Gamma_{0,\mathrm{D}}$	Dirichlet partition of boundary in reference configuration
Γ_{N}	Neumann partition of boundary in spatial configuration
$\Gamma_{0,\mathrm{N}}$	Neumann partition of boundary in reference configuration
$\Gamma^{\mathrm{F}}_{\mathrm{in}}$	Fluid inflow boundary in spatial configuration
$\Gamma^{\mathrm{F}}_{\mathrm{out}}$	Fluid outflow boundary in spatial configuration
$\tilde{\Gamma}$	Boundary for volume coupling (structural part)
$\hat{\Gamma}$	Boundary for volume coupling (fluid part)

Spatial discretisation

$\mathbf{M}$	Discrete mass matrix
$\mathbf{N}$	Discrete linear viscous and non-linear convective terms
$\mathbf{G}$	Discrete gradient operator
$\mathbf{f}_{\mathrm{int}}$	Discrete internal force vector
$\mathbf{f}_{\mathrm{ext}}$	Discrete external force vector

Time integration

α_m,α_f,β^*	Parameters for generalised-α method
θ	Parameter for one-step-θ method
n	Time step
Δt	Time step size

Linearisation

$\mathbf{r}$	Discrete non-linear residual
$\tilde{\mathbf{r}}$	Discrete linearised residual
$\mathbf{K}_{\mathrm{T}}$	Stiffness matrix
K	Stiffness matrix entry
LHS	Left hand side
RHS	Right hand side
i	Linear iteration

Fully resolved fluid dynamics

ρ^{F}	Density of the fluid
ν^{F}	Kinematic viscosity of the fluid
μ^{F}	Dynamic viscosity of the fluid
$\mathbf{u}^{\mathrm{F}}$	Fluid velocity
p^{F}	Fluid pressure
$\mathbf{f}^{\mathrm{F}}$	Fluid body force
$\boldsymbol{\varepsilon}$	Strain rate tensor
$\boldsymbol{\sigma}^{\mathrm{F}}$	Fluid stress tensor
$\mathbf{h}^{\mathrm{F}}$	Fluid traction
$\mathbf{v}, q$	Weighting functions for fluid velocity/pressure

Fully resolved structural mechanics

ρ^{S}	Density of the tissue structure
$\mathbf{d}^{\mathrm{S}}$	Structural displacements
$\mathbf{b}^{\mathrm{S}}$	Structural body forces
$\mathbf{t}^{\mathrm{S}}$	Traction force on structure
$\mathbf{F}$	Deformation gradient
$\bar{\mathbf{F}}$	Isochoric part of $\mathbf{F}$
J	Determinant of $\mathbf{F}$
$\mathbf{C}$	Right Cauchy-Green tensor
$\bar{\mathbf{C}}$	Isochoric part of $\mathbf{C}$
$\mathbf{S}$	Second Piola-Kirchhoff stress tensor
I_1, I_2, I_3	First, second, and third invariant of $\mathbf{C}$
$\bar{I}_1, \bar{I}_2, \bar{I}_3$	First, second, and third invariant of $\bar{\mathbf{C}}$
Ψ	Strain energy density function (SEF)
E^{S}	Young's modulus
ν^{S}	Poisson's ratio
k_n	Constant for polynomial SEF of order n
κ, β	Parameters for Ogden material law

Fluid-structure interaction

$\mathbf{d}^{\mathrm{A}}$	ALE displacements
φ	Mapping between ALE reference and spatial configuration

Transport dynamics

D	Diffusion coefficient
$\mathbf{q}$	Flux vector
$\mathbf{j}_l$	Electrical current density

Global lung mechanics

C_{rs}	Respiratory system compliance
P_{aw}	Airway pressure drop
Q_{aw}	Airway flow
R_{rs}	Respiratory system resistance
V_{rs}	Respiratory system volume

Fully resolved volumetrically coupled lung modelling

ΔV^S	Structural volume change
ΔV^F	Fluid volume change
$\boldsymbol{\lambda}$	Discrete Lagrange multiplier
k^{S}_{1-3}	Equivalent thorax stiffness region 1-3
t^*	Normalised time
$V^*_{\mathrm{air,m}}$	Normalised lung volume
Q^*	Normalised airway flow

Reduced-dimensional lung modelling

A	Luminal area of an airway
A_0	Luminal area of an airway under zero transmural pressure
A^{lb}_i	Outlet area of the peripheral airway supplying acinus i
A^{lb}	Outlet area of all peripheral airways in one lobe
B	Serial viscous contribution in Maxwell model
B_{a}	Parallel viscous contribution in Maxwell model
β	Shape-determining parameter in acinus material law
C	Capacitance of an airway
d_{aw}	Diameter of an airway
d_{min}	Minimum diameter of an airway
dt	Time increment
E_{aw}	Young's modulus of airway wall
E_1	Parallel stiffness in Maxwell model
E_2	Serial stiffness in Maxwell model
$\varepsilon_{\mathrm{glob}}$	Global strain of the lung
$\varepsilon_{\mathrm{vol}}$	Volumetric strain of an acinus
$\varepsilon^{\mathrm{max}}_{\mathrm{vol}}$	Maximum volumetric strain of an acinus
γ	Generation dependent prefactor for flow resistance
γ_0	Surface tension for liquid contained in airway
$\mathrm{HU}_{\mathrm{avg}}$	Average lung Hounsfield unit in CT scan
i	Index of current acinus
I	Inductance of an airway

κ	Slope-determining parameter in acinus material law
κ_0	Baseline stiffness in acinus material law
l	Length of an airway
l_{min}	Minimum length of an airway
L_{sp}	Height of the lung in supine position
μ	Dynamic viscosity of air
N_i	Number of neighbouring acini and pleural spaces for acinus i
n_{max}	Maximum generation number in the airway tree
ν_{aw}	Poisson ratio for the airway wall
P_{ac}	Pressure difference across an acinus
P_{alv},P_{a}	Alveolar pressure
$\tilde{P}_{\text{ext}}$	External pressure of an airway
P_1	Pressure at inlet of an airway
P_2	Pressure at outlet of an airway
P_{intr}	Inter-acinar pressure
P_o, P_c	Critical pressures for reopening/closure
P_{Pl}	Pleural pressure
ΔP	Pressure drop along an airway
ΔP_{Pl}	Difference of pleural pressure between most ventral/dorsal point and centre point of the lung
Φ_{w}	Phase shift for airway wall radial expansion
Re	Reynolds number
Q_1	Flow at inlet of an airway
Q_2	Flow at outlet of an airway
Q_{ac}	Flow into single acinus
Q_{i}	Flow into single alveolar duct
R	Nonlinear resistance of an airway
R_{visc}	Visco-elastic resistance in airway expansion
R_μ	Viscous flow resistance
R_{conv}	Convective flow resistance
ρ	Density of air
s_o, s_c	Time constant for reopening/closure
t	Time in measurement/simulation
t_{aw}	Thickness of airway wall
T_{w}	Time constant for airway radial expansion
V_{ac}	Current volume of an acinus
$V_{\text{ac,0}}$	Volume of an acinus at the stress free state
V_i	Volume of an alveolar duct
V_i^o	Volume of an alveolar duct at the stress free state
V^{lb}	Volume of lobe at end-expiration
x	Spatial coordinate of point in the lung in gravity direction
x_0	Spatial coordinate of centre point of the lung in gravity direction

Image Registration

d	Dimensionality of the image
$\mathbf{L}^{\mathrm{R}}$	Coordinates of landmark points in the reference image
$\mathbf{L}^{\mathrm{T}}$	Coordinates of landmark points in the target image
$\mathcal{I}_{\mathcal{R}}$	Reference image
$\mathcal{I}_{\mathcal{T}}$	Target image
$\varphi^{\mathcal{T}}$	Image registration transformation
$\mathcal{J}$	Image registration functional
$\mathcal{D}$	Difference metric
$\mathcal{S}$	Regulariser
$\mathbf{u}^{\mathcal{T}}$	Registration displacement field
$\alpha^{\mathcal{T}}$	Regularsation prefactor
$\mathbf{h}^{\mathcal{T}}$	Transformation field increment
$\mathbf{J}_e$	Jacobian for image registration

Alveolar ventilation and lung tissue bioimpedance

A_{C}	Cross-sectional area of the cubic-shaped sample
dL_{C}	Length increment for deformation
d_{elec}	Diameter of electrodes in EIT monitoring
d_{tp}	Diameter of circular training points
ΔL_{C}	Length change after displacement
ε_{V}	Volume fraction of tissue structure
h_{el}	Element size
I^{E}	Electrical current
L_{C}	Edge length of the cubic-shaped sample
NF	Noise factor for image reconstruction
$\mathbf{\Phi}^{\mathrm{E}}$	Electrical potential
R^{E}	Electrical resistance
ρ_{el}	Element quality measure
$\rho^{\mathrm{E}}_{\mathrm{eff}}$	Effective tissue resistivity
$\rho^{\mathrm{S}}_{\mathrm{TLC}}$	Homogenised tissue density at TLC
σ^{E}	Electrical condictivity
τ	Geometrical tortuosity
τ^{E}	Electrical tortuosity
U^{E}	Electrical potential difference
V_{tissue}	Tissue volume of the cubic-shaped sample

Gas exchange mechanisms in neonatal ventilation

i	Imaginary unit
J_0	0-th Bessel function of the first kind
FiO_2	Fraction of inspired oxygen
f	Respiration frequency
T	Time period
U_0	Velocity amplitude (harmonic)
ω	Angular frequency
α	Womersley number
i	Lung region index
j	Airway index
N	Number of lung regions
c	Prefactor accounting for lung heterogeneity
C_{eq}^{i}	Equivalent compliance for lung region i
C_{eq}^{*}	Equivalent compliance in case of homogeneous lung
P^{i}	Pressure at outlet supplying lung region i
Q^{i}	Flow into lung region i
R_{eq}^{i}	Equivalent resistance for airway tree region i
R^{j}	Resistance for airway j
$R_{\text{eq}}^{\text{tl}}$	Equivalent resistance for pharynx/larynx
ΔV^{i}	Volume change of lung region i

Abbreviations

ADI	Anisotropic deformation index
ALE	Arbitrary Lagrangian Eulerian
ALI	Acute lung injury
AMG	Algebraic multi grid
ARDS	Acute respiratory distress syndrome
BGS	Block Gauss-Seidel
CFD	Computational fluid dynamics
CT	Computed tomography
CPAP	continuous positive airway pressure
DPPC	dipalmitoyl phosphatdylcholine
EELV	End-expiratory lung volume
EIT	Electrical impedance tomography
FE	Finite Element
FRC	Functional residual capacity
FSI	Fluid-structure interaction
GREIT	Graz consensus reconstruction algorithm for EIT
HFOV	High-frequency oscillatory ventilation
HU	Hounsfield units

LES	Large-eddy simulation
MDCT	Multi-detector computed tomography
MRI	Magnetic resonance imaging
MP-RAGE	Magnetisation-prepared rapid gradient-echo
P-V	Pressure-volume
PEEP	Positive end-expiratory pressure
PET	Positron emission tomography
PSPG	Pressure-stabilising Petrov-Galerkin
R/D	Recruitment/derecruitment
RANS	Reynolds-averaged Navier-Stokes
SD	Standard deviation
SEF	Strain energy density function
SIMPLE	Semi-implicit method for pressure-linked equations
SPECT	Single-photon emission computed tomography
SRXTM	Synchrotron-based X-ray tomographic microscopy
TLC	Total lung capacity
TV	Tidal volume
VALI	Ventilator-associated lung injury
VILI	Ventilator-induced lung injury

1. Introduction

The human lung is a fascinating and at the same time a relatively young example of computational biomechanics and its application in medicine. Surprisingly, still relatively little detail is known about the behaviour of the lung at multiple scales and their interaction in a mechanical and biological sense.

Medical knowledge about the respiratory system often arises from large multi-centre trials with several thousand enrolled patients or from black-box engineering approaches that try to fit lung behaviour to quantities that can be relatively easy measured - preferably airway pressure and flow at the mouthpiece of a spirometer or a mechanical ventilator. The basis for this measured behaviour, i.e., the underlying physics of airflow dynamics and tissue mechanics in an organ of complex structure and function remains, however, often unexplored.

Throughout this work, a different and novel perspective on respiratory care will be applied. The lung will be seen as a composition of different fields and scales, their underlying physics, and how they interact with each other. Powerful new light will be shed on black-box engineering, and lung modelling approaches will be developed that can help to provide a deeper insight into respiratory physiology, to understand different types of acute and chronic lung diseases and to assess better treatment options in cases of severe respiratory dysfunction. A close integration of clinical monitoring methods will ensure lung model development and interpretation with strong medical relevance.

To understand the lung as a complex organ in its structure and function, basic anatomy and physiology will be introduced at the start.

1.1. Anatomy and physiology of the human respiratory system

1.1.1. Conducting passages

Following the path of oxygen during inspiration, fresh air firstly flows through the conducting passages beginning with the nasal cavity, the pharynx, and the larynx which are often denoted as upper airways (see Figure 1.1). In case of mechanical ventilation, the nasal cavity, the pharynx and the larynx are omitted if they are bypassed via an endotracheal tube (see e.g., Chapter 4). The upper airways are followed by the lower airways starting with the trachea, down to the main bronchi, the lobar bronchi and several generations of bronchioles. If the trachea is defined as generation zero, the tracheo-bronchial tree can be characterised as a dichotomous branching tree of conducting airways ending at the terminal bronchioles in generation 16 (see Figure 1.1).

The branching pattern follows relatively strict rules and generates a fractal-like space-filling geometry penetrating further into the lung and subsequently reducing its dimensions. Interestingly, Majumdar et *al.* [216] have shown that the radius ratio between a parent airway and its

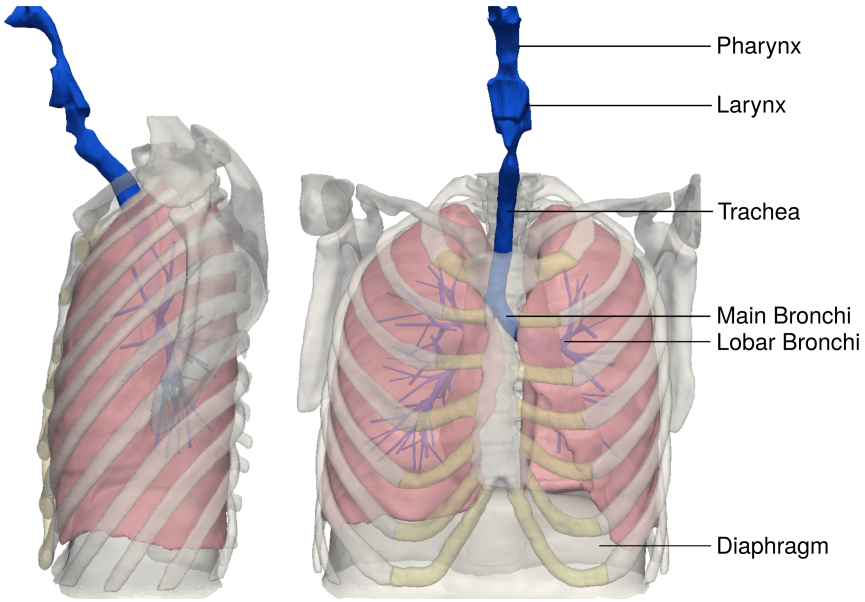

Figure 1.1.: Lung anatomy for a healthy adult subject.

two daughters follows a factor of 0.876 for the major and 0.686 for the minor daughter airway. Further, Weibel [357] found that the length-to-diameter ratio is 3.75 independent of the airway generation and that the number of daughter airways in one generation is on average 1.4 times the number of their parents. Further regularities in the branching tree structure have been identified in [99, 166] and can similarly be observed in other mammalian species, e.g., in mice [232].

In Figure 1.2, the branching structure, the total luminal area A_{lm} per generation, and the resulting average airflow velocity $\bar{u}$ for a standard breath with a tracheal flow of 0.5 l/s [281] is shown for a healthy human subject. It can be seen that luminal area almost increases exponentially and that average airflow velocity decreases almost exponentially from generation to generation. Therefore, gas transport mechanisms in larger airways are mainly driven by convection while in higher generations mainly diffusion mechanisms are dominant. The entire volume of the airway tree, also referred to as dead space, as the conducting airways do not take part in gas exchange, is approximately 150 ml in an adult human [141]. More details on the morphometry of conducting airways can be found in [166, 167, 356]. For children, equivalent data can be found in [168] and [230].

The composition of the airway wall is strongly dependent on the tree generation. While all airways consist of a smooth muscular wall and several membranes, the trachea is additionally stabilised by stiff cartilage rings to prevent collapse during forced breathing manoeuvres or coughing. This amount of cartilage decreases in the main bronchi, where still cartilage plates exist, down to the small bronchioles, where no cartilage is present. This leads to different physiological properties on different airway generations and will be discussed in detail in Appendix C. In brief, larger airways remain open by the stiffness of their walls, while smaller airways are regulated in diameter by surrounding connective lung tissue, the so-called peribronchium. The detailed interplay between airways and their surrounding lung tissue will be discussed in detail in Section 2.1.

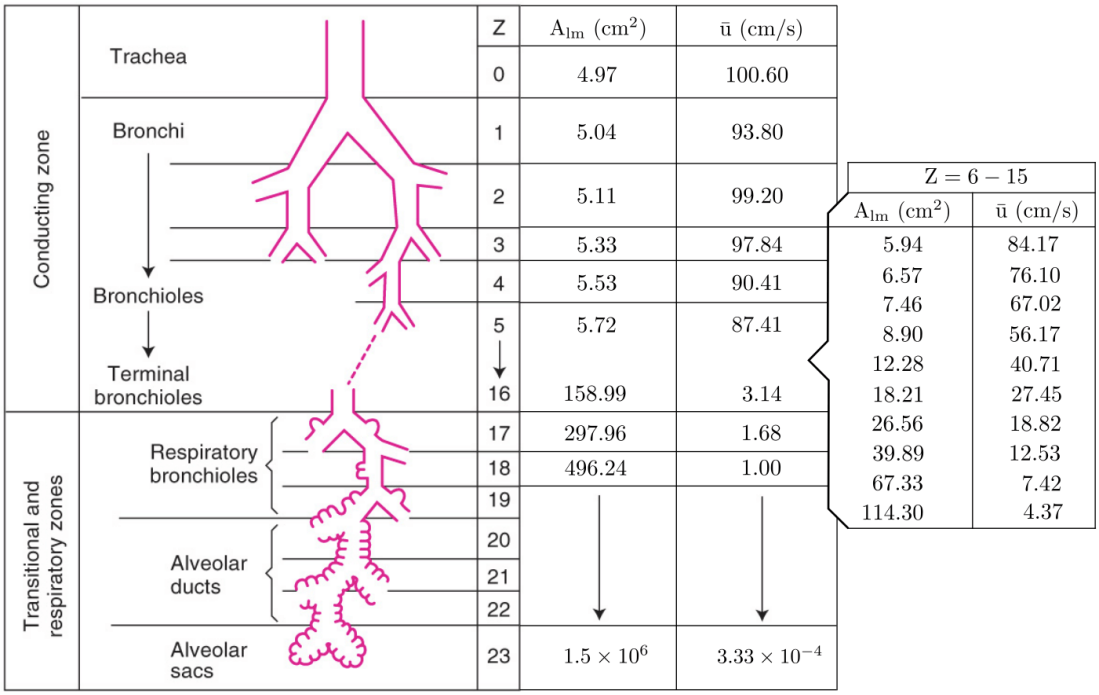

Z	A_{lm} (cm^2)	$\bar{u}$ (cm/s)
0	4.97	100.60
1	5.04	93.80
2	5.11	99.20
3	5.33	97.84
4	5.53	90.41
5	5.72	87.41
↓		
16	158.99	3.14
17	297.96	1.68
18	496.24	1.00
19	↓	↓
20		
21		
22		
23	1.5×10^6	3.33×10^{-4}

Z = 6 − 15	
A_{lm} (cm^2)	$\bar{u}$ (cm/s)
5.94	84.17
6.57	76.10
7.46	67.02
8.90	56.17
12.28	40.71
18.21	27.45
26.56	18.82
39.89	12.53
67.33	7.42
114.30	4.37

Figure 1.2.: Branching structure for a healthy adult human subject. Z denotes the generation number, A_{lm} the total luminal area of all airways in one generation and $\bar{u}$ the average airflow velocity resulting from division of tracheal flow by the total luminal area. Image adapted from [359].

1.1.2. Respiratory part

Beyond the conducting airways, the lung consists of eight further respiratory generations containing respiratory bronchioles (generation 17-19), alveolar ducts (generations 20-22), and alveoli (generation 23), where the gas exchange takes place.

Ochs et *al.* [249] found that a human lung consists of approximately 500 million alveoli which span an alveolar surface of $140m^2$ [356]. An ensemble of alveoli is often interpreted as a "bunch of grapes" [266] for illustrative purposes. In reality, however, alveoli are air spaces separated from each other via thin alveolar walls which contain the capillary network for gas exchange. The real morphometry of lung tissue follows the principle of a dense packing of single alveoli forming a sponge-like micro-structure visualised in Figure 1.3. The goal of this structure is to maximise the surface area for gas exchange in a given lung tissue volume.

Generations 17-23 are united to the so-called acini of which approximately 30,000 exist in the human body. Following the definition by Hafeli-Bleuer and Weibel [144], an acinus begins at the first respiratory bronchiole. The acinus contains all respiratory structures further downstream in a way to provide maximum surface area for alveoli and a minimum total diffusion length for oxygen transfer. A more detailed discussion of the alveolar micro-structure will be given in Appendix D.

On the macroscopic scale, lung tissue is subdivided into five lobes, three in the right and two in the left lung. The single lobes are separated by serous membranes and form individual

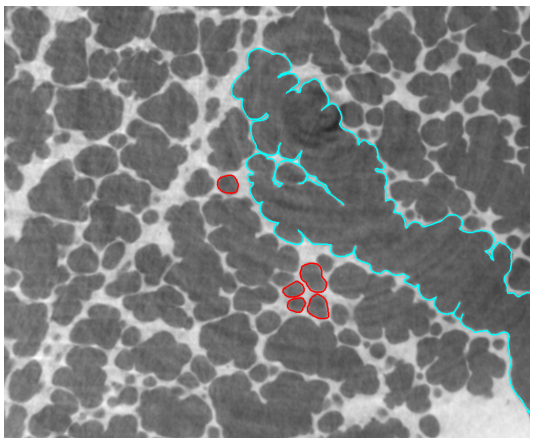

Figure 1.3.: Synchrotron-based X-ray tomographic microscopy (SRXTM) image of rat lung tissue filled at 25cmH_2O modified from [272]. Single alveolar walls are visible as bright tissue structures. The blue boundary marks an alveolar duct. The red colour encloses single alveoli in this section.

compartments that are e.g., visible in computed tomography (CT) scans. On the proximal side, the five lobes are enclosed by the visceral pleura while the intercostal muscles are bounded by the parietal pleura. The pleural cavity in between is filled with liquid which allows sliding movement of the lung within the thoracic space. The next subdivision level of the lobes are lung segments, which are presented in Chapter 4 in more detail.

One crucial characteristic of lung tissue is the lining with a thin layer of liquid on the inside of the alveoli. The most important component of this liquid lining is the so-called surfactant, whose full composition and its role in breathing will be summarised in the subsequent section. Therewith lung tissue consists of the following components seen from a macroscopic view: tissue septa ($\sim$7%), pre-/post-capillaries ($\sim$1%), and alveolar/duct air ($\sim$92%) [356]. This combination of components will be referred to as parenchyma in the following derivations.

1.1.3. Mechanics of Breathing

The interplay between conducting passages (see Chapter 1.1.1) and the characteristic tissue morphology (see Chapter 1.1.2) as well as the liquid lining of lung tissue significantly govern the mechanics of breathing.

In healthy quiet breathing, respiration is driven by contraction of the respiratory muscles, mainly the diaphragm which contracts and generates a negative pressure that induces airflow into the lungs. This process can be assisted by the accessory respiratory muscles including the intercostals, the abdominal muscles and other accessory muscle groups. Expiration is passive in quiet breathing and determined by the elastic recoil forces of lung tissue and the chest wall. In forced manoeuvres, expiration is assisted by the respiratory muscles described previously.

In classical physiology, the elastic properties of the lung are often quantified via pressure and flow measurements at the mouthpiece/endotracheal tube represented as pressure-volume (P-V) curves of the lung (see Figure e.g., 1.5). The P-V curves show that the elastic behaviour of the

lung is generally non-linear. However, within a certain pressure/volume range applied pressure and lung volume show an almost linear relationship. The slope of the P-V curve in this range is denoted as compliance

$$C_{rs} = \frac{\Delta V_{rs}}{\Delta P_{aw}} \tag{1.1}$$

where ΔV_{rs} is the measured change in respiratory system volume at the corresponding measured airway pressure drop ΔP_{aw}. The elastic properties of lung tissue are mainly determined by collagen and elastin fibres in the alveolar walls as well as by surface tension at the tissue-air interface influenced by surfactant. Surfactant is produced by type II alveolar epithelial cells and contains dipalmitoyl phosphatdylcholine (DPPC) [359]. With this surface active agents, surfactant reduces surface tension of the liquid layer lining the alveolar wall and thus significantly facilitates breathing. Absence of surfactant or deliberate removal, e.g., following the Lavage-Protocol [295] results in reduced lung compliance, alveolar atelectasis and leads to pulmonary oedema [359]. For further information on surfactant properties and related replacement therapy the reader is referred to [97, 174].

Pulmonary resistance arising from flow resistance in the conducting airways is defined as

$$R_{rs} = \frac{\Delta P_{aw}}{Q_{aw}} \tag{1.2}$$

where Q_{aw} the measured flow in the airway. The resistance can be quantified using e.g., forced manoeuvres. Resistance is different between expiration and inspiration due to compression/expansion of airways subjected to the varying airway external pressures during respiration. As mentioned previously (see Chapter 1.1.1), smaller airways have no stabilising cartilage structures and thus their behaviour is a mainly passive reaction on the pressure difference between airway inner pressure and the pressure of surrounding lung tissue. In some cases, e.g., in allergic reactions of the airway smooth muscle, active contraction will play a role.

In a clinical setting, the global behaviour of the lung is mainly described with the previously defined resistance (R_{rs}) and compliance (C_{rs}). This approach is, however, extremely oversimplified. Even in a healthy subject, there are several causes that lead to an uneven ventilation of lung tissue locally, including the dynamic compression of airways, different regional compliance of tissue and chest wall, and the influence of gravity [359]. In patients with lung disease the regional differences in ventilation become decisive and raise the interest of the medical community for a more exact assessment of regional lung function. The computational lung models introduced in this thesis are well-suited to provide such detailed regional information, required e.g., for predicting adequate ventilation strategies in case of respiratory dysfunction.

1.2. Lung damage mechanisms and protective ventilation strategies

1.2.1. Ventilator-associated/Ventilator-induced Lung Injury

If a person is unable to breath spontaneously, mechanical ventilation becomes a standard therapeutic procedure to provide temporal assistance to the respiratory muscles providing sufficient

gas exchange, e.g., during planned interventions in anaesthetised subjects. For patients suffering from acute or chronic respiratory failure such as Acute Lung Injury (ALI) or Acute Respiratory Distress Syndrome (ARDS) [271], mechanical ventilation becomes a necessary life-saving treatment. Unfortunately, despite being life-saving, mechanical ventilation is associated with potentially deleterious side effects, therefore termed Ventilator-associated/Ventilator-induced Lung Injury (VALI/VILI). Following the detailed argumentation by Slutsky and Raineri [312] and the review by Nieman et *al.* [242] regional mechanical overdistension is a key factor in Ventilator-Induced Lung Injury. Physical forces which are e.g., generated at ventilation with high tidal volumes lead to several structural and functional consequences at cellular scale triggered by mechanical overdistension (see Figure 1.4). A second group of mechanisms that can cause lung injury occurs at ventilation with extremely low tidal volumes. In that case, the provided oxygen supply might be too low and lead to regional hypoxia, i.e., a shortage of oxygen. Furthermore, peripheral lung structures may start to collapse at low lung volumes and be damaged during cyclic reopening in inspiration. It is believed that a so-called "air-finger" which is travelling through an airway initially closed by a liquid bridge will abrase the inner cell layer and lead to lung damage [33, 126, 127, 157, 182, 223, 313]. A more detailed description of reopening/closure will be discussed in Chapter 2.

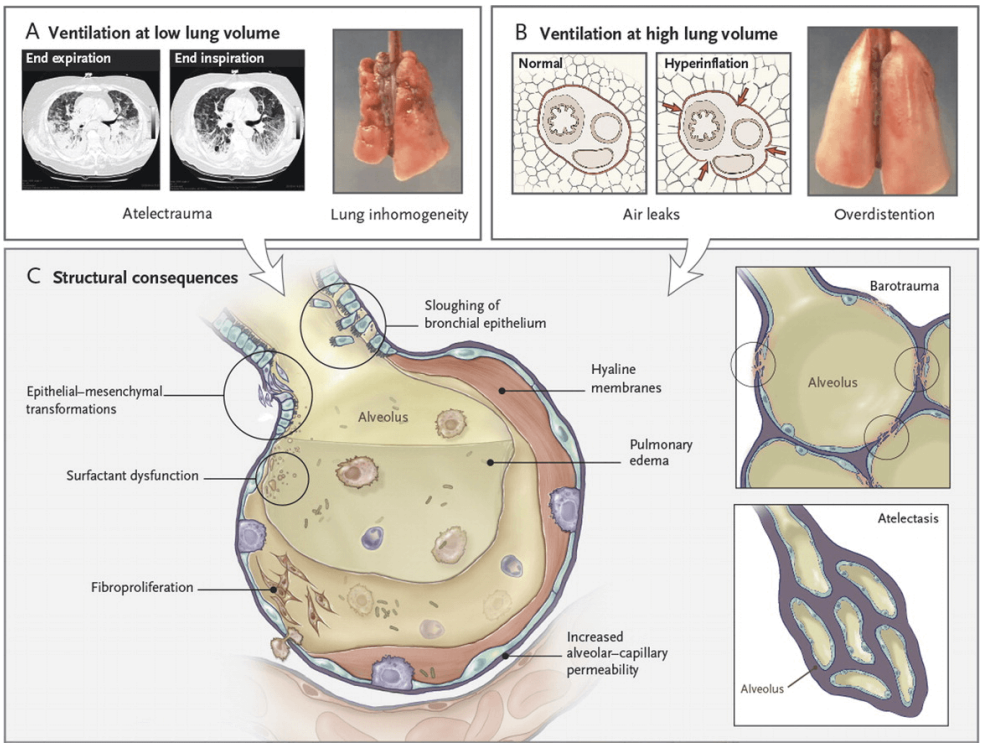

Figure 1.4.: Overview over lung damage mechanisms at low lung volumes (Panel A) and high lung volumes (Panel B). The mechanical loading exerted on lung tissue leads to structural, biological and physiological consequences on the alveolar scale (Panel C) and can lead to multi-organ dysfunction. Adapted from [312] with permission.

The high physical forces exerted on lung tissue may trigger the release of intercellular mediators [340]. Some of them will directly injure the lung and others indirectly via inducing subsequent developmental stages, e.g., fibrosis. Ultimately, this process will lead to multi-organ failure of an improperly ventilated patient [310].

1.2.2. Protective ventilation strategies

Following the awareness of potentially harmful effects in mechanical ventilation, several advances have been made in clinical treatment to date (see e.g., [336]). One of the most famous studies in this context is the reduction in tidal volume from conventional 12ml/kg to 6ml/kg predicted body weight which significantly decreased mortality [14]. Since then, several so-called protective ventilation strategies have been proposed including high positive end-expiratory pressure (PEEP) [45, 229], high frequency oscillatory ventilation (HFOV) [88], addition of single sighs [257] or noisy ventilation [318], prone positioning [140], heavy use of recruitment manoeuvres [255] or a combination of individually adjusted high PEEP and lowering of tidal volume [9, 349]. One goal of all these approaches is to bring regional alveolar ventilation to a stage where alveolar overdistension and collapse are avoided and where still enough oxygen is provided to the lung (see Figure 1.5).

The relative importance of each measure is, however, still barely understood [10]. Moreover, some techniques could even increase mortality, e.g., HFOV in patients suffering from early ARDS [95]. The remaining uncertainty in choosing the best ventilatory strategy for an individual patient is mainly due to the fact that it is unknown, how exactly air distribution, alveolar recruitment and regional lung overstraining are affected by the changes in ventilation settings. Questions regarding e.g., the optimal PEEP in ARDS [200] can probably not be solved for all patients identically. There might be general recommendations for single patient groups, however none for an individual patient. In the same way in which the current stage of disease is individual for a patient, treatment has to be tailored to individual patient needs. This is the main idea behind patient-tailored protective ventilatory treatment presented in this thesis.

1.3. Clinical Monitoring Methods

Recognition of the harmful side effects and the availability of protective ventilation strategies made up a new challenge in clinical monitoring of ventilation quality. Chiumello et *al.* [58] suggest that widely used measurement of global lung function may be an inaccurate surrogate for regional strain and overdistension. Further, it has been shown, that maximum regional strain in an ARDS patient may be up to 45% higher than global strain defined as ratio between tidal volume (TV) and functional residual capacity (FRC) [285].

To obtain more exact regional information, better imaging methods do exist in clinical practice. CT e.g., has a high spatial resolution with excellent anatomical accuracy allowing the sensitive detection of lung recruitment, derecruitment and inhomogeneities [75, 113]. However, CT is not available as point of care examination and potentially dangerous patient transports are required for every CT examination. Furthermore, CT scans lead to high radiation exposure which limits the repeatability of examinations in line with ethical guidelines.

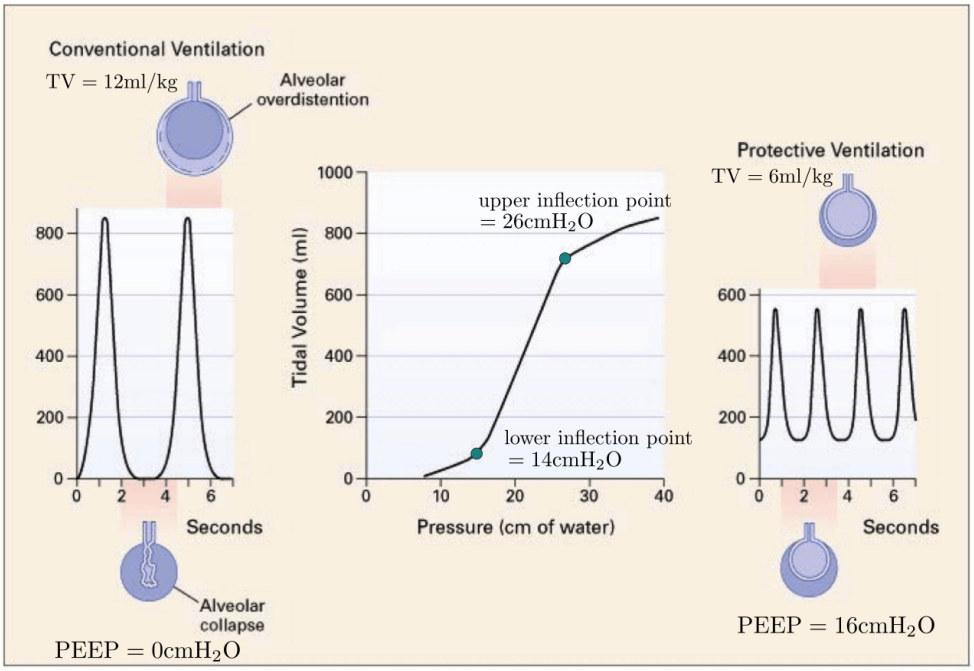

Figure 1.5.: Comparison between conventional and protective mechanical ventilation in a 70 kg patient suffering from ARDS. The conventional strategy with a tidal volume of TV = 12 ml/kg leads to cyclic collapse and overdistension of lung tissue. The P-V curve reveals a lower inflection point at 14 cmH_2O and an upper inflection point at 26 cmH_2O. Thus ventilation with a PEEP of 2 cmH_2O above the lower inflection point and a reduced tidal volume leads to adequate tissue aeration without mechanical damage of the lung. Adapted from [336] with permission.

Further, respiratory-gated positron emission tomography (PET) has been used to measure regional ventilation based on inhaled radiomarkers [360]. Though being spatially accurate, the same drawbacks as for CT imaging prevent the application of PET in a wide clinical practice. Further details on radiation-based medical imaging will be presented in Chapter 4.

A third approach based on the measurement of regionally changing electrical tissue impedance does exist in respiratory imaging and is due to its underlying principle termed electrical impedance tomography (EIT) [46, 48, 107]. EIT works without harmful X-ray radiation and is thus a promising long-time monitoring method for regional lung ventilation that will be presented in the next section.

1.3.1. Electrical Impedance Tomography (EIT)

Electrical impedance tomography (EIT) is a non-invasive, radiation-free imaging modality that allows the assessment of regional ventilation distribution at the bedside (see Figure 1.6 and [46, 48, 103, 107]).

In commercially available EIT systems suitable for chest EIT, a set of 16 (PulmoVista® 500 tomograph, Dräger medical, Lübeck, Germany) or 32 (BB^{2}® tomograph, Swisstom, Landquart,

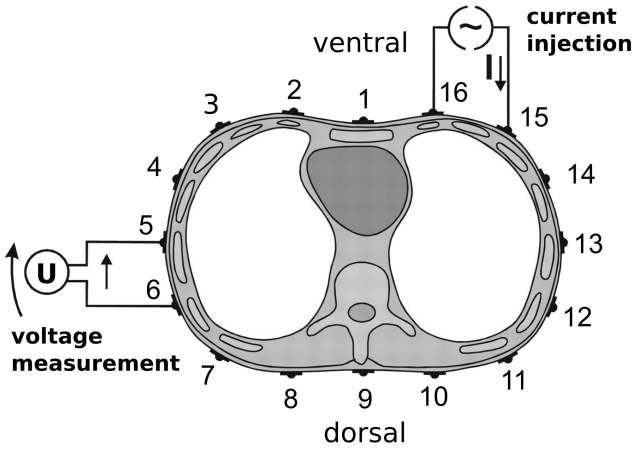

Figure 1.6.: Schematic of EIT imaging. A rotating stimulating current I is injected between adjacent electrodes and voltage U is measured between the remaining electrodes. Adapted from [104] with permission.

Switzerland) electrodes is placed on the patient's chest circumference in one plane. To generate EIT images, small alternating currents with a frequency of 50 kHz are sent into the studied subject, usually between adjacent pairs of electrodes. The resulting potential differences are detected by the remaining set of electrodes. By rotating the current injection around the chest circumference between all adjacent pairs of electrodes, a set of $\mathrm{N} = 208$ voltage measurements is obtained if 16 electrodes are used. This rotation procedure is repeated 50 times per second, where each rotation records voltages for a full image state. The acquired data is subsequently used for image reconstruction and generates an image with low spatial resolution (usually 32×32 px^2) and high temporal resolution (usually 50 Hz) of the patient's lung in the monitored plane.

EIT performs well in lung imaging as tissue resistivity considerably changes with ventilation. This is due to the inclusion of more insulating air in the alveoli and results in higher voltage measurements for the corresponding lung region. However, it is worth noticing that today clinically used impedance tomography observations mainly show functional physiological quantities (f-EIT). In respiratory f-EIT, a dynamic low resolution image visualises regional changes in electrical bioimpedance of lung tissue and thus the amount of regionally contained air against a predefined baseline, usually end-expiratory lung volume (EELV). In this work, any reference to EIT always means f-EIT. Also, state-of-the-art reconstruction algorithms such as the Graz consensus reconstruction algorithm for EIT (GREIT) [2] are reconstruction algorithms suitable for f-EIT.

In general, absolute EIT (a-EIT) [82] could be performed enabling a reconstruction of absolute tissue bioimpedance and thus a detailed identification of regions in the human body of different morphology similar to CT. However, absolute EIT measurements suffer from small errors in electrode positioning, variability in contact impedance at the skin and different individual thorax anatomy which altogether lead to reconstruction problems in the mathematically ill-posed problem of image reconstruction [163]. Therefore, they are not used in a clinical setting today.

Using the EIT, several groups have successfully carried out ventilation studies on neonates [27, 233], adults [224, 348, 350], in different body positions [208, 274] and even in microgravity

[104]. In this work, EIT is used for validation of regional tissue aeration resulting from computational lung modelling and will be presented in full detail in Chapter 5 and 6.

1.4. Objectives of this work

The content of this thesis was developed at the Institute of Computational Mechanics at Technische Universität München. All experimental work was performed in our Institute's section of the biology laboratory at the Zentralinstitut für Medizintechnik (IMETUM) at Technische Universität München. High Performance Computing (HPC) resources were provided via our Institute's HPC cluster and by the Leibniz Supercomputing Centre under the projects pr32ne "Coupled Problems in Computational Modeling of the Respiratory System" and pr83te "High Performance Methods for Computational Fluid Dynamics including Multiphysics Scenarios".

The main goals of this work are: (i) to build a toolbox of novel respiratory models based on the underlying physics of airflow and tissue dynamics; (ii) to apply these models to several patient-specific and clinically relevant settings in respiratory care and to validate all computed results against clinical measurements; (iii) to quantify regional overdistension and the possibility of collapse and reopening as main damage mechanisms in respiratory care and (iv) to exemplary show and evaluate patient-specific response to certain protective therapeutic measures suggested from clinical studies.

All models developed in this work are implemented in the finite element (FE) code BACI [353] and are partially based on previously reported approaches. The availability of BACI as a C++ based parallel multi-physics code allows integration of several third-party libraries such as general mesh decompositioning [299] and further parts of the Trilinos project [153] to address the solution of large-scale problems in biomedical engineering performed in this thesis.

The remainder of this work is organised as follows: In Chapter 2, the basic mathematical formulations for all investigated physical fields, i.e., fluid mechanics, solid mechanics, their interaction as well as transport dynamics will be introduced. Further, ideas for model simplification including dimensional reduction of the single components will be presented for investigations where such a simplified behaviour is applicable. Thereby, several novelties in respiratory modelling will be introduced at the relevant locations including e.g., the dynamics of airway closure and reopening, and the interaction between airways and the stabilising effect of surrounding lung tissue. In Chapter 3 models of airflow dynamics in and structural mechanics of the bronchial tree are combined with representations of lung tissue towards four coupled models in respiratory mechanics. Each of the four coupled models will be motivated in its underlying modelling idea and assumptions, evaluated in the novelty against previously reported methods, and discussed for possible scenarios of application and limitations in a clinical practice.

In the subsequent Chapters 4 to 7, the derived models are applied to real patient-specific settings in respiratory care. Chapter 4 focuses on fully three-dimensionally resolved representation of lung mechanics and a comparison between natural spontaneous breathing and mechanical ventilation in the same subject.

In Chapter 5, a first step towards validation of computed results with EIT is made. Therefore, a relationship between regional air content and bioimpedance of lung tissue is derived from simulations on highly-resolved imaging-based geometries of lung tissue.

Chapter 6 then combines advanced computational lung modelling and validation with EIT. The predictive capabilities of a powerful reduced-dimensional lung model are evaluated in a clinical setting and the quality of results is compared to global measurements. Further, a novel "virtual EIT" module is proposed to simulate EIT monitoring based on computed regional lung aeration. The resulting "virtual EIT" convincingly matches clinically measured EIT and raises the hope that the proposed novel computational models can be verified and are actually well-equipped to represent real lung behaviour.

Finally, in Chapter 7, the respiratory models are applied in a setting where the promise of good ventilation is highest - in the first breaths in life of neonates. Their yet incomplete lung structure and function requires special ventilation techniques which are up to now not fully understood. In Chapter 7, light will be shed on the efficiency of oxygenation using this special ventilatory techniques.

The achieved steps in computational modelling of respiratory mechanics that were made in this thesis are summarised and discussed in Chapter 8.

Further, possible directions for future research in the field of respiratory mechanics will be given going towards stresses and strains on the level of the alveolar wall in Appendix D and an experimental characterisation of the airway wall in Appendix C.

Part I.

Modeling Respiratory Mechanics

2. Basic mathematical formulations

The objective of this chapter is to give an overview over basic mathematical formulations that are required to accurately model respiratory mechanics. This comprises the incompressible Navier-Stokes equations for fully resolved three-dimensional fluid flow as well as dimensionally reduced fluid dynamics models. Further, the equations of non-linear solid mechanics are outlined accompanied by a dimensionally reduced model for soft tissue based on a generalised Maxwell model. Afterwards the interaction between fluid dynamics and structural mechanics in terms of fluid-structure interaction will be briefly discussed. Together, the four governing equations ((i) three-dimensional incompressible Navier-Stokes equations, (ii) reduced-dimensional fluid dynamics equations, (iii) three-dimensional non-linear solid mechanics equations, and (iv) generalised Maxwell equations) describe the building blocks for novel lung models presented in Chapter 3. Three recent extensions to the previously reported governing equations are outlined in this work. These include (i) the complex dynamics of airway closure and reopening in a dimensionally reduced fluid formulation, (ii) the important feature of lung interdependence in a dimensionally reduced structural model for soft tissue, and (iii) the interaction between lung tissue and embedded conducting airways.

Finally, the transport equations including the advection-diffusion equation will be presented, e.g., to model oxygen transport in the airflow. Moreover, the governing equations for EIT monitoring, i.e., the Laplace equations for electrostatics are outlined. A final objective of this chapter is to introduce basic notations for all physical fields that will be used throughout the rest of this work.

The content of this chapter is partly based on previous publications by the author, namely [283, 284, 286, 347, 372], which are used here with permission.

2.1. Fluid dynamics

The governing equations of fluid dynamics are one key component in respiratory modelling. In this work, fluid dynamics in the lung will be seen at two different resolutions: in a fully resolved three-dimensional (*3D*) formulation, or in a dimensionally reduced (*0D*) description. Fluid flow in the fully resolved three-dimensional case is governed by the incompressible Navier-Stokes equations and exhibits an extremely high level of detail (see Section 2.1.1). Using the methods of dimensional reduction, also known from cardiovascular mathematics [101], a solution for respiratory flow can be computed much faster and still exhibits physiologically realistic characteristics. The detailed dimensional reduction of the governing equations for fluid flow will be presented in Section 2.1.2.

More information on mathematical formulations of fluid flow can be found in [90] and [136]. Further ideas for dimensional reduction and suitable solution strategies are provided in [5, 101] specifically for the cardiovascular system and will be adapted to respiratory flow in the following.

2.1.1. Incompressible Navier-Stokes equations

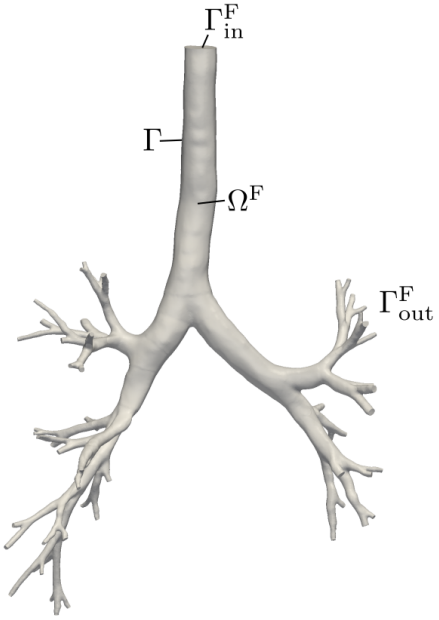

Figure 2.1.: First eight generations of a human bronchial tree pictured as fully resolved three-dimensional fluid domain Ω^{F}. The visualised inflow and outflow boundaries $\Gamma^{\mathrm{F}}_{\mathrm{in/out}}$ refer to the inhalation phase and are switched during exhalation.

Figure 2.1 shows a schematic representation of the fully resolved first eight generations of a human bronchial tree. Fluid flow in the domain Ω^{F} is governed by the incompressible Navier-Stokes equations. The assumption of incompressibility is well justified in this work, as air flows at velocities smaller than 20 m s^{-1} under physiological conditions (see e.g., Section 1.1.1, Chapter 4, and [72]). Hence, the Mach number is smaller than 0.2 and incompressibility of airflow can be assumed following [250]. Further, the fluid is assumed to be Newtonian with a constant density ρ^{F} and a constant kinematic viscosity ν^{F}.

The governing Navier-Stokes equations comprising the momentum equation, expressed in convective form, and the continuity equation read in Eulerian formulation

$$\frac{\partial \mathbf{u}^{\mathrm{F}}}{\partial t} + \mathbf{u}^{\mathrm{F}} \cdot \nabla \mathbf{u}^{\mathrm{F}} + \nabla p^{\mathrm{F}} - 2\nu^{\mathrm{F}} \nabla \cdot \boldsymbol{\varepsilon}(\mathbf{u}^{\mathrm{F}}) = \mathbf{f}^{\mathrm{F}} \quad \text{on} \quad \Omega^{\mathrm{F}} \times [0,t], \tag{2.1}$$

$$\nabla \cdot \mathbf{u}^{\mathrm{F}} = 0 \quad \text{on} \quad \Omega^{\mathrm{F}} \times [0,t]. \tag{2.2}$$

Here, the velocity vector is denoted as $\mathbf{u}^{\mathrm{F}}(\mathbf{x},t)$ and the kinematic pressure as $p^{\mathrm{F}}(\mathbf{x},t)$. The spatial coordinates are represented by $\mathbf{x} = (x_1, x_2, x_3)^{\mathrm{T}}$ and the time by t. The strain rate tensor $\boldsymbol{\varepsilon}(\mathbf{u}^{\mathrm{F}})$ is defined as

$$\boldsymbol{\varepsilon}(\mathbf{u}^{\mathrm{F}}) = \frac{1}{2}\left(\nabla \mathbf{u}^{\mathrm{F}} + \left(\nabla \mathbf{u}^{\mathrm{F}}\right)^{\mathrm{T}}\right) \tag{2.3}$$

and a volume force vector on the fluid is denoted as $\mathbf{f}^{\mathrm{F}}$. For a more detailed derivation of the governing equations for fully resolved three-dimensional fluid flow the reader is referred to [90] and [136] as well as [263].

The system of non-linear equations (2.1) and (2.2) are complemented by the following initial conditions (index 0) and boundary conditions for the velocity $\mathbf{u}^{\mathrm{F}}$ on the Dirichlet boundary $\Gamma_{\mathrm{D}}^{\mathrm{F}}$ and for the fluid traction $\mathbf{h}^{\mathrm{F}}$ for the Neumann boundary $\Gamma_{\mathrm{N}}^{\mathrm{F}}$

$$\mathbf{u}^{\mathrm{F}}(t=0) = \mathbf{u}_0^{\mathrm{F}} \quad \text{in} \quad \Omega_0^{\mathrm{F}}, \tag{2.4}$$

$$\mathbf{u}^{\mathrm{F}} = \hat{\mathbf{u}}^{\mathrm{F}} \quad \text{on} \quad \Gamma_{\mathrm{D}}^{\mathrm{F}} \times [0,t], \tag{2.5}$$

$$\mathbf{h}^{\mathrm{F}} = \hat{\mathbf{h}}^{\mathrm{F}} \quad \text{on} \quad \Gamma_{\mathrm{N}}^{\mathrm{F}} \times [0,t]. \tag{2.6}$$

The assignment of correct boundary conditions for the incompressible Navier-Stokes equations is critical to obtain a well-posed mathematical problem. Not all combinations of boundary conditions on the wall Γ, the inlet $\Gamma_{\mathrm{in}}^{\mathrm{F}}$ and the outlets $\Gamma_{\mathrm{out}}^{\mathrm{F}}$ pictured in Figure 2.1 are permitted following the argumentation in [136]. Further, the definition of the inlet and outlets of the fluid domain in Figure 2.1 is only valid during the inhalation phase. As the lung is the only organ in the human body, where flow fully reverses several times per minute, special considerations have to be made to accurately model exhalation, where inflow and outflow are switched.

One method to handle the occurring backflow into the domain is provided in [134]. Their approach, briefly recalled here, guarantees stability of airflow at the boundaries denoted as outlets $\Gamma_{\mathrm{out}}^{\mathrm{F}}$ during the exhalation phase, i.e., when actual inflow at these boundaries occurs. Following the approach by Gravemeier et *al.* [134] the traction at a Neumann boundary condition reads

$$-u_n^{\mathrm{F,in}}\mathbf{u}^{\mathrm{F}} - p^{\mathrm{F}}\mathbf{n} + 2\nu^{\mathrm{F}}\boldsymbol{\varepsilon}(\mathbf{u}^{\mathrm{F}}) \cdot \mathbf{n} = \mathbf{h}^{\mathrm{F}} \tag{2.7}$$

and is applied differently in case of inflow and outflow. The normal inflow velocity

$$u_n^{\mathrm{F,in}} = \frac{u_n^{\mathrm{F}} - |u_n^{\mathrm{F}}|}{2} \tag{2.8}$$

with

$$u_n^{\mathrm{F}} = \mathbf{u}^{\mathrm{F}} \cdot \mathbf{n} \tag{2.9}$$

and the outward-pointing unit normal vector $\mathbf{n}$ on the boundary is equal to u_n^{F} on a Neumann boundary which is also an inflow boundary $\Gamma_{\mathrm{N,in}}^{\mathrm{F}}$. On an outflow Neumann boundary $\Gamma_{\mathrm{N,out}}^{\mathrm{F}}$, $u_n^{\mathrm{F,in}}$ is zero and only the traction without the first term in Eq. (2.7) is prescribed.

Introducing the weighting functions $\mathbf{v}$ for the velocity and q for the pressure, the weak formulation of the Navier-Stokes momentum equation in a finite element context reads

$$\begin{aligned}\left(\mathbf{v}, \frac{\partial \mathbf{u}^{\mathrm{F}}}{\partial t}\right)_{\Omega^{\mathrm{F}}} + \left(\mathbf{v}, \mathbf{u}^{\mathrm{F}} \cdot \nabla \mathbf{u}^{\mathrm{F}}\right)_{\Omega^{\mathrm{F}}} - \left(\nabla \cdot \mathbf{v}, p^{\mathrm{F}}\right)_{\Omega^{\mathrm{F}}} + \left(\boldsymbol{\varepsilon}(\mathbf{v}), 2\nu^{\mathrm{F}}\boldsymbol{\varepsilon}(\mathbf{u}^{\mathrm{F,in}})\right)_{\Omega^{\mathrm{F}}} \\ - \underbrace{\left(\mathbf{v}, u_n^{\mathrm{F}}\mathbf{u}^{\mathrm{F}}\right)_{\Gamma_{\mathrm{N}}^{\mathrm{F}}}}_{\text{Neumann-inflow term}} = \left(\mathbf{v}, \mathbf{f}\right)_{\Omega^{\mathrm{F}}} + \left(\mathbf{v}, \mathbf{h}^{\mathrm{F}}\right)_{\Gamma_{\mathrm{N}}^{\mathrm{F}}}.\end{aligned} \tag{2.10}$$

Analogously the continuity equation can be written in a weak formulation as

$$\left(q, \nabla \cdot \mathbf{u}^{\mathrm{F}}\right)_{\Omega^{F}} = 0. \tag{2.11}$$

Compared to the classical weak formulation of the Navier-Stokes equations Eq. (2.10) is complemented by the first term in the second line. This term is no artificially added term but results

naturally from the integration by parts of Eq. (2.1). In many applications this term is omitted, if no part of the Neumann boundary is an inflow boundary $\Gamma^{\mathrm{F}}_{\mathrm{N,in}}$. If, however, inflow occurs at a Neumann boundary (e.g., during the exhalation phase in respiration) fluid flow would become unstable without such a formulation.

After spatial discretisation with finite elements, the semi-discrete from of the incompressible Navier-Stokes equations can be written as

$$\mathbf{M}^{\mathrm{F}}\dot{\mathbf{u}}^{\mathrm{F}} + \mathbf{N}^{\mathrm{F}}(\mathbf{u}^{\mathrm{F}}) + \mathbf{G}^{\mathrm{F}}\mathbf{p}^{\mathrm{F}} = \mathbf{f}^{\mathrm{F}}_{\mathrm{ext}} \tag{2.12}$$

$$\mathbf{G}^{\mathrm{F},T}\mathbf{u}^{\mathrm{F}} = \mathbf{0}. \tag{2.13}$$

with the fluid mass matrix $\mathbf{M}^{\mathrm{F}}$, the matrix $\mathbf{N}^{\mathrm{F}}(\mathbf{u}^{\mathrm{F}})$ containing the linear inner forces and the non-linear convective term, the discrete gradient operator $\mathbf{G}^{\mathrm{F}}$ and the external forces on the fluid $\mathbf{f}^{\mathrm{F}}_{\mathrm{ext}}$ [191]. The dot indicates a standard time derivative $\dot{()} = \partial()/\partial t$.

For discretisation in time of Eq. (2.12) and Eq. (2.13) a one-step-θ time integration scheme is used where the superscript $n+1$ denotes the current and n the previous time step. Inserting into Eq. (2.12) and Eq. (2.13) yields in Matrix notation

$$\begin{bmatrix} \mathbf{M}^{\mathrm{F}} + \theta\Delta t\mathbf{N}^{\mathrm{F}}\left(\mathbf{u}^{\mathrm{F},n+1}\right) & \theta\Delta t\mathbf{G}^{\mathrm{F}} \\ \mathbf{G}^{\mathrm{F},T} & \mathbf{0} \end{bmatrix} \begin{bmatrix} \mathbf{u}^{\mathrm{F},n+1} \\ \mathbf{p}^{\mathrm{F},n+1} \end{bmatrix} = \begin{bmatrix} \mathbf{M}^{\mathrm{F}}\left(\mathbf{u}^{\mathrm{F},n} + (1-\theta)\Delta t\dot{\mathbf{u}}^{\mathrm{F},n}\right) + \mathbf{f}^{\mathrm{F}}_{\mathrm{ext}} \\ \mathbf{0} \end{bmatrix}. \tag{2.14}$$

Remark 1: Discretisation with finite elements requires additional stabilisation terms in Eq. (2.14) which are not written here for brevity. For fully resolved fluid dynamics computations performed in this work, three classical stabilisation terms are used. To allow for equal-order interpolation, a pressure-stabilising Petrov-Galerkin (PSPG) term [171] is applied. Further, both a grad-div and a streamline upwind Petrov-Galerkin term [44] are included. For more details on stabilisation techniques, the reader is referred to [134, 172].

In the following sections of this work, the incompressible Navier-Stokes equations will merely be represented in full matrix expression, but rather via the non-linear discrete fluid operator

$$\mathbf{F}\left(\mathbf{u}^{\mathrm{F},n+1}, \mathbf{p}^{\mathrm{F},n+1}\right) = \mathbf{f}^{\mathrm{F,n+1}} \tag{2.15}$$

or the discrete non-linear residuum

$$\mathbf{r}^{\mathrm{F},n+1}\left(\mathbf{u}^{\mathrm{F},n+1}, \mathbf{p}^{\mathrm{F},n+1}\right) = \mathbf{F}\left(\mathbf{u}^{\mathrm{F},n+1}, \mathbf{p}^{\mathrm{F},n+1}\right) - \mathbf{f}^{\mathrm{F,n+1}}. \tag{2.16}$$

To obtain a solution of the Navier-Stokes equations, the non-linear residual $\mathbf{r}^{\mathrm{F},n+1}$ has to be zero. In this work, the solution is found using the Newton-Raphson method, which is in the following introduced for an arbitrary non-linear residuum $\mathbf{r}$. This residuum $\mathbf{r}$ is approximated via its linearised residuum $\tilde{\mathbf{r}}$ coming from a first order Taylor expansion around the solution vector $\mathbf{x}_i$ of the last iteration step i

$$\tilde{\mathbf{r}} = \mathbf{r}(\mathbf{x}_i) + \underbrace{\left.\frac{\partial \mathbf{r}(\mathbf{x})}{\partial \mathbf{x}}\right|_{\mathbf{x}_i}}_{\mathbf{K}_{\mathrm{T}}} \Delta\mathbf{x}_{i+1} = \mathbf{r}(\mathbf{x}_i) + \mathbf{K}_{\mathrm{T}}\Delta\mathbf{x}_{i+1}. \tag{2.17}$$

The current iteration step is indicated via the index $i+1$. The matrix $\mathbf{K}_\mathrm{T}$ denotes the effective tangential "stiffness" matrix and contains the linearisation of the residual with respect to the solution vector. To obtain the root of the linearised residual Eq. (2.17) the linear system of equations has to be solved

$$\mathbf{K}_\mathrm{T}\Delta\mathbf{x}_{i+1} = -\mathbf{r}(\mathbf{x}_i) \tag{2.18}$$

and the solution vector is updated following

$$\mathbf{x}_{i+1} = \mathbf{x}_i + \Delta\mathbf{x}_{i+1}. \tag{2.19}$$

The iteration procedure is repeated until a given tolerance criterion is met. In this work, the L2-norm of the residual is used as convergence criterion and has to be smaller than the given tolerance $||\mathbf{r}(\mathbf{x}_{i+1})|| < \mathrm{tol}$. For more details on the Newton method for the Navier-Stokes equations, the reader is referred to [191, 192].

2.1.2. Reduced-dimensional fluid dynamics equations

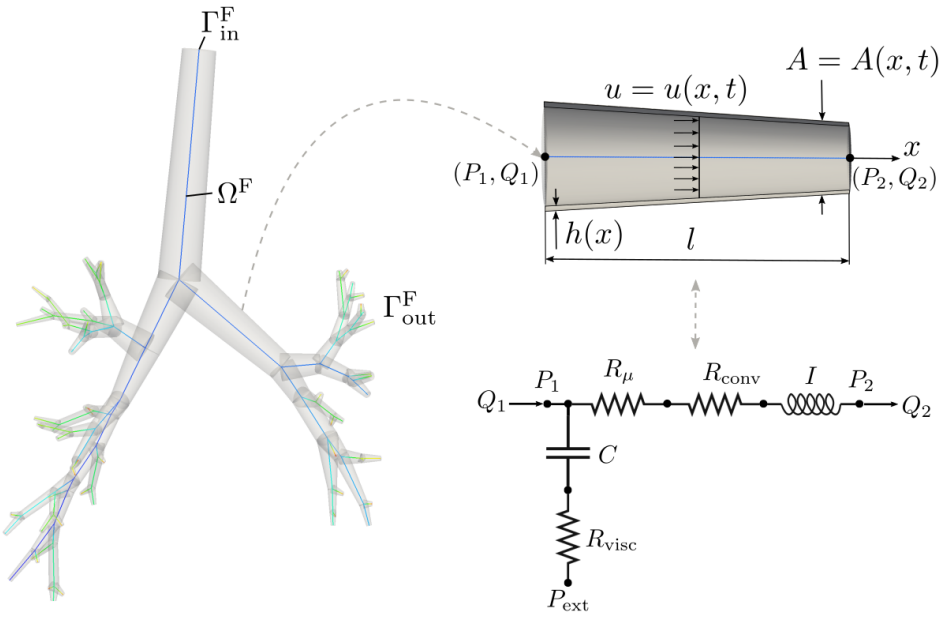

Figure 2.2.: First eight generations of a human bronchial tree visualised as reduced-dimensional formulation (left). The coloured centerline shows the connection of the single airway segments pictured as grey cylinders. The colouring of the centerline refers to different generation numbers. Illustration of a one-dimensional airway and notation used to describe flow in the simple compliant tube (right top). Electrical analogy of a reduced-dimensional fluid dynamics model representing Eq. (2.47) and Eq. (2.48) (right bottom). Image adapted from [176].

Under certain assumptions, flow in the conducting airways can be described via reduced-dimensional models derived from the governing equations for fully resolved fluid flow. The

applicability of such reduced-dimensional descriptions in questions of respiratory mechanics will be discussed in detail in Chapter 3. Here, the basic mathematical formulation will be derived for one-dimensional (*1D*) and zero-dimensional or lumped (*0D*) models.

2.1.2.1. *1D* fluid flow formulation

The derivation of *1D* flow equations is widely known in cardiovascular mathematics and the reader is referred to [5, 101, 305] for further details. Only the main features are briefly recovered here.

Airways are seen as straight compliant tubes aligned in x-direction as visualised in Figure 2.2 (right top). It is further assumed that the flow in an airway segment is axisymmetric and fully developed. The derivation of the *1D* formulation then applies the Reynolds transport theorem for an airway control volume V^{F} with the velocity profile integrated in radial direction in a cross-sectional slice. The conservation of mass and momentum for an incompressible fluid in a compliant airway control volume then read

$$\frac{\partial A}{\partial t} + \frac{\partial Q}{\partial x} = 0, \tag{2.20}$$

$$\frac{\partial Q}{\partial t} + \frac{\partial}{\partial x}\left(\alpha \frac{Q^2}{A}\right) + \frac{A}{\rho}\left(\frac{\partial p}{\partial x}\right) + K_{\mathrm{R}}\frac{Q}{A} = 0. \tag{2.21}$$

The cross-sectional area of the airway is denoted as A, the averaged flow in a cross-section as Q, the tube inner pressure as p and K_{R} represents the losses due to friction. Here, K_{R} quantifies the viscous resistance per unit length of the tube [306]. The axial direction of the tube is denoted as x and the time as t.

To close the system of equations, a non-linear relationship for pressure p dependent on the cross-sectional area A is formulated from a dynamic equilibrium of forces in radial direction following [99, 101, 196]

$$p = p_{\mathrm{ext}} + \beta_{\mathrm{w}}\left(\sqrt{A} - \sqrt{A_0}\right) + \frac{\gamma_{\mathrm{w}}}{A\sqrt{A}}\frac{\partial A}{\partial t}. \tag{2.22}$$

Here, p_{ext} is the tube external pressure, A_0 is the area at static equilibrium and β_{w} is defined by

$$\beta_{\mathrm{w}} = \frac{\sqrt{\pi} h_{\mathrm{w}} E_{\mathrm{w}}}{(1-\nu_{\mathrm{w}}^2) A_0} \tag{2.23}$$

in accordance with [101]. The vessel thickness is denoted as h_{w}, the Young's modulus of the wall as E_{w} and the Poisson ratio of the vessel wall ν_{w}. As biological tissues are almost incompressible, the Poisson ratio is assumed to be $\nu_{\mathrm{w}} = 0.49$ for the airway wall [101]. The variable γ_{w} is a visco-elastic coefficient that quantifies the temporal delay of changes in the cross-sectional area with respect to pressure changes. Following [177], the visco-elastic coefficient is defined via a visco-elastic time constant T_{w} and a visco-elastic phase shift Φ_{w} as

$$\gamma_{\mathrm{w}} = \frac{T_{\mathrm{w}} \tan\left(\Phi_{\mathrm{w}}\right) \beta_{\mathrm{w}}}{4\pi}. \tag{2.24}$$

2.1.2.2. *0D* fluid flow formulation

The equations Eq. (2.20) and Eq. (2.21) form a hyperbolic system of equations which exhibits a wave propagation character important e.g., in cardiovascular flow. With physical and geometrical parameters of airflow representative chosen for the 8th generation of the lung [66, 236], the material parameter β_w can be computed as

$$\beta_\mathrm{w} = \frac{\sqrt{\pi} h_\mathrm{w} E_\mathrm{w}}{(1-\nu_\mathrm{w}^2) A_0} = \frac{\sqrt{\pi} \cdot 0.9 \text{ mm} \cdot 15 \text{ kPa}}{(1-0.49^2) \cdot \pi \cdot (1.2 \text{ mm})^2} = 6.96 \text{ kPa mm}^{-1} \tag{2.25}$$

and results in a pressure wave speed c [101] of

$$c = \sqrt{\frac{\beta_\mathrm{w}\sqrt{A}}{2\rho^\mathrm{F}}} = \sqrt{\frac{6.96 \text{ kPa mm}^{-1} \cdot \sqrt{\pi \cdot (1.2 \text{ mm})^2}}{2 \cdot 10^{-6} \text{ g mm}^{-3}}} = 94.2 \text{ m s}^{-1}. \tag{2.26}$$

This means that in respiratory physiology pressure wave speed $c \approx 94$ m s^{-1} is much higher than actual fluid flow velocity ($u \leq 1$ m s^{-1} in small airways [359]). Given the typical length of an airway segment, the propagation time for the pressure wave is thus so small compared to the timescales of fluid flow, that the dynamics of wave propagation can be omitted if one is interested in fluid flow resolved on physiologically realistic timescales larger than $\Delta t = \Delta x / c \approx 0.09$ ms with $\Delta x < 9$ mm being the average length of an airway segment in the 8th generation.

Following the derivations in [101] and [177], averaging of pressure p, cross-sectional area A, and flow Q along the axial direction of an airway segment ($x_1 < x < x_2$) then leads to a simplification of the *1D* wave propagation equations towards the *0D* airway model. With definition of a mean volumetric flow rate over the entire airway segment of length $l = |x_2 - x_1|$ as

$$\hat{Q} = \frac{1}{l} \int_{x_1}^{x_2} \left(\int_A u dA \right) dx = \frac{1}{l} \int_{x_1}^{x_2} Q(x) dx, \tag{2.27}$$

a mean pressure as

$$\hat{p} = \frac{1}{l} \int_{x_1}^{x_2} p dx, \tag{2.28}$$

a mean tube external pressure as

$$\hat{p}_\mathrm{ext} = \frac{1}{l} \int_{x_1}^{x_2} p_\mathrm{ext} dx, \tag{2.29}$$

and a mean area as

$$\hat{A} = \frac{1}{l} \int_{x_1}^{x_2} A dx \tag{2.30}$$

Eq. (2.20) and Eq. (2.21) can be integrated in the axial direction. Detailed mathematics of the derivation can be found in Appendix A. For the continuity equation Eq. (2.20), integration results in

$$\int_{x_1}^{x_2} \left(\frac{\partial A}{\partial t} + \frac{\partial Q}{\partial x} \right) dx = 0 \tag{2.31}$$

$$\Rightarrow l \frac{d\hat{A}}{dt} + Q_2 - Q_1 = 0 \tag{2.32}$$

with

$$Q_1 = Q(x_1, t) \text{ and } Q_2 = Q(x_2, t). \tag{2.33}$$

For the momentum equation, it is additionally assumed that the variations of A and β_w along the x-direction are small compared to those of p and Q. This is particularly true if the distance for axial integration is small, and allows to replace A in equation Eq. (2.21) with a constant value usually chosen as A_0. With this simplification the axial integration of Eq. (2.21) reads

$$\int_{x_1}^{x_2} \left(\frac{\partial Q}{\partial t} + \frac{\partial}{\partial x}\left(\alpha \frac{Q^2}{A}\right) + \frac{A}{\rho}\left(\frac{\partial p}{\partial x}\right) + K_\mathrm{R}\frac{Q}{A}\right) dx = 0 \tag{2.34}$$

$$\Rightarrow \frac{\rho l}{A_0}\frac{d\hat{Q}}{dt} + \frac{2\alpha\rho}{A_0^2}\left(Q_2 - Q_1\right)Q_2 + P_2 - P_1 + \frac{\rho K_R l}{A_0^2}\hat{Q} = 0. \tag{2.35}$$

with

$$P_1 = p(x_1, t) \text{ and } P_2 = p(x_2, t). \tag{2.36}$$

The system of *0D* equations has to be closed by integrating the wall mechanics law from Eq. (2.22) in axial direction

$$\int_{x_1}^{x_2} \frac{\partial p}{\partial t} dx = \int_{x_1}^{x_2} \frac{\partial}{\partial t}\left(p_\mathrm{ext} + \beta_\mathrm{w}(\sqrt{A} - \sqrt{A_0}) + \frac{\gamma_\mathrm{w}}{A\sqrt{A}}\frac{\partial A}{\partial t}\right) \tag{2.37}$$

$$\Rightarrow \frac{2\sqrt{A}l}{\beta_\mathrm{w}}\left(\frac{d\hat{p}}{dt} - \frac{d\hat{p}_\mathrm{ext}}{dt}\right) + Q_2 - Q_1 + \frac{2\sqrt{A}l}{\beta_\mathrm{w}}\frac{\gamma_\mathrm{w}}{A\sqrt{A}l}\left(\frac{dQ_2}{dt} - \frac{dQ_1}{dt}\right) = 0 \tag{2.38}$$

The two equations Eq. (2.35) and Eq. (2.38) build the *0D* system of equations. Such *0D* formulations are often visualised using electrical analogies (see Figure 2.2). To exploit this analogy, the constants in Eq. (2.35) and Eq. (2.38) are rearranged to build an inductance I, a convective and a visco-elastic resistance R_conv and R_μ as well as a compliance C. The resistance R_visc represents the visco-elastic behaviour of the airway wall in case of volume changes of the airway segment.

$$I = \frac{\rho l}{A_0} = \frac{4\rho l}{\pi d_0^2} \tag{2.39}$$

$$R_\mathrm{conv} = \frac{2\alpha\rho}{A_0^2}\left(Q_2 - Q_1\right) \tag{2.40}$$

$$R_\mu = \frac{\rho K_R l}{A_0^2} \tag{2.41}$$

$$C = \frac{2\sqrt{A}l}{\beta_\mathrm{w}} = \frac{2\cdot(1-\nu_\mathrm{w})^2\cdot(A_0\sqrt{A}l)}{E_\mathrm{w}h_\mathrm{w}\sqrt{\pi}} \tag{2.42}$$

$$R_\mathrm{visc} = \frac{\gamma_\mathrm{w}}{A\sqrt{A}l} = \frac{T_\mathrm{w}\tan\Phi_\mathrm{w}}{2\pi C} \tag{2.43}$$

Here, d_0 denotes the diameter of an airway segment at static equilibrium, ρ the density of air, and Eq. (2.23) and Eq. (2.24) are used. Still, the viscous flow resistance R_μ (containing the

constant K_R) is not fully specified. In case of laminar, transitional or turbulent flow, the non-linear resistance of the conducting airways modelling viscous and turbulent losses in the flow is determined by

$$R_\mu = \frac{128\mu l}{\pi d_{\text{aw}}^4} \begin{cases} \gamma \left(\text{Re}\frac{d_{\text{aw}}}{l}\right)^{1/2} & \text{if Re} \geq \frac{l}{\gamma^2 d_{\text{aw}}} \\ 1 & \text{if Re} < \frac{l}{\gamma^2 d_{\text{aw}}} \end{cases} \tag{2.44}$$

following the idea in [176, 177]. The first term of Eq. (2.44) denotes the Poiseuille resistance for laminar flow through an airway with diameter d_{aw} and a parabolic velocity profile. The generation dependent prefactor γ respecting potential turbulence was determined experimentally by [93] and is listed in Table 2.1. The Reynolds number Re is defined as

$$\text{Re} = \frac{4\rho\,|Q_{\text{in}}|}{\mu\pi d_{\text{aw}}}. \tag{2.45}$$

With this definition the airway model decides whether purely viscous or additional turbulent losses had to be respected depending on the flow. It is noted that also other (simpler) approaches to account for turbulent flow resistance are available [258, 277].

Table 2.1.: Prefactor γ for different airway generations taken from [93]

Generation	0	1	2	3	4	5	6	7	>7
γ	0.162	0.239	0.244	0.295	0.175	0.303	0.356	0.566	0.327

Finally, the mean pressure $\hat{p}$ and the mean flow are approximated via the variables

$$\hat{p} \approx P_1 \;\text{ and }\; \hat{Q} \approx Q_2 \;\text{ and }\; \hat{p}_{\text{ext}} \approx (P_{\text{ext},1} + P_{\text{ext},2})/2 \tag{2.46}$$

which is again valid for a short airway segment [176]. Then the final *0D* flow model reads

$$C\left(\frac{dP_1}{dt} - \frac{dP_{\text{ext}}}{dt}\right) + Q_2 - Q_1 + C \cdot R_{\text{visc}}\left(\frac{dQ_2}{dt} - \frac{dQ_1}{dt}\right) = 0, \tag{2.47}$$

$$I\frac{dQ_2}{dt} + (R_\mu + R_{\text{conv}}) \cdot Q_2 + P_2 - P_1 = 0. \tag{2.48}$$

An electrical circuit representing the *0D* flow model in Eq. (2.47) and Eq. (2.48) is shown in Figure 2.2 (right bottom). Eq. (2.47) is obtained following the vertical path of the electrical circuit and Eq. (2.48) is coming from the horizontal path.

Discretisation in space using finite elements and in time using a backward Euler scheme results in the discrete non-linear formulation of the *0D* flow model for a single airway segment in matrix notation

$$\begin{bmatrix} -K_{\text{aw}} - K_{\text{aw,vis}} & K_{\text{aw}} \\ K_{\text{aw}} & -K_{\text{aw}} \end{bmatrix} \begin{bmatrix} P_1^{n+1} \\ P_2^{n+1} \end{bmatrix} = \begin{bmatrix} -Q^{n+1} - RHS_1^n \\ Q^{n+1} + RHS_2^n \end{bmatrix}. \tag{2.49}$$

or in brief written as *0D* fluid operator

$$\mathbf{K}\mathbf{P}^{n+1} = \mathbf{Q}^{n+1} + \mathbf{RHS}^n \tag{2.50}$$

The detailed discretisation procedure and the meaning of all abbreviation terms of Eq. (2.49) and Eq. (2.50) are outlined in Appendix B. The *0D* flow problem can again be solved via a Newton scheme (see Section 2.1.1).

2.1.2.3. Extension 1: Reopening dynamics in *0D* fluid flow

The presented reduced-dimensional flow model in Eq. (2.47) and Eq. (2.48) is able to respect diameter changes of the single airway segments via the compliance C. Still, one effect that has been missing in the derived reduced-dimensional flow model so far is full collapse and reopening of terminal structures during the respiration process. This behaviour, also termed recruitment (i.e., reopening) and derecruitment (i.e., collapse), or in brief R/D, is of utmost importance in respiratory care [195].

Two basic physical principles are associated with the occurrence of R/D in the lungs. The first one is the formation and breakup of a liquid bridge across the airway lumen. This theory of occluding fluid also known as "liquid plug" has been reported in several experimental and numerical studies [53, 375, 376]. The second effect is an elastic collapse of airways due to low inner pressure and retention of this state by the adherent forces of the airway's inner liquid lining [119, 181, 261]. The dynamic net effects arising from these reopening mechanisms have been combined in an empirical R/D model in [22]. Further, this empirical model has been suitable to mimic the behaviour of airway recruitment and derecruitment in mice [222]. Finally, it has been extended towards a symmetrical [211] and asymmetrical tree structure [293] and towards a quantification of lung damage introduced by reopening [145, 314].

Following the approach in [22, 211, 222], airways can exist in two states, either fully open or fully closed. Their current state is represented via a virtual trajectory variable $0 \leq x \leq 1$ where $x = 0$ corresponds to a fully closed and $x = 1$ to a fully open airway segment. The transition between these two states follows the trajectory law

$$\frac{dx(t)}{dt} = \begin{cases} s_{\mathrm{o}} \left(P_{\mathrm{aw}} - P_{\mathrm{o}} \right) & \text{for} \quad P_{\mathrm{aw}} > P_{\mathrm{o}} \\ s_{\mathrm{c}} \left(P_{\mathrm{aw}} - P_{\mathrm{c}} \right) & \text{for} \quad P_{\mathrm{aw}} < P_{\mathrm{c}} \\ 0 & \text{else.} \end{cases} \tag{2.51}$$

Here, the airway pressure P_{aw} is the average of airway pressures at its two ends $P_{\mathrm{aw}} = \left(P_1 + P_2 \right) / 2$. The critical opening pressure for an airway segment is denoted as P_{o} and the critical closing pressure as P_{c}. The reopening pressure of an airway segment is defined by a relationship [237] linking the diameter d_{aw} of an airway segment and the surface tension γ_0 of the liquid contained in the airway via

$$P_{\mathrm{o}} = 8.3 \cdot 2\gamma_0 / d_{\mathrm{aw}} \tag{2.52}$$

The two constants s_{o} and s_{c} set the reopening and closing speed together with the pressure differences $P_{\mathrm{aw}} - P_{\mathrm{o}}$ in case of reopening and $P_{\mathrm{aw}} - P_{\mathrm{c}}$ in case of closure (see Eq. (2.49)).

The governing equations for airway recruitment/derecruitment dynamics Eq. (2.51) are discretised in time using a forward Euler time integration scheme. The trajectory value in the current time step then reads

$$x^{n+1} = x^n + \left. \frac{dx(t)}{dt} \right|_n \Delta t.$$

In case an airway is initially closed and its trajectory variable x exceeds 1 the airway is instantly opened. Analogously, if the airway is initially open and x falls below 0 it is immediately closed. Closure of an airway segment is represented by a finite resistance value of

$R_\mu = 10^{10}$ cmH$_2$O s mL^{-1} [211]. Further, all airways and acini downstream the collapsed airway become derecruited immediately.

A validation of the implemented computational approach for simple scenarios of recruitment and derecruitment taken from [22] is presented in Appendix A. It is important to mention, that the decision for opening/closure is solved within the non-linear iteration loop of reduced-dimensional fluid equations, which means that a non-linearity coming from the reopening is directly included in the flow and vice versa. This enables investigations in highly non-linear avalanche-like patterns of reopening [321].

2.2. Structural mechanics

The objective of this section is to introduce the governing equations of soft tissue mechanics as the second key component in modelling respiratory mechanics. Again, two possible levels of resolution are existent to describe the mechanical behaviour of lung tissue. On the view of a three-dimensional continuum, lung tissue follows the equations of non-linear solid mechanics introduced in Section 2.2.1. Using seminal experimental work on lung tissue characterisation, two suitable constitutive laws are available to characterise lung tissue properties in a continuum sense [29, 273]. Following the concept of dimensional reduction on the other hand, simpler descriptions of lung tissue mechanics can be derived either directly from available continuum models, or from other experimental data such as the well-known alveolar duct model by Denny and Schroter [83, 85, 86] (see Section 2.2.2).

2.2.1. Non-linear solid mechanics

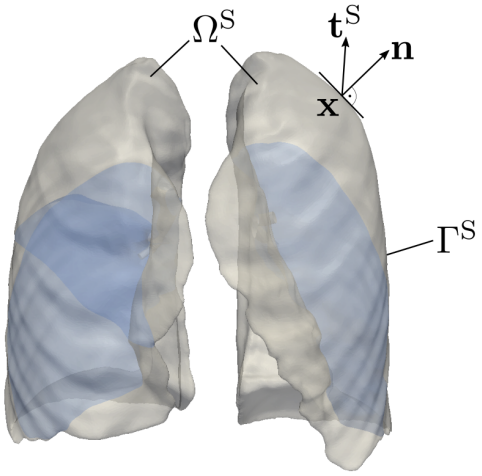

Figure 2.3.: The lung visualised in continuum mechanical description. The outer boundary of the left and right lung is marked in gray. The interfaces between neighbouring lobes in the left and right lung are marked in blue.

2.2.1.1. Governing equations

The mechanics of soft tissue in the continuum view are governed by the equations of non-linear elastodynamics describing a dynamic balance of momentum in an infinitesimal element of the structural domain Ω^{S}. It is important to note that the continuum description does not only apply to lung parenchyma defined in Section 1.1.2 and pictured in Figure 2.3, but can also be used for single alveolar walls modelled as continuum, e.g. in Chapter 5. The equations in the strong form read

$$\rho^{\mathrm{S}} \frac{d^2 \mathbf{d}^{\mathrm{S}}}{dt^2} = \nabla \cdot (\mathbf{F} \cdot \mathbf{S}) + \rho^{\mathrm{S}} \mathbf{b}^{\mathrm{S}} \text{ on } \Omega^{\mathrm{S}} \times [0, t]. \tag{2.53}$$

Here, ρ^{S} denotes density of the tissue and $\mathbf{d}^{\mathrm{S}}$ tissue displacements. The deformation gradient $\mathbf{F}$ is defined as

$$\mathbf{F} = \frac{\partial \mathbf{x}(\mathbf{X}_0, t)}{\partial \mathbf{X}_0} \tag{2.54}$$

with $\mathbf{x}$ being the spatial coordinates in current configuration and $\mathbf{X}_0$ in the reference configuration. The deformation gradient $\mathbf{F}$ can be interpreted as mapping from the reference to the current configuration (push forward). The tensor $\mathbf{S}$ denotes the second Piola-Kirchhoff stress tensor and results from a constitutive law explained in more detail in the next section. The vector $\mathbf{b}^{\mathrm{S}}$ denotes potential body forces.

Eq. (2.31) is completed by a suitable set of initial conditions for the displacements $\mathbf{d}^{\mathrm{S}}$ and the velocities $\dot{\mathbf{d}}^{\mathrm{S}}$ in the reference structural domain Ω_0^{S}

$$\mathbf{d}^{\mathrm{S}}(t=0) = \hat{\mathbf{d}}_0^{\mathrm{S}} \quad \text{in} \quad \Omega_0^{\mathrm{S}}, \tag{2.55}$$

$$\dot{\mathbf{d}}^{\mathrm{S}}(t=0) = \hat{\dot{\mathbf{d}}}_0^{\mathrm{S}} \quad \text{in} \quad \Omega_0^{\mathrm{S}}. \tag{2.56}$$

The boundary conditions on the Dirichlet boundary $\Gamma_{\mathrm{D}}^{\mathrm{S}}$ and on the Neumann boundary $\Gamma_{\mathrm{N}}^{\mathrm{S}}$ also in the reference configuration read

$$\mathbf{d}^{\mathrm{S}} = \hat{\mathbf{d}}^{\mathrm{S}} \quad \text{on} \quad \Gamma_{0,\mathrm{D}}^{\mathrm{S}} \times [0, t], \tag{2.57}$$

$$(\mathbf{F} \cdot \mathbf{S}) \cdot \mathbf{n}_0 = \hat{\mathbf{t}}^{\mathrm{S}} \quad \text{on} \quad \Gamma_{0,\mathrm{N}}^{\mathrm{S}} \times [0, t]. \tag{2.58}$$

Similar to the way presented for the Navier-Stokes equations in Section 2.1.1, a finite element formulation for the fully resolved non-linear solid mechanics equations would now require a weak formulation of Eq. (2.53) and Eq. (2.58). This weak formulation is then discretised in space and results in the semi-discrete equations of motion for fully resolved structural mechanics

$$\mathbf{M}^{\mathrm{S}} \ddot{\mathbf{d}}^{\mathrm{S}} + \mathbf{f}_{\mathrm{int}}^{\mathrm{S}} = \mathbf{f}_{\mathrm{ext}}^{\mathrm{S}} \tag{2.59}$$

with the structural mass matrix $\mathbf{M}^{\mathrm{S}}$, the non-linear vector of internal forces $\mathbf{f}_{\mathrm{int}}^{\mathrm{S}}$ and the vector of the applied volume and boundary forces $\mathbf{f}_{\mathrm{ext}}^{\mathrm{S}}$.

For discretisation of Eq. (2.59) in time a generalised-α method [64] is used and the discrete equations of non-linear elastodynamics read

$$\begin{aligned}
&\frac{1-\alpha_m}{\beta^* \Delta t^2}\mathbf{M}^{\mathrm{S}}\mathbf{d}^{\mathrm{S},n+1} + (1-\alpha_f)\,\mathbf{f}_{\mathrm{int}}^{\mathrm{S}}\left(\mathbf{d}^{\mathrm{S},n+1}\right) \\
&= (1-\alpha_f)\,\mathbf{f}_{\mathrm{ext}}^{\mathrm{S},n+1} + \alpha_f \mathbf{f}_{\mathrm{ext}}^{\mathrm{S},n} \\
&+ \mathbf{M}^{\mathrm{S}}\left(\frac{1-\alpha_m}{\beta^* \Delta t^2}\mathbf{d}^{\mathrm{S},n} + \frac{1-\alpha_m}{\beta^* \Delta t}\dot{\mathbf{d}}^{\mathrm{S},n} + \frac{1-\alpha_m-2\beta^*}{2\beta^*}\ddot{\mathbf{d}}^{\mathrm{S},n}\right) \\
&- \alpha_f \mathbf{f}_{\mathrm{int}}^{\mathrm{S}}\left(\mathbf{d}^{n}\right).
\end{aligned} \tag{2.60}$$

In the rest of this work, the equations of non-linear elastodynamics will be abbreviated as non-linear discrete structural operator

$$\mathbf{S}\left(\mathbf{d}^{\mathrm{S},n+1}\right) = \mathbf{f}^{\mathrm{S},n+1} \tag{2.61}$$

or the corresponding non-linear discrete residuum

$$\mathbf{r}^{\mathrm{S},n+1}\left(\mathbf{d}^{\mathrm{S},n+1}\right) = \mathbf{S}\left(\mathbf{d}^{\mathrm{S},n+1}\right) - \mathbf{f}^{\mathrm{S},n+1}. \tag{2.62}$$

Again, the solution of the non-linear structural problem is obtained via a Newton method explained in detail in [191]. For more information on the procedure sketched above the reader is e.g., referred to [164, 191, 377].

2.2.1.2. Suitable constitutive laws characterising lung tissue behaviour

A constitutive law for lung tissue is defined via a suitable non-linear strain-energy density function (SEF) Ψ which is able to describe the mechanical behaviour of lung tissue e.g., observed in experiments [29, 273]. Strain-energy density functions Ψ are often formulated with the right Cauchy-Green tensor $\mathbf{C}$ defined as

$$\mathbf{C} = \mathbf{F}^T\mathbf{F} \tag{2.63}$$

and the invariants of $\mathbf{C}$

$$I_1(\mathbf{C}) = tr(\mathbf{C}) \tag{2.64}$$

$$I_2(\mathbf{C}) = \frac{1}{2}\cdot\left(tr(\mathbf{C})^2 - tr(\mathbf{C}^2)\right) \tag{2.65}$$

$$I_3(\mathbf{C}) = det(\mathbf{C}). \tag{2.66}$$

From the strain-energy-density functions, the Second Piola-Kirchhoff stress tensor $\mathbf{S}$ can be obtained via

$$\mathbf{S} = 2\frac{\partial \Psi(\mathbf{C})}{\partial \mathbf{C}} \tag{2.67}$$

$$= 2\left(\frac{\partial \Psi}{\partial I_1} + I_1\frac{\partial \Psi}{\partial I_2}\right)\mathbf{I} - 2\frac{\partial \Psi}{\partial I_2}\mathbf{C} + 2I_3\frac{\partial \Psi}{\partial I_3}\mathbf{C}^{-1}. \tag{2.68}$$

For lung tissue in particular two strain-energy-density functions are identified from experiments: a Neo-Hookean like [35] law or alternatively a polynomial law combined with an Ogden [251] material law. The Neo-Hookean like strain energy function [35] based on the invariants of the right Cauchy-Green tensor $\mathbf{C}$ reads

$$\Psi_{\text{Neo}}(\mathbf{C}) = \frac{E}{4-4\nu^{\text{S}}}(I_1 - 3) + \frac{E(1-2\nu^{\text{S}})}{4\nu^{\text{S}} + 4(\nu^{\text{S}})^2}(I_3^{-\frac{\nu^{\text{S}}}{1-2\nu^{\text{S}}}} - 1). \tag{2.69}$$

The experimentally identified constitutive parameters for lung parenchyma yield a Young's modulus of $E = 6.75$ kPa and a Poisson's ratio of $\nu^{\text{S}} = 0.3$ [273]. The Poisson ratio lower than 0.5 indicates compressibility of lung parenchyma. This compressibility does not apply to single alveolar walls, but results from the changes in the contained alveolar air in the parenchyma (see Section 1.1.2).

A second possible constitutive law for lung tissue that has been reported previously is based on a combination of a third order polynomial function combined with an Ogden material law [251]. This function is motivated by the so-called isochoric-volumetric split where the deformation gradient $\mathbf{F}$ is split multiplicatively in an isochoric (i.e., volume preserving) part $\bar{\mathbf{F}}$ and a purely volumetric part following

$$\mathbf{F} = J^{1/3}\bar{\mathbf{F}} \tag{2.70}$$

with

$$J = det(\mathbf{F}). \tag{2.71}$$

The split (or modified) right Cauchy-Green tensor then reads

$$\mathbf{C} = J^{2/3}\bar{\mathbf{C}} \tag{2.72}$$

and the modified invariants

$$\bar{I}_1 = I_1 J^{-2/3} \text{ and } \bar{I}_2 = I_2 J^{-4/3}. \tag{2.73}$$

Finally, with these definitions, the constitutive law for lung tissue presented in [29] reads

$$\Psi_{\text{Poly}}(\mathbf{C}) = k_1\left(\bar{I}_1 - 3\right) + k_3\left(\bar{I}_1 - 3\right)^3 + \frac{\kappa}{\beta^2}\left(\beta \ln J + J^{-\beta} - 1\right) \tag{2.74}$$

with the parameters k_1, k_3, κ and β. The last summand represents the Ogden material law [251].

The definition of further constitutive laws for lung tissue may be possible respecting the underlying requirements for strain-energy-density functions, namely the polyconvexity. For more details on the topic and for a listing of further constitutive laws for biomechanical soft tissues the reader is referred to [17].

2.2.2. Reduced-dimensional lung tissue mechanics equations

The development of a reduced-dimensional model for lung tissue is motivated by the fact that the mechanical behaviour of the respiratory base unit, i.e., the alveolar duct is well known [83, 85,

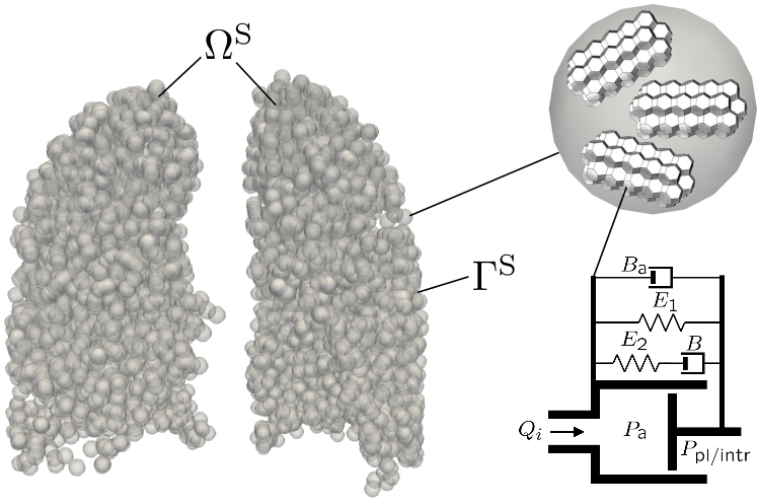

Figure 2.4.: Lung tissue visualised as reduced-dimensional model. The grey spheres represent the pulmonary acini. A single pulmonary acinus is filled with several alveolar ducts. A single alveolar duct is modelled via the generalised Maxwell model consisting of two springs and two dashpots connected as indicated. Image adapted from [176, 283].

86]. Therefore, a non-linear visco-elastic four-element Maxwell model has been developed in [176] and [283] which mimics this known behaviour of an alveolar duct. A single four-element Maxwell model is visualised in Figure 2.4 and consists of two springs E_1, E_2 and two dashpots B_1, B_2. The governing equations for this Maxwell model read

$$P_{\mathrm{ad}} + \frac{B}{E_2}\left(\frac{dP_{\mathrm{ad}}}{dt}\right) = \left(\frac{BB_a}{E_2}\right)\left(\frac{d^2V_i}{dt^2}\right) + (B_a + B)\left(\frac{dV_i}{dt}\right) + \frac{B}{E_2}\left(\frac{dP_{E1}}{dt}\right) + P_{E1}. \tag{2.75}$$

where

$$P_{E1} = E_1 \cdot (V_i - V_i^{\mathrm{o}}). \tag{2.76}$$

Here, V_i is the volume of an alveolar duct and V_i^{o} is the volume of an alveolar duct at the stress free state. The pressure P_{ad} of an alveolar duct is calculated as

$$P_{\mathrm{ad}} = P_{\mathrm{alv}} - P_{\mathrm{pl/intr}}.$$

where P_{alv} is the alveolar pressure and $P_{\mathrm{pl/intr}}$ is the pressure surrounding an alveolar duct. The single components of the four-element Maxwell model B, B_{a} and E_2 are constant and taken from literature [176]. The spring E_1 is non-linear to reproduce the behaviour of the lung under various conditions and large volume and pressure variations. The non-linearity of the spring E_1 requires a Newton-Raphson scheme for solution of the alveolar duct equation in the simulation of lung tissue. For more details on the solution of the non-linear duct equations, the reader is referred to [283].

It is well known that alveolar ducts have sigmoidal like P-V curves [86]. Such a double stiffening behaviour prevents the alveolar duct on the one hand from overinflation and on the other hand from collapse. In this work, the non-linear term E_1 is modelled using the following "double exponential stiffening" function [283]

$$E_1 = E_1^{\mathrm{u}} + E_1^{\mathrm{l}}, \tag{2.77}$$

$$E_1^{\mathrm{u}} = E_1^{\mathrm{o}} + b\left(V_i - V_i^{\mathrm{o}}\right) + \kappa^{\mathrm{u}} e^{\tau^{\mathrm{u}}\left(V_i - V_i^{\mathrm{o}}\right)}, \tag{2.78}$$

$$E_1^{\mathrm{l}} = \kappa^{\mathrm{l}} e^{\tau^{\mathrm{l}}\left(V_i - V_i^{\mathrm{o}}\right)}. \tag{2.79}$$

The parameters in Eq (2.75) are calibrated to the quasi-static P-V curves of a saline washed alveolar duct in [86] and to the dynamic loading at 1 Hz therein. As shown in [283] the calibrated parameters are well suited to mimic the behaviour of an alveolar duct presented in [86].

It is also possible to calibrate the alveolar duct with more sophisticated resolved *3D* models of the alveolar region including surfactant effects as presented in [273, 361]. A calibration from *3D* models allows to see the whole acinus as a *0D* element consisting of several ducts while maintaining its visco-elastic mechanical properties (e.g., investigated in [4, 220, 225]). In this work, such an approach is presented for the experimentally determined Ogden like material law from Section 2.2.1. It is assumed that a single alveolar duct within an acinus undergoes pure volumetric deformation during respiration. Even though the inflation of a single alveolar duct may be volumetric, this can result in an anisotropic deformation of the whole organ, e.g., if single ducts deform by a different magnitude in different locations. Such anisotropic behaviour is also observed by [11]. An exact derivation of the *0D* material law for the Ogden like alveolar duct resulting from the strain energy function is given in Appendix B. The resulting relationship between pressure and volume of an alveolar duct reads

$$P_{\mathrm{ad}} = \frac{\kappa}{\beta}\frac{V_i^o}{V_i}\left(1 - \left(\frac{V_i^o}{V_i}\right)^{\beta}\right) \tag{2.80}$$

Here, the initial volume of an alveolar duct for zero end-expiratory pressure was given as V_i^o and its current volume as V_i . Following the law in Eq. (2.80) a shape determining parameter β and a slope determining parameter κ uniquely define the relationship between pressure and current volume for each alveolar duct. This means that only two parameters have to be fit e.g., to represent patient specific lung behaviour with the Ogden like alveolar duct compared to six parameters in case of the "double exponential stiffening" function. An example of such a successful calibration to patient data will be presented in Chapter 6. However, the Ogden like alveolar duct is not able to mimic the lower part of the P-V curve where alveolar reopening occurs. Therefore, it is well suited for usage if reopening dynamics are modelled explicitly, e.g., via including the closure/reopening dynamics described in Section 2.1.2 for the terminal bronchi supplying single alveolar ducts.

Following [176, 283], an acinus is assumed to be built out of N_{ad} parallel alveolar ducts having the same properties. This means that the total air flow rate Q_{ac} in an acinus can be defined as

$$Q_{\mathrm{ac}} = \sum_{i=1}^{N_{\mathrm{ad}}} Q_i = N_{\mathrm{ad}} Q_i \tag{2.81}$$

with Q_i being the flow in a single alveolar duct. The volume of an acinus V_{ac} is denoted as

$$V_{\text{ac}} = \sum_{i=1}^{N_{\text{ad}}} V_i = N_{\text{ad}} V_i. \tag{2.82}$$

Thus an acinar model can be derived from Eq (2.75) as

$$\begin{aligned} N_{\text{ad}} P_{\text{ac}} + N_{\text{ad}} \frac{B}{E_2} \left(\frac{dP_{\text{ac}}}{dt} \right) = \left(\frac{BB_a}{E_2} \right) \left(\frac{d^2 V_{\text{ac}}}{dt^2} \right) + (B_a + B) \left(\frac{dV_{\text{ac}}}{dt} \right) \\ + N_{\text{ad}} \frac{B}{E_2} \left(\frac{dP_{E1}}{dt} \right) + N_{\text{ad}} P_{E1}. \end{aligned} \tag{2.83}$$

Similar to the *0D* flow model, discretisation with finite elements in space and a backward Euler scheme in time leads to the matrix formulation of the reduced-dimensional lung tissue mechanics equations

$$\begin{bmatrix} -K_{ac} & K_{ac} \\ K_{ac} & -K_{ac} \end{bmatrix} \begin{bmatrix} P_{\text{alv}}^{n+1} \\ P_{\text{pl/intr}}^{n+1} \end{bmatrix} = \begin{bmatrix} -Q_{\text{ac}}^{n+1} - LHS^n \\ Q_{\text{ac}}^{n+1} + LHS^n \end{bmatrix}. \tag{2.84}$$

A detailed derivation and definition of the abbreviated variables can be found in Appendix B.

2.2.2.1. Extension 2: Lung interdependence equations

An important effect that adds significant stability to the lung is the interaction between neighbouring air spaces, or whole acini, known as lung interdependence [228]. Contrary to the former use of Laplace's law for inflation of a single acinus, relevant studies have shown that the morphology of lung tissue is not made of single spheres but rather out of a polygonal tissue structure with embedded air spaces (see e.g. Figure 1.3 and [266]). This tissue "matrix" allows to transfer forces between air spaces that share a common wall and introduces an interdependence in the inflation of neighbouring alveoli/acini.

The concept of lung interdependence has for the first time been described in the seminal work by Mead et *al.* [228]. They stated that single air spaces are solely distended by forces coming from the surrounding tissue. An effective pressure which then distends the currently observed air space can be derived from these forces by relating them on the areas on which they act. In homogeneously distended lungs, the effective pressure corresponds to transpulmonary pressure. In heterogeneously distended diseased lungs, the effective pressure deviates from transpulmonary pressure and it is of utmost importance to accurately respect this deviation for a reliable quantification of stress distribution in a diseased lung.

In terms of computational modelling, lung interdependence is inherent in the fully resolved three-dimensional representation of lung tissue presented in Section 2.2.1. In the dimensionally reduced structural models, the effect of interdependence could not be modelled until [177, 283] and inter-alveolar interactions have only be respected by the underlying airway tree in terms of pendelluft flows [156]. Including the concept of lung interdependence leads to several advances in reduced-dimensional respiratory modelling. First, it allows to apply pleural pressure only to those acini which are in direct contact with the pleura while in previous approaches (e.g., [176])

pleural pressure had to be assigned to all acini. Respecting interdependence, a physiologically correct distribution of pleural pressure inside the lung is obtained automatically. Further, volume competition and several effects resulting from possible sources of heterogeneity during inflation can now be modelled directly via the lung tissue.

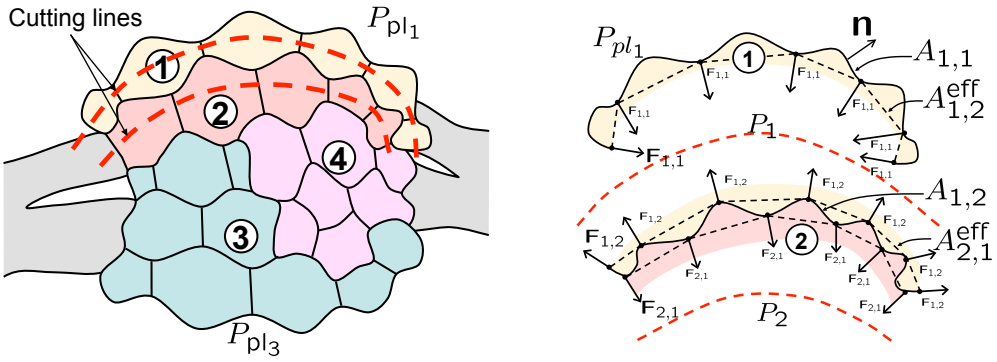

Figure 2.5.: Schematic representation showing an ensemble of four colour-coded acini (left) and the balance of forces along the two cutting lines through acinus 1 and acinus 2 (right). Images adapted from [177, 283].

A first attempt in computational modelling of interdependence has been presented in [177], however, without true validation. A thorough derivation of the equations for lung interdependence is presented in [283] and only the main ideas are recalled here. Figure 2.5 shows an exemplary ensemble of four colour-coded acini (numbers 1-4). The subscript $(\cdot)_{\mathrm{ac}}$ is omitted here for brevity. Each acinus consists of several single alveoli where the alveolar walls are indicated by thin black lines in a region of the same colour. Acini 2 and 3 are supplied with air via two bronchioli from the left and acini 1 and 4 via two bronchioli from the right displayed in grey. The outer boundaries of acini 1 and 3 which are not connected to the bronchioli are seen as pleural surfaces and subjected to pleural pressures P_{pl_1} and P_{pl_3}, respectively. Following the approach in [228] a static balance of forces is computed along two cutting lines in Figure 2.5. This static balance of forces exemplary written for acinus 1 can be found in [177] and [283]. For a general case where an acinus i is surrounded by multiple acini j, the balance of forces has to sum over all neighbouring acini j and their corresponding interface surfaces $A^{\mathrm{eff}}_{j,i}$ with acinus i

$$P_i A^{\mathrm{eff}}_i - \sum F_{i,i} - P_{\mathrm{pl}_i} A^{\mathrm{eff}}_{i,i} - \sum_{j \neq i} P_j A^{\mathrm{eff}}_{j,i} + \sum_{j \neq i} F_{j,i} = 0. \tag{2.85}$$

with P_i being the inner pressure of acinus i, A^{eff}_i its entire effective surface and $A^{\mathrm{eff}}_{i,i}$ its surface in contact with the pleural pressure P_{pl_i}.

Additionally, an inter-acinar pressure P_{intr_i} is defined as a fictitious pressure that replaces the forces $\sum F_{i,i}$ generated by its own elastic recoil and the forces $\sum F_{j,i}$ generated from the elastic recoil of the neighbouring acini, or mathematically

$$\sum F_{i,i} = \left(P_i - P_{\mathrm{intr}_i}\right) A^{\mathrm{eff}}_i, \tag{2.86}$$

$$\sum_{j \neq i} F_{j,i} = \sum_{j \neq i} \left(P_i - P_{\mathrm{intr}_j}\right) A^{\mathrm{eff}}_{j,i}. \tag{2.87}$$

Referencing to A_i^{eff}, Eq. (2.85) can be rewritten as

$$P_{\text{intr}_i} - P_{\text{pl}_i} \frac{A_{i,i}^{\text{eff}}}{A_i^{\text{eff}}} - \sum_{j \neq i} P_{\text{intr}_j} \frac{A_{j,i}^{\text{eff}}}{A_i^{\text{eff}}} = 0. \tag{2.88}$$

Throughout this work it is assumed that the surface area of an acinus is shared equally by its neighbouring acini. This implies that $A_{i,k}^{\text{eff}} = A_{i,j}^{\text{eff}}$ in Eq (2.88) and leads to the final interdependence equation for an acinus i

$$P_{\text{intr}_i} - \frac{P_{\text{pl}_i}}{N_i} - \sum_{j \neq i} \frac{P_{\text{intr}_j}}{N_i} = 0, \tag{2.89}$$

where N_i is the total number of neighbouring acini and pleural spaces of the observed acinus i.

In practice, the number of neighbouring acini N_i of the current acinus under observation is obtained from a search algorithm [177, 283]. For more details and a in-depth discussion of lung interdependence, the reader is referred to [177, 283].

2.2.2.2. Extension 3: Equations for airway-acinus interaction

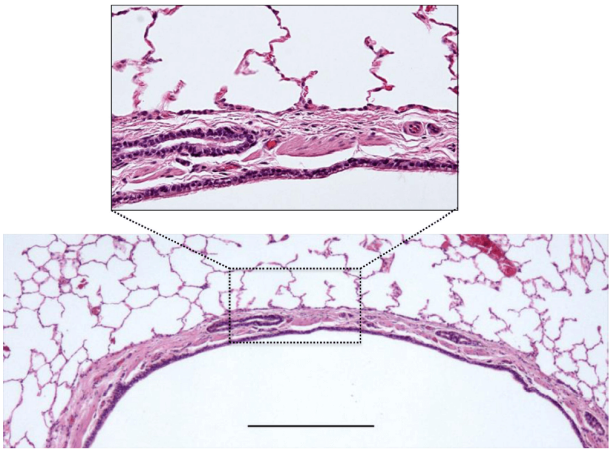

Figure 2.6.: Histological section showing an airway embedded into the alveoli. Image are taken from [256] with permission.

Similar to the concept of lung interdependence described for neighbouring alveolar/acinar structures, the underlying balance of forces also exists for airways embedded into the alveoli. This means that the airways sense the pressure coming from the surrounding tissue and react accordingly, i.e., with compression in case of higher external pressure or with expansion in case of lower surrounding pressure.

A detailed investigation on the interaction between airways and surrounding tissue can be found in [212, 256] and the references therein. Here it is assumed that the same balance of forces holds for airway-acinus interaction as for acinar interdependence (see Eq. (2.89)). However, now the pressure required for static equilibrium is not the pressure of the current acinus, but

the external pressure P_{ext_i} of the current airway segment under observation (see Eq. (2.47)). Further, it is assumed that airways have no contact with the pleura and thus the pleural pressure contribution can be omitted. The governing equation for airway-acinus interaction then reads

$$P_{\text{ext}_i} - \sum_{j \neq i} \frac{P_{\text{intr}_j}}{N_i} = 0, \tag{2.90}$$

where N_i is the total number of neighbouring acini of the observed airway segment i.

In practice, the neighbouring acini for an airway segment are detected via a search algorithm analogue to the acinar interdependence search algorithm (see e.g., [283]).

2.3. Fluid-structure interaction in Arbitrary Lagrangian-Eulerian formulation

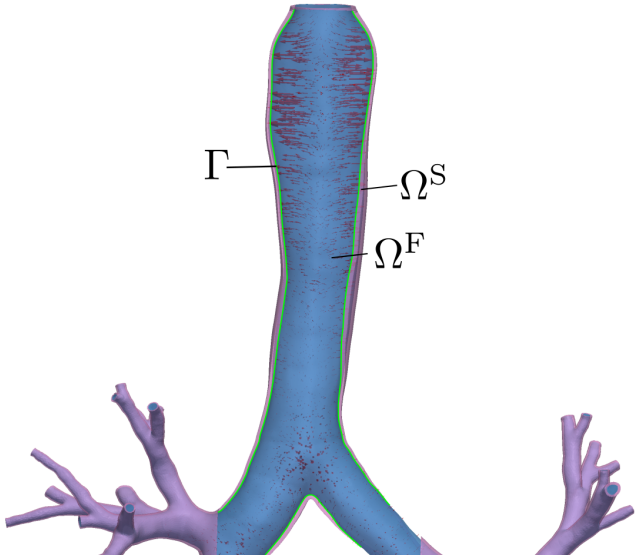

Figure 2.7.: An example of fluid-structure interaction between airflow pictured in blue and compliant airway walls pictured in red. The interface Γ marked in green is moving due to the fluid pressure. The red arrows indicate movement of the fluid domain following an Arbitrary Lagrangian-Eulerian (ALE) approach.

As outlined in the previous sections, airflow in the lung does not occur in rigid tubes but rather in flexible airways which deform during respiration depending on the airflow. To model this effect in fully resolved three-dimensional simulations, fluid-structure interaction (FSI) algorithms have to be considered.

For an extensive review on available FSI algorithms, with a specific focus on biomedical problems, the reader is referred to [193]. In brief, two approaches exist to model the interaction between fluid and solid domains: Partitioned schemes e.g., presented in [123, 191, 333], profit from the separate computation of the single fields with standard field solvers and possibly iterate

the coupling conditions at the interface until the FSI problem is converged. Monolithic schemes on the other hand, build a fully coupled non-linear FSI problem including the individual fields and coupling conditions. They provide a simultaneous solution for unknowns in all involved fields and have been successfully used in several cardiovascular and respiratory applications [150, 151, 352]. Recently, monolithic approaches have been shown to be the favourable choice in simulating FSI problems between incompressible fluid flow and elastic soft tissue [193] and are therefore used to model the interaction between airflow and compliant airway wall in the fully resolved *3D* lung models of this work (see Chapter 3).

To extend the governing equations of fluid flow introduced in Section 2.1.1 towards FSI, the fluid domain Ω^{F} is assumed to deform with the moving interface Γ (see Figure 2.7). One possibility to account for the moving interface Γ is the Arbitrary Lagrangian-Eulerian (ALE) approach. This approach is characterised by introducing a third, non-physical field which accounts for a continuously deforming fluid domain Ω^{F}. The deformation of the fluid domain depends on the interface displacements $\mathbf{d}_{\Gamma}^{\mathrm{S}}$ coming from the structure Ω^{S}. An arbitrary mapping $\varphi(\mathbf{d}_{\Gamma}^{\mathrm{S}}, \mathbf{x}_0, t)$ is defined for the ALE displacements $\mathbf{d}^{\mathrm{A}}$ in the fluid domain depending on the interface displacements $\mathbf{d}_{\Gamma}^{\mathrm{S}}$ and the initial coordinates $\mathbf{x}_0$ of the fluid domain

$$\mathbf{d}^{\mathrm{A}} = \varphi(\mathbf{d}_{\Gamma}^{\mathrm{S}}, \mathbf{x}_0, t) \quad \text{on} \quad \Omega^{\mathrm{F}} \times [0, t]. \tag{2.91}$$

In this work, the mapping is realised as an elastic pseudo-structure and follows the governing equations of elastostatics

$$\nabla \cdot \left(\mathbf{F}(\mathbf{d}^{\mathrm{A}}, \mathbf{d}_{\Gamma}^{\mathrm{S}}) \cdot \mathbf{S}(\mathbf{d}^{\mathrm{A}}, \mathbf{d}_{\Gamma}^{\mathrm{S}}) \right) = \mathbf{0} \quad \text{on} \quad \Omega^{\mathrm{F}} \times [0, t]. \tag{2.92}$$

with the deformation gradient $\mathbf{F}(\mathbf{d}^{\mathrm{A}}, \mathbf{d}_{\Gamma}^{\mathrm{S}})$ and the second Piola-Kirchhoff stress tensor $\mathbf{S}(\mathbf{d}^{\mathrm{A}}, \mathbf{d}_{\Gamma}^{\mathrm{S}})$ of the ALE field. The only boundary conditions applied to the ALE field are those coming from the interface displacements $\mathbf{d}_{\Gamma}^{\mathrm{S}}$ on a full Dirichlet boundary of the ALE field.

Spatial discretisation with finite elements similar to the structural equations in Section 2.2.1 results in the discrete linear mesh motion equation

$$\mathbf{K}^{\mathrm{A}} \mathbf{d}^{\mathrm{A},n+1} = \mathbf{f}^{\mathrm{A}} \left(\mathbf{d}_{\Gamma}^{\mathrm{S},n+1} \right) \tag{2.93}$$

in brief denoted as discrete linear ALE operator

$$\mathbf{A} \left(\mathbf{d}^{\mathrm{A},n+1} \right) = \mathbf{0} \tag{2.94}$$

which is equal to the discrete linear ALE residual

$$\mathbf{r}^{\mathrm{A}} \left(\mathbf{d}^{\mathrm{A},n+1}, \mathbf{d}_{\Gamma}^{\mathrm{S},n+1} \right) = \mathbf{A} \left(\mathbf{d}^{\mathrm{A},n+1} \right). \tag{2.95}$$

Reformulating the governing equations for fluid flow, i.e., the incompressible Navier-Stokes equations in the deformable domain yields

$$\left. \frac{\partial \mathbf{u}^{\mathrm{F}}}{\partial t} \right|_{\mathbf{x}_0} + \left(\mathbf{u}^{\mathrm{F}} - \dot{\mathbf{d}}^{\mathrm{A}} \right) \cdot \nabla \mathbf{u}^{\mathrm{F}} + \nabla p^{\mathrm{F}} - 2\nu^{\mathrm{F}} \nabla \cdot \boldsymbol{\varepsilon}(\mathbf{u}^{\mathrm{F}}) = \mathbf{f}^{\mathrm{F}}, \tag{2.96}$$

$$\nabla \cdot \mathbf{u}^{\mathrm{F}} = 0 \tag{2.97}$$

where the time derivative of the ALE field defined as

$$\left.\frac{\partial \mathbf{u}^{\mathrm{F}}}{\partial t}\right|_{\mathbf{x}_0} = \frac{\partial \mathbf{u}^{\mathrm{F}}}{\partial t} + \dot{\mathbf{d}}^{\mathrm{A}} \cdot \nabla \mathbf{u}^{\mathrm{F}}. \tag{2.98}$$

For the incompressible Navier-Stokes equations in ALE formulation, the same boundary conditions as presented in Section 2.1.1 hold. Also, spatial discretisation with finite elements and temporal discretisation with a one-step-θ scheme leads to the discrete non-linear Navier-Stokes equations presented in Eq. (2.14). However, now all matrix entries depend on the mesh motion $\mathbf{d}^{\mathrm{A},n+1}$ and thereby implicitly on the deformation of the interface $\mathbf{d}_{\Gamma}^{\mathrm{S},n+1}$. The non-linear discrete fluid operator then changes to

$$\mathbf{F}\left(\mathbf{u}^{\mathrm{F},n+1}, \mathbf{d}^{\mathrm{A},n+1}, \mathbf{d}_{\Gamma}^{\mathrm{S},n+1}\right) = \mathbf{f}^{\mathrm{F,n+1}}. \tag{2.99}$$

For brevity, the discrete fluid pressure $\mathbf{p}^{\mathrm{F},n+1}$ and the discrete fluid velocity $\mathbf{u}^{\mathrm{F},n+1}$ have been merged into the vector $\mathbf{u}^{\mathrm{F},n+1}$. Finally, the discrete non-linear residuum of the Navier-Stokes equations in ALE formulation reads

$$\mathbf{r}^{\mathrm{F},n+1}\left(\mathbf{u}^{\mathrm{F},n+1}, \mathbf{d}^{\mathrm{A},n+1}, \mathbf{d}_{\Gamma}^{\mathrm{S},n+1}\right) = \mathbf{F}\left(\mathbf{u}^{\mathrm{F},n+1}, \mathbf{d}^{\mathrm{A},n+1}, \mathbf{d}_{\Gamma}^{\mathrm{S},n+1}\right) - \mathbf{f}^{\mathrm{F,n+1}}. \tag{2.100}$$

Additionally, at the FSI interface Γ the following coupling conditions hold

$$\boldsymbol{\sigma}^{\mathrm{F}} \cdot \mathbf{n} = \boldsymbol{\sigma}^{\mathrm{S}} \cdot \mathbf{n} \quad \text{on} \quad \Gamma, \tag{2.101}$$

$$\mathbf{u}^{\mathrm{F}} = \dot{\mathbf{d}}^{\mathrm{S}} \quad \text{on} \quad \Gamma, \tag{2.102}$$

$$\mathbf{d}^{\mathrm{A}} = \mathbf{d}^{\mathrm{S}} \quad \text{on} \quad \Gamma. \tag{2.103}$$

Here, $\boldsymbol{\sigma}^{\mathrm{F}}$ denotes the stress tensor of a Newtonian fluid

$$\boldsymbol{\sigma}^{\mathrm{F}} = -p^{\mathrm{F}}\mathbf{I} + 2\mu^{\mathrm{F}}\varepsilon(\mathbf{u}^{\mathrm{F}}) \tag{2.104}$$

with dynamic viscosity $\mu^{\mathrm{F}} = \nu^{\mathrm{F}} \cdot \rho^{\mathrm{F}}$ and the previously defined strain rate tensor $\varepsilon(\mathbf{u}^{\mathrm{F}})$. The tensor $\boldsymbol{\sigma}^{\mathrm{S}}$ denotes the stress tensor of the structure and $\mathbf{n}$ a unit normal vector on the interface Γ.

To solve the FSI problem in a monolithic fashion, the discrete non-linear residuals of all involved fields have to be zero, i.e., Eq. (2.62), Eq. (2.95), and Eq. (2.100) are recalled as

$$\mathbf{r}^{\mathrm{S}}(\mathbf{d}^{\mathrm{S}}) = 0, \tag{2.105}$$

$$\mathbf{r}^{\mathrm{A}}(\mathbf{d}^{\mathrm{A}}, \mathbf{d}_{\Gamma}^{\mathrm{S}}) = 0, \tag{2.106}$$

$$\mathbf{r}^{\mathrm{F}}(\mathbf{u}^{\mathrm{F}}, \mathbf{d}^{\mathrm{A}}, \mathbf{d}_{\Gamma}^{\mathrm{S}}) = 0. \tag{2.107}$$

The residuals correspond to the governing equations of structural mechanics, the equations for ALE grid motion and the incompressible Navier-Stokes equations for fluid flow. The unknowns in the above equations are the discrete vectors of structural displacements $\mathbf{d}^{\mathrm{S}}$, fluid grid displacements $\mathbf{d}^{\mathrm{A}}$ and the fluid velocity and pressure merged in $\mathbf{u}^{\mathrm{F}}$. All residuals correspond to the current time step $n+1$ and for brevity the superscript $n+1$ is omitted.

The system of non-linear equations Eq. (2.105) - Eq. (2.107) is solved at each time step of the FSI simulation. Following the Newton scheme introduced in Eq. (2.17), the linearisation of Eq. (2.105) - Eq. (2.107) reads

$$\begin{bmatrix} \frac{\partial \mathbf{r}^{\mathrm{S}}}{\partial \mathbf{d}^{\mathrm{S}}} & \mathbf{0} & \frac{\partial \mathbf{d}^{\mathrm{S}}}{\partial \mathbf{d}^{\mathrm{S}}} \\ \mathbf{0} & \frac{\partial \mathbf{r}^{\mathrm{A}}}{\partial \mathbf{d}^{\mathrm{A}}} & \frac{\partial \mathbf{r}^{\mathrm{A}}}{\partial \mathbf{u}^{\mathrm{F}}} \\ \frac{\partial \mathbf{r}^{\mathrm{F}}}{\partial \mathbf{d}^{\mathrm{S}}} & \frac{\partial \mathbf{r}^{\mathrm{F}}}{\partial \mathbf{d}^{\mathrm{A}}} & \frac{\partial \mathbf{r}^{\mathrm{F}}}{\partial \mathbf{u}^{\mathrm{F}}} \end{bmatrix}_i \begin{bmatrix} \Delta \mathbf{d}^{\mathrm{S}} \\ \Delta \mathbf{d}^{\mathrm{A}} \\ \Delta \mathbf{u}^{\mathrm{F}} \end{bmatrix}_i = - \begin{bmatrix} \mathbf{r}^{\mathrm{S}} \\ \mathbf{r}^{\mathrm{A}} \\ \mathbf{r}^{\mathrm{F}} \end{bmatrix}_i . \tag{2.108}$$

Solution of this system of equations yields the unknown solution increments for $\Delta \mathbf{d}^{\mathrm{S}}$, $\Delta \mathbf{d}^{\mathrm{A}}, \Delta \mathbf{u}^{\mathrm{F}}$ and the solution vector for the next iteration step $i+1$ is updated via

$$\mathbf{d}^{\mathrm{S}}_{i+1} = \mathbf{d}^{\mathrm{S}}_i + \Delta \mathbf{d}^{\mathrm{S}}_i, \tag{2.109}$$

$$\mathbf{d}^{\mathrm{A}}_{i+1} = \mathbf{d}^{\mathrm{A}}_i + \Delta \mathbf{d}^{\mathrm{A}}_i, \tag{2.110}$$

$$\mathbf{u}^{\mathrm{F}}_{i+1} = \mathbf{u}^{\mathrm{F}}_i + \Delta \mathbf{u}^{\mathrm{F}}_i. \tag{2.111}$$

It is important to note that the matrix entry representing the fluid equations $\partial \mathbf{r}^{\mathrm{F}} / \partial \mathbf{u}^{\mathrm{F}}$ has a saddle point structure resulting from the incompressible Navier-Stokes equations Eq. (2.97). Such a matrix structure requires special solution techniques e.g., presented in [52, 77]. For specific details on solution techniques for the FSI problem, the reader is referred to [191, 347].

2.4. Transport dynamics

2.4.1. Advection-diffusion equation

Up to now, the basic mathematical formulations have been presented to investigate airflow and lung tissue dynamics under various conditions. The primary function of the lung is, however, gas exchange and its simulation should be the ultimate goal in respiratory modelling as soon as ventilation is sufficiently understood.

Important steps towards gas exchange in the lung have been presented by Sapoval et *al.* [296] and in the references therein. Further, a one-dimensional tree like model for gas exchange has been proposed in [225] and [220], however, without a realistic tree structure for airways and blood vessels. Oxygen transfer in the acinus has been investigated by Filoche et *al.* [96] and Weibel et *al.* [358]. An reduced-dimensional model for oxygen exchange on a realistic airway and vessel tree geometry has recently been presented in [177, 286]. Such an approach is valuable for simulation of gas transport and exchange in the entire lung during spontaneous breathing and under classical mechanical ventilation techniques. Some ventilatory settings, e.g., HFOV presented in Chapter 7 require a fully resolved three-dimensional solution of the fluid and transport equations to capture all essential physiological effects. In terms of fully resolved three-dimensional simulations of gas transport in the lung, several publications are available e.g., in [187, 373]. However, many of them lack correct boundary conditions for fluid flow at the outlets of the fully resolved fluid domain. The approach by Choi et *al.* [60] used realistic boundary

conditions at the outlets by coupling with a reduced-dimensional tree. However, they do not explicitly solve for the oxygen concentration but use a so-called stretch rate analysis as surrogate for scalar mixing. A more detailed overview over previous approaches in simulating gas transport will be given together with the literature review on lung modelling in Section 3.1. In conclusion, compared to previously reported approaches of oxygen transport our approach is the first one to really compute the scalar oxygen concentration on a fully resolved three-dimensional patient-specific airway geometry with perfect match of anatomical data [356, 357] and realistic boundary conditions.

The the transport of a scalar quantity ϕ in the scalar domain Ω^ϕ is governed by the advection-diffusion equation which reads in local form

$$\frac{\partial \phi}{\partial t} + \nabla \cdot (\phi \mathbf{u} - D \nabla \phi) - \sigma(\phi) = 0 \quad \text{on} \quad \Omega^\phi \times [0, t]. \tag{2.112}$$

Here, D denotes the diffusivity and $\mathbf{u}$ the velocity of the scalar quantity. The reaction term $\sigma(\phi)$ is neglected for the rest of this work. A quantity often used in the classical scalar transport process is the flux $\mathbf{q}$

$$\mathbf{q} = \mathbf{u}\phi - D \nabla \phi \tag{2.113}$$

where the first term indicates a convective and the second term a diffusive transport.

Currently, the transport equations are written in conservative form and in spatial Eulerian configuration. For use in coupled problems, such as transport in the previously introduced FSI, Eq. (2.112) is rewritten in convective ALE formulation with the ALE grid velocity $\mathbf{u}^{\mathrm{A}}$ as

$$\frac{\partial \phi}{\partial t} + (\mathbf{u} - \mathbf{u}^{\mathrm{A}}) \nabla \phi - \nabla (D \nabla \phi) = 0. \tag{2.114}$$

The equation is complemented by the following initial and boundary conditions

$$\phi(t = 0) = \phi_0 \quad \text{on} \quad \Omega_0^\phi, \tag{2.115}$$

$$\phi = \hat{\phi} \quad \text{on} \quad \Gamma_D^\phi, \tag{2.116}$$

$$D \frac{\partial \phi}{\partial \mathbf{n}} = \hat{\mathbf{h}}^\phi \quad \text{on} \quad \Gamma_N^\phi \tag{2.117}$$

with a prescribed diffusive flux $\hat{\mathbf{h}}^\phi$.

Usually the transport equations are one-way coupled with the flow, i.e., transport of the scalar is dependent on the flow but flow is not dependent on the change of the scalar. Therefore, the advection-diffusion of the scalar is solved after the solution of the fluid (or FSI) problem is converged and $\mathbf{u} = \mathbf{u}^{\mathrm{F}}$ and $\mathbf{u}^{\mathrm{A}}$ are known. An example simulation including scalar transport will be given in Chapter 7 of this work in terms of oxygen transport in a neonatal lung.

2.4.2. Laplace equation

The last governing equation presented in this section is the Laplace equation. It is not directly linked to modelling respiratory mechanics itself but rather to model its monitoring. The previously described method of EIT (see Section 1.3.1) performs well in lung imaging and is therefore

also used for validation in this work. A "virtual EIT" module described in Chapter 6 mimics the EIT monitoring process based on the regional ventilation coming from any of the coupled lung models.

The physics behind the EIT monitoring process are those of electrostatics governed by the Laplace equation

$$\nabla \cdot \left(-\sigma^{\mathrm{E}} \nabla \Phi^{\mathrm{E}}(\mathbf{x})\right) = 0 \quad \text{on} \quad \Omega^{\mathrm{E}}. \tag{2.118}$$

Eq. (2.118) provides a relationship for the distribution of voltage $\Phi^{\mathrm{E}}(\mathbf{x})$ in the electrical domain Ω^{E} depending on the conductivity $\sigma^{\mathrm{E}}(\mathbf{x})$, where $\mathbf{x}$ again denotes the spatial coordinates in the current configuration. The equation is complemented by the following boundary conditions: The absolute potential level is usually set at the reference electrode via

$$\Phi^{\mathrm{E}} = \hat{\Phi}^{\mathrm{E}} \quad \text{on} \quad \Gamma^{\mathrm{E}}_{D}. \tag{2.119}$$

At the l-th electrode, an injected current density $\mathbf{j}_l$ is applied as a Neumann boundary

$$\sigma \frac{\partial \Phi^{\mathrm{E}}}{\partial \mathbf{n}} = \mathbf{j}_l \quad \text{on} \quad \Gamma^{\mathrm{E}}_{N,l}. \tag{2.120}$$

On the remaining boundaries, no-flux conditions are applied. A detailed finite element solution procedure for the Laplace equation can e.g., be found in [262] among others. More information on the virtual EIT monitoring process in practice will be given in Chapter 6.

2.5. Concluding remarks

A brief overview over basic mathematical formulations that are required to model lung behaviour in a physiologically meaningful sense has been given in this chapter. For the sake of brevity and non-repetitiveness, only the strong equations and the main ideas for suitable solution strategies have been presented in this work using the finite element method. The understanding of the non-linear residuals is sufficient to follow the ideas in computational respiratory modelling presented in the remainder of this work. For the interested reader, a variety of suitable literature on the single fields and their solution strategies has been given.

In the following chapter, the single introduced fields will serve as basic ingredients towards development of four novel coupled models in respiratory mechanics. The quantity and variety of different physical fields glances an idea that it is extremely complex to model respiratory mechanics at full length for each problem at hand. Therefore, suitable combinations of the single fields and recommendations for the use of dimensionally reduced equations will be given for exemplary applications in a clinical setting.

3. Coupled computational models of the respiratory system

The following chapter introduces computational models of the respiratory system available today. First, a comprehensive literature review and classification of previously reported modelling approaches used in respiratory mechanics is given (Section 3.1).

In Section 3.2, advanced computational models of the lung are introduced with a special focus on methods that are (i) based on the underlying physics of airflow dynamics and lung tissue mechanics, and (ii) able to tackle the interaction between these two physical fields. This interaction is essential in respiration and its modelling is necessary to accurately represent lung physiology.

Four novel "coupled" approaches are presented in this work which fulfil the two basic modelling criteria mentioned above. The four approaches result from combining one of the two possible levels of resolution for fluid flow described in Chapter 2 with one of the two underlying equations for lung tissue mechanics. Model introduction follows the same logical structure for each of the four methods in Section 3.2. The single approaches are introduced starting with their underlying modelling idea and assumptions. Further, the mathematical formulation, the novelty against previous approaches, possible scenarios of application, and limitations in a clinical practice are explained. The complexity of this new generation of coupled models is reviewed and strategies are presented for sensible and target-oriented use of dimensionally reduced governing equations derived in Chapter 2.

From the inherent complexity it becomes clear that there is no "one-size-fits-all" approach in the modelling of respiratory mechanics but one has to choose from a variety of different concepts to solve the current problem at hand [286]. A fair comparison presented in this chapter should guide the reader towards an adequate modelling approach for current and future questions in respiratory mechanics.

This chapter is primarily based on two previous publications by the author, which are re-used here with permission. Section 3.1 is taken from [286, 287]. Sections 3.2 and 3.3 are taken from [286, 347, 372].

3.1. Literature review

Recalling the past 50 years, classical lung modelling approaches from a physiological/clinical perspective were until recently mainly limited to parameter-fitting of single compartment model parameters (see below). However, from a biomechanical view, respiration covers a variety of complex and interacting phenomena including fluid dynamical, tissue mechanical, and gas transport processes. Specific phenomena are directly linked to observed immunological reactions and to the current health state of a patient, but often difficult to measure *in vivo* due to both ethical and technical reasons. Therefore, various efforts have been made in mechanical and mathemati-

cal modelling of the lung to (i) study isolated effects which are hard to assess in a subject *in vivo*, (ii) to advance medical imaging and functional diagnostic, and (iii) to finally assist in patient-specific treatment planning and optimisation. The current goal is to develop predictive models based on the underlying physics of the lung, driven by the awareness that it is more powerful to understand underlying processes in respiratory biomechanics than to only see their effects in clinical monitoring and medical imaging of a patient.

In this section, an overview of the current state of the art in modelling respiratory biomechanics is provided. Following basic lung anatomy (see Section 1.1), models for the conducting zone, the respiratory zone and coupled models combining both zones are available. Each zone can be realised at different levels of resolution, either as fully resolved three-dimensional continuum or as dimensionally reduced model. Corresponding governing equations for the conducting and respiratory zone at the two mentioned levels of resolution have been derived in Chapter 2. A classification following these two criteria (i) conducting zone/respiratory zone and (ii) reduced/continuum based description is visualised in Figure 3.1. In the subsequent sections the classified approaches will be discussed in detail from single zone towards more complex models in respiratory biomechanics. The coupled lung models developed in this work are included in this overview for completeness and will be discussed in detail in Section 3.2.

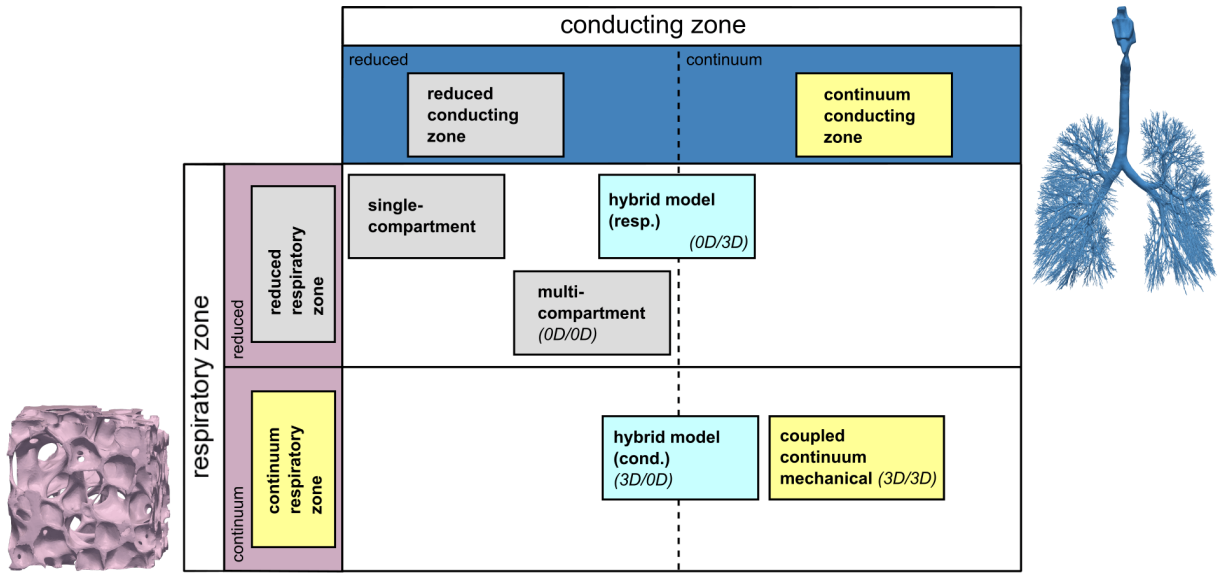

Figure 3.1.: Classification of models in respiratory biomechanics. Approaches for the respiratory and the conducting zone can be found in the red and blue parts of the table. Models combining both zones are given in the white part of the table. Reduced models are highlighted in grey, continuum models in yellow and hybrid (i.e., combined continuum and reduced) models in light blue. The coupled approaches developed in Section 3.2 of this work are marked in italics in the overview. Image adapted from [287] with permission.

3.1.1. Reduced models of the conducting zone

Several decades ago, modelling approaches in respiratory biomechanics were restricted to reduced-dimensional observations of the conducting zone only [93, 196, 258, 259, 277]. These models were motivated by the fact that the anatomy of the branching airway tree has been well known from lung casts which contained statistically relevant geometrical data up to the 16th generation of the airway tree [166, 356]. Specific effects observed in lung physiology were attributed to this complex branching airway tree structure and the flow patterns within.

At that time, computational methods were not powerful enough to resolve the flow field in the entire conducting airway tree in three dimensions. Therefore, simplified approaches computing a flow resistance for each airway segment based on its geometrical dimensions have been used. These resistance models were mainly based on observations of laminar and turbulent flow in rigid pipes and the corresponding solutions e.g., Poiseuille's resistance or modifications respecting turbulence [93, 196, 258, 259, 277].

The assumption required for such reduced-dimensional models of the conducting zone was the applicability of the derived reduced-dimensional pressure-flow relationships in the airways under physiological conditions (see Section 2.1.2 for details).

A detailed derivation of the dimensional reduction can be found in Section 2.1.2. Another possible mathematical approach to build a formulation for airflow is the assumption that the Womersley solution holds for each airway segment [12, 69]. Then, an equivalent impedance can be computed to account for the viscous resistance, compliance, and inertance of airflow in each airway segment. The resistances [93, 196, 258, 259, 277] or impedances [12, 69] for single airway segments can then been combined to a network specified by the anatomy of the airway tree. Such tree models have been used for computations of airflow throughout the entire conducting zone.

Dimensionally reduced models of the conducting zone have marked an important first step towards building up the discipline of airflow modelling in respiratory biomechanics. The applied resistance models were derived from basic physics of pipe flow and are perfectly valid in the physiological range of airflow in the lungs [12, 69, 93, 176]. Reduced-dimensional models of the conducting zone have successfully been used to investigate the resistance distribution across different generations of the airway tree [93]. Further, the effect of expiratory flow limitation has been investigated using the extension of flexible airway walls [196]. Expiratory flow limitation describes the maximum flow rate at which a subject is able to exhale. This flow rate cannot be increased with a higher positive pleural pressure generated by the respiratory muscles due to the involved compression of the flexible airways and the resulting increase in flow resistance.

One major limitation of these models has, however, been the lack of respiratory tissue with all its important effects in lung physiology. Therefore, today models of the conducting zone have been extended by adequate representations of the respiratory zone towards reduced-dimensional coupled models presented later in this work (see Section 3.1.5).

3.1.2. Continuum models of the conducting zone

If a detailed spatial resolution of the airflow field is crucial, continuum mechanics based conducting zone models can be used. In this case, airflow is modelled in two-dimensional or three-

dimensional geometries of the conducting airways (see e.g., [19–21, 39, 51, 71, 72, 79, 205, 207, 226, 334, 366]).

Previously, idealised geometric representations - i.e., individual tubes or a system of bifurcating tubes have been used predominantly. Well-known examples are the Weibel [356] and Horsfield [166] tree models, which are based on general morphological data about branching angles and generation-dependent airway diameters and lengths [226, 378]. Recently, the importance of patient-specific geometric features for the development of airflow patterns has gained more attention. Consequently, many models (see e.g., [19–21, 51, 60, 71, 72, 79, 93, 205, 210, 366]) are now based on imaging-based geometries, i.e., geometric reconstructions from e.g., bronchoscopic, X-ray, MR, or CT data. However, due to the limited resolution of imaging techniques and the high computational cost related to three-dimensional patient-specific geometric models, it is neither possible nor reasonable to resolve all airways in the conducting zone with such a level of detail.

Airflow in the resolved conducting zone is governed by the incompressible Navier-Stokes equations (see Section 2.1.1). It is known that a high-speed jet is formed as air passes through the larynx [72, 205]. Resulting turbulence effects can affect flow patterns in the trachea and bronchi but are believed to decay already after few generations of airways [72]. Depending on the specific region of interest, some models consider the influence of potential turbulence effects either by resolving all relevant spatial and time scales (i.e., in a direct numerical simulation) or by applying turbulence models such as large-eddy simulation (LES) [197] or Reynolds-averaged Navier-Stokes (RANS) models [186, 187, 207].

The models of the larger airways mentioned so far consider the airway walls as being rigid. This assumption may be a first approximation for the walls of the trachea and the first airway generations containing a significant amount of cartilage. However, the composition of the airway wall changes over the generations and smaller airways are considerably more compliant (see Appendix C). To account for the mutual interaction of airflow and airway wall deformation in higher airway generations, so-called fluid-structure interaction (FSI) models [148, 149, 193, 352, 366] have been proposed as an alternative to classical computational fluid dynamics (CFD) models. Apart from enabling the prediction of realistic airflow patterns in the deforming airways, FSI models also allow for the quantification of airway wall stresses and strains.

Airways are embedded in the surrounding lung tissue, which exerts stresses on the airway walls during breathing or mechanical ventilation. Some models account for this so-called parenchymal tethering effect by introducing non-linear springs attached to the outside of the airway walls or considering an additional, empirically derived tethering pressure to the airway model [212, 213]. This way, the changes in flow characteristics as a consequence of disease-related alterations in the tethering forces can be investigated theoretically.

Most existing continuum models of the conducting zone resolve only a part of the conducting zone. At the truncated airways, suitable outflow boundary conditions have to be specified. Often, rather simple boundary conditions such as a priori defined outlet pressures [19–21, 39, 51, 60, 71, 72, 366], velocity profiles [205, 210], or mass flow percentages [79, 93, 197, 369] are prescribed. Alternatively, pressure or mass flow rate at equivalent interior locations of resolved pathways can be mapped randomly to the outlets of truncated branches within a lung model [207, 334]. Other approaches have been based on subject specific boundary conditions to model the outflow from specific regions of the lung based on imaging data [89, 369, 370]. These imaging-based outflow rates are only valid for the specific flow scenario under image acquisition. However, they are of

great value to validate a computed flow and radio marker distribution against available clinical measurements in this specific scenario.

The resulting numerical models have e.g., been applied in studying the effect of patient-specific as compared to idealised simplified geometries [329]. Further, the impact of pathological geometry changes (e.g., airway obstructions) on simulated airflow patterns has been surveyed [21]. Besides, the consequences of rapid inhalation (e.g., during sniffing) on airflow dynamics have been studied [20, 51].

Another important application field of continuum models of the conducting zone is the investigation of airway stability and reopening [32, 138, 148, 149, 169, 201, 327]. Small airways are prone to fluid-elastic instabilities that can lead to their collapse and occlusion by a liquid bridge formed by the airway liquid lining [138]. Since a persistent occlusion of the airways can lead to a severe impairment of gas exchange, medical treatment aims at a quick reopening of airways [195]. At the same time, however, tissue forces resulting from the propagation of the air finger into the liquid-filled airway have to be minimised to avoid cellular injury and inflammation [33, 169, 182, 327, 367]. Continuum models of the conducting zone can be used to determine (i) the propagation speed of the air finger as a function of the applied pressure and (ii) the stresses in the airway wall.

Continuum models of the conducting zone are also the basis for the prediction of particle transport and deposition in the lung [39, 186–188, 378]. Example scenarios are targeted drug delivery and the inhalation of toxic pollutants from the environment. For this type of application, the continuum models of the conducting zone have to be extended by a particle transport formulation and appropriate absorption boundary conditions. In several studies, the influence of physical parameters (e.g., flow rate and particle size) as well as model parameters (e.g., time-dependent versus steady flow conditions, idealised versus imaging-based geometry) on particle deposition patterns and deposition efficiency have been investigated [70, 79].

3.1.3. Reduced models of the respiratory zone

Similar to the conducting zone, the first models of the respiratory zone were restricted to reduced-dimensional observations [83–87]. These approaches were motivated by the fact that the respiratory zone is composed of a huge number of small clustered units (i.e., the alveolar ducts) similar in their architecture. If the properties of a single alveolar duct can be expressed in a reduced-dimensional sense, the entire respiratory zone can then be adequately described.

Models based on this idea have replicated alveolar tissue as a network of pin-jointed line elements (i.e., springs and dashpots) representing bundles of collagen and elastin fibres [83, 86]. These line elements are arranged at the edges and across the surfaces of regular polyhedra representing individual alveoli. Additionally, surface tension effects at the air-wall interface caused by surfactant, can be respected using membrane elements across the surfaces of these polyhedra [86].

The main assumption that is required for a reduced-dimensional model of the respiratory zone is, that the chosen alveolar geometry and arrangement as well as constitutive model for the line-elements are representative for human lung tissue.

Inflation/deflation of such alveolar clusters then allows to compute quasi-static or dynamic relationships between pressure and volume of an alveolar duct [86]. These relationships provide a computationally very efficient representation of the respiratory zone based on the underlying

physics of collagen/elastin fibres and surfactant. They are used, e.g., as terminal units in coupled lung models to mimic the behaviour of the respiratory zone and to quantify regional inflation of lung tissue (see Section 3.1.5 and [176]). Further, reduced-dimensional models of the respiratory zone have also been used to study the effect of different diseases on the behaviour of lung tissue. For instance, by eliminating single pin-jointed line elements within a cluster, an emphysemic condition has been modelled [322]. By this means, failure of single alveolar walls on the microscopic scale has been related to a disease-related tissue softening on the macroscopic scale. Finally, spring models of the respiratory zone have been used to investigate the volume-competition between different lung regions during inflation in a simplified way and to quantify interactions between neighbouring air spaces in health and disease [228]. Still, reduced models of the respiratory zone are only describing one part of the lung, namely the respiratory zone. Therefore, they are limited to isolated observations of this region or have to be coupled to an adequate model of the conducting zone as presented in the Section 3.1.5.

3.1.4. Continuum models of the respiratory zone

For a more detailed investigation of phenomena in the respiratory zone, continuum mechanics based models of single alveoli, alveolar ducts, or entire acini have been developed in the past. Many of these models are based on artificial geometric representations of individual alveoli ranging from simple spherical or polyhedral shapes [78, 84, 184, 185, 190] to more realistic irregular cells [189]. Some approaches also use imaging-based reconstructions, e.g., obtained from synchrotron-based X-ray microscopic tomography [143, 298]. However, due to the small size of the air spaces and required high radiation doses, *in vivo* imaging of alveolar structures remains difficult.

Continuum models of the respiratory zone have been used to study acinar flow phenomena in detail. Despite the low Reynolds numbers, airflow in this region is still complex due to its unique architecture [296] and the rhythmic expansion and contraction of the tissue during respiration [161]. For instance, recirculating structures and radial flows induced by the septal wall movement can be found in the alveolar cavities. In addition to acinar flow patterns, transport, mixing, and deposition of particles have been studied extensively [152, 159–162, 248, 253, 304, 324, 325]. Applications include the prediction of acinar aerosol deposition for therapeutic delivery and the assessment of health risks associated with inhaled hazardous particles [253]. Furthermore, the transport of oxygen molecules through the acinus and the exchange of oxygen at the blood-gas barrier has been simulated [162]. Finally, continuum mechanics based models of the respiratory zone have also been applied to investigate alveolar stresses and strains [272]. This way, strain hotspots have been identified which are at risk of overdistension during mechanical ventilation. Since stresses and strains cannot be measured experimentally, continuum models of the respiratory zone can make an important contribution to a better understanding of involved stress raising phenomena and associated risks at tissue overdistension (see Appendix D).

As with all isolated models of parts of the respiratory system, the formulation of physiologically reasonable boundary conditions (i.e., flow boundary conditions, boundary loads, and deformations) is difficult. In reality, the modelled alveolar or acinar structure is connected to the conducting zone and embedded in the surrounding respiratory zone. However, most existing models presented in this section are not capable of considering these connections adequately.

3.1.5. Reduced-dimensional coupled lung models

In the majority of applications, both a representation of the conducting zone as well as the respiratory zone are necessary to cover all aspects that are relevant for an accurate description of lung physiology. If, however, no detailed resolution of the flow field in the conducting zone and no fully resolved continuum mechanical description of the respiratory zone is required, the lung can be represented using reduced-dimensional models (see Section 2.1.2 and 2.2.2). These simplified reduced-dimensional representations in respiratory biomechanics comprise approaches ranging from pure phenomenological single-compartment models (see below) to imaging-based, physiologically realistic approaches grounded on the physics of previously introduced airflow dynamics and tissue mechanics. The *0D/0D* model developed in this work is one example for such physiologically realistic approaches and will be derived in detail in Section 3.2.

3.1.5.1. Single-compartment models

Single-compartment models consist of a single pipe representing the conducting airways which is connected to a single elastic compartment representing lung parenchyma. The motivation behind these models is that the resistance of the entire conducting airway tree can be combined into a single equivalent (pipe) resistance R. Further, the compliance of all tissue components in the respiratory zone and the elastic properties of the chest wall are united into a single equivalent (compartment) compliance C. The mechanical behaviour of the lung can then be expressed via fitting these two parameters (i.e., resistance and compliance; see Section 1.1.3) to patient measurements using the method of least squares (see e.g., [24]).

Since this approach is no physically based model in a strict sense, no modelling assumptions in a strict sense apply. The only two necessary assumptions for single-compartment models are that the chosen model equation is able to replicate lung behaviour and that a sufficient number of clinical measurements of pressure, flow and volume exists to fit the required parameters. A further assumption that is implicit in the representation via a single compartment is that the fit mechanical behaviour is averaged over the entire organ. This means that any regional differences in lung function are omitted in these models.

Depending on the complexity of the model, different realisations for resistance and compliance are conceivable [24, 225]. If both the resistance and the compliance are constant the so-called linear single-compartment model is obtained. Several investigations have, however, shown that both the conducting zone and the respiratory zone contain significant sources of non-linearity [24]. To begin with the respiratory zone, clinically measured transpulmonary pressures at different lung volumes recorded as quasi-static P-V measurements have revealed that the lung shows a sigmoidal-like inflation/deflation behaviour [124, 260, 346]. This behaviour can be successfully described using exponential mathematical functions of transpulmonary pressure depending on lung volume. Following the argumentation in Section 1.2.2, especially the lower (collapse) and the upper (overstraining) parts of such P-V curves are important in respiratory care. Observing the conducting zone, airflow through the larynx and in the larger airways can become turbulent [72, 205] especially at high flow rates or in cases of highly pulsatile flows which leads to a flow-dependent non-linear resistance e.g., described in [93, 196, 258, 259, 277]. Further, the pressure difference between the inside of a conducting airway and its surrounding causes diameter changes of the compliant airway and thus changes in resistance with the air-

way diameter. This effect leads to resistance differences between inspiration and expiration [93] due to the varying pleural pressure that is propagated to the airways surrounding and ultimately defines expiratory flow limitation explained previously [196].

In general, single-compartment models are a phenomenological description of lung mechanics based on mathematical equations. The required parameters namely equivalent resistance and equivalent compliance (see Section 1.1.3) are fit from clinical pressure and flow measurements allowing a quick and easy assessment of basic respiratory function [24, 202, 301]. The required fitting algorithms for linear and for non-linear models are easy to implement, they operate in real-time and deliver values that are easy to interpret in a clinical setting. Still, these models do not have a strict physical background and rather have to be seen as a fitting technique. With more effects included e.g., non-linearity [124, 260, 346] or a relationship for recruitment/derecruitment [145, 314], single-compartment models become more realistic and allow a better adaption to the physiology of the lung. On the other hand, each additional parameter requires more reliable data for fitting and thus the model becomes less predictive. Finally, one major drawback of the single compartment models is that no specific anatomy of the patient can be respected and no regional information on mechanical overstraining or recruited/derecruited regions can be given.

Despite these limitations, single-compartment models are up to now the widest used modelling approach in respiratory biomechanics and still under development. They have successfully served as starting point for investigations of gas transport and transfer into the blood [220] and for general coupling with the cardiovascular system [117]. Further, they have been used in diagnosis of respiratory diseases as an easy to apply bedside tool in respiratory care. Recently, single-compartment models have been extended by a functionality to quantify ventilator-associated lung injury resulting from recruitment/derecruitment and overstraining [145, 314]. Finally, single-compartment models have successfully been applied in optimising ventilatory settings in several randomised clinical trials [9, 302, 349]. Nevertheless as it has been proven that the extent of lung heterogeneity is directly linked to disease severity and mortality [75], it would be desirable to use more precise regional models for this optimisation task.

3.1.5.2. Multi-compartment models

Multi-compartment models are the next step towards more realistic modelling of respiratory biomechanics. They comprise all approaches that are characterised by multiple reduced-dimensional components for both the conducting and the respiratory zone of the lung. Thus they mark the transition from pure phenomenological approaches towards physically motivated models in respiratory biomechanics [12, 13, 24, 176, 211, 225, 293]. In general, multi-compartment models are motivated by the idea that a reduced-dimensional description is the most efficient way to describe respiratory biomechanics on the organ-level and the awareness that the lack of regional information has to be overcome to allow precise conclusions in a clinical setting.

Pure phenomenological multi-compartment models are characterised by a parallel arrangement of single-compartment models with distributed parameter values for equivalent resistance and compliance extended by models governing recruitment/derecruitment dynamics [22, 25, 155, 222, 315–317]. The same assumptions hold as for single-compartment models except for the assumption that the behaviour is averaged over the entire organ (see Section 3.1.5). Required model parameters are still identified via fitting to patient measurements.

Physically motivated multi-compartment models are presented in detail in Section 3.2.4. In brief, they combine a physically sound formulation for fluid flow in an anatomically correct airway tree with a realistic model for lung tissue. In Section 3.2.4, a pre-existing approach [176] is extended by all capabilities that are necessary to adequately describe the behaviour of the lung grounded on the underlying physics of the organ.

Essentially all multi-compartment models [12, 13, 24, 176, 211, 225, 293] are a functional relationship between pressure and flow in the conducting and the respiratory zone and allow for a spatial resolution of computed quantities in different regions of the lung. With the possibility to respect spatially distributed material properties and regionally varying recruitment/derecruitment properties as well as gravitational effects, they allow a more realistic examination of lung function. Simple parallel arrangements of single-compartment models are still phenomenological representations of lung mechanics that have to be fit to measurements and thus are easy to adapt to a specific patient. The predictive character of these models suffers from the fact that it is not understood what happens in scenarios beyond those where fitting data are available. Conclusions e.g., on higher pressures than those measured are then only a more sophisticated mathematical extrapolation without deeper knowledge about potential critical points in system behaviour and thus dangerous for prediction in a clinical application.

Physics based multi-compartment models allow a deeper insight into airflow throughout a network of compliant airway segments and inflation of (visco-)elastic lung tissue. In these models, the descriptions of the conducting and the respiratory zone are derived from physically sound airflow dynamics and tissue mechanics. The coupling between both zones is presented in detail in Section 3.2.4.

So far, several questions in respiratory biomechanics have successfully been investigated using multi-compartment models. Most importantly, reopening dynamics of collapsed lung regions in ARDS have been assessed using several setups of parallel multi-compartment models [22, 25, 155, 222, 315–317]. In this context the optimal moments, pressures and duration of deep inflations during mechanical ventilation could be determined.

Physically motivated multi-compartment models have been able to predict airflow in a healthy airway tree from a mathematical point of view [131] and investigated the optimality and robustness of this bronchial tree structure [227]. A second key aspect in multi-compartment modelling is the simulation of highly detailed airflow distribution and ventilation in the lung. This has been impressively shown in human [176] and canine [12, 69] lungs. In [176] multi-compartment models could almost exactly reproduce the results from continuum models. Besides, the propagation of a liquid plug in a complex network of reduced-dimensional airways could be studied [293] and the associated frequency dependency of conducting airway and lung tissue behaviour could be determined. Basic concepts of recruitment/derecruitment have been studied on various tree geometries [211] and quantified along with overstraining in critically ill patients [13]. The multi-compartment models have successfully enabled the identification of minimally injurious modes of ventilation in this context.

Nevertheless, current physically motivated multi-compartment models are still lacking important phenomena in respiratory biomechanics such as lung interdependence or parenchymal tethering. A novel physically motivated reduced-dimensional multi-compartment model containing these effects will be derived in Section 3.2.4.

3.1.6. Hybrid representations of the respiratory system

Hybrid models constitute the next level of detail in modelling respiratory biomechanics. They are used if only one zone requires specific attention and has to be modelled as a continuum while the other one can be respected using a reduced-dimensional approach. By coupling reduced and resolved representations, the interaction between the conducting and the respiratory zone of the lung is automatically assured. In practice, there are two main possibilities how such hybrid models can be composed. First, a continuum mechanical description of the conducting zone can be linked to a reduced-dimensional model of the respiratory zone. According to the zone that is resolved as continuum, this variant is denoted hybrid (conducting) in the overview (see Figure 3.1). Second, a reduced-dimensional model of the conducting zone can be coupled to a continuum mechanical description of the respiratory zone, denoted as hybrid (respiratory). The models denoted as *3D/0D* and *0D/3D* developed in this work also belong into the category of hybrid models and will be derived in full detail in Section 3.2.

3.1.6.1. Hybrid model (conducting)

For some investigations, only the conducting zone is required to be resolved in full detail as far as possible from available imaging data, while phenomena related to the terminal airways and the respiratory tissue are of no specific interest. Still, the influence of the airways downstream to the fully resolved ones and the respiratory zone cannot be neglected for a realistic description of airflow in the conducting zone. Therefore, the effects of flow resistance in smaller non-resolved airways, and the inflation of lung tissue have to be modelled via appropriate boundary conditions at the terminal ends of the fully resolved airway tree. The idea is to respect all downstream effects that generate dynamic pressures during inflation/deflation of the lung in a reduced-dimensional fashion. Additionally, a storage capacity for the air that leaves the fully resolved tree during inspiration and can consistently re-enter the domain during expiration is provided. Hence, the model denoted as hybrid (conducting) is essentially a continuum description of the conducting zone extended by appropriate couplings/boundary conditions to take into account all effects that occur downstream the fully resolved region.

Required assumptions for this hybrid approach will be reviewed in detail in Section 3.2.2.

Airflow in the continuum part of the conducting zone of such hybrid models is governed by the the incompressible Navier-Stokes equations. Further, fluid-structure interaction and parenchymal tethering effects can be considered (see Section 3.1.2). One possibility to respect further downstream regions is to couple the continuum conducting zone to a reduced-dimensional multi-compartment tree-like model accounting for the resistance and compliance of the smaller non-resolved airways [60, 71, 132, 176, 187, 209, 246, 370] and tissue. Thereby, physically-based information can be included into the hybrid (conducting) model such as the dimensions and connection of the non-resolved airways coming from a tree-growing algorithm [328]. At the terminal ends of that tree, a reduced-dimensional respiratory zone model is attached as known from physically based multi-compartment models (see e.g., [176, 206]).

Important applications of the hybrid (conducting) models are in general all problems where a detailed flow field in resolvable airways is required and where induced deformation and distortion of the bronchial geometry is small. These requirements usually hold in large airways which are stiff enough to prevent large deformation. Possible examples of such scenarios have already

been mentioned in Section 3.1.2 and virtually all of these investigations would profit from a hybrid representation of the respiratory zone.

So far, a hybrid (conducting) model consisting of a continuum description of the upper airways was coupled to an artificial airway tree in [209]. They found that the upper airways contribute the largest part to entire lung resistance [209]. Grandmont et *al.* [132] have presented a two-dimensional example of such a hybrid (conducting) model and tested the sensitivity of the model with respect to resistance variations in the attached resistive tree. These studies were extended to three dimensions [15] and revealed that the hybrid (conducting) model is perfectly suitable to describe airflow in the proximal part of the bronchial tree. Further, it has been shown that the hybrid (conducting) model is able to reproduce flow patterns similar to those obtained from functional medical imaging [89]. The findings so far confirmed that the outlet boundary conditions of the hybrid (conducting) model are suitable to model lung structure and function [71, 330] and can be used along with medical imaging data [370] and particle transport [206]. Comparing a hybrid (conducting) approach and a physics-based multi-compartment model, Ismail et *al.* [176] have shown that multi-compartment models can almost exactly reproduce flow results in respiration. Recently, hybrid (conducting) models have been applied to particle distribution studies and compared to experiments [246, 247]. One particular interesting application [60] in mechanical ventilation that is particularly suitable for this hybrid model is the ventilation with high frequencies and low tidal volumes known as high frequency oscillatory ventilation. In that case introduced deformation is low due to low tidal volumes and a resolved fluid field is required to fully understand the complex mixing processes in the conducting system during this efficient technique of mechanical ventilation. A detailed mathematical derivation for a coupled hybrid conducting model will be presented in Section 3.2.2.

3.1.6.2. Hybrid model (respiratory)

A second approach of hybrid modelling is used if processes on the macroscopic tissue scale require specific attention (e.g., to quantify tissue overdistension) whereas airflow in the conducting system is only of interest inasmuch as it is responsible for the distribution of air in the respiratory zone. In this case, a suitable hybrid model can be realised by combining a physically based reduced-dimensional model of the conducting zone with a continuum mechanical imaging-based description of the respiratory zone. The geometry of the airway tree can be obtained using tree growing algorithms [176, 328] within the hull geometry of the lung segmented from a CT or magnetic resonance imaging (MRI) scan.

Usage of the hybrid (respiratory) model with a reduced conducting and resolved respiratory zone requires some assumptions that will be presented in detail in Section 3.2.3.

The governing equations for the hybrid (respiratory) model depend on the model of the respiratory zone while the conducting zone is represented as reduced fluid domain. For a porous representation of lung tissue, details can be found in [30]. For a solid domain model of the respiratory zone, a detailed derivation is provided in Section 3.2.3.

So far, only one approach has been reported using a hybrid (respiratory) model [30]. Their results give an insight on the consequences of airway constriction, reduced tissue elasticity, and show distributions of alveolar pressure, ventilation and corresponding tissue stress.

Additional hybrid couplings are conceivable, e.g., a continuum mechanical description of the large airways combined with a reduced-dimensional description of the small airways in the con-

ducting zone and a fully resolved representation of the respiratory zone. However, such approaches have not been reported to date. The decision which part has to be resolved as continuum and which one is sufficiently modelled with reduced approaches can be tailored to the current question to be investigated. In this way, very efficient and modular hybrid models can be generated to exactly fulfil the specific requirements for the specific application.

3.1.7. Continuum coupled lung models

Continuum mechanics based overall lung models offer the possibility to simulate coupled phenomena in two- or three-dimensional representations of both the conducting and the respiratory zone at a high level of detail [372]. This model is derived in detail in Section 3.2.1 and discussed in Chapter 4 of this work.

3.1.8. Concluding remarks

In current literature a variety of approaches exist for modelling respiratory biomechanics and their sensible usage is largely dependent on the problem to be investigated. For clinical monitoring of a patient with plenty of measurement data available and a fast and only global classification required at bedside, phenomenological fitting approaches are a quite reasonable choice. For more advanced investigations with single effects to be isolated or even to be predicted, realistic respiratory models grounded on the underlying physics of airflow dynamics and soft tissue mechanics are a powerful approach. They allow a deeper insight into physiological effects beyond classical black-box parameterisations of lung function.

In very specific cases, realistic predictions are possible based on models comprising the conducting or respiratory zone only. The majority of phenomena in respiratory biomechanics, however, live from the interplay between the conducting and the respiratory zone and how alterations in one zone ultimately affect the behaviour of the other. Therefore, coupled models considering both zones and their interaction will be derived in Section 3.2 and their potential will be reviewed throughout the rest of this work.

3.2. Novel coupled computational models of the respiratory system

In the subsequent sections, various coupled approaches in respiratory mechanics will be introduced and discussed as presented in Figure 3.2. Starting from the most general (and complex) fully resolved continuum mechanical models for conducting airways and lung tissue, successively further assumptions will be reviewed that allow simplification towards easier and computationally cheaper tree-like *0D* representations of the lung still accurately representing its underlying physics. A specific focus will be put on the interaction between airflow and tissue behaviour in terms of consistent coupled computational models for respiratory mechanics. Possible fields of application will be given for each model to guide the reader towards the best solution strategy for a given clinical or research question.

The novel coupled approaches presented in this section are partly based on previously reported methods which will be referenced where applicable. The description starts with the most

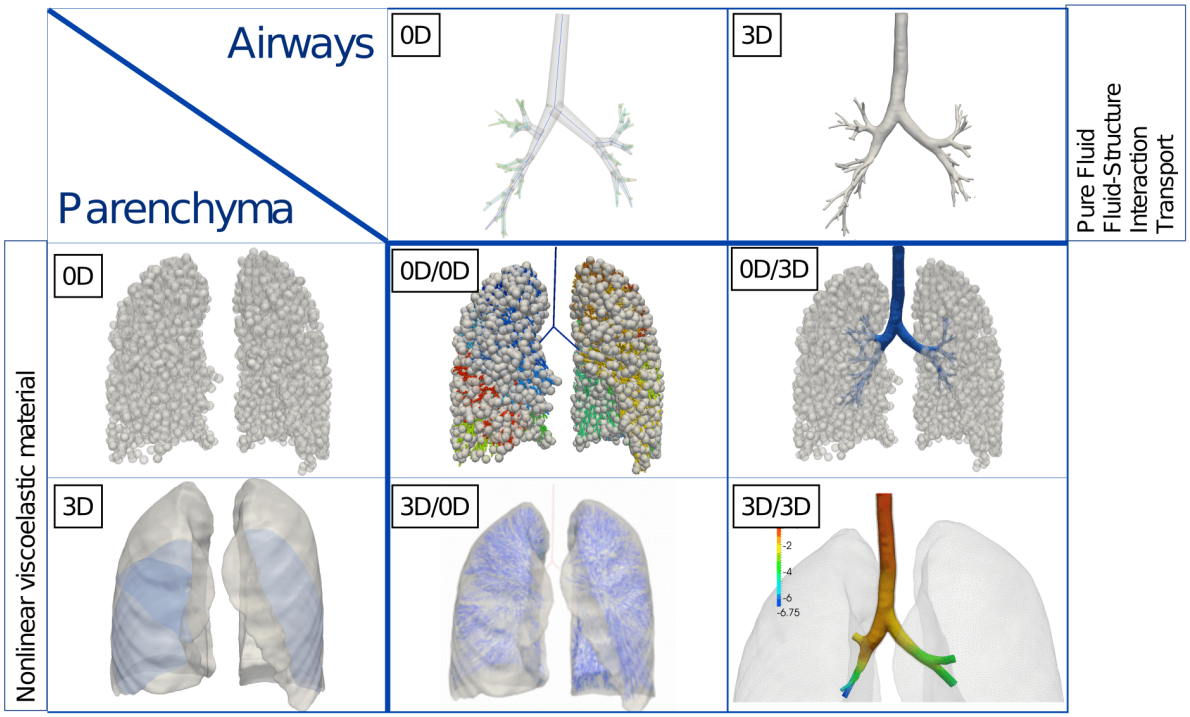

Figure 3.2.: Overview over the coupled lung models developed in this work. Each of the four coupled models consists of conducting airways and lung parenchyma. Each of these two building blocks can either be realised as fully resolved field denoted as *3D* or as a reduced-dimensional representation denoted as *0D*. The basic mathematical formulations of the single fields have been introduced in Chapter 2. For a classification of the four approaches within the state of the art, see Figure 3.1. Image adopted from [286] with permission.

complex model in the table denoted as *3D/3D*. This is in contradiction to the classical engineering approach of starting simple and getting more complex if needed. However, in this case it is well justified since, so little can be measured in the respiratory system that often the only way to check certain assumptions or effects is given by the most general and highest resolved models.

3.2.1. Fully resolved volumetrically coupled models *(3D/3D)*

3.2.1.1. Motivation and model description

The first and most general approach in the overview is motivated by the fact that certain questions in respiratory mechanics require both a fully resolved deformable three-dimensional fluid domain and a realistic three-dimensional structural representation of the lung. However, these two fields are not behaving independently from each other but are coupled in their action and reaction. First, the embedding of the tree in surrounding lung tissue provides correct tethering forces and thus realistic strength against local collapse and hyperinflation of both airways and lung tissue. Secondly and even more important, flow throughout the conducting airways is naturally coupled to regional inflation of the respiratory part of the lung.

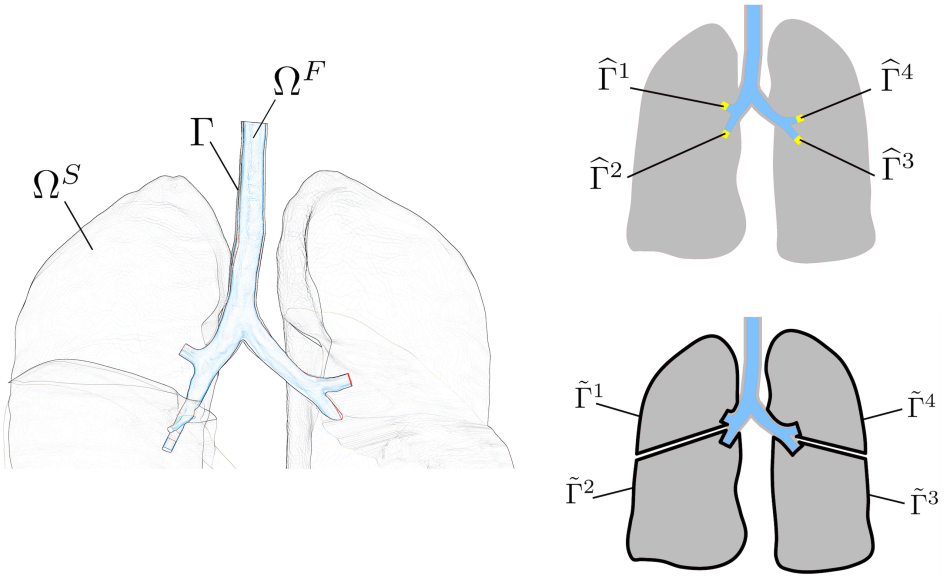

Figure 3.3.: Model schematic for the approach denoted as *3D/3D*. The deformable fluid domain is denoted as Ω^F, the structure as Ω^S and the interface for classical fluid-structure interaction as Γ. The novel volumetric coupling is realised between the fluid outlets $\hat{\Gamma}$ and the structural domains bounded by $\tilde{\Gamma}$. All fluid that leaves an outlet $\hat{\Gamma}$ has to increase the volume of its associated region $\tilde{\Gamma}$. For easier display the sketch is exemplified for the main bronchi leading to the five lobes of the lung (left). For the definition of the boundaries of the structural domain a slice of the lung is used where only four lobar bronchi are visible (right). The marked boundaries correspond to the anatomically correct boundaries of the single lobes obtained from the CT scan.

Therefore, a core element and the main novelty of the approach denoted as *3D/3D* compared to previous fluid and FSI approaches of the bronchial tree [126, 149, 352, 366] is the mutual volumetric coupling between fluid flow and regional deformation of lung tissue [372]. Conducting passages of the tree are only resolved as far as necessary for the current investigation and all downstream passages are modelled as a homogenised solid domain of lung tissue containing alveolar walls, small airways and blood vessels (see Figure 3.3). The introduced volumetric coupling approach respects inflation of a tissue region dependent on the fluid flow leaving the associated tree outlet. Vice versa deformation of a tissue region e.g., via contraction of the associated muscles, creates a volume flow at the current fluid outlet and drives airflow throughout the tree. This is remarkable as apart from a zero-pressure at the mouth/nasal cavity there is no need to impose additional boundary conditions to the deformable fluid domain for such a scenario.

The underlying well justified assumptions for this and for all following models are that air can be seen as a Newtonian fluid and the flow as incompressible in the physiological regime (for explanation see Section 2.1.1). Further, airway walls and small blood vessels in the parenchyma can be seen as incompressible due to their high water content and the well-grounded assumption that water can be seen as incompressible at the timescales relevant in respiratory mechanics. Therefore, all air which leaves the compliant airways and enters a region of lung tissue has to increase air spaces therein, i.e., the pores of the sponge-like micro-structure (see Figure 3.4 for

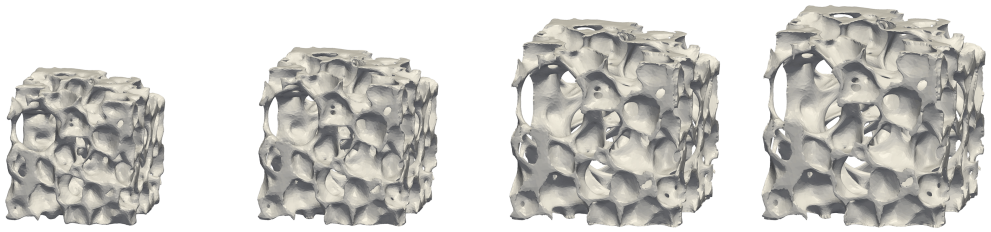

Figure 3.4.: Exemplary inflation states for incompressible lung tissue doubling the enclosed volume of air in the parenchyma block while the volume of tissue remains constant. Geometry taken from [272]

different exemplary states of parenchymal inflation). Fluid flow leaving a fully resolved airway and the volume of the homogenised parenchymal region are directly coupled via the volumetric constraint [372].

3.2.1.2. Mathematical formulation

The realisation of this volumetric coupling within a framework of classical fluid-structure interaction is presented in Figure 3.3 and will be briefly sketched for a four outlet case in the following. Airflow in the deformable fluid domain Ω^F is governed by the incompressible Navier-Stokes equations in ALE formulation represented by the discrete non-linear residuum

$$\mathbf{r}^{\mathrm{F}}(\mathbf{u}^{\mathrm{F}}, \mathbf{d}^{\mathrm{A}}, \mathbf{d}^{\mathrm{S}}) = \mathbf{0} \tag{3.1}$$

(see Eq. (2.100)). The deformation of lung tissue in the homogenised lung tissue Ω^S is described via the non-linear elastodynamics equations and the corresponding discrete non-linear residuum

$$\mathbf{r}^{\mathrm{S}}(\mathbf{d}^{\mathrm{S}}) = \mathbf{0} \tag{3.2}$$

(see Eq. (2.62)). A classical FSI interface denoted as Γ is used to represent the interaction between airflow and deformation of the airway wall. In this context, the deformable fluid domain is characterised via the ALE field equations indicated via the discrete non-linear residuum

$$\mathbf{r}^{\mathrm{A}}(\mathbf{d}^{\mathrm{A}}, \mathbf{d}^{\mathrm{S}}) = \mathbf{0} \tag{3.3}$$

(see Eq. (2.95)). The complete governing equations for this pure FSI problem including the interface conditions have been presented in Section 2.3.

As a novelty, for each pictured outlet of the fully resolved compliant airways $\hat{\Gamma}^i$ a volumetric constraint is introduced that couples fluid flow $Q^{\mathrm{F},i}$ to the volume change $\Delta V^{\mathrm{S},i}$ of the regions bounded by $\tilde{\Gamma}^i$ in a defined time-interval. The number of outlets and homogenised solid domains is arbitrary and depends on specific requirements of the question at hand. For clarity, the superscript i is therefore omitted here. The volumetric constraint can then be expressed in form of a discrete non-linear residual

$$\mathbf{r}^{\mathrm{C}}(\mathbf{u}^{\mathrm{F}}, \mathbf{d}^{\mathrm{S}}) = \Delta V^{\mathrm{S}} - \Delta V^{\mathrm{F}} = \mathbf{0}. \tag{3.4}$$

In practice, the volume change ΔV^{S} of a parenchymal region can be computed as

$$\Delta V^{\mathrm{S}} = V^{\mathrm{S}}_{n+1} - V^{\mathrm{S}}_{n} \tag{3.5}$$

where calculation of the volume of the parenchymal region exploits the divergence theorem

$$V^{\mathrm{S}} = \frac{1}{3}\int_{\Omega^{\mathrm{S}}} \nabla \cdot x(\tilde{\Gamma}^{\mathrm{S}}) dV = \frac{1}{3}\int_{\tilde{\Gamma}^{\mathrm{S}}} x(\tilde{\Gamma}^{\mathrm{S}}) \cdot \mathbf{n} dA. \tag{3.6}$$

Here, n denotes the time step, the vector $\mathbf{x}(\tilde{\Gamma}^{\mathrm{S}})$ represents the coordinates of the deforming boundary $\tilde{\Gamma}^{\mathrm{S}}$ and $\mathbf{n}$ the local unit normal vector on this boundary. The integrated fluid flow in the time step $\Delta t = [t_n, t_{n+1}]$ is calculated as

$$\Delta V^{\mathrm{F}} = \int_{t_n}^{t_{n+1}} Q^{\mathrm{F}} dt \tag{3.7}$$

with the fluid flow coming from integrating the convective ALE velocity across the outlet surface area A of the outlet $\hat{\Gamma}^{\mathrm{F},i}$ with the unit normal vector $\mathbf{n}$

$$Q^{\mathrm{F}} = \int_{\hat{\Gamma}} \left(\mathbf{u}^{\mathrm{F}} - \dot{\mathbf{d}}^{\mathrm{A}}\right) \cdot \mathbf{n} dA. \tag{3.8}$$

To build a monolithic system of equations, the constraint residual $\mathbf{r}^{\mathrm{C}}$ is included in the classical monolithic FSI problem Eq. (2.105) - Eq. (2.107) written as compound residual $\mathbf{r}^{\mathrm{FSI}}(\mathbf{x}^{\mathrm{FSI}})$ via a Lagrange multiplier λ

$$\mathbf{r}^{\mathrm{FSI}} + \lambda \frac{\partial \mathbf{r}^{\mathrm{C}}}{\partial \mathbf{x}^{\mathrm{FSI}}} = \mathbf{0}, \tag{3.9}$$

$$\mathbf{r}^{\mathrm{C}} = \mathbf{0}. \tag{3.10}$$

Linearisation with a Newton scheme as introduced in Eq. (2.17) reads for Eq. (3.9) and Eq. (3.10)

$$\begin{bmatrix} \frac{\partial \mathbf{r}^{\mathrm{S}}}{\partial \mathbf{d}^{\mathrm{S}}} & \mathbf{0} & \frac{\partial \mathbf{d}^{\mathrm{S}}}{\partial \mathbf{d}^{\mathrm{S}}} & \left(\frac{\partial \mathbf{r}^{\mathrm{C}}}{\partial \mathbf{d}^{\mathrm{S}}}\right)^T \\ \mathbf{0} & \frac{\partial \mathbf{r}^{\mathrm{A}}}{\partial \mathbf{d}^{\mathrm{A}}} & \frac{\partial \mathbf{r}^{\mathrm{A}}}{\partial \mathbf{u}^{\mathrm{F}}} & \mathbf{0} \\ \frac{\partial \mathbf{r}^{\mathrm{F}}}{\partial \mathbf{d}^{\mathrm{S}}} & \frac{\partial \mathbf{r}^{\mathrm{F}}}{\partial \mathbf{d}^{\mathrm{A}}} & \frac{\partial \mathbf{r}^{\mathrm{F}}}{\partial \mathbf{u}^{\mathrm{F}}} & \left(\frac{\partial \mathbf{r}^{\mathrm{C}}}{\partial \mathbf{u}^{\mathrm{F}}}\right)^T \\ \frac{\partial \mathbf{u}^{\mathrm{C}}}{\partial \mathbf{d}^{\mathrm{S}}} & \mathbf{0} & \frac{\partial \mathbf{r}^{\mathrm{C}}}{\partial \mathbf{u}^{\mathrm{F}}} & \mathbf{0} \end{bmatrix}_i \begin{bmatrix} \Delta \mathbf{d}^{\mathrm{S}} \\ \Delta \mathbf{d}^{\mathrm{A}} \\ \Delta \mathbf{u}^{\mathrm{F}} \\ \Delta \boldsymbol{\lambda}^{\mathrm{C}} \end{bmatrix}_i = - \begin{bmatrix} \mathbf{r}^{\mathrm{S}} \\ \mathbf{r}^{\mathrm{A}} \\ \mathbf{r}^{\mathrm{F}} \\ \mathbf{r}^{\mathrm{C}} \end{bmatrix}_i \tag{3.11}$$

with i denoting the iteration step. The upper left 3×3 matrix block in Eq. (3.11) is essentially the same as in classical monolithic FSI problems introduced in Section 2.3. The fourth row and column marked in yellow result from the volumetric constraint. This constraint leads to a saddle point structure of the entire system matrix (see zero matrix block on the last main diagonal entry) and requires special solution techniques for the linear system of equations Eq. (3.11). In this

work, an approach based on the semi-implicit method for pressure-linked equations (SIMPLE) [52], which was developed for the saddle point system of the Navier-Stokes equations, is used [347]. Finally, the discrete solution vectors for structural displacements, ALE displacements, fluid velocity and pressure, and the Lagrange multiplier in the next iteration step $i+1$ are updated via

$$\mathbf{d}^{\mathrm{S}}_{i+1} = \mathbf{d}^{\mathrm{S}}_{i} + \Delta\mathbf{d}^{\mathrm{S}}_{i} \tag{3.12}$$

$$\mathbf{d}^{\mathrm{A}}_{i+1} = \mathbf{d}^{\mathrm{A}}_{i} + \Delta\mathbf{d}^{\mathrm{A}}_{i} \tag{3.13}$$

$$\mathbf{u}^{\mathrm{F}}_{i+1} = \mathbf{u}^{\mathrm{F}}_{i} + \Delta\mathbf{u}^{\mathrm{F}}_{i} \tag{3.14}$$

$$\boldsymbol{\lambda}^{\mathrm{C}}_{i+1} = \boldsymbol{\lambda}^{\mathrm{C}}_{i} + \Delta\lambda^{\mathrm{C}}_{i}. \tag{3.15}$$

For more details on an efficient solution of the resulting system of equations for the *3D/3D* model the reader is referred to [347, 372].

3.2.1.3. Discussion and example applications

In brief, the model presented as *3D/3D* in our overview is an FSI problem extended by the idea that all fluid flow that enters or leaves an outlet of the deformable fluid domain has to change the volume of the associated parenchymal region inducing deformation.

The advancements compared to pure fluid and FSI models are apparent. The volumetrically coupled *3D/3D* model induces a consistent deformation of the fluid and structural domains which is governed by the current flow characteristics and not prescribed from additional information such as imaging data recorded under different or ambiguous flow conditions. Further, correct boundary conditions are applied at the last fully resolved generation of airways of the deformable fluid domain. The other way round, local tissue deformation induces the correct airflow in the compliant airways without any need of prescribing additional boundary conditions to the fluid. Thereby, physiologically reasonable kinematic constraints can be imposed on the *3D* parenchyma model (e.g., presented in Chapter 4). This allows consistent expiration based on the previously inspired local volume in each branch. It is important to mention that flow entering the domain at each branch does not have a prescribed velocity profile, but the profile is allowed to develop under the current flow conditions. This requires, however, stabilisation of backflow into the domain as already mentioned in Section 2.1.1 and reported in [31, 134].

The point of volumetric coupling is to be chosen carefully for each setting. Full resolution of a further generation of airways in the tree doubles the number of outlets and significantly increases complexity and computational cost. If this, however, does not come along with simultaneous knowledge of material parameters or sufficient resolution of imaging data for geometry generation, a further uncertainty is introduced which needs to be taken into account or could considerably corrupt results and derived conclusions. Previous studies have shown that turbulent effects in the trachea abate after the 3rd to 4th generation [72]. At the level of the 8th generation, the associated tissue regions correspond to single lung segments with an approximate size of $20 - 30$ mm (see Chapter 4). This is usually sufficient for most studies to resolve heterogeneity between different tissue regions obtainable e.g., from imaging data.

With this considerations, one proposed area of use for the *3D/3D* model is for example simulation of a fully resolved strain state during mechanical ventilation of heterogeneous lungs. The fully resolved model is able to quantify volumetric and isochoric strain components which

can be transferred towards loading of the micro-scale using a multi-scale coupling approach [361]. This is especially interesting in understanding the onset and progression of diseases such as VILI/VALI which are assumed to be linked to excessive strain and repetitive collapse and opening of alveolar structures [312]. Further, it is possible to drive respiration by local tissue deformation acquired e.g., from a time series of imaging data over the breathing cycle [179]. In the same course the model is able to deduce local mechanical tissue properties in an inverse sense by simulating distortion during inflation and deflation and comparing with imaging data. By this means suspicious tissue regions such as cancerous areas might be identified. Prediction and tracking of local tumour movement during quiet breathing is also conceivable and provides valuable information for radiation therapy planning. Example applications for the *3D/3D* model will be presented in Chapter 4.

The generality of this modelling approach, the interaction between different physical fields and the possible high resolution of the domains, however lead to computational costs that limit the applicability in a real-time clinical setting. Although efficient solution strategies have been developed for this problem and show almost optimal scalability on high performance computing platforms [347], a single breath of the model can take up to more than one day of computing time. One possibility that builds upon availability of this general approach is the investigation of simpler dimensionally reduced models which might show similar results in certain applications but significantly reduce computing time. In the following, such simplified models for different applications in respiratory mechanics will be introduced. It is, however, important to keep in mind that evaluation of their performance for novel applications might require learning steps from the fully resolved model.

The underlying equations of the discussed *3D/3D* model have been reported earlier [363, 372] and been used for academic examples with up to five fluid outlets and tissue domains. Within this work the *3D/3D* approach is, for the first time, applied to a realistic lung model resolving airways and corresponding tissue regions up to the eighth tree generation (see also Chapter 4).

3.2.2. Reduced-dimensional structure and fully resolved three-dimensional fluid *(0D/3D)*

3.2.2.1. Motivation and model description

A first simplification of the previously described model is applicable if a fully resolved fluid domain (rigid or coupled with surrounding flexible airway walls) is required, while a three-dimensionally resolved structural representation can be omitted. At the terminal ends of a fully resolved deformable fluid domain, appropriate boundary conditions have to be defined representing the omitted lung tissue [71, 176, 225]. Here, the terminal ends of the fully resolved tree are defined by the current region of interest, the available computational resources, or simply by the resolution of available imaging data. The effect of tissue inflation and the resistance of the airways further downstream generate dynamic pressures at the outlets which are clearly different to the zero-traction or constant pressure ones which are often used by the biomechanics community [19–21, 39, 51, 60, 71, 72, 366]. Further, there has to be a storage possibility for outflowing volume during inspiration at each outlet which must allow flow to re-enter the domain for consistent representation of expiration without prescription of intransparent patient-specific boundary conditions as e.g., done in [369].

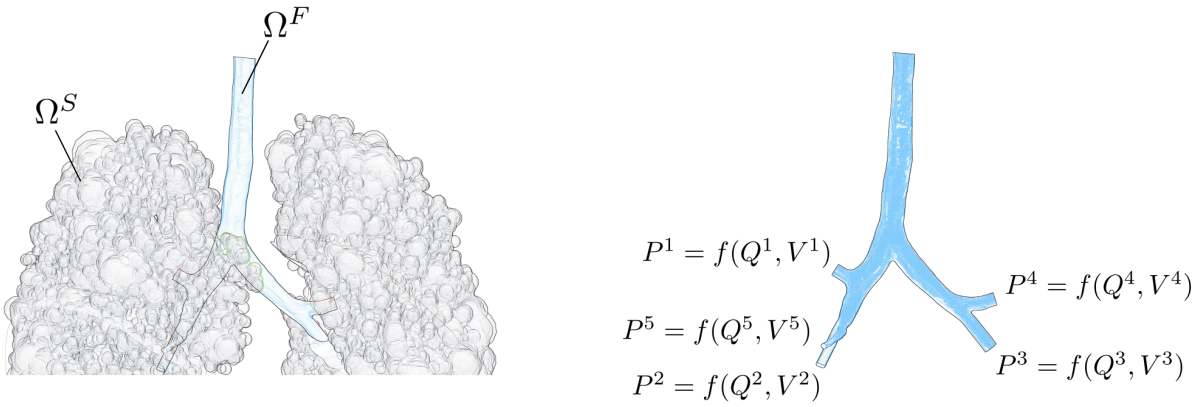

Figure 3.5.: Schematic for the *0D/3D* model consisting of a fully resolved deformable fluid domain Ω^F and a reduced model of lung tissue Ω^S realised as flow- and volume-dependent non-linear boundary conditions $P = P(Q, V)$. For easier display the sketch is exemplified for five outlets only.

Therefore in this work, the tissue region associated to each outlet is modelled via a non-linear flow and volume dependent pressure boundary condition

$$P = P(V, Q) \tag{3.16}$$

Depending on the size of the tissue region and its material properties, a linear or non-linear pressure-flow-volume relationship can be derived to represent the downstream airway tree and the lung tissue stiffness at each of the outlets (see Figure 3.5).

This derivation can for example be realised from detailed experimental and numerical data on an alveolar duct model [83, 85, 86]. Single alveolar ducts can then be collocated to build the tissue regions supplied by a fully resolved airway. Alternatively, regional functional diagnostics can be included and it is generally possible to prescribe any linear or non-linear function that represents the known regional resistance and compliance at each of the outlets. One particular established concept here is to compute an equivalent resistance R_{eq} for the airway tree further downstream the current outlet based on the geometrical dimensions of the smaller airways. This equivalent resistance is then combined with an equivalent compliance C_{eq} of the lung tissue in question towards

$$P(V, Q) = R_{eq} \cdot Q + \frac{1}{C_{eq}} \cdot V \tag{3.17}$$

with

$$Q = \int_{\Gamma_{\text{out}}} \mathbf{u}^{\text{F}} dA, \quad V = \int_{t_1}^{t_2} Q dt. \tag{3.18}$$

One assumption which is inherent in using a functional relationship for flow-dependent outlet pressures is that there are no recirculation zones occurring across the fluid outlets. This means that cutting after the third or fourth generation is usually physiologically realistic, as turbulence

has almost vanished then [72]. It is further assumed that tree elongation induced by inflation of lung tissue is small [183]. Thus, there is no significant distortion of the deformable fluid domain especially in terms of branching angles that could alternate recirculation zones at bifurcations within the domain and associated particle flow during respiration. The radial expansion of the airway tree, which leads to different cross sections during in- and expiration or in cases of bronchoconstriction, can be included in this approach via respecting fluid-structure interaction with flexible airway walls as presented in Section 2.3. In such studies the stabilising effect of surrounding tissue can e.g., be modelled via simple springs with the stiffness of lung parenchyma attached to the outside of airway walls.

The novelty of the *0D/3D* concept is characterised by two core effects: First, a computation of correct pressure levels at the outlets of the compliant airways is enabled. Second, fluid volume leaving the deformable domain can be stored and re-enter the domain for consistent modelling of expiration again making use of sophisticated stabilisation techniques [31, 134]. Without such a storage possibility it is not known how much air flows back into the domain from different outlets and additional assumptions have to be included for modelling expiration. An accurate possibility to model storage is of particular importance in the relevant case of simulating heterogeneous lungs, air trapping, or collateral ventilation. The storage possibility is also the main difference to previously used Windkessel or impedance models [71] which might provide a correct pressure niveau dependent on the flow but lack the possibility of storage.

3.2.2.2. Mathematical formulation

The underlying mathematical formulation of airflow is governed by the fully resolved incompressible Navier-Stokes equations possibly including FSI. Following Eq. (2.16) the discretised residuum of the incompressible Navier-Stokes equations extended by the non-linear pressure boundary condition $P(Q,V)$ is denoted as

$$\mathbf{r}^{\mathrm{F}}\left(\mathbf{u}^{\mathrm{F}},\mathbf{p}^{\mathrm{F}}\right)=\mathbf{F}\left(\mathbf{u}^{\mathrm{F}},\mathbf{p}^{\mathrm{F}}\right)-\mathbf{f}^{\mathrm{F}}\left(\mathbf{u}^{\mathrm{F}},\mathbf{p}^{\mathrm{F}}\right). \tag{3.19}$$

All quantities refer to the current timestep $n+1$ and therefore this superscript is omitted. By definition, the discrete vector $\mathbf{f}^{\mathrm{F}}\left(\mathbf{u}^{\mathrm{F}},\mathbf{p}^{\mathrm{F}}\right)$ contains the applied discrete boundary term $\mathbf{h}^{\mathrm{F}}(\mathbf{u}^{\mathrm{F}})$ (see Eq. (2.14) and Eq. (2.7)). This applied boundary term $\mathbf{h}^{\mathrm{F}}(\mathbf{u}^{\mathrm{F}})$ now includes the discrete non-linear relationship between the discrete pressure $\mathbf{P}$, flow $\mathbf{Q}$ and the volume $\mathbf{V}$ of the attached tissue region to be modelled at the outflow boundary. The applied boundary term then reads

$$\begin{aligned}\mathbf{h}(\mathbf{u}^{\mathrm{F}}) &= -u_n^{\mathrm{in,F}}\mathbf{u}^{\mathrm{F}}-\mathbf{p}^{\mathrm{F}}\mathbf{n}+2\nu\boldsymbol{\varepsilon}(\mathbf{u}^{\mathrm{F}})\mathbf{n} &(3.20)\\ &= -u_n^{\mathrm{in,F}}\mathbf{u}^{\mathrm{F}}-\mathbf{P}(\mathbf{Q},\mathbf{V})\mathbf{n}+2\nu\boldsymbol{\varepsilon}(\mathbf{u}^{\mathrm{F}})\mathbf{n}. &(3.21)\end{aligned}$$

To avoid iterative solution of the flow and volume dependent boundary pressure at the current outlet, a linearisation of the flow and volume dependent pressure boundary condition can be included in the Navier-Stokes equations and directly be solved within the Newton procedure of the fluid problem. Following Eq. (2.17), the linearised momentum equation reads

$$\frac{\partial\mathbf{r}^{\mathrm{F}}}{\partial\mathbf{u}_i^{\mathrm{F}}}\Delta\mathbf{u}_i^{\mathrm{F}}+\frac{\partial\mathbf{r}^{\mathrm{F}}}{\partial\mathbf{p}_i^{\mathrm{F}}}\Delta\mathbf{p}_i^{\mathrm{F}}=-\mathbf{r}_i^{\mathrm{F}} \tag{3.22}$$

with the index i indicating the last Newton iteration step. Recalling Eq. (2.17) and Eq. (3.19), the non-linear residuum including the flow and volume dependent pressure boundary condition has to be linearised as

$$\frac{\partial \mathbf{r}^{\mathrm{F}}}{\partial \mathbf{u}_i^{\mathrm{F}}} = \mathbf{K}_{\mathrm{uu},i}^{\mathrm{F}} - \frac{\partial \mathbf{h}(\mathbf{u}^{\mathrm{F}})}{\partial \mathbf{u}_i^{\mathrm{F}}} \tag{3.23}$$

$$= \mathbf{K}_{\mathrm{uu},i}^{\mathrm{F}} - \left(-u_n^{\mathrm{F,in}} - \frac{\partial \mathbf{P}(Q,V)}{\partial \mathbf{u}^{\mathrm{F}}} + 2\nu \mathbf{n} \frac{\partial \boldsymbol{\varepsilon}(\mathbf{u}^{\mathrm{F}})}{\partial \mathbf{u}^{\mathrm{F}}} \right). \tag{3.24}$$

In the residuum $\mathbf{r}_i^{\mathrm{F}}$ on the right hand side of Eq. (3.25), the corresponding boundary term $\mathbf{h}(\mathbf{u}^{\mathrm{F}})$ also has to be included consistently. This leads to the final linearised system of equations for the *0D/3D* lung model written as pure fluid mechanical problem.

$$\begin{bmatrix} \mathbf{K}_{\mathrm{uu}}^{\mathrm{F}} - \dfrac{\partial \mathbf{h}(\mathbf{u}^{\mathrm{F}})}{\partial \mathbf{u}^{\mathrm{F}}} & \mathbf{K}_{\mathrm{up}}^{\mathrm{F}} \\ \mathbf{K}_{\mathrm{pu}}^{\mathrm{F}} & \mathbf{K}_{\mathrm{pp}}^{\mathrm{F}} \end{bmatrix}_i \begin{bmatrix} \Delta \mathbf{u}^{\mathrm{F}} \\ \Delta \mathbf{p}^{\mathrm{F}} \end{bmatrix}_i = -\mathbf{r}_i^{\mathrm{F}}. \tag{3.25}$$

The additional term in the matrix compared to the pure incompressible Navier-Stokes equations is marked in yellow in Eq. (3.25). Finally, the discrete solution vectors for velocity and pressure in the next iteration step $i+1$ are updated via

$$\mathbf{u}_{i+1}^{\mathrm{F}} = \mathbf{u}_i^{\mathrm{F}} + \Delta \mathbf{u}_i^{\mathrm{F}} \tag{3.26}$$

$$\mathbf{p}_{i+1}^{\mathrm{F}} = \mathbf{p}_i^{\mathrm{F}} + \Delta \mathbf{p}_i^{\mathrm{F}}. \tag{3.27}$$

For more details on this computationally efficient approach, the reader is referred to [134].

3.2.2.3. Discussion and example applications

In summary, the *0D/3D* model is a classical fluid or FSI problem extended by a non-linear boundary condition for the outlet pressure dependent on current flow into and volume of the tissue to be modelled. For efficiency, the boundary condition is linearised within the system of equations of the fluid/FSI problem and can be solved within the same Newton step, i.e., no further iteration loop is needed for computing the boundary pressure.

The coupling of a fully resolved deformable fluid domain with resistive airway trees (hybrid (conducting) model) is similar to the approach derived here and can also provide correct pressures. Whether such hybrid (conducting) models are able to model expiration depends on availability of storage capacity at the terminal ends of the tree. Availability of a storage capability applies e.g., to [132, 176, 187, 209, 246, 370]. If flow quantities in the resistive tree are not of interest, the *0D/3D* is, however, a more efficient approach than the previously reported hybrid (conducting) ones.

The novelty against previous approaches seems small, however, it has great impact in the field of respiratory biomechanics. Without a representation of small airway structures and lung tissue, fluid flow would mainly be characterised by the geometry of large resolvable airways and their resistance. However, the large airways might supply single regions in which the peripheral airway structures are collapsed and thus exhibit a much higher flow resistance. Also, they

can supply tissue regions with increased stiffness or collapse which significantly hinders incoming airflow. Therefore, the entire system including all downstream effects of a fully resolved airway has to be respected for physiologically meaningful lung simulations. Without such considerations, ventilation of diseased regions would be over-estimated. Also, transport of curative aerosols to rehabilitate original lung function in such regions would be overrated. Further, one needs a storage capacity for lung volume during inspiration which can re-enter the domain during exhalation. This is also the reason why classical Windkessel or impedance models have to be extended, as they are not able to store the entire outflowing volume and their application would lead to mass-loss over the breathing cycle.

As mentioned previously, the lung is the only organ in the human body which is flown through by gas in two directions. Interesting phenomena have, however, so far mainly be investigated during inspiration due to lack of appropriate boundary conditions. Now, also studies of phenomena which occur during the phase of flow reversal or even only after a few cycles are possible. This might lead to totally different patterns of particle deposition or carbon-dioxide clearance than assumed today.

In general the *0D/3D* approach as a pure fluid mechanical problem is recommended to study flow in larger airways that are stiff enough and/or for small tidal volumes that do not cause too much deformation and distortion of the bronchial geometry. Next to several examples mentioned previously [32, 70–72, 137, 138, 205, 209, 370], many investigations in transitional and turbulent flow phenomena [19, 20, 51, 60] and transport [187, 210, 246, 247, 373] can profit from this type of model. The extension towards FSI investigations is possible in general and follows the single steps in Section 2.3. Studies, which are claiming that FSI is not required for the bronchial tree have to be checked carefully [366]. If such statements are made without correct representation of outflow boundaries, dynamic pressure changes during respiration are purely based on flow resistance and will be under-estimated. Consequently smaller pressures under-estimate tree deformation in radial direction. The applicability of a pure fluid mechanical formulation versus FSI for investigations using the *0D/3D* model will be discussed in detail in Chapter 7.

The *0D/3D* model formulated in this section has been newly developed within this work based on the incompressible Navier-Stokes equations (see Section 2.1.1) and an available efficient formulation for handling backflow into the fluid domain [134].

3.2.3. Fully resolved three-dimensional structure and reduced-dimensional fluid *(3D/0D)*

3.2.3.1. Motivation and model description

Analogously to the previously described model also a simplification of the deformable fluid domain is possible while the structural part of the lung remains fully resolved.

This can be realised via the concept of dimensional reduction of the compliant airway segments presented in Section 2.1.2. Under certain assumptions (see Section 2.1.2), the velocity profile can be integrated in radial and axial direction towards a zero-dimensional (*0D*) formulation. Outlet pressures and flows of the *0D* formulation are further coupled to the volume changes of the associated structural regions and thus airflow is again linked to structural deformation (see Figure 3.6).

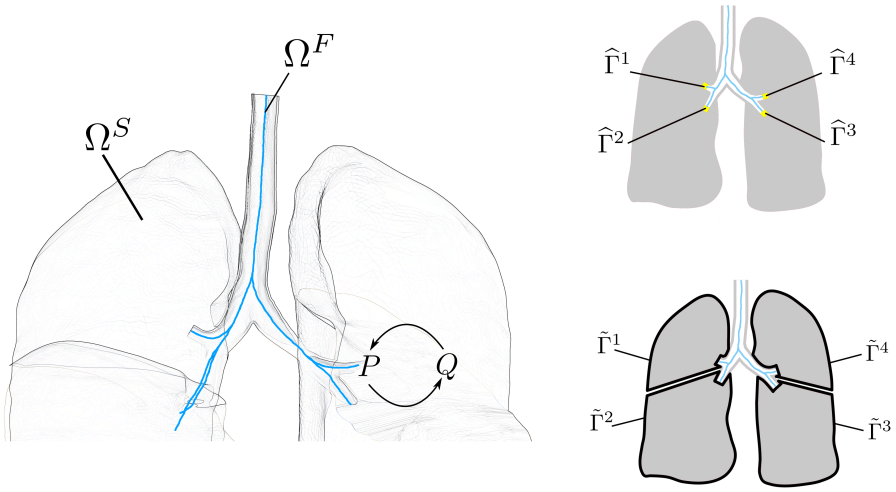

Figure 3.6.: Schematic of the *3D/0D* model with a fully resolved lung tissue and a reduced-dimensional formulation for the compliant airways indicated as centerline. The pressure P and airflow Q at the fluid outlets $\hat{\Gamma}$ are coupled to the inflation of the associated structural regions denoted as $\tilde{\Gamma}$. For easier display the sketch is exemplified for four of the five lobar bronchi visible in this lung slice only (see also Figure 3.3). The marked boundaries correspond to the anatomically correct boundaries of the five lung lobes visible in this lung slice.

The novelty of this approach compared to those in Section 3.1.6 lies in the availability of an efficient reduced-dimensional flow model with all benefits of a fully resolved structure with known material behaviour [29, 273]. This covers a fully resolved and local quantification of stresses and strains in the parenchyma. Further, an effect known as lung interdependence (see [228] and Section 2.2.2) is inherent in all fully resolved structural models. Physically, interdependence is the interaction between neighbouring air spaces which share a common alveolar wall. If single airspaces expand or shrink, this influences their neighbours towards shrinking/expansion such that there is no overlap or gap between them. Interdependence is thus an important concept to add stability to the lung against local over-inflation or collapse by the stiffness of surrounding tissue. Finally, the *3D/0D* model offers a possibility to prescribe imaging-based regional deformation of lung tissue to a fast reduced-dimensional flow model.

The derivation of a reduced-dimensional set of fluid equations requires some assumptions which are outlined in Section 2.1.2 in full detail.

3.2.3.2. Mathematical formulation

To reuse the efficient field solvers for the *3D* structure and for *0D* compliant airways in this work, the formulation of the *3D/0D* model is presented and solved using a partitioned scheme. Following the ideas in [191], the degrees of freedom of both fields are split into coupling degrees of freedom and the remaining inner degrees of freedom I. In case of the *3D* structure,

the coupling degrees of freedom are contained in $\tilde{\Gamma}$ and for the *0D* fluid in $\hat{\Gamma}$ (see Figure 3.6). With this split, the structural operator $\mathbf{S}\left(\mathbf{d}^{\mathrm{S},n+1}\right) = \mathbf{f}^{\mathrm{S}}$ (Eq. (2.61)) and the *0D* fluid operator $\mathbf{K}\left(\mathbf{P}^{n+1}\right) = \mathbf{Q} + \mathbf{RHS}$ (Eq. (2.50)) read

$$\begin{bmatrix} \mathbf{S}_{II} & \mathbf{S}_{I\tilde{\Gamma}} \\ \mathbf{S}_{\tilde{\Gamma}I} & \mathbf{S}_{\tilde{\Gamma}\tilde{\Gamma}} \end{bmatrix} \begin{bmatrix} \mathbf{d}_I^{\mathrm{S}} \\ \mathbf{d}_{\tilde{\Gamma}}^{\mathrm{S}} \end{bmatrix} = \begin{bmatrix} \mathbf{f}_I^{\mathrm{S}} \\ \mathbf{f}_{\tilde{\Gamma}}^{\mathrm{S}} \end{bmatrix}, \tag{3.28}$$

$$\begin{bmatrix} \mathbf{K}_{II} & \mathbf{K}_{I\hat{\Gamma}} \\ \mathbf{K}_{\hat{\Gamma}I} & \mathbf{K}_{\hat{\Gamma}\hat{\Gamma}} \end{bmatrix} \begin{bmatrix} \mathbf{P}_I \\ \mathbf{P}_{\hat{\Gamma}} \end{bmatrix} = \begin{bmatrix} \mathbf{Q}_I + \mathbf{RHS}_I \\ \mathbf{Q}_{\hat{\Gamma}} + \mathbf{RHS}_{\hat{\Gamma}} \end{bmatrix}. \tag{3.29}$$

With these definitions the partitioned scheme is realised with the following single steps:

1. Starting point is a suitable prediction of the structural displacement of the interface $\mathbf{d}_{\tilde{\Gamma},i}^{\mathrm{S}}$.

2. Calculate the flow $\mathbf{Q}_{\tilde{\Gamma},i}$ into the region bounded by $\tilde{\Gamma}$ resulting from the displacements $\mathbf{d}_{\tilde{\Gamma},i}^{\mathrm{S}}$ using Eq. (3.5) and Eq. (3.6).

3. Solve the *0D* fluid problem with the flow $\mathbf{Q}_{\tilde{\Gamma},i}$ prescribed at the outlets $\hat{\Gamma}$ to obtain the pressure $\mathbf{P}_{I,i}$ inside the *0D* domain and $\mathbf{P}_{\hat{\Gamma},i}$ at the coupling points $\hat{\Gamma}$

$$\begin{bmatrix} \mathbf{P}_I \\ \mathbf{P}_{\hat{\Gamma}} \end{bmatrix}_i = \begin{bmatrix} \mathbf{K}_{II} & \mathbf{K}_{I\hat{\Gamma}} \\ \mathbf{K}_{\hat{\Gamma}I} & \mathbf{K}_{\hat{\Gamma}\hat{\Gamma}} \end{bmatrix}_i^{-1} \begin{bmatrix} \mathbf{Q}_I + \mathbf{RHS}_I \\ \mathbf{Q}_{\hat{\Gamma}} + \mathbf{RHS}_{\hat{\Gamma}} \end{bmatrix}_i. \tag{3.30}$$

4. Transfer this coupling pressure $\mathbf{P}_{\hat{\Gamma},i}$ to the *3D* structural problem and solve the structural equation for the applied coupling pressure $\mathbf{P}_{\hat{\Gamma},i}$ to obtain the structural displacements $\mathbf{d}_I$ inside the domain and the new displacements on the boundary $\mathbf{d}_{\tilde{\Gamma}}$.

$$\begin{bmatrix} \mathbf{d}_I^{\mathrm{S}} \\ \mathbf{d}_{\tilde{\Gamma}}^{\mathrm{S}} \end{bmatrix}_i = \begin{bmatrix} \mathbf{S}_{II} & \mathbf{S}_{I\tilde{\Gamma}} \\ \mathbf{S}_{\tilde{\Gamma}I} & \mathbf{S}_{\tilde{\Gamma}\tilde{\Gamma}} \end{bmatrix}_i^{-1} \begin{bmatrix} \mathbf{f}_I^{\mathrm{S}} \\ \mathbf{f}_{\tilde{\Gamma}}^{\mathrm{S}} - \mathbf{P}_{\hat{\Gamma}\cdot} \end{bmatrix}_i. \tag{3.31}$$

To obtain a converged solution for the coupling between the two fields, steps 2 to 4 are repeated iteratively until the coupling pressure $P_{\hat{\Gamma}}$ and the coupling flow $Q_{\tilde{\Gamma}}$ do not change from one iteration to the next. With each iteration the index i is increased. In strict mathematical writing the solution is converged if

$$||\mathbf{P}_{\hat{\Gamma},i+1} - \mathbf{P}_{\hat{\Gamma},i}|| < \text{tol} \quad \text{and} \quad ||\mathbf{Q}_{\tilde{\Gamma},i+1} - \mathbf{Q}_{\tilde{\Gamma},i}|| < \text{tol} \tag{3.32}$$

where tol denotes a given tolerance.

To accelerate the convergence behaviour, a relaxation step can be performed for the coupling pressure between step 3 and step 4. Instead of the pressure computed from step 3, now denoted as $\tilde{\mathbf{P}}_{\hat{\Gamma},i+1}$, a relaxed pressure $\mathbf{P}_{\hat{\Gamma},i+1}$ is computed as

$$\mathbf{P}_{\hat{\Gamma},i+1} = \omega_i \tilde{\mathbf{P}}_{\hat{\Gamma},i+1} + (1 - \omega_i)\mathbf{P}_{\hat{\Gamma},i} \tag{3.33}$$

with the pressure from the previous iteration step $\mathbf{P}_{\hat{\Gamma},i}$. As relaxation parameter ω_i constant values $0 < \omega_i < 1$ can be used. In case more than two iterations have been performed, the

Aitken Δ^2 method [175] can be used as an efficient method to speed up convergence for each coupling pressure $P_{\hat{\Gamma}}$ at a single outlet

$$P_{\hat{\Gamma},i+2} = \omega_{i+1}\tilde{P}_{\hat{\Gamma},i+2} + (1-\omega_{i+1})P_{\hat{\Gamma},i+1} \tag{3.34}$$

with

$$\omega_{i+1} = \frac{P_{\hat{\Gamma},i} - P_{\hat{\Gamma},i+1}}{P_{\hat{\Gamma},i} - \tilde{P}_{\hat{\Gamma},i+1} - P_{\hat{\Gamma},i+1} + P_{\hat{\Gamma},i+2}}. \tag{3.35}$$

Obviously, the *3D/0D* model can also be formulated and solved in a monolithic way as given e.g., for FSI in Section 2.3. A similar approach to the *3D/0D* model that includes coupling of reduced-dimensional fluid with a poroelastic structure has been derived in [30] in full detail.

3.2.3.3. Discussion and example applications

The model denoted as *3D/0D* is essentially a combination of pressure and flow computed from well-known reduced-dimensional fluid models with volume changes and tractions of a fully resolved structure.

This concept is valuable if mainly structural aspects of the lung are to be investigated. Here, the reduced-dimensional representation supplies a simple and computationally cheap solution of the fluid quantities and its effect on structural deformation/inflation.

It is important to mention that even though turbulence cannot be resolved with the reduced-dimensional fluid approach, the effect of turbulence can be modelled. This means that if the *0D* model detects an airway with a higher Reynolds number than those defined as critical for the straight tube ($\mathrm{Re}_{\mathrm{crit}} = 2300$) the resistance will be adapted following the approach by [176, 258, 277]. It is worth to annotate that it is also possible to gain further tree generations e.g., from a tree-growing algorithm introduced in the next section. This allows finer subdivision of the tissue structure in smaller compartments and higher resolution of heterogeneity as would be possible with the airway tree segmentable from imaging data. Finally, kinematic constraints acting on the lung surface as a result of the deformation of the thoracic cage and the diaphragm can be respected.

Possible areas of usage for such an approach are investigations of detailed strain states during mechanical ventilation. As e.g., VILI/VALI are predominantly influenced by structural stresses and strains [242], a reduction of the deformable fluid domain might be conceivable. Under the same aspects a full resolution of the deformable fluid domain might be negligible for diagnosis of regions with suspicious material behaviour or tumour tracking applications. The main benefit of this approach as compared to the *3D/3D* model are the associated computational costs. In comparison with the *3D/3D* model the *3D/0D* approach is approximately 10 times faster for the same patient-specific geometry and boundary conditions described in detail in [372].

The building blocks for the *3D/0D* model, namely the fluid and structure operators as well as the coupling iteration have been available within [353]. A stable coupling with a consistent time integration scheme and the Aitken Δ^2 method for this model have been realised within this work.

3.2.4. Reduced-dimensional lung model *(0D/0D)*

3.2.4.1. Motivation and model description

The most efficient and reduced model is the one presented as *0D/0D* in the overview (Figure 3.2). This approach combines a reduced-dimensional formulation for compliant airways (see Section 2.1.2) with a functional relationship between pressure and volume of the terminal units of the tree (see Section 2.2.2). This approach is conceivable if no fully resolved fluid velocity profile is necessary for the current investigation and solely pressure and flow should be computed in the compliant airway segments. Further, on the structural side many cases only require the magnitude of regional strain while a detailed composition of isochoric and volumetric components is negligible. Then, a *0D* tree of compliant airways with up to 23 generations can be generated via a tree-growing algorithm [176, 328] providing high spatial resolution for *0D/0D* modelling (see Figure 3.7).

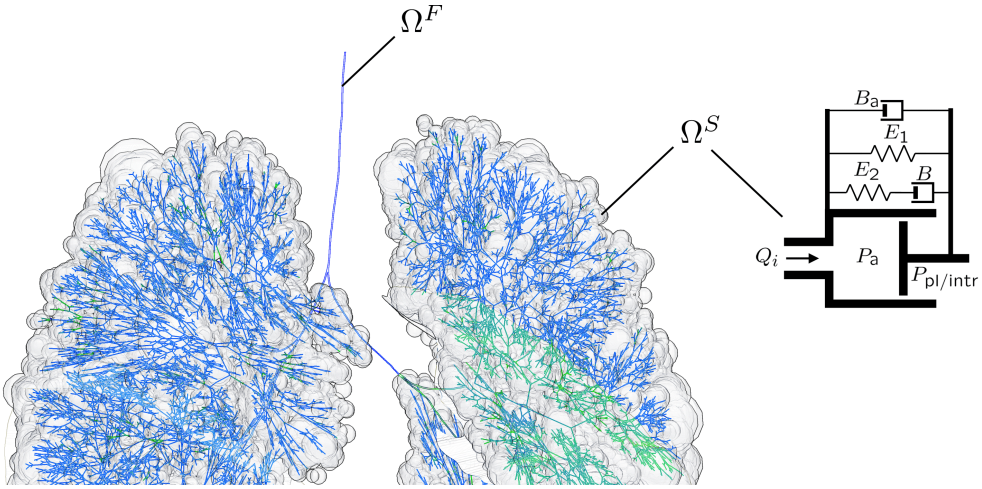

Figure 3.7.: Schematic of the model denoted as *0D/0D*. This model is composed of reduced-dimensional compliant airways Ω^F indicated by the centerline of the bronchial tree generated via a tree-growing algorithm. The non-linear acini Ω^S are represented via a Maxwell-model consisting of (non-)linear springs E_1, E_2 and dashpots B_1, B_2 that mimic the relationship between the pressure difference $P_{\mathrm{a(lv)}} - P_{pl/intr}$ and flow Q_i into lung tissue.

In fact many extremely efficient models in computational modelling of the respiratory system live from the fact that the airway tree is a well understood dichotomous branching structure. The branching patterns as well as diameter and length ratios are very well documented for humans [176, 216, 328, 356, 357] and for other species such as mice, which are often used in experiments [232]. This means that no segmentation of the entire tree is required to generate a patient-specific respiratory model. The hull geometry of the lung and the directional vector of the lobar bronchi are sufficient to generate a realistic coupled *0D/0D* model for each patient individually.

The assumptions for dimensional reduction of the deformable fluid domain are explained in Section 2.1.2 and are repeated briefly. The velocity profile of airflow is seen as axisymmetric, fully developed and airway curvature is neglected for velocity integration in radial direction.

For further integration in axial direction the pulsatile character of airflow is omitted as it is not relevant on the timescales of fluid flow in an airway segment (see Section 2.1.2). These assumptions are perfectly valid under (patho-)physiological conditions and the *0D* compliant airways are able to reproduce the pressure and flow properties of a fully resolved *3D* patient-specific fluid domain as shown in [176]. Further, it is assumed that the behaviour of lung tissue at the terminal ends of the tree, i.e., of the alveolar ducts, can be represented via a functional relationship. Detailed experimental and numerical investigations on alveolar ducts are available in the seminal work by Denny & Schroter [83, 85, 86] and it has been shown that a non-linear Maxwell model perfectly matches static pressure-volume and dynamic curves presented in these studies (see Section 2.2.2 and [283]).

One novelty compared to existing reduced-dimensional models [30, 49, 331] is the previously explained (see Section 3.2.3) ability to take into account and consistently model turbulence effects [93, 100, 176, 258, 277]. Further, the generation-dependent resistance model by van Ertbruggen [93] is only valid during inspiration. Therefore, the radius reduction of the convective ducts during expiration is respected via an additional equation for determination of airway radius dependent on the pressure difference across the wall and visco-elastic airway compliance (see Section 2.1.2). In the same course, airways are not only able to change its diameter but also to fully recruit and derecruit following the dynamic laws derived by the Bates group (see Section 2.1.2 and [22, 211, 222]). As a tissue model the non-linear Maxwell model from Section 2.2.2 and [283] is used which has been shown to be valid over the entire physiological pressure range. A final novelty overcomes the lack of tissue interdependence - a main objection against the usage of reduced-dimensional models so far. Recently, this concept has been proposed (partly in previous work [177] and finally in [283]) for reduced-dimensional lung models. Now, model volume-competition between inflating neighbouring acinar ducts can be respected resolving previous misconception [266]. In addition, the interaction between airways and surrounding parenchyma [212, 213] can be taken into account (see Section 2.2.2).

3.2.4.2. Mathematical formulation

Fluid flow in the deformable *0D* fluid domain Ω^F indicated by the centerline of the tree in Figure 3.7 is governed by the *0D* formulation for pressure and flow. The governing equations can be taken from Eq. (2.49) and the single matrix entries are in detail explained in Appendix A. For a single airway segment they read

$$\begin{bmatrix} -K_{aw} - K_{aw,\text{vis}} & K_{aw} \\ K_{aw} & -K_{aw} \end{bmatrix} \begin{bmatrix} P_1^{n+1} \\ P_2^{n+1} \end{bmatrix} = \begin{bmatrix} -Q_{aw}^{n+1} - RHS_1^n \\ Q_{aw}^{n+1} + RHS_2^n \end{bmatrix}. \tag{3.36}$$

Flow Q into the single acini Ω^S is then described via the generalised Maxwell model consisting of (non-)linear springs and dashpots and is dependent on the pressure difference $P_{\text{alv}} - P_{pl/intr}$ (see Eq. (2.84)).

$$\begin{bmatrix} -K_{ac} & K_{ac} \\ K_{ac} & -K_{ac} \end{bmatrix} \begin{bmatrix} P_{\text{alv}}^{n+1} \\ P_{\text{pl/intr}}^{n+1} \end{bmatrix} = \begin{bmatrix} -Q_{ac}^{n+1} - LHS^n \\ Q_{ac}^{n+1} + LHS^n \end{bmatrix}. \tag{3.37}$$

In case of an acinus that is in contact with the pleura, i.e., the hull contour of the lung, a pleural pressure P_{pl} is prescribed. In case the current acinus is located inside the domain it is surrounded by neighbouring acini and consequently an averaged interdependence pressure P_{intr} is used. Interdependency is then basically taken into account by linking external acinar pressures and thus propagates forces between neighbouring acini. How this is done in practice can be seen in Section 2.2.2.

For solving the full problem, the "stiffness" matrices of airways and acini are assembled into a single system matrix, a single solution vector containing the pressures $\mathbf{P}^{n+1}$ and a single right hand side containing the fluxes $\mathbf{Q}^{n+1}$. For a simplified example consisting of one airway and one acinus connected at $P_2^{n+1} = P_a^{n+1}$ and $Q_a^{n+1}w = Q^{n+1_{ac}}$ this reads

$$\begin{bmatrix} -K_{aw} - K_{aw,\text{vis}} & K_{aw} & \\ K_{aw} & -K_{aw} - K_{ac} & K_{ac} \\ & K_{ac} & -K_{ac} \end{bmatrix} \begin{bmatrix} P_1^{n+1} \\ P_2^{n+1} \\ P_{\text{pl/intr}}^{n+1} \end{bmatrix} = \begin{bmatrix} -Q_{aw}^{n+1} - RHS_1^n \\ RHS_2^n - LHS^n \\ Q_{ac}^{n+1} + LHS^n \end{bmatrix} \tag{3.38}$$

or in brief

$$\mathbf{K}_{aw,ac}\mathbf{P}^{n+1} = \mathbf{Q}^{*,n+1}. \tag{3.39}$$

A classical Newton method (see Eq. (2.17)) is then applied to solve the non-linear set of equations Eq. (3.38). The corresponding discrete non-linear residual of the *0D/0D* model is written as

$$\mathbf{r}_{aw,ac}^{n+1} = \mathbf{K}_{aw,ac}\mathbf{P}^{n+1} - \mathbf{Q}^{*,n+1} \tag{3.40}$$

and the linearised system of equations to be solved as

$$\frac{\partial \mathbf{r}_{aw,ac}^{n+1}}{\partial \mathbf{P}_i^{n+1}} \Delta \mathbf{P}_i^{n+1} = -\mathbf{r}_{aw,ac,i}^{n+1}. \tag{3.41}$$

Again, the solution of the new iteration step $i+1$ is obtained as

$$\mathbf{P}_{i+1}^{n+1} = \mathbf{P}_i^{n+1} + \Delta \mathbf{P}_i^{n+1}. \tag{3.42}$$

$$\tag{3.43}$$

Additionally, collapsed and open states for each airway are computed via virtual trajectories. A decision between fully open and closed state is dependent on current and previous airway inner pressure, the critical open/closing pressure and the two time constants for closure/reopening derived in Section 2.1.2. If an airway is collapsed, the value for its resistance R_μ contained in K_{aw} will be increased to a high value and thus hinder airflow in that specific region as outlined in Section 2.1.2. It is worth to mention that the decision whether an airway is open or collapsed is solved iteratively with the pressure P_{i+1}^{n+1} and the flow Q_{i+1}^{n+1} of the full *0D/0D* problem. This means that e.g., effects of avalanche reopening [321] can be simulated which requires the daughter airways to open almost instantly with their parent in the tree.

For a more detailed derivation of the mathematical formulation and solution of the complete *0D/0D* model, the reader is referred to [176, 283].

3.2.4.3. Discussion and example applications

The last presented *0D/0D* model is essentially a dimensionally reduced relationship between pressure and flow in the compliant airways and in the visco-elastic acini equipped with all properties that are necessary to accurately describe the underlying physics of the lung. Extensions include interdependence (see Section 2.2.2), flexible airways able to collapse and reopen (see Section 2.1.2 and [211]), and an acinar model that is valid over the entire physiological pressure range (see Section 2.2.2 and [283]).

Such a model is often sufficient for answering clinical questions especially when considering the quality of input data. Errors in segmented geometries due to low resolution and contrast in medical imaging might e.g., introduce errors in velocity profiles such that only averaged flow remains as reliable quantity. Also, local pleural pressure measurements which are challenging [326] can corrupt a derivation of strain components and sometimes allow only quantification of absolute magnitude. Further, time is a critical component limiting computation and detailed interpretation of fully resolved quantities in a clinical setting. Many more questions arise when trying to bring a computational model into a clinical setting, i.e., to bedside. An important one might be: "Is something computed that is already contained as model input or can possibly never been validated in reality?", and an answer will be provided in Chapter 6 of this work.

The described *0D/0D* model actually performs well in many of these points. It is in good agreement with fully resolved three-dimensional simulations of airflow [176] which underlines the quality of results in realistic settings. Further, the model is still built on solid mathematical ground and thus requires no extensive fitting as single and multi-compartments do. All important phenomena such as interdependence and recruitment or derecruitment are included and successfully tested in patient-specific examples or experimental animal studies [211]. This patient-specific case also shows that the *0D/0D* approach is 100-500 times faster than *3D/3D* for same patient. Further its predictive capability is verified against clinical measurements [285].

In retrospect, the *0D/0D* approach meets several points of motivation that have led to development of computational lung models. It (i) enables to isolate certain effects computationally e.g., by changing parameters such as peak ventilatory pressure and allows evaluation of resulting local ventilation. Second (ii) the model gives an additional insight into regional tissue aeration and mechanical strain distribution which is not obtainable from imaging data. Finally (iii) the model shows a predictive capability as it is not built upon extensive fitting of clinical measurements but can be validated against such data globally and regionally (see Chapter 6). Thereby pre-computation of certain therapy options can be performed and resulting optimal strategies can be applied to the patient only if the computationally prediction shows improved outcome. Inadequate or high-risk-high-reward settings do not have to be tested at a real patient.

Possible areas of application of the *0D/0D* approach are the investigation of VILI/VALI mainly because the *0D* compliant airways are comparably good as the *3D* [176] and because regional strain magnitude is already an extremely valuable quantity compared to current clinical investigations [267]. Another application is the evaluation of collapse and the design of possible reopening manoeuvres *in silico* as one example for high-risk-high-reward manoeuvre. Examples for such investigations will be presented in Chapter 6. Further, this model is applicable as relatively robust basic approach for further gas-exchange models.

Potential directions for further research in this context might be the integration of patient-specific thorax boundary conditions and investigations on collapse and reopening pressures in a

realistic unsymmetrical patient-specific tree geometry investigating phenomena with high impact hypothesised previously [321].

The basic *0D/0D* model has been existing previously [176] and a first formulation for lung interdependence has been reported in [177], yet with an incomplete validation. Within this work and in [283], the validation for lung interdependence has been completed. In addition, the *0D/0D* model has been extended by reduced-dimensional reopening dynamics and the equations for airway-acinus interaction (see Chapter 2). Finally, the extended *0D/0D* model has been used in predicting patient-specific ventilatory response (see Chapter 6).

3.3. Summary

In this chapter, four coupled models of the respiratory system have been presented which are derived from underlying physical principles described in Chapter 2 and consistently represent the interaction between fluid flow and tissue inflation in the lung. The road from fully resolved *3D/3D* towards simpler dimensionally reduced models has been walked down introducing all necessary assumptions and resulting limitations of the single approaches. Finally, one ends up with a coupled computational respiratory model (*0D/0D*), which is both fast to compute and reliable in its quality of clinical prediction. For a number of clinically relevant questions such models seem to be the most promising approach to deliver patient-specific regional pressure and flow quantities and to meet the challenge of optimising ventilation in a clinical setting, e.g., presented in Chapter 6.

Part II.

Patient-specific Application and Validation

In Part II of this work, three relevant applications from clinical practice are presented to show the power and potential of the single lung models, developed in Part I, in three representative patient-specific settings in respiratory care.

The presented investigations start with the basic scenario of healthy quiet breathing. The model used for this investigation is the fully resolved volumetrically coupled *3D/3D* model to ensure that all aspects in respiration are adequately captured and that no effects are lost due to model simplification/dimensional reduction. The main goal of this scenario is to learn how lung motion, tissue inflation and airflow distribution work in detail under normal breathing conditions and to define a baseline state for lung behaviour in a healthy human subject. Then, the transition is made for the same patient towards the case of mechanical ventilation respecting kinematic constraints given by the passive thorax and the relaxed respiratory muscles. Different clinically relevant mechanical ventilation protocols are further tested *in silico* and evaluated with respect to lung motion, regional ventilation and airflow patterns compared to the healthy case.

In Chapter 5, a relationship between alveolar air content and lung tissue bioimpedance is derived from the microstructural architecture of lung tissue to prepare validation of regional ventilation with EIT.

The second scenario, presented in Chapter 6, goes one step further towards clinical applicability of respiratory modelling and focuses on simulating an ARDS patient under pressure-controlled mechanical ventilation using the efficient *0D/0D* model. Lessons learned from the fully resolved observations of airflow and tissue inflation (see Chapter 4) allow the usage of simplified modelling approaches in this setting in good agreement with real physiology. Additionally, a novel "virtual EIT" module is developed to monitor computed regional ventilation in close interaction with clinical measurements. The "virtual EIT" approach works almost in real time with the simulation of regional ventilation and allows successful validation of computed results against clinical measurements. Further, the coupling between "virtual EIT" and the *0D/0D* lung model allows impressive prediction of patient-specific response to certain therapeutic measures.

Finally, the third application relevant in a clinical setting is concerned with specific ventilation patterns in respiratory care of neonates, namely the previously (see Chapter 1) mentioned mechanical ventilation with high frequency and low tidal volumes including oxygen transport. Due to hypothesised special vortex structures, specific attention is put on airflow in the bronchial tree, which is represented as fully resolved continuum, while for lung tissue a dimensionally reduced description is used. The resulting *0D/3D* model of a neonatal human lung is described in detail in Chapter 7 and outlines flow phenomena responsible for an efficient oxygenation during HFOV in neonates.

In summary, the examples outlined in Part II of this work represent three highly relevant applications in pulmonary medicine. In each single example, the used computational model provides novel insight into respiratory physiology, can be validated against clinical measurements, and helps to assess the most efficient treatment options for neonatal or adult patients involved. The three examples are discussed in detail in the following chapters of this work.

4. Fully resolved three-dimensional volumetrically coupled model

Developing medical treatment strategies for acute and chronic respiratory diseases mentioned in Chapter 1 requires three basic aspects in respiratory care: (i) a precise diagnosis of a patient's individual anatomy and pathophysiology; (ii) a deep understanding of lung structure and function; and (iii) a reliable prediction of patient-specific response to certain therapeutic measures. Modern medical imaging methods can provide important insight into the first and partly into the second aspect. However, they lack in predicting further states beyond the imaged ones (step (ii)). Advanced computational lung models derived in Part I of this work are able to fill this gap and by incorporating the underlying physics of the organ they can provide the third, predictive aspect in respiratory care.

Thereto, in this chapter, the most general and highest resolved *3D/3D* model available in respiratory mechanics is built up from patient-specific medical imaging data. Then, lung motion during healthy quiet breathing is tracked and airflow, airway deformation, and regional tissue inflation are computed for this scenario at a level of detail that has never been visible so far. Further, four different scenarios of mechanical ventilation are simulated assuming that the same patient would develop an ARDS. Computed results show the difference between active breathing and mechanical ventilation in terms of airflow, pressure and regional ventilation quantities. These quantities provide a deeper insight into lung behaviour during image acquisition and for situations beyond the imaged ones. Ultimately, respiratory modelling may help to predict suitable treatment options in respiratory care reducing the need for additional image acquisition.

4.1. Introduction to fully resolved patient-specific lung modelling

One major challenge in managing patients with acute respiratory disease such as ARDS is to assist in ventilation in an almost normal manner without inducing additional damage to the patient's lung (see Section 1.2). Thereto, several so-called lung protective ventilation strategies have been proposed where the most promising ones are those that can be individualised to specific patient needs [9, 128, 349]. To develop such lung protective ventilation protocols and to adequately adapt them to an individual patient, three aspects are required to ensure best possible treatment and optimal patient recovery: (i) a precise diagnosis of individual patient anatomy and pathophysiology; (ii) a deep understanding of respiratory mechanics and biology in health and disease; and (iii) a reliable prediction of patient-specific response to certain therapeutic measures.

Unfortunately, widely available global measurements of lung function cannot give a full insight into the regional behaviour of the lung and the correlation between lung structure and function. Considering e.g., a standard pulmonary function test indicates that the lung of a patient is working at 50%, it remains unclear whether the entire lung of this patient is working at 50%, or if one half is operating fully normal, while the other half is not working at all. These two possibilities would, however, have a decisive impact on administration of further clinical treatment.

Modern medical imaging such as multi-detector computed tomography (MDCT), hyperpolarised gas MRI, PET or single photon emission computed tomography (SPECT) have successfully advanced insight into regional lung behaviour and thus significantly contributed to the first two of the above mentioned aspects in respiratory care. To begin with, MDCT has revealed human anatomy in high detail. In terms of pulmonary imaging, this ability has been used to identify collapsed lung regions, accumulation of liquid, and to estimate ventilation in different, distinct regions of the lung [214]. If two CT images are available, one at full expiration and the other at full inspiration, anatomical differences between the two states haven been used to set PEEP levels and to identify potential regions of recruitment [59, 112, 116]. This so-called inspiratory/expiratory imaging is one of the first functional applications beyond pure anatomical imaging. To further allow for investigations of gas transport processes and mixing, stable gaseous radiomarkers such as Xenon (Xe) or Krypton (Kr) have been added to the airflow operating as contrast agents. These gases can be tracked in a time series of CT images and offer an insight into regional ventilation at high resolution. To avoid the high radiation doses for subsequent acquisition of CT images, hyperpolarised pulmonary MRI imaging has been developed and associated tracking of gaseous radiomarkers has been realised by hyperpolarised noble gas contrast agents such as Helium (^{3}He) or Xenon (^{129}Xe). Relevant examples can e.g., found in [307]. The hyperpolarised noble gas MRI imaging provides a method to visualise regional distribution of inhaled gas during the wash-in and wash-out phases and during static breath-hold. However, potential biological reactions to the involved radiomarker gases (e.g., the anaesthetic effect of Xenon) are not fully resolved, and the influence of carrier gases is still a topic of ongoing research [235]. Further, medical imaging of critically diseased patients dependent on a mechanical ventilator is difficult per se and even more challenging, if additional dosing of gaseous tracers is involved. Therefore, improved methods to omit the radiomarker gases have been developed recording a time series of 3D-CT scans. These methods are named 4D-CT imaging for three spatial dimensions in addition to the time. Recording a 4D-CT scan series usually takes 10-20 minutes of total examination time and exposes the patient to 30-40mSv of radiation (1-5 times the annual background radiation [307]). Non-rigid image registration (see Section 4.2.4) is then used to extract a detailed ventilation map over the entire breathing cycle [179]. Ventilation maps have successfully been validated against hyperpolarised ^{3}He studies with good agreement [108, 275] and provided a deeper insight into ventilation from a scientific point of view.

Despite all these advances, the insight provided by medical imaging is limited to the currently imaged state. To fulfil the important step towards prediction of suitable clinical treatment, various modelling approaches in respiratory biomechanics have been introduced (see Chapter 3). Such models are able to mimic the behaviour of the lung based on measurements and/or information from medical imaging. Previous approaches in this context have already extracted patient-specific three-dimensional and one-dimensional airway tree geometries from medical imaging data [329]. Further, regional ventilation, computed via image registration maps, has been applied

as so-called patient-specific flow rate boundary conditions in simulations of airflow in rigid airway tree geometries [330, 369]. The idea of combining image registration of a temporal series of CT scans with CFD models of the airway tree has then subsequently been refined until today. Yin et *al.* [370] have shown that registration of three images over the breathing cycle allows the assessment of lung non-linearity. Jahani et *al.* [178] extended the three-images-approach by a temporal interpolation curve for lung movement coming from global flow monitoring. The temporal interpolation curve improves the representation of dynamic changes in ventilation and the anisotropy in lung deformation. Next to healthy subjects, these methods have also been applied to sub-groups of asthmatic patients [61, 62], and several studies on aerosol distribution profit from the findings of CFD combined with image registration [206]. Finally, such approaches have not only been successfully used on the macroscopic organ level, but also on smaller acinar structures to e.g., assess non-isotropic inflation and deformation of the acinus [194].

Still, the investigations conducted so far are only replications of the imaged states without any predictive evidence. In this chapter, replication is taken as a first step and a healthy human lung during tidal breathing is simulated at the start. An exact tracking of lung motion is obtained via image registration, and regional tissue inflation is coupled to the simultaneous computation of airflow field data using a volumetrically constrained fluid-structure interaction approach (see Section 3.2.1). This procedure is not conducted for pure replication of the imaged state but to validate the *3D/3D* model in a case where detailed imaging data are available. The idea is to learn more about kinematic constraints of the lung and regional ventilation distribution in healthy tidal breathing. The novelty is then the transition of all acquired knowledge towards further unknown scenarios such as pressure and volume controlled mechanical ventilation of a patient. To introduce as little modelling assumptions as possible, the most realistic and highest resolved *3D/3D* model known in computational respiratory mechanics is used for all investigations in this chapter together with physiologically realistic representations of the thorax as explained in the following sections. The final goal of this work is to provide a tool that can get more information from available imaging data using an intelligent and physics based underlying computational lung model and to allow an estimation of therapy success using certain lung protective measures. We try to answer the question, whether inspiratory/expiratory or 4D-CT imaging is necessary for setting adequate ventilation parameters and outline how much knowledge is obtainable from more advanced usage of a single available CT scan without need for further image acquisition.

4.2. Material and Methods

4.2.1. Imaging Data

The methods described in this chapter are presented for a case where a multitude of imaging data is available for model generation/validation and specifically two CT data sets are used for the analysis. First, a highly resolved three-dimensional patient-specific end-expiratory CT scan of a 42 year old male subject with a FRC of 2.65 l and a total lung capacity (TLC) of 4.76 l is provided by the Diagnostische Radiologie (Stuttgart, Germany; from [18]). This scan has a pixel size and slice thickness of $0.6855 \times 0.6855 \times 0.7344$ mm and is in the following referred to as scan A. Scan A is perfectly suited for extraction of patient-specific anatomy of the bronchial tree, the lung lobe contours, and the thorax due to its high resolution.

The second CT data set contains a time series of ten three-dimensional CT scans over the breathing cycle provided by the Deformable Image Registration database (case 6, from [54]). These 4D-CT images are acquired as part of the radiotherapy planning process for the treatment of thoracic malignancies at the University of Texas M. D. Anderson Cancer Center (Houston, Texas). The chosen scan is in the following denoted as scan B and contains a matched subject with similar lung dimensions as measured in scan A. Scan B has a pixel size and slice thickness of $0.97 \times 0.97 \times 2.5$ mm and is slightly coarser than scan A. Further, scan B is equipped with 419 landmark points for which the exact coordinates $\mathbf{L}^{\mathrm{R}}$ are identified by radiologists for each of the ten points in time comprising an entire breathing cycle. The coordinates of the landmark points can be used for validation of regional lung motion at each point in time (see Section 4.3.2).

The 4D-CT data (scan B) are not used for all simulated scenarios of respiration presented in this chapter. Actually, scan B is only employed for extraction of lung motion in this work. The transfer of motion data between scan A and scan B relies on a mapping technique using the principles outlined in Section 4.2.4.

4.2.2. Patient-specific geometry generation

4.2.2.1. Bronchial tree

For geometry generation, the airway lumen of the visible bronchial tree starting at the trachea and ending at the 8th generation of conducting airways is segmented from scan A. The pharynx and the larynx are omitted in this study as they are passed by an endotracheal tube during ventilation. Segmentation is performed using the software Mimics (version 16.0, Materialise, Leuven, Belgium) and the resulting surface is marked in blue in Figure 4.1 (left). This lumen surface serves as boundary for the fluid domain and as interface for fluid-structure interaction in the simulations presented in this section. A three-dimensional tetrahedral mesh is generated for the fluid domain using the open-source software Gmsh (version 2.9.3; from [125]) with a mesh resolution of 0.37 mm resulting in 1.849.412 fluid elements.

In the following, air in the fluid domain is modelled as Newtonian fluid with a kinematic viscosity of $\nu^{\mathrm{F}} = 17$ mm^2 s^{-1} and a density of $\rho^{\mathrm{F}} = 1$ kg m^{-3}.

Further, to respect the airway wall structures with its different physiological properties, a wall thickness is extruded upon the airway lumen surface with different wall thickness and different material properties for each generation. The extrusion procedure is realised using Gmsh (version 2.9.3; from [125]) and the generation-dependent thickness of the extruded wall is given in Table 4.1 in line with [236]. Extrusion is performed in such a way that at least two layers of tetrahedral elements are created across the wall thickness [291] for each airway to minimise locking phenomena. The resulting three-dimensional tetrahedral mesh of the airway wall has a resolution of 0.37 mm and contains 2.014.606 structural elements (see Figure 4.1).

The airway wall is modelled via a Neo-Hookean like constitutive law [35] introduced in Section 2.2.1. The Young's modulus of the airway wall is chosen as $E^{\mathrm{S}}_{\mathrm{aw}} = 60.75$ kPa similar to the values reported in [66], the Poisson ratio as $\nu^{\mathrm{S}}_{\mathrm{aw}} = 0.49$ and the density as $\rho^{\mathrm{S}}_{\mathrm{aw}} = 1000$ kg m^{-3}.

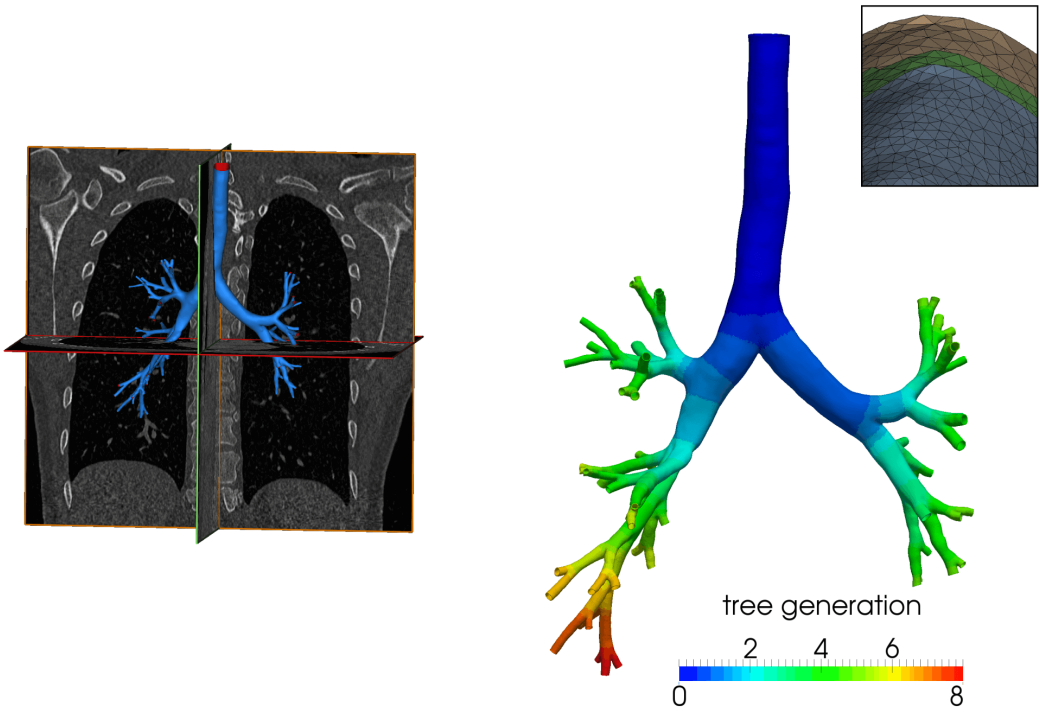

Figure 4.1.: Visualisation of the CT scan A and the segmented airway lumen surface of the visible bronchial tree starting at the trachea and ending at the 8th airway generation marked in blue (left). Extruded airway wall geometry for different marked tree generations (right). The detailed view of the airway wall shows that at least two layers of elements are used for meshing the airway wall across its thickness.

Table 4.1.: Generation-dependent wall thickness of airways in the bronchial tree according to [236]. The values are given as mean ± standard deviation. The mean values are used for extrusion of the airway wall.

Tree generation	0	1	2	3	4	5
Wall thickness [mm]	1.4 ± 0.1	1.3 ± 0.1	1.3 ± 0.1	1.3 ± 0.1	1.2 ± 0.1	1.0 ± 0.1
Tree generation	6	7	8	9	10	
Wall thickness [mm]	1.0 ± 0.1	0.9 ± 0.1	0.9 ± 0.1	0.9 ± 0.1	0.9 ± 0.1	

4.2.2.2. Lung parenchyma

The contours of the single lung lobes are also segmented from CT scan A using Mimics (version 16.0, Materialise, Leuven, Belgium) and are visualised in Figure 4.2 (left). The geometry of the bronchial tree, i.e., the airway lumen and extruded walls, are dissected from the segmented lobe contours via Boolean subtraction. The remaining geometry of the lobes is meshed with tetrahedral elements using Gmsh (version 2.9.3; from [125]) with a mesh resolution of 1.0 mm resulting in 1.384.726 elements for the three-dimensional representation of lung tissue.

Further, to allow for a more detailed investigation of regional tissue ventilation, the single lung lobes are split into sub-regions in such a way that each outlet of the bronchial tree supplies only one distinct tissue region. Subdivision is performed with a so-called lobe-splitting algorithm which attributes each tetrahedral element of the tissue mesh to the nearest tree outlet. The segmented contours of the lobes are thereby preserved, i.e., it is not possible that an element of one lobe is attributed to a bronchial tree outlet located in another lobe in line with human anatomy. The lobe splitting procedure results in 64 lung tissue regions corresponding to 64 outlets of the bronchial tree. Between each tree outlet and its associated tissue region a volumetric coupling will be introduced as outlined in Section 4.2.3. The sub-regions of lung tissue are visualised in Figure 4.2 (right) and their conformity with human anatomy will be evaluated in Section 4.3.1.

Following the experimental work by Rausch et *al.* [273], a Neo-Hookean like material law [35] is used for lung parenchyma with a Young's modulus of $E^{\mathrm{S}}_{\mathrm{par}} = 6.75$ kPa, a Poisson ratio of $\nu^{\mathrm{S}}_{\mathrm{par}} = 0.3$ and a density of $\rho^{\mathrm{S}}_{\mathrm{par}} = 1000$ kg m^{-3}. It is noted that for the mechanical ventilation scenarios presented in Section 4.2.5 the Young's modulus of the parenchyma in the left lower lobe is increased towards $E^{\mathrm{S}*}_{\mathrm{par}} = 27$ kPa to model a regional atelectasis in the left lower lobe.

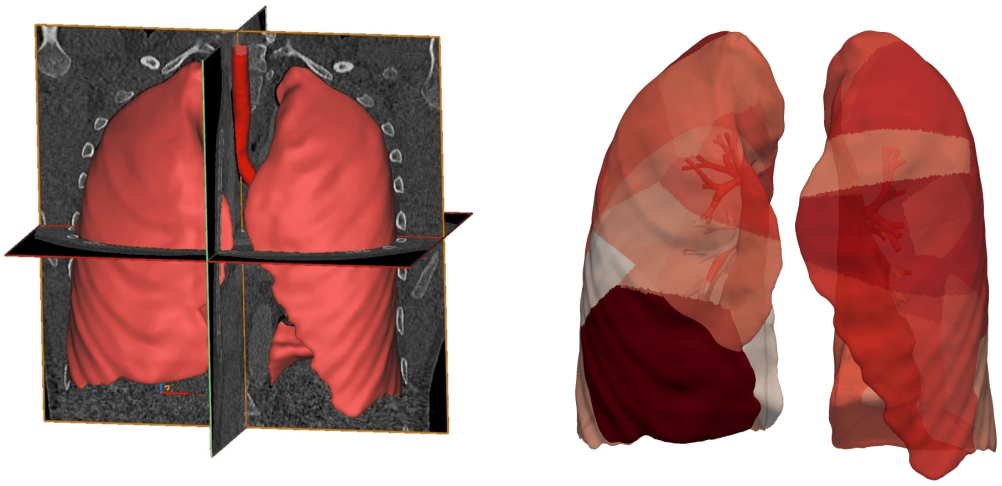

Figure 4.2.: Visualisation of the CT scan A and the segmented contours of the lung lobes marked in red (left). The split lung tissue is pictured in the right.

4.2.2.3. Thoracic cage

Finally, the geometry of the thoracic cage, consisting of spine, ribs, costal cartilage, respiratory muscles and diaphragm, is segmented from scan A using Mimics (version 16.0, Materialise, Leuven, Belgium). From this step, a thoracic cage is obtained where the space that is normally filled by the lungs remains empty. The single components of the thoracic cage are meshed in three dimensions with tetrahedral elements and a resolution of 1.7 mm resulting in 1.557.721 elements.

To respect the effect of the thorax, a quasi-static structural simulation of thorax motion is performed for different pressure conditions in the pleural cavity and the resulting equivalent thorax

stiffness is applied to the *3D/3D* lung model. Quasi-static thorax deformation is governed by the non-linear structural mechanics equations introduced in Section 2.2.1. The single components of the thoracic cage are each assigned with a physiological density and stiffness reported in literature [57]. The spine and the ribs are modelled by a Neo-Hookean like material law [35] (see Section 2.2.1) with a Young's modulus of $E^{\mathrm{S}}_{\mathrm{bone}} = 13$ MPa and a Poisson's ratio of $\nu^{\mathrm{S}}_{\mathrm{bone}} = 0.3$. For bony structures a density of $\rho^{\mathrm{S}}_{\mathrm{bone}} = 1300$ kg m^{-3} is chosen. The costal cartilage and the diaphragm plate are also modelled by a Neo-Hookean like constitutive law with a Young's modulus of $E^{\mathrm{S}}_{\mathrm{cartilage}} = 3$ MPa and a Poisson's ratio of $\nu^{\mathrm{S}}_{\mathrm{cartilage}} = 0.3$. The density of cartilage s assumed to be $\rho^{\mathrm{S}}_{\mathrm{cartilage}} = 1100$ kg m^{-3}. Muscular tissue is represented by a decoupled isochoric/volumetric strain-energy density function consisting of a linear term, a fourth order polynomial term and an Ogden like volumetric term [251] (see Section 2.2.1). The corresponding parameters are $k^{\mathrm{S}}_{1,\mathrm{muscle}} = 12.39$ kPa, $k^{\mathrm{S}}_{4,\mathrm{muscle}} = 200$ kPa, $\kappa_{\mathrm{muscle}} = 5000$ kPa, and $\beta_{\mathrm{muscle}} = -2.0$. The density of muscular tissue mainly consisting of water is $\rho^{\mathrm{S}}_{\mathrm{muscle}} = 1000$ kg m^{-3}.

The displacements of the upper and lower back surface that are in contact with the CT bed are set to zero in the structural simulation of the thorax, as they are not moving during quiet breathing. On the inside of the pleural cavity different pressures are applied perpendicular to the surface to study regional thorax motion at different pleural pressures. The resulting deformation allows to derive a regional equivalent thorax stiffness for each point on the inside of the pleural cavity. In our case, measurements of volume inside the pleural cavity for different applied pleural pressures show good agreement with pressure-volume curves reported for the thorax [300] (see Figure 4.3). Computation of an equivalent regional thorax stiffness results in two zones, one in vicinity of the ribs and the other in the region of the diaphragm. The corresponding equivalent stiffnesses are $k^{\mathrm{S}}_1 = 0.35$ kPa for the ribcage and $k^{\mathrm{S}}_2 = 0.15$ kPa for the diaphragm. In all cases of mechanical ventilation, i.e., when the thorax is passive, these stiffnesses are applied to the outer lung surface as additional kinematic constraint via

$$\mathbf{t}^{\mathrm{S}} = k^{\mathrm{S}}_{1,2,3} \cdot d^{\mathrm{S}} \cdot \mathbf{n} \tag{4.1}$$

where $\mathbf{t}^{\mathrm{S}}$ is the additional traction on, and $d^{\mathrm{S}} \cdot \mathbf{n}$ the normal displacements of the lung hull (see Section 2.2.1). It is noted that the same principle is used to model the tissue surrounding the trachea with a stiffness of $k^{\mathrm{S}}_3 = 2.0$ kPa.

4.2.3. Remarks on the volumetrically coupled *3D/3D* lung model

For all investigations in respiratory mechanics presented in this chapter, the fully resolved volumetrically coupled *3D/3D* model is used (see Section 3.2.1). The full resolution and the generality of the model ensure that all effects in respiration are adequately captured.

In brief, the fully resolved volumetrically coupled *3D/3D* model consists of two couplings between the previously generated components: (i) the interaction between airflow and airway wall represented as classical FSI problem and (ii) the volumetric coupling between airflow leaving the fluid domain and tissue inflation of the region associated to each airway outlet (see Figure 4.4). The governing equations of the fully resolved volumetrically coupled lung model can be found in Section 3.2.1.

Efficient solution strategies for the monolithic implementation of the volumetrically coupled *3D/3D* model can be found in [347]. In this work, the approach denoted as SIMPLE(BGS(AMG))

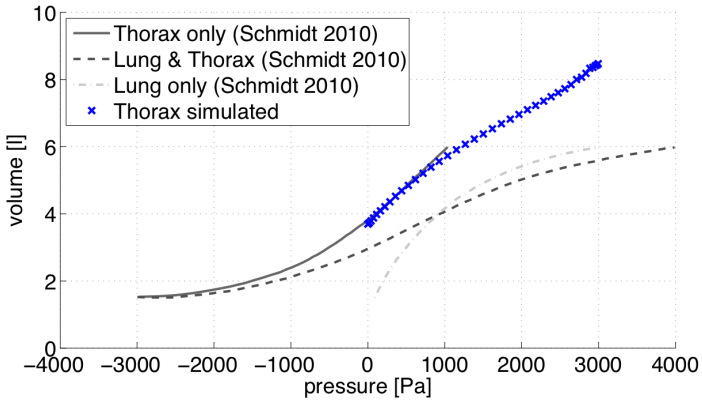

Figure 4.3.: Pressure-volume curves of the simulated imaging-based thorax geometry compared to literature values [300]. For better comparison, the simulated curve is scaled in such a way that the FRC in both cases is equal.

is used which basically uses the SIMPLE technique [52] to separate the volumetric constraint from the standard FSI problem. The remaining standard FSI problem is then solved using previously reported multigrid preconditioners for FSI [121]. Here, a block Gauss-Seidel (BGS) to uncouple the FSI problem wrapped around an algebraic multigrid method (AMG) solving the system is applied. For more details on this method, the reader is referred to [347].

In the following, two basic scenarios will be simulated: (i) healthy quiet breathing driven by the non-linear motion of the diaphragm and the respiratory muscles; and (ii) mechanical ventilation with prescribed airflow at the trachea inlet and passive behaviour of the thoracic cage. Details on these two setups will be presented in the following sections.

4.2.4. Lung motion tracking and active quiet breathing

To simulate healthy quiet breathing driven by the non-linear motion of the diaphragm and the respiratory muscles, their exact movement has to be known. In this work, respiratory motion is extracted from a time series of ten CT scans (see Section 4.2.1) using an image registration algorithm described in detail in the following.

4.2.4.1. Image registration

Following the definition by Fischer and Modersitzki [98], image registration is a process in which various images of the same scene captured at different times, perspectives, or with different modalities are aligned. In practice, several approaches exist in image registration [146] and in this work, a voxel based approach that relies directly on the grey values of each voxel is used.

The core elements of such an approach are two data sets with the dimensions $d \in \{2, 3\}$ denoted as reference image $\mathcal{I}_{\mathcal{R}}$ and target image $\mathcal{I}_{\mathcal{T}}$. Aim of the registration process is to find an optimal transformation $\boldsymbol{\varphi}^{\mathcal{T}}(\mathbf{x})$ which maps the template image $\mathcal{I}_{\mathcal{T}}$ to the reference image $\mathcal{I}_{\mathcal{R}}$ as close as possible [98]. Here, template and reference image correspond to chronologically consecutive 3D lung CT scans during one breath between which motion is detected. The unknown

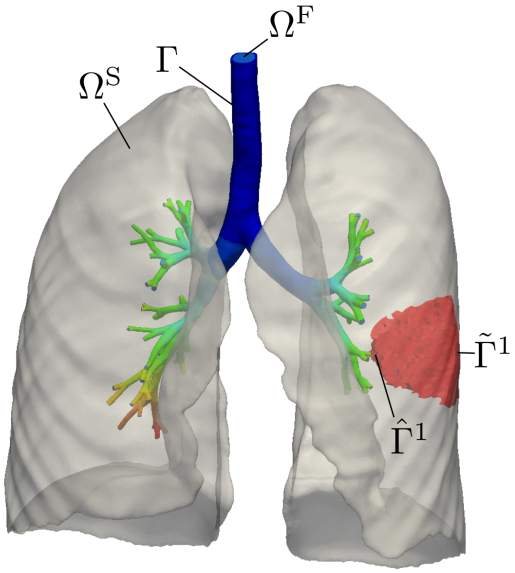

Figure 4.4.: Patient-specific *3D/3D* lung model containing the fluid domain Ω^{F}, the airway wall and the FSI interface Γ. Further, one exemplary tissue sub-region resulting from the lobe-splitting procedure is marked in red. This region is bounded by the surface $\tilde{\Gamma}^1$ and supplied with air from the fluid outlet $\hat{\Gamma}^1$. For details on the coupling, the reader is referred to Section 3.2.1.

transformation is defined as

$$\boldsymbol{\varphi}^{\mathcal{T}}(\mathbf{x}) = \mathbf{x} + \mathbf{u}^{\mathcal{T}}(\mathbf{x}) \tag{4.2}$$

where $\mathbf{u}^{\mathcal{T}}(\mathbf{x})$ denotes a d-dimensional vector field and $\mathbf{x}$ the material coordinates.

In order to find the optimal transformation for the mathematically ill-posed image registration problem, the optimisation problem

$$\mathcal{J}\left(\mathcal{I}_{\mathcal{T}}, \mathcal{I}_{\mathcal{R}}, \mathbf{u}^{\mathcal{T}}\right) = \mathcal{D}\left(\mathcal{I}_{\mathcal{T}}, \mathcal{I}_{\mathcal{R}}, \mathbf{u}^{\mathcal{T}}\right) + \alpha^{\mathcal{T}} \mathcal{S}\left(\mathbf{u}^{\mathcal{T}}\right) \rightarrow \underset{\mathbf{u}^{\mathcal{T}}}{min} \tag{4.3}$$

has to be solved [98]. Here, $\mathcal{D}\left(\mathcal{I}_{\mathcal{T}}, \mathcal{I}_{\mathcal{R}}, \mathbf{u}^{\mathcal{T}}\right)$ denotes the difference metric quantifying the difference between the reference and the template image. The term $\mathcal{S}\left(\mathbf{u}^{\mathcal{T}}\right)$ characterises the regulariser which shall prevent local minima in the optimisation process. The regulariser is weighted by the prefactor $\alpha^{\mathcal{T}}$ where $\alpha^{\mathcal{T}} = 0$ means no regularisation and $\alpha^{\mathcal{T}} = 1$ full regularisation of the problem.

The difference metric used in this work is the sum of squared differences (SSD) error defined as

$$\mathcal{D}^{\mathrm{SSD}}\left(\mathcal{I}_{\mathcal{T}}, \mathcal{I}_{\mathcal{R}}, \mathbf{u}^{\mathcal{T}}\right) = \int_{\Omega} \left[I_{\mathcal{T}}\left(\mathbf{x} + \mathbf{u}^{\mathcal{T}}(\mathbf{x})\right) - I_{\mathcal{R}}(\mathbf{x})\right]^2 d\mathbf{x} \tag{4.4}$$

where $I_{\mathcal{T}}$ and $I_{\mathcal{R}}$ denote the pixel wise grey values of the image.

As regulariser, a diffusive approach is chosen to avoid unphysiological deformation of the image. The diffusive regularisation term reads

$$\mathcal{S}^{\text{diff}}\left(\mathbf{u}^{\mathcal{T}}\right) = \frac{1}{2}\sum_{j=1}^{d}\int_{\Omega} ||\nabla\, u_j^{\mathcal{T}}||^2 d\mathbf{x} \tag{4.5}$$

where $u_j^{\mathcal{T}}$ denotes the j-th component of the displacement field $\mathbf{u}^{\mathcal{T}}$.

To solve the optimisation problem from Eq. (4.3), a Gauß-Newton method is applied (see e.g., Section 2.1.1). The increment of the transformation field is computed as

$$\mathbf{h}^{\mathcal{T}} = -\tau\left(\mathbf{J}_e^T\mathbf{J}_e\right)^{-1}\nabla\mathcal{J}\left(\mathcal{I}_{\mathcal{T}}, \mathcal{I}_{\mathcal{R}}, \mathbf{u}^{\mathcal{T}}\right) \tag{4.6}$$

and an iterative update of the transformation via

$$\boldsymbol{\varphi}_{i+1}^{\mathcal{T}} = \boldsymbol{\varphi}_i^{\mathcal{T}} + \mathbf{h}^{\mathcal{T}} \tag{4.7}$$

where i indicates the current and $i+1$ the next iteration step. In this work a fixed number of iterations is given to obtain a solution with the number of iterations specified below.

In addition to the Gauß-Newton scheme [142], a multiresolution approach [203] is used that collocates voxel grey values on several grid levels and computes the solution on the coarsest grid level first. The converged solution on the coarse grid is then used as initial guess on the next finer grid level. The multiresolution approach accelerates convergence and avoids local minima in the optimisation process [203].

The image registration methods applied in this work are implemented in Matlab (Release 2012b, The MathWorks, Inc., Natick, Massachusetts, USA) and have been reported previously for two-dimensional problems [29]. In the next section, specific details for the 4D-CT lung registration are given.

4.2.4.2. Lung motion tracking

For the motion tracking presented in this work, CT scan B is cropped to reduce the image size of all 10 scans over time. Further, for convergence improvement, a clean black background, the so-called padding of 40 px is added in all directions [122]. The new images then have a dimension of $592 \times 592 \times 221$ pixel with the previously described resolution of scan B (see Section 4.2.1).

Image resolution is conducted sequentially, i.e., from time T_0 to T_1 ($T_0 \rightarrow T_1$), $T_1 \rightarrow T_2$, until $T_8 \rightarrow T_9$. The times T_0 to T_4 correspond to inspiration and the remaining T_5 to T_9 to expiration. Registration is performed using five resolution levels and $i = [5, 300, 200, 20, 1]$ iterations from the coarsest to the finest level. All computations are performed on a six core Intel® Xeon® workstation with 47.1 GB RAM and computation time for one registration step is approximately two hours. The resulting displacement fields $\boldsymbol{\varphi}^{\mathcal{T}}(\mathbf{x})$ for each step are stored to track the motion of the lung. To account for motion non-linearity and the asymmetry between inspiration and expiration, the temporal evolution of the deformation is extracted from the ten scans and a time curve is interpolated from a reference point on the diaphragm surface (see Figure 4.5). The displacement field resulting from image registration is validated against measurements in Section 4.3.1.

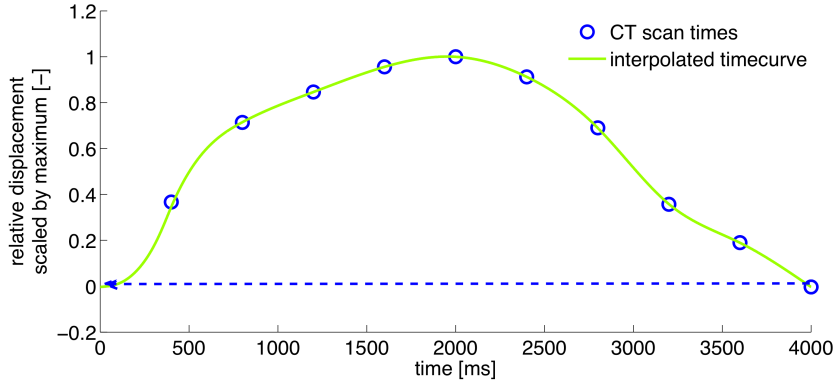

Figure 4.5.: Temporal evolution of the tracked displacements scales by the maximum displacement. The blue markers visualise the ten scanned states. The green curve is the interpolated temporal evolution from the ten scans.

To drive respiration by active motion of the lung, the computed displacements are prescribed to the lung hull contour of the *3D/3D* model at each point in time. Additionally, a zero reference pressure is set at the trachea inlet. The computation is performed with a time step of 0.5 ms and a convergence criterion of 10^{-6} in the non-linear residual. Results for this scenario of healthy quiet breathing are presented in Section 4.3.2.

4.2.5. Scenarios of mechanical ventilation

4.2.5.1. Ribcage model and resulting kinematic constraints on the lung

In case of mechanical ventilation, the patient is paralysed, the respiratory muscles are relaxed and contrary to active breathing act only passive, i.e., as an additional stiffness on the lung's surface. To respect this effect, an equivalent thorax stiffness derived in Section 4.2.2 is applied to the lung hull surface.

4.2.5.2. Applied mechanical ventilation profiles

Following clinical guidelines, four different scenarios of mechanical ventilation are computed for the simulated diseased patient with the atelectasis in the left lower lobe. They include pressure- and volume-controlled mechanical ventilation, prone positioning, and moderate high-frequency oscillatory ventilation, which are all assumed to be lung protective ventilation strategies (see Section 1.2). The applied flow boundary conditions in the four scenarios are visualised in Figure 4.6. Scenario (a) mimics pressure-controlled mechanical ventilation in supine position. Thereto, the resulting flow from a clinically applied pressure curve is taken and prescribed at the trachea inlet. Further, gravity is simulated as a body force $\mathbf{b}^{\mathrm{S}} = \rho^{\mathrm{S}} \cdot \mathbf{g}$ where $\mathbf{g} = 9.81\ \mathrm{m\ s^{-2}}$ is applied in dorsal direction. In scenario (b), the same flow curve at the tracheal inlet is prescribed as in scenario (a) but the body force is applied in ventral direction to mimic prone positioning. In scenario (c), the patient is brought to supine position and a volume-controlled mechanical ventilation profile is prescribed at the trachea inlet. Finally, in scenario (d) a moderate high-

frequency oscillatory flow profile is applied at the trachea as outlined in Figure 4.6 (d). The patient is again in supine position.

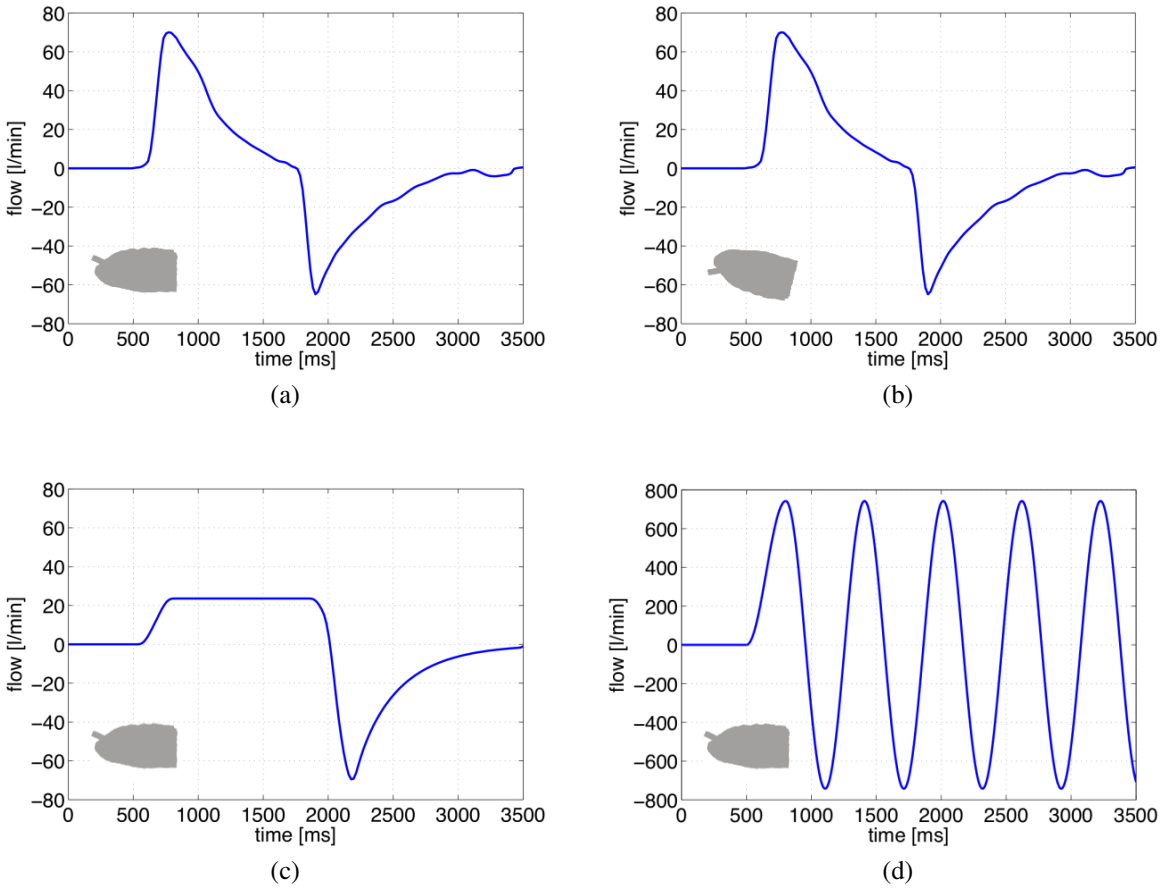

Figure 4.6.: Applied flow curves at the trachea inlet for the mechanical ventilation scenarios (a)-(d). The curves for scenario (a)-(c) are using the same scale, the scale for scenario (d) is by a factor of ten larger to visualise the higher flow values during moderate HFOV. Positioning of the patient is indicated via the schematic in the images.

In scenarios (a)-(c) one breathing cycle and in scenario (d) five breathing cycles are simulated with a time step of 0.25 ms. The solution is converged if the non-linear residual is smaller than 10^{-6}. Results for the mechanical ventilation scenarios (a)-(d) are presented in Section 4.3.3.

4.3. Results

4.3.1. Lobe-splitting results

In Figure 4.7, lung tissue regions resulting from the lobe-splitting algorithm and single bronchopulmonary segments reported in anatomy [239] are visualised. A bronchopulmonary segment is the smallest discrete topological and functional unit of the lung and supplied by a tertiary

bronchus (i.e., bronchial tree generation three to four). This means that the subdivision resulting from the lobe-splitting algorithm is finer than the subdivision into bronchopulmonary segments and corresponding regions in the model are combined for comparison with the segments reported in [239].

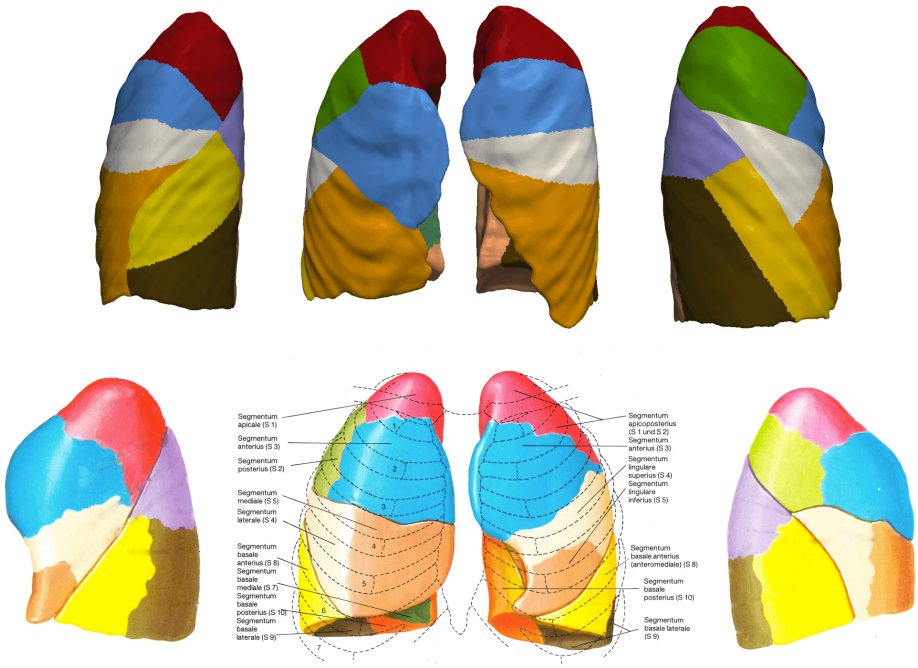

Figure 4.7.: Comparison between single lung regions generated from the lobe-splitting procedure (top row) and bronchopulmonary segments reported in literature (bottom row). Image adopted from [239] with permission.

For a quantitative comparison, the single segmental volumes resulting from the lobe-splitting procedure are compared to previously reported literature values [59] in Table 4.2. The algorithmically split and the anatomically reported lung regions match almost perfectly in all parts of the lung both visually (see Figure 4.7) and quantitatively (see Table 4.2). The main visual differences are a less pronounced vertical subdivision line for the left lower and the right lower lobe (marked in brown/yellow), and a smaller inferior segment of the left upper lobe (marked in orange) compared to anatomical data [239]. Considering that the difference is rather small and that quantitative results match almost perfectly, the variation can be attributed to patient-specific anatomy in scan A. A good overall conformity between literature and model supports the fact that the subdivision of lung parenchyma into sub-regions is correctly represented in the patient-specific *3D/3D* lung model.

4.3.2. Results for healthy quiet breathing

4.3.2.1. Image registration accuracy

The accuracy of the registration based motion tracking is evaluated computing the target registration error (TRE) for specific experimentally determined landmark points. The TRE is defined as

Table 4.2.: Percentage of overall lung volume contained in pulmonary sub-regions obtained from lobe-splitting procedure compared to anatomical data reported by Chiumello et *al.* [59].

	Lobe-splitting	*Anatomical data*		*Lobe splitting*	*Anatomical data*
Right lung	(55.37)	(54.6)	**Left lung**	(44.63)	(45.3)
Right upper lobe	(18.37)	(20.9)	**Left upper lobe**	(14.97)	(12.0)
Apical	5.81	6.9	Apical Posterior	9.07	6.0
Posterior	7.00	6.9	Anterior	5.89	6.0
Anterior	5.56	6.9			
Right medium lobe	(10.87)	(9.0)	**Lingula**	(9.33)	(8.7)
Lateral	5.23	4.5	Superior	3.97	4.3
Medial	5.64	4.5	Inferior	5.36	4.3
Right lower lobe	(26.12)	(24.7)	**Left lower lobe**	(20.34)	(24.6)
Superior	5.60	4.9	Superior	4.19	6.1
Medial-basal	2.35	4.9	Anterior-basal	5.35	6.1
Anterior-basal	6.59	4.9	Lateral-basal	5.27	6.1
Lateral-basal	5.72	4.9	Posterior-basal	5.53	6.1
Posterior-basal	5.86	4.9			

the difference between a measured landmark coordinate $\mathbf{L}^{\mathrm{R}}$ and the coordinate of the reference point $\boldsymbol{\varphi}^{\mathcal{T}}\left(\mathbf{L}^{\mathrm{T}}\right)$ transformed via image registration

$$\mathrm{TRE} = |\boldsymbol{\varphi}^{\mathcal{T}}\left(\mathbf{L}^{\mathrm{T}}\right) - \mathbf{L}^{\mathrm{R}}|. \tag{4.8}$$

Averaging over the $n = 419$ landmark points identified for scan B, a mean target registration error can be computed following

$$\mathrm{TRE}_{\mathrm{mean}} = \frac{1}{n}\sum_{i=1}^{n} |\boldsymbol{\varphi}^{\mathcal{T}}\left(\mathbf{L}_i^{\mathrm{T}}\right) - \mathbf{L}_i^{\mathrm{R}}|. \tag{4.9}$$

The mean TRE for the transformations $T_0 \rightarrow T_{10}$ is visualised in Figure 4.8. In all cases, the mean TRE lies between 0.8 and 1.5 mm which is remarkable as it is smaller than the image resolution of scan B ($0.97\times0.97\times2.5$ mm). This means that the used image registration approach is as accurate as possible from the available imaging data. Further, regional motion of the lung can be exactly tracked and be applied to the patient-specific *3D/3D* lung model for realistic simulation of active quiet breathing. Two exemplary displacement field states, one for inspiration and one for expiration are visualised in two dimensions in Figure 4.9 and allow an estimate of regional lung motion during the recorded quiet breathing. The main motion direction vectored downwards in the diaphragm area is expected for tidal breathing mainly driven by motion of the diaphragm.

4.3.2.2. Global ventilation and regional ventilation

On the basis of the extracted lung model anatomy and motion, deformation-driven active quiet breathing is simulated and computed total lung volume and flow rate are visualised in Figure

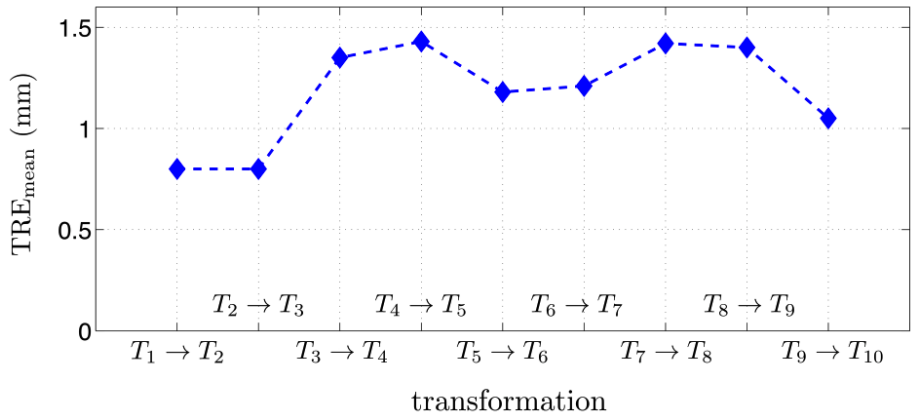

Figure 4.8.: Mean TRE for the single transformation steps between imaging time T_1 and T_{10}.

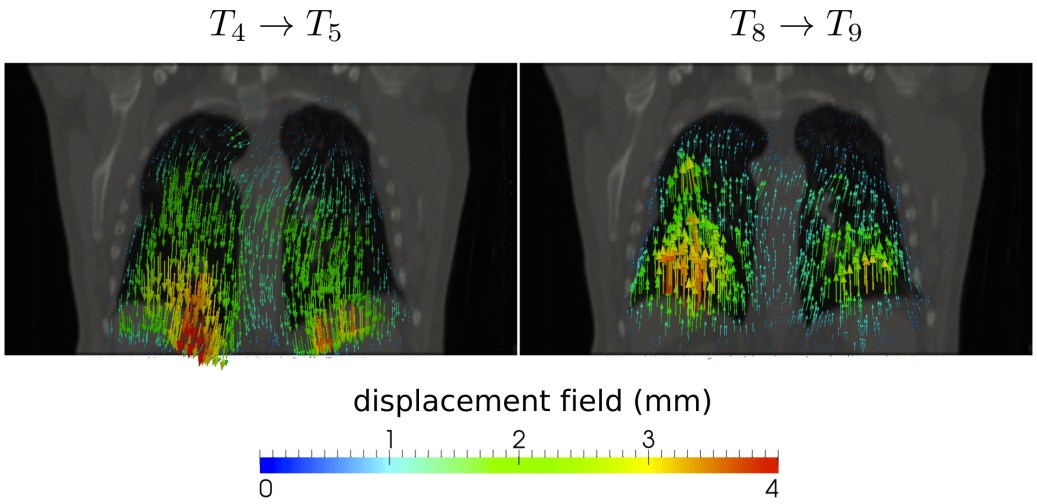

Figure 4.9.: Two exemplary computed transformations visualised via displacement vectors in a coronal slice of the CT image. The transformation $T_4 \rightarrow T_5$ corresponds to the state at end inspiration and shows a downwards vectored motion direction with maximum values in the region of the diaphragm (left). The transformation $T_8 \rightarrow T_9$ corresponds to the last state before end expiration and shows an upwards vectored motion (right).

4.10. For comparison with the work by Jahani et *al.* [179], the time, volume and flow quantities

have been normalised as follows:

$$t^* = \frac{t}{|t_{\mathrm{EI}} - t_{\mathrm{EE}}|}, \tag{4.10}$$

$$V^*_{\mathrm{air,m}} = \frac{V_{\mathrm{air,m}}(t) - V_{\mathrm{air,m,EE}}}{V_{\mathrm{air,m,EI}} - V_{\mathrm{air,m,EE}}}, \tag{4.11}$$

$$Q^* = \frac{dV^*_{\mathrm{air,m}}}{dt^*}. \tag{4.12}$$

Here, the subscripts EE and EI refer to end-expiratory and end-inspiratory state. Then, $|t_{\mathrm{EI}} - t_{\mathrm{EE}}| = 2.0$ s normalises the inspiratory/expiratory times each to 1. Eq. (4.11) denotes the normalised volume with respect to the tidal volume in the case computed as $V_{\mathrm{air,m,EI}} - V_{\mathrm{air,m,EE}} = 0.4391$ l and Q^* refers to the normalised flow. The resulting flow rate curve shows similar values and characteristics as the curve in [179]. Inspiration starts rapidly with high absolute flow values which are even higher in the patient of this work. Towards the end of the inspiration phase, flow drops and remains at smaller values until the end of the inspiration phase. During expiration, flow again increases faster than in [179] and drops towards the end of the period. Differences between the two curves can be explained with the fact that patients in [179] have been trained to breathe regularly during the study and were guided by a rolling-seal piston device. Breathing in this work is completely free and thus more unsteady across the cycle. Nevertheless, the good agreement supports the physiological relevance of this work.

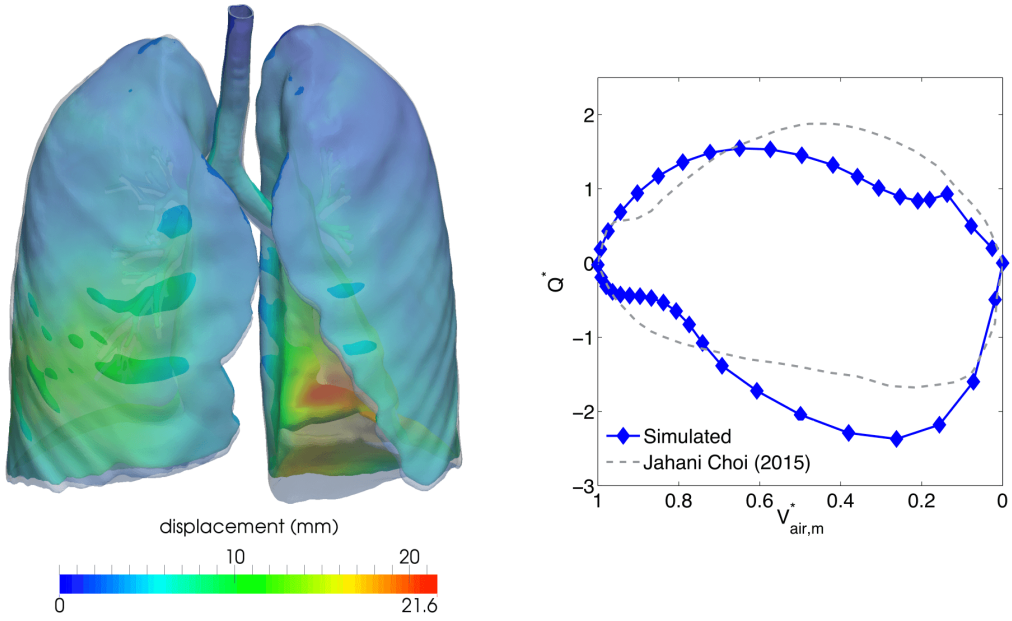

Figure 4.10.: Deformation of the lung at end-expiratory (coloured) and end-inspiratory state (light grey; left). The colours indicate the deformation from end-expiratory to end-inspiratory state. The computed flow-volume curve shows good agreement with previously reported work [179] (right).

Additionally, a detailed distribution of airflow pressure and velocity in the resolved part of the conducting zone is visualised in Figure 4.11. Pressure during inspiration is negative in the entire

domain with a zero reference point at the trachea inlet as specified. The negative pressure develops at the outlets as a result of lung tissue expansion and sucks air throughout the conducting into the respiratory zone. Pressure values are lower in branches with a higher resistance throughout the tree e.g., observed in the left lower lobe. The resulting pressure difference between inspiration and expiration at the marked outlet in the left bottom lobe equals -0.85 cmH_2O and is slightly smaller than clinically reported values of -1.0 cmH_2O [141]. The difference is due to the fact that the resistance of the pharynx, larynx and of the airway generations 9-16 is not taken into account in this work (see also limitations in Section 4.4.4).

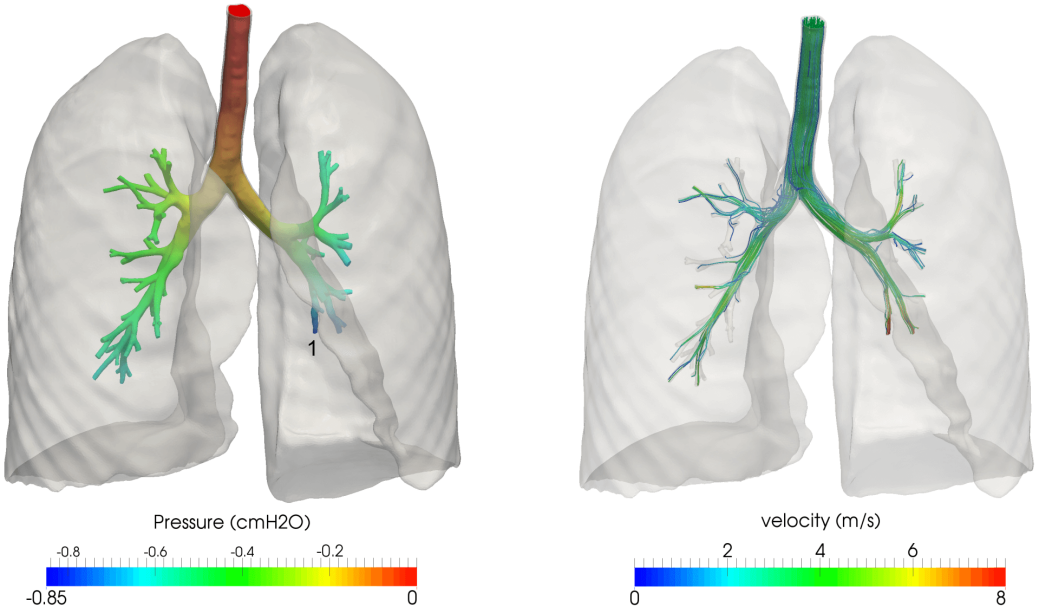

Figure 4.11.: Airflow pressure at maximum inspiration ($t = 2.0$ s) throughout the bronchial tree (left). The tree outlet marked as 1 develops the lowest pressure of 0.85 cmH_2O. Velocity streamlines at the point of maximum flow ($t = 0.5$ s; right).

Resulting velocity patterns in the airflow are presented in Figure 4.11 (right) for the point of maximum flow during inspiration. Velocity values remain in the range of 0 to 8 m s^{-1} throughout the resolved bronchial tree close to values reported by [72]. The streamlines indicate that flow remains laminar during the entire respiratory cycle if the laryngeal jet is omitted.

Finally, computed regional ventilation results are presented for maximum inspiration in Figure 4.15 compared to the mechanical ventilation cases.

4.3.3. Results for different scenarios of mechanical ventilation

In the following, resulting tissue deformation and airflow quantities are presented for all four mechanical ventilation scenarios specified in Section 4.2.5. The tidal volumes resulting from the prescribed flow read for the cases (a)-(d): $TV_{(a)} = 0.429$ l, $TV_{(b)} = 0.424$ l, $TV_{(c)} = 0.378$ l, and $TV_{(d)} = 0.1$ l.

Figure 4.13 visualises resulting displacements for the four scenarios at full inspiration. It can be seen that tissue deformation does not show a preferred direction as known from healthy ac-

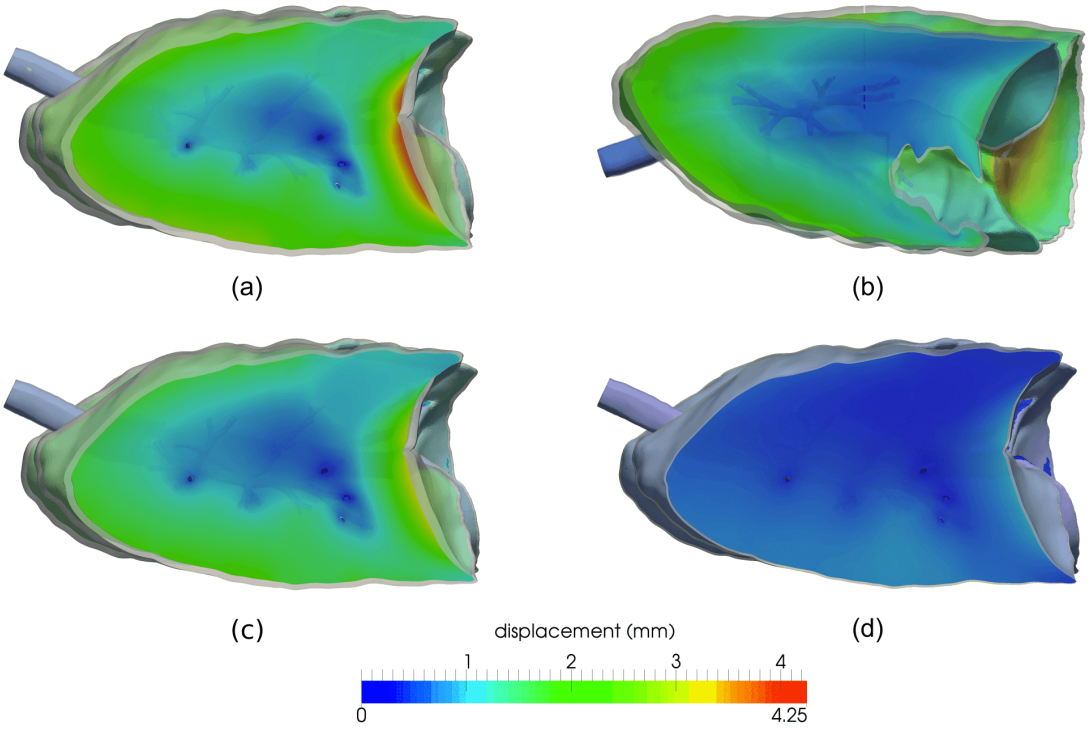

Figure 4.12.: Clipped view of warped regional tissue displacements at end inspiration ($t_{(a)} = t_{(b)} = 1.725$ s, $t_{(c)} = 1.95$ s, $t_{(d)} = 0.95$s) for the mechanical ventilation scenarios (a)-(d). For comparison, the same colour scale is chosen for all four scenarios.

tive breathing. One can observe a slightly pronounced downwards movement in all four cases attributable to the kinematic constraints on the lung. However, this movement is not as pronounced as known from active breathing (see Section 4.3.2). Also, deformation is quite similar for all four scenarios of mechanical ventilation with smaller values in the HFOV case where a smaller tidal volume is applied.

Looking at the pressures that are required to drive the desired flow in the simulations reveals several aspects characteristic for mechanical ventilation. First, pressure is always positive throughout the entire domain in all four scenarios. This positive pressure forces air into the respiratory system and overcomes the elastic recoil forces of lung tissue and thorax to initiate inflation. The required absolute pressure values thereto are much higher than in healthy breathing, where only the resistance of the airways tree has to be overcome. The pressure at the ends of the bronchial tree (i.e., that is seen by the tissue) is by a factor of ten higher than in active healthy breathing. A maximum pressure of 17 cmH_2O at the trachea inlet is in line with measurements for a patient with a left lower lobe atelectasis (see Chapter 6). Pressure in the HFOV are lower due to the lower supplied tidal volume.

A view on the velocity streamlines in all four mechanical ventilation scenarios outlines that airflow velocities in scenarios (a)-(c) are similar to those in healthy breathing ($0 - 5$ m s^{-1}). Again, in airways beyond the third generation of the bronchial tree, airflow remains laminar and no secondary flow patterns can be observed.

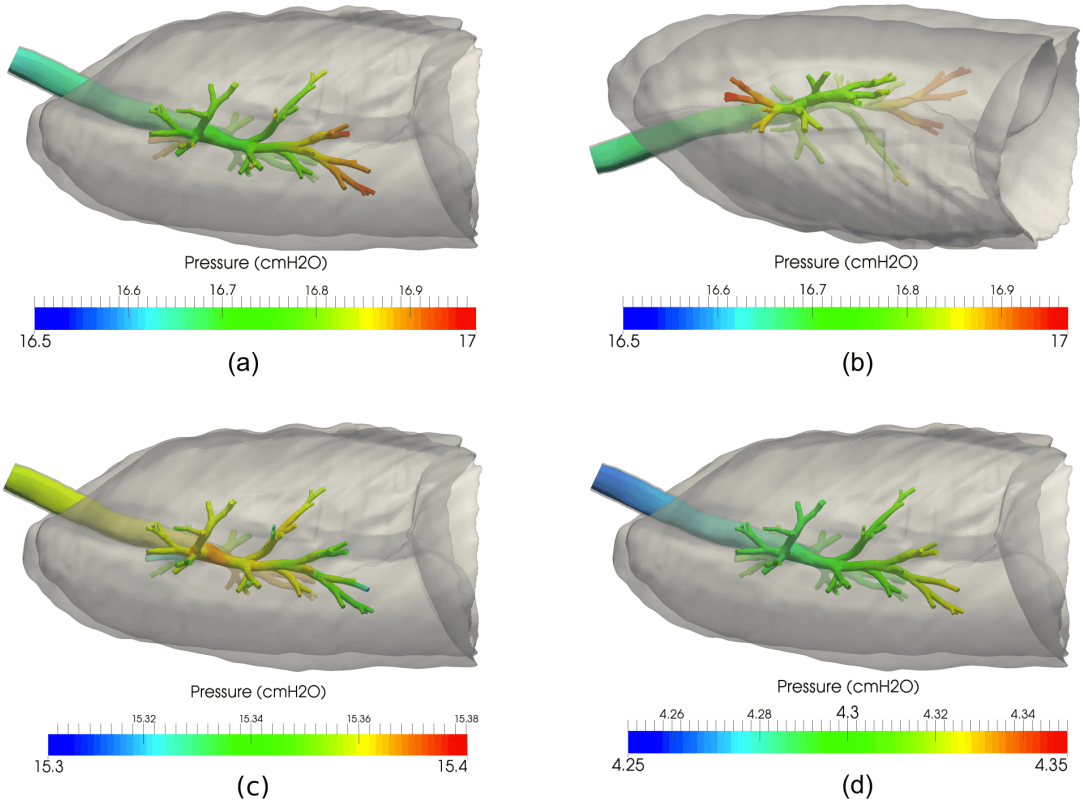

Figure 4.13.: View on regional pressures at maximum pressure ($t_{(a)} = t_{(b)} = 1.85$ s, $t_{(c)} = 1.875$ s, $t_{(d)} = 1.56$s) for the mechanical ventilation scenarios (a)-(d).

A comparison of regional ventilation between healthy quiet breathing and mechanical ventilation is visualised in Figure 4.15. It becomes visible that regional ventilation is higher in the lower region of the lung during healthy quiet breathing. During mechanical ventilation, a significant heterogeneity is introduced to the regional ventilation pattern coming from the regional atelectasis in the left lower lobe. This observation holds for all mechanical vent profiles and indicates that none of the applied ventilation profiles can restore the ventilation pattern achieved during healthy quiet breathing.

4.4. Discussion

The core novelty of this chapter is that a combination of medical imaging and computational lung modelling can result in a powerful tool advancing diagnostics and treatment in respiratory care. The lung as an organ obeys the basic physics of airflow and tissue dynamics and their detailed solution in a patient-specific setting provides a deep insight into individual lung behaviour. Further, computational lung modelling can deliver additional information to available medical imaging data including a detailed assessment of airflow pressure and velocity in the resolved bronchial tree. The presented methods are applicable to both active breathing and mechanical ventilation scenarios and their clinical relevance will be discussed in detail in the following.

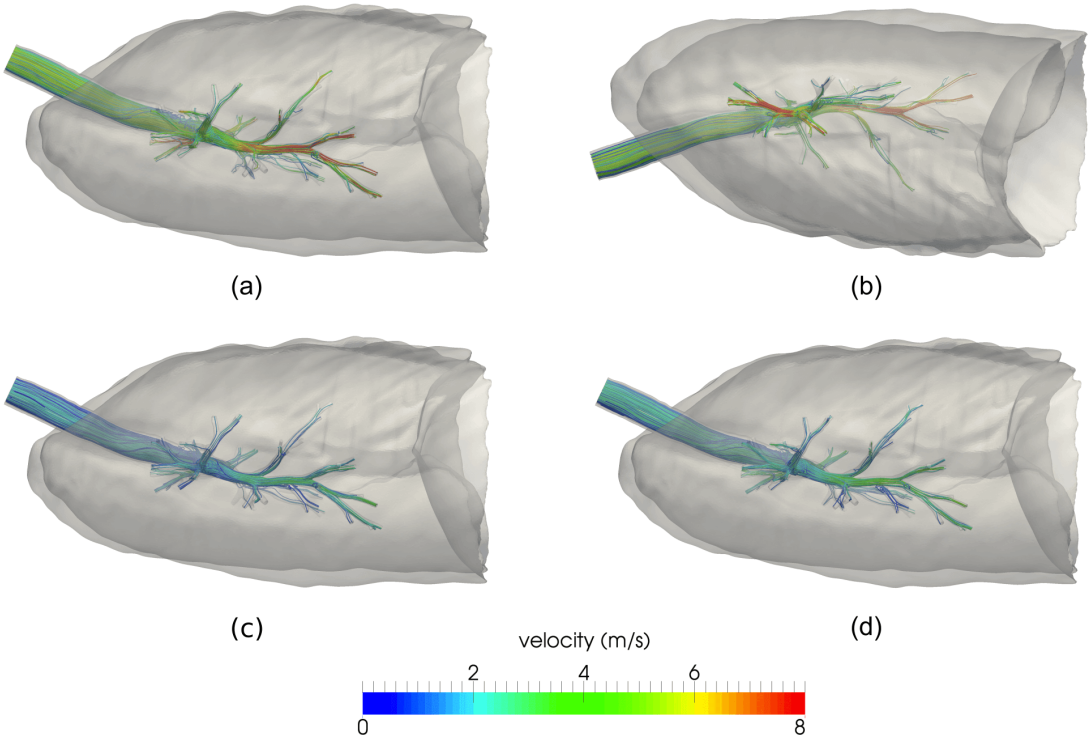

Figure 4.14.: View on regional airflow velocities at maximum flow ($t_{(a)} = t_{(b)} = 0.875$ s, $t_{(c)} = 1.625$ s, $t_{(d)} = 0.8$s) for the mechanical ventilation scenarios (a)-(d). For comparison, the same colour scale is chosen for all four scenarios.

4.4.1. Mimicking respiratory physiology

An important factor for using computational lung models in clinical diagnostics and therapy is their ability to mimic real respiratory physiology. The lung model presented in this chapter is derived from highly resolved medical imaging data with an accuracy higher than 1.0 mm. The first eight generations of the bronchial tree are fully resolved, which is more than previous approaches in respiratory care (e.g., [370]) have captured. Additionally, deformation of airway walls with variable wall thickness is considered an important extension to previous FSI approaches investigating deformation of bronchial tree during breathing [352]. In general, the use of varying material parameters for different tree generations would be possible. However, due to the lack of experimental data on airway wall properties (a topic that will be addressed in Appendix C), a single stiffness in the range reported in literature [66] is used for all airways in the bronchial tree.

The proposed anatomically accurate subdivision of the lung parenchyma into 64 sub-regions allows a more detailed investigation of regional inflation beyond the level of complete lung lobes that has been possible so far [179, 372]. Further, the applied volumetric coupling of airflow in the conducting with with regional tissue inflation on the respiratory part of the lung enables a consistent modelling of respiration in the entire organ. Remarkably, for the first time, this approach allows a consistent modelling of inspiration and expiration over several breathing cycles without prescription of unphysiological flow boundary conditions as e.g., done in [235, 369].

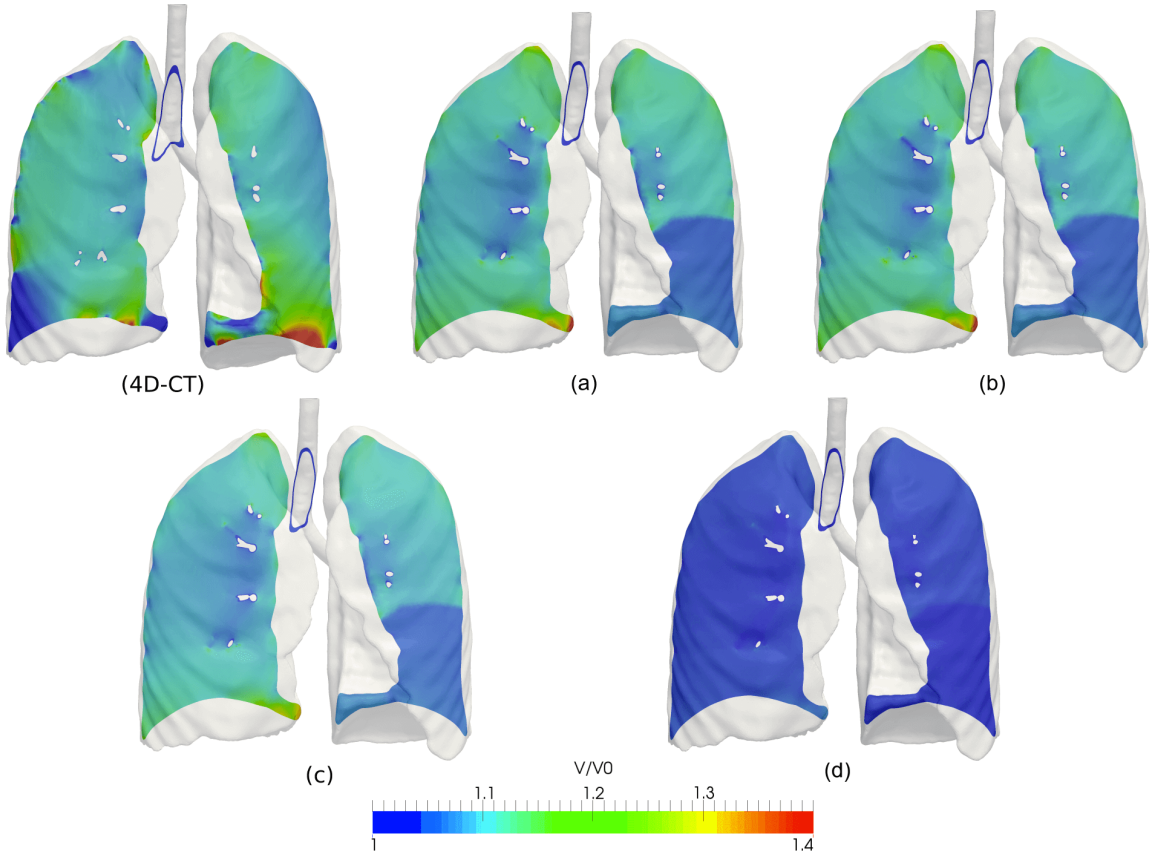

Figure 4.15.: View of regional tissue inflation at end inspiration ($t_{(4D-CT)} = 2.0$ s ,$t_{(a)} = t_{(b)} = 1.725$ s, $t_{(c)} = 1.95$ s, $t_{(d)} = 0.95$s) relative to end-expiration for 4D-CT derived natural breathing and all four mechanical ventilation scenarios (a)-(d). For comparison, the same colour scale is chosen for all four scenarios.

Finally, the thoracic cage (see e.g., Figure 1.1) is important in respiratory mechanics as it introduces kinematic constraints to the lung both during active spontaneous breathing and during passive mechanical ventilation. Under active breathing conditions, the diaphragm is the main driver of flow in the respiratory system, while under mechanical ventilation, the thoracic cage and the diaphragm impose kinematic constraints on the lungs that have to be taken into account. The availability of an imaging based thorax model equips the presented *3D/3D* lung model with a method to consider kinematic constraints determined by the ribcage and the diaphragm.

With all these aspects, the presented *3D/3D* approach is - to the careful knowledge of the author - one of the physiologically most realistic and highest resolved models in respiratory mechanics available so far.

4.4.2. Additional insight into available medical imaging data

Assessment of non-linear regional lung motion and resulting tissue inflation via image registration has been proposed recently [178, 179, 369, 370]. Nevertheless, this is the first approach

among them which uses a direct method to evaluate the quality of the extracted deformation fields based on distinct landmark points in the scan throughout the entire breathing cycle. Previous models only validated global measurements of lung volume between registration-derived lung volume and global volume measurements at the mouthpiece [179, 369]. Even though this is a valid idea, it does not necessarily imply a local correlation between real and registration-based regional lung motion. Validation in this work using $n = 419$ landmark points distributed uniformly across the lung is much more accurate in terms of regional validation of movement and supports the fact that non-linear local lung motion is tracked correctly within the accuracy of image resolution.

Regarding the derived normalised flow quantities, inconsistencies are known during tidal breathing between different patients and even within the same patient for different breathing cycles [38, 63, 243]. Therefore it is remarkable that the flow curve computed in this study is quite similar to the flow curve reported previously [179]. It is reasonable that the free tidal breathing observed in this study introduces a greater variability into the flow curve and thus leads to a more irregular shape in Figure 4.10 than trained quiet breathing in [179]. However, it may also be that normal untrained free breathing is a closer representation of the breathing process in nature.

A multitude of observations would now be possible with this highly accurate registration-based motion tracking fields including investigations in regional inflation on the basis of single lung segments, or the characterisation of regional deformation anisotropy using the anisotropic deformation index (ADI) [11]. However, the focus of this work lies on additional information that can actually be obtained from existing medical imaging data incorporating the underlying physics of the lung via *3D/3D* modelling. A detailed investigation in airflow pressure and velocity are important points of such additional information that cannot be extracted from imaging data alone. The knowledge on velocity within the airways can help to exactly distribute particles within the flow and to release pharmaceuticals on the basis of certain shear stress patterns locally [297].

The information of actually seeing pressure levels throughout the tree and the velocity patterns are further valuable in the case of bronchoconstriction, [21] and airway narrowing in asthmatic subjects where velocity profiles are significantly altered and can now be studied without hyperpolarised contrast agents delivering the same regional information. Still, the presented methods need further validation e.g., against hyperpolarised Helium studies. In the long term, they might be able to deliver important airflow information in patients where hyperpolarised Helium investigations are not possible.

4.4.3. Computing states beyond those imaged

Application of the derived *3D/3D* lung model in four mechanical ventilation scenarios demonstrates the possibilities that come along with such a general approach. Using the underlying physics, it is possible to prescribe various ventilation settings *in silico* and to simultaneously respect kinematic constraints given by the thorax. Computed results for these ventilation scenarios reveal the following main differences between active healthy quiet breathing and mechanical ventilation.

First, deformation of lung tissue is different to those in healthy breathing in all four modes of mechanical ventilation even though similar tidal volumes are applied. Regional ventilation is more heterogeneous and less deformation occurs in the diaphragm region compared to active

breathing. Second, a high positive pressure is required to drive a mechanical ventilation profile and to create an equilibrium force to flow resistance, tissue recoil and the passive thorax stiffness. Absolute pressure values can be up to ten times higher than the small negative pressures required for active breathing. This impressively shows how fast pressure can rise and lead to barotrauma [10]. Third, the velocity profiles and resulting flow distributions during mechanical ventilation are considerably different compared to healthy quiet breathing. This is especially important when curative aerosols are administered to a ventilated patient to ensure correct dosing in the desired regions of the lung.

These three important differences between healthy quiet breathing and mechanical ventilation lead to the fact that medical imaging and previous simulation studies [235, 369, 370] which have been conducted during active quiet breathing are of limited use when it comes to investigations under mechanical ventilation. Previous approaches would require imaging to be performed under ventilatory conditions for each parameter setting anew, which might interfere with clinical treatment and is questionable respecting ethical guidelines on radiation. Even if possible, previously reported methods would still remain in an observable position, while the methods presented in this work provide the first - yet not validated - steps towards predictive modelling of patient-specific mechanical ventilation. The model grounded on underlying physics of airflow and tissue dynamics works equally well both for active quiet breathing and mechanical ventilation. However, quantitative conclusions are still beyond the scope of this pilot study due to to several limitations outlined in the following.

Finally, one important aspect of this chapter is that both in healthy active quiet breathing and in many cases of mechanical ventilation, flow remains laminar in the airways beyond the third generations of the bronchial tree. This fact confirms the findings in [72]. Therefore, as no complex turbulent flow patterns have to be resolved, this allows to use simpler dimensionally reduced models for investigations in pulmonary airflow with good accuracy (see Chapter 6). It is important to note that reduced dimensional models can actually model turbulence, i.e., if turbulence would occur, it's physics would be correctly recovered. However turbulent flow patterns, would not be resolved in three dimensions. One example, where turbulence and secondary flows actually need to be resolved will be presented in Chapter 8 investigating specific ventilation techniques in neonatal care.

4.4.4. Limitations

The modelling methodology presented in this chapter advances several methods used in diagnostics today. Nevertheless, three important limitations do exist in this study that for now preclude its applicability in a clinical setting: First, segmentation of the bronchial tree omits the pharynx/larynx and can only resolve the first eight generations of the bronchial tree with sufficient accuracy from the available imaging data while further downstream generations are neglected. This leads to underestimated values for total flow resistance in the conducting part and ultimately towards underestimated pressure values. One potential remedy is a morphologically correct tree growing algorithm for higher generation airways (see [328] and Chapter 5). Further, exact segmentation of the pharynx/larynx is possible as presented in [19]. Second, the currently used material law has been identified for rat lung tissue [273] and lacks a viscous component to respect temporal evolution of lung tissue behaviour. This might lead to the observed close results in regional deformation/ventilation for different mechanical ventilation profiles which might not

occur in reality. Finally, currently no validation is available for the mechanical ventilation scenarios in terms of regional ventilation, pressure, or airflow velocity. Further chapters will focus on validation of computationally predicted with actual measured results of regional ventilation (see Chapter 5 and 6).

4.5. Conclusion

In this chapter, a volumetrically coupled *3D/3D* lung model has been presented as one of the physiologically most realistic and highest resolved computational approaches in respiratory modelling known today. The anatomy of airways and lung tissue is derived from a single patient-specific CT scan and the conducting and the respiratory part of the lung are coupled via the methods presented in Section 3.2.1. This coupling results in the first model in respiratory mechanics which can simultaneously simulate airflow, deformation of the airway walls and regional tissue inflation during inspiration and expiration.

With this setup, two basic cases of respiration are investigated: (i) active quiet breathing driven by the non-linear motion of the diaphragm and the respiratory muscles using information from a time series of 4D-CT data; (ii) four scenarios of mechanical ventilation integrating clinically relevant flow profiles and kinematic constraints in consequence of the passive ribcage/diaphragm.

Important information are obtained in addition to those coming from medical imaging and significant differences between active quiet breathing and mechanical ventilation are identified. Therefore, the presented model is a powerful approach to learn more about healthy quiet breathing and mechanical ventilation and to extend knowledge from available imaging data in terms of regional pressures and flow velocities.

Finally, the presented *3D/3D* model reveals that fluid flow remains laminar in higher airway generations for healthy quiet breathing and a variety of parameter settings in mechanical ventilation excluding HFOV. Therefore, for many investigations in mechanical ventilation dimensionally reduced lung models can be used with almost perfect accuracy as presented in Chapter 6.

5. Alveolar ventilation and lung tissue bioimpedance

One key problem in modelling respiratory biomechanics is validation of computed quantities with available measurement data. Therefore, in this chapter, a link between the computed regional ventilation and electrical bioimpedance of lung parenchyma, which can be measured by EIT, is derived as preparation step towards model validation with EIT.

For derivation, two murine three-dimensional alveolar microstructures obtained from synchrotron-based X-ray tomography are each exposed to a constant potential difference for different states of ventilation in a finite element simulation. While the alveolar wall volume remains constant during stretch, the enclosed air volume varies, similar to the lung's volume during ventilation. The enclosed air, serving as insulator in the alveolar microstructure, determines the resulting current and accordingly local tissue bioimpedance. From this investigation a relationship between lung tissue bioimpedance and regional alveolar ventilation can be derived. The relationship shows linear dependency between air content and tissue impedance and renders available experimentally derived data more precisely.

The content of this chapter is primarily based on a previous publication by the author [284], which is re-used here with permission.

5.1. Pulmonary EIT imaging

Over the past thirty years EIT has proven to be a reliable tool for monitoring physiological processes in the human body such as cardiac activity [47, 106, 241], gastric emptying [48], or respiration [3, 36, 103, 106, 107]. EIT has become especially popular in imaging regional lung ventilation as it is the only non-invasive, radiation-free method that is suitable for long-term imaging of ventilation at bedside. The high temporal resolution of EIT imaging, the prevention of hazardous radiation and the availability at bedside make it perfectly suited for regional validation of computational lung models developed in this work.

Details on the principle of EIT are outlined in Section 1.3.1. Good imaging contrast is obtained in pulmonary EIT imaging as tissue resistivity/impedance considerably changes with ventilation. This is due to the variation of the resulting pathway length for the electrical current when e.g., a higher volume of air is enclosed in the alveoli. However, so far only qualitative impedance changes were observed and a quantitative link between the measured tissue impedance and the amplitude of local ventilation is still missing.

First attempts towards linking regional ventilation and lung tissue bioimpedance qualitatively have been made by Nopp et *al.* [244] with an experimental approach on excised lungs of slaughtered calves and later [245] with an idealised alveolar geometry model based on a thin-walled cube. Since then several groups have stated correlations between impedance and air content

in lung tissue [110, 111, 238, 292, 303, 354, 374], though with high variability ranging from 3.4 Ωm to 28.6 Ωm for tissue resistivity at FRC to 6.72 Ωm to 40 Ωm at TLC.

In this chapter, a novel approach is presented where electrical tissue resistivity is directly based on the real alveolar micro-structure of lung parenchyma at different states of ventilation. Effective lung tissue resistivity is determined by comparing the electrical behaviour of fully resolved alveolar microstructures with the results of a homogenised parenchyma.

5.2. Material and Methods

To determine the resistivity of lung tissue, lungs from young adult rats are harvested according to [298]. After staining with heavy metals and paraffin embedding these samples are scanned in the TOMCAT beamline (SLS, Paul Scherrer Institut, Villingen, Switzerland) and a three-dimensional volume is reconstructed from the obtained images enhancing the process described in [272]. The resulting alveolar walls are meshed with tetrahedral finite elements and stretched uniformly in all directions in a stepwise manner until the cubical-shaped sample volume is increased by a factor of four. At each step of the simulation the air content of the cubical-shaped microstructure is calculated. Additionally, the current resulting from a potential difference between two opposite surfaces of the sample is measured. A correlation between resistivity of the tissue and alveolar air content is then derived following the procedure described in detail in the following sections.

5.2.1. Sample preparation, scanning and mesh generation

Sample preparation and scanning is performed following the protocol described in detail in [298]. The handling of animals before and during the experiments, as well as the experiments themselves were approved by the local authorities. The process for segmentation of single alveolar wall structures from the scanned images described in [272] is enhanced using the software package Amira 4.1.2 (FEI, Oregon, United States). All enhancements are described in detail below.

Two regions of the scanned images are chosen as reference volumes of approximately the same size in order to account for the inhomogenity in lung parenchyma due to the presence of small airways. The first sample is taken from a homogeneous tissue region (Figure 5.1, left), whereas the second sample is extracted from a region that is crossed by a small airway at the top surface (Figure 5.1, right). Segmentation is initially performed by using the 'magic wand' operations and corrected manually in locations where the automatic operations delivered poor quality. The surface of the resulting volume is triangulated and exported in STL file format. It is annotated that as proven in [272] the extracted volumes match morphological and morphometrical data [341].

To overcome the problem of sharp triangles resulting in poor numerical performance a process to maximise mesh quality using the open source software MeshLab [67] is established. First, the surface is subdivided with the 'Butterfly Subdivision' algorithm and cleaned from all remaining self-intersecting faces and holes if present. The result is a fine background mesh. Afterwards, a Poisson surface reconstruction (Octree Depth: 11, Solver Divide: 9) is applied to create a smooth and regular triangulated surface based on the geometry provided by the background

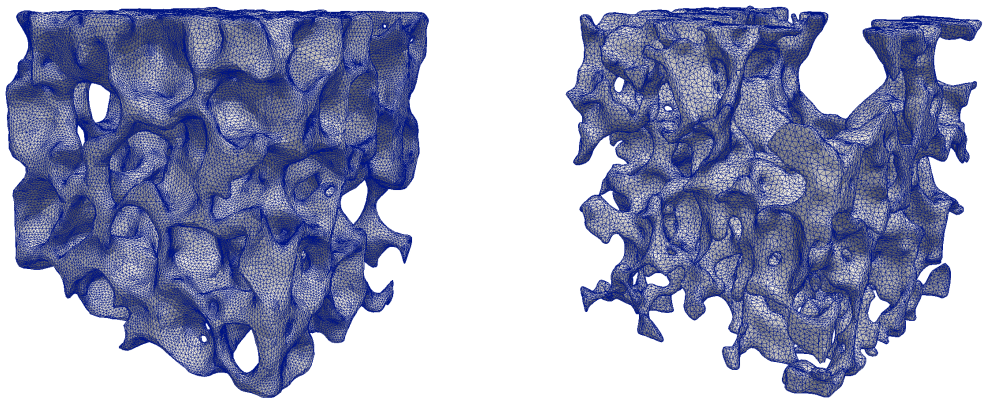

Figure 5.1.: Reconstructed cubical-shaped volume meshes of synchrotron-based X-ray tomography scans of the alveolar microstructure. The left sample is taken from a region of homogenous tissue, whereas the right sample exhibits an inhomogenity due to the crossing of a small airway at the top surface. Taken from [284] with permission.

mesh. One could now coarsen the surface mesh with the 'Quadric Edge Collapse Decimation' filter to reduce element size. In these simulations, however, the fine mesh is used since the resulting element size has been proven to be spatially converged in previous studies [272]. Finally, the resulting surface triangulation is exported in STL format and 3D meshed in Gmsh [125] using a Delaunay algorithm. The element size specified at the surface is kept for the volumetric meshing process. The six sides of the cubical-shaped sample were split into single surfaces to apply structural and electrical boundary conditions later. It is important to emphasise that though the mesh quality (see Figure 5.2 for comparison) is improved significantly through the described process, resulting in faster convergence and better performance of the simulations, the geometry of the alveolar wall ensembles has not changed. This is achieved by avoiding stronger smoothing operators such as Laplacian smoothing with high smoothing factors. Data on the final geometries are shown in Table 5.1.

Table 5.1.: Properties of the mesh for the two alveolar wall geometries used in this study.

	Sample 1 "homogeneous"	*Sample 2 "bronchiole"*
Sample edge length L_C $[\mu m]$	200	210
Tissue volume V_{tissue} $[\mu m^3]$	2.7×10^6	2.0×10^6
Element size h_{el} $[\mu m]$	2.25	2.85
Number of elements	2,272,169	1,486,483
Degrees of freedom	1,428,708	940,599

5.2.2. Structural simulation

Presented simulations consist of two parts, namely a structural simulation which deforms the sample uniformly in all directions according to the governing equations of soft tissue mechanics, and an electrical simulation that applies a potential difference between two opposite surfaces

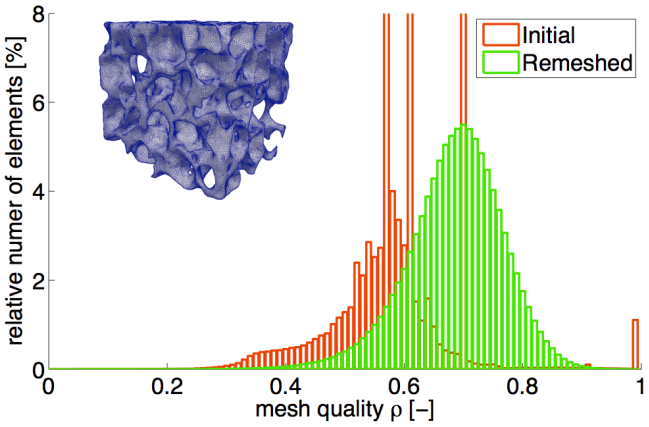

Figure 5.2.: Mesh quality before (orange) and after the improved meshing strategy (green). The mesh quality ρ_{el} is defined as the ratio of the smallest edge to the largest edge of a tetrahedron. A mesh quality of $\rho_{\text{el}} = 1.0$ indicates an ideal tetrahedron. Taken from [284] with permission.

of the stretched samples. Both algorithms are one-way coupled, meaning the structural deformation of the alveolar wall influences the potential distribution and the current flow throughout the tissue, whereas changes in potential and current do not affect structural deformations. This reflects physical behaviour in reality.

The governing equations for soft tissue mechanics on the structural domain Ω^{S}, which is equal to the electrical domain Ω^{E}, are those of non-linear elastodynamics presented in Section 2.2.1. To model the alveolar wall, a Neo-Hookean material law (see Section 2.2.1 and [35]) with a Young's modulus of $E^{\text{S}} = 6.75$ kPa determined from previous experiments [273] is used. A Poisson's ratio of $\nu^{\text{S}} = 0.49$ is chosen to account for the incompressibility of the alvolar wall mainly consisting of water. Tissue density ρ^{S} is set to $\rho^{S} = 1050\ \text{kg/m}^3$. As mechanical boundary conditions pure Dirichlet boundary conditions were applied on all six surfaces of the cubical-shaped sample in order to deform the sample (edge length L_{C}) uniformly in all dimensions (see Figure 5.3). An equilibrium state is computed every $dL_{\text{C}} = 10\ \mu$m of prescribed boundary displacements up to the maximum stretch of $\Delta L_{\text{C}} = 100\ \mu$m, which corresponds to a volume increase of a factor of almost four. At every step the air content and the tissue volume are computed in terms of the filling factor FF introduced by Nopp [244]

$$\text{FF} = \frac{V_{\text{air}}}{V_{\text{tissue}}} = \frac{L_{\text{C}}^3 - V_{\text{tissue}}}{V_{\text{tissue}}} = \frac{L_{\text{C}}^3}{V_{\text{tissue}}} - 1 \tag{5.1}$$

and the deformed geometries serve as a basis for the electrical simulations as described in the next section.

5.2.3. Electrical simulation

For the electrical simulation the system is described by the Laplace equation (see Section 2.4.2) giving a relation for the distribution of voltage $\Phi^{\text{E}}(\mathbf{x})$ in the domain Ω^{E} depending on the conductivity $\sigma^{\text{E}}(\mathbf{x})$. The potential is fixed on two opposite surfaces of the cubical-shaped sample

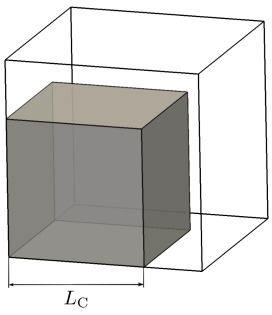

Figure 5.3.: Illustration of uniform stretch in all three dimensions. The initial sample volume is shaded in gray while the current configuration at stretch is visualised in wireframe mode. Adopted from [284] with permission.

(Dirichlet boundary conditions Γ_D^E). On the remaining surfaces, no-flux boundary conditions are applied. As a result of the applied potential difference a constant current flow on both surfaces ① and ② (see Figure 5.4),

$$I^{\mathrm{E}} = \int_{\Gamma^{\mathrm{D}}_{\mathrm{E},1/2}} (\sigma^{\mathrm{E}} \nabla \Phi^{\mathrm{E}}) \cdot \mathbf{n} \, \mathrm{d}\, A \tag{5.2}$$

can be measured in the simulations. For the conductivity $\sigma^{\mathrm{E}}(\mathbf{x})$ the model introduced by Nopp [244, 245] is used, where lung parenchyma consists of 85% blood-filled capillaries (conductivity $\sigma^{\mathrm{E}}_{\mathrm{B}} = 0.655\ \Omega^{-1}\mathrm{m}^{-1}$), 12% epithelial cells (conductivity $\sigma^{\mathrm{E}}_{\mathrm{E}} = 1.0\ \Omega^{-1}\mathrm{m}^{-1}$) and 3% intercellular fluid (conductivity $\sigma^{\mathrm{E}}_{\mathrm{I}} = 2.0\ \Omega^{-1}\mathrm{m}^{-1}$; see Section 1.1.1). For the complete alveolar wall this results in a conductivity of $\sigma^{\mathrm{E}}_{\mathrm{Alv}} = 0.7284\ \Omega^{-1}\mathrm{m}^{-1}$. The applied potential difference is $U^{\mathrm{E}} = \Phi^{\mathrm{E}}_1 - \Phi^{\mathrm{E}}_2 = 10\ V$ and one quasi-static electrical step is required until the simulation is converged.

All simulations are performed in the in-house multiphysics code BACI [353] and the electrical problem is solved in every $dL_{\mathrm{C}} = 10\ \mu$m increment of the structural problem. The deformed alveolar geometry is automatically updated before each electrical simulation.

5.2.4. Correlation between resistivity and filling factor

The electrical simulations of different deformation states can be used to find a link between the local resistivity of the lung tissue sample and its air content. For this purpose a homogenisation approach (see, e.g., [28, 351]) is used to replace the resolved porous microgeometry by a uniform domain as depicted in Figure 5.4 (right). By this approach, the influence of the porous structure on the current flow is modeled by the so-called effective conductivity $\sigma^{\mathrm{E}}_{\mathrm{eff}}$ which depends on two additional geometrical parameters contributing to the alveolar wall conductivity $\sigma^{\mathrm{E}}_{\mathrm{Alv}}$ (see, e.g., in [165])

$$\sigma^{\mathrm{E}}_{\mathrm{eff}} = \frac{\varepsilon_{\mathrm{V}}}{\tau^{\mathrm{E}}(\varepsilon_{\mathrm{V}})} \sigma^{\mathrm{E}}_{\mathrm{Alv}} \tag{5.3}$$

where ε_{V} denotes the volume fraction of the alveolar wall and $\tau^{\mathrm{E}}(\varepsilon_{\mathrm{V}})$ the tortuosity depending on the actual state of sample deformation. As explained, e.g., in [68], the tortuosity can be seen as an elongation of the current pathways through the porous microstructure in relation to the

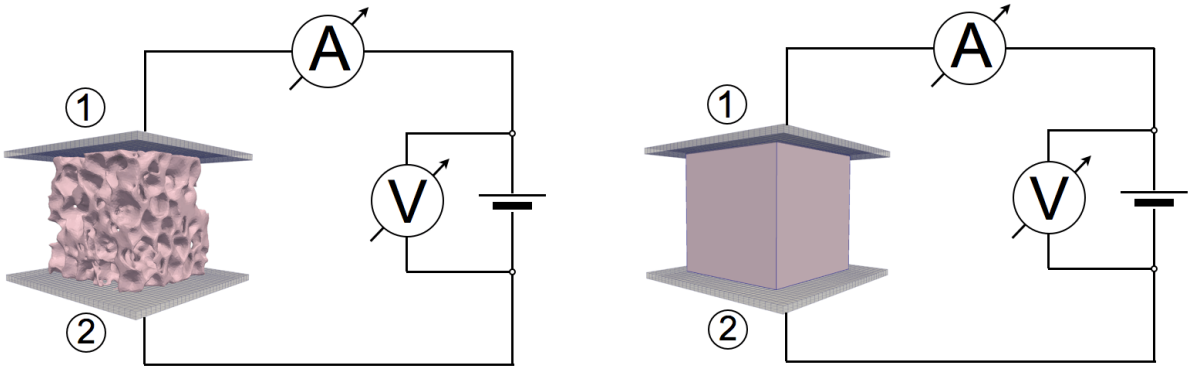

Figure 5.4.: Electrical simulation setup. A known potential difference is applied between opposite surfaces of the cubical-shaped alveolar microstructure (left) and the homogenised sample (right). The corresponding current flow between the surfaces 1 and 2 is measured. Taken from [284] with permission.

shortest straight line distance L_C between the surfaces ① and ②. In this specific case, τ is called geometrical tortuosity. The volume fraction ε_V of the alveolar wall is defined as

$$\varepsilon_\mathrm{V} = \frac{V_\mathrm{tissue}}{V_\mathrm{air} + V_\mathrm{tissue}} = \frac{V_\mathrm{tissue}}{L_\mathrm{C}^3} \tag{5.4}$$

and can be reformulated in terms of the filling factor FF

$$\varepsilon_\mathrm{V} = (\mathrm{FF} + 1)^{-1}. \tag{5.5}$$

Consequently, Eq. (5.3) can also be written as a relation between the local effective resistivity $\rho^\mathrm{E}_\mathrm{eff} = \frac{1}{\sigma^\mathrm{E}_\mathrm{eff}}$ and the local filling factor

$$\rho^\mathrm{E}_\mathrm{eff} = \frac{\tau^\mathrm{E}(\varepsilon_\mathrm{V})}{\sigma^\mathrm{E}_\mathrm{Alv}} (\mathrm{FF} + 1) \tag{5.6}$$

depending only on the alveolar wall conductivity and the tortuosity. In order to use Eq. (5.6) as a quantitative link between resistivity and filling factor, it is necessary to determine the tortuosity for a representative sample of lung tissue. If the representativeness of the samples is guaranteed, the homogenisation approach as well as the correlation in Eq. (5.6) are also applicable to the entire lung volume.

From the known potential difference $U^\mathrm{E} = \Phi^\mathrm{E}_1 - \Phi^\mathrm{E}_2$ and the measured current flow $I^\mathrm{E}(\varepsilon_\mathrm{V})$ the actual resistance of the tissue volume can be calculated based on Ohm's law

$$R^\mathrm{E} = \frac{U^\mathrm{E}}{I^\mathrm{E}(\varepsilon_\mathrm{V})}. \tag{5.7}$$

As shown, e.g., in [364], the resistance can also be expressed in terms of the effective conductivity

$$R^\mathrm{E} = \frac{1}{\sigma^\mathrm{E}_\mathrm{eff}} \frac{L_\mathrm{C}}{A_\mathrm{C}} = \frac{1}{\sigma^\mathrm{E}_\mathrm{Alv}} \frac{\tau^\mathrm{E}(\varepsilon_\mathrm{V})}{\varepsilon_\mathrm{V}} \frac{L_\mathrm{C}}{A_\mathrm{C}} \tag{5.8}$$

where L_C is the edge length and A_C the cross-sectional area of sample. By comparison of Eq. (5.7) and Eq. (5.8) the tortuosity of the homogenised sample can be calculated as

$$\tau^E(\varepsilon_V) = \varepsilon_V \sigma^E_{Alv} \frac{A_C}{L_C} \frac{U^E}{I^E(\varepsilon_V)}. \tag{5.9}$$

It is important to emphasise that all microstructural effects influencing the conductivity, as e.g., the variation of pore diameter, the roughness of the wall, are all incorporated into the tortuosity calculated by Eq. (5.9) (see, e.g., [364]). As a result, the tortuosity τ^E cannot be interpreted anymore as a pure elongation of the current path. To underline this, the tortuosity calculated by Eq. (5.9) is called electrical tortuosity. However, Eq. (5.9) is still valid and can be applied to the entire lung tissue as long as the sample with all microstructural effects is representative.

5.3. Results

5.3.1. Undeformed state

In Table 5.2 the tissue volume fraction ε_V, the filling factor FF and the direction-dependent current flow I^E throughout the cubical-shaped alveolar geometries in all three directions (i.e., $X =$ left-right, $Y =$ bottom-top, $Z =$ front-back) at the initial undeformed state are listed. Based on these values Eq. (5.9) is used to calculate the direction-dependent tortuosity to investigate any anisotropic effects of the microstructure. While the homogeneous sample shows almost no dependency on the direction of applied voltage ($\tau^{E,X} = 1.715$, $\tau^{E,Y} = 1.711$, $\tau^{E,Z} = 1.720$), the geometry crossed by the small airway shows higher absolute values and slight variations in the tortuosity ($\tau^{E,X} = 2.39$, $\tau^{E,Y} = 2.21$, $\tau^{E,Z} = 2.20$). The mean tortuosities $\bar{\tau}^E$ for both samples averaged over all three directions are listed in Table 5.2.

Table 5.2.: Geometrical and electrical parameters in the undeformed state for both geometries.

	Sample 1 "homogeneous"	*Sample 2 "bronchiole"*
Volume fraction of tissue ε_V	0.319	0.214
Filling factor FF	2.10	3.66
Current flow $I^{E,X}[mA]$	0.26944	0.1367
Current flow $I^{E,Y}[mA]$	0.27256	0.14786
Current flow $I^{E,Z}[mA]$	0.26624	0.1474
Mean tortuosity $\bar{\tau}^E$,	1.71	2.27

5.3.2. Linear model during stretch

Assuming that the mean tortuosity $\bar{\tau}^E$ remains constant during stretching of the sample (an assumption that will be investigated below), Eq. (5.6) is reduced to the following linear relation (Eq. (5.10)) and can be used to calculate the mean effective resistivity $\bar{\rho}^E_{eff}$ for both samples in the range of FF $\in [1.0; 8.0]$.

$$\bar{\rho}^E_{eff} = \frac{\bar{\tau}^E}{\sigma^E_{Alv}} (FF + 1) \tag{5.10}$$

Physiological filling factors are usually in the range of 2.0 to 6.0 [244]. The resulting resistivities for both samples are plotted in Figure 5.5 in comparison with previous studies and will be discussed in detail in the subsequent section.

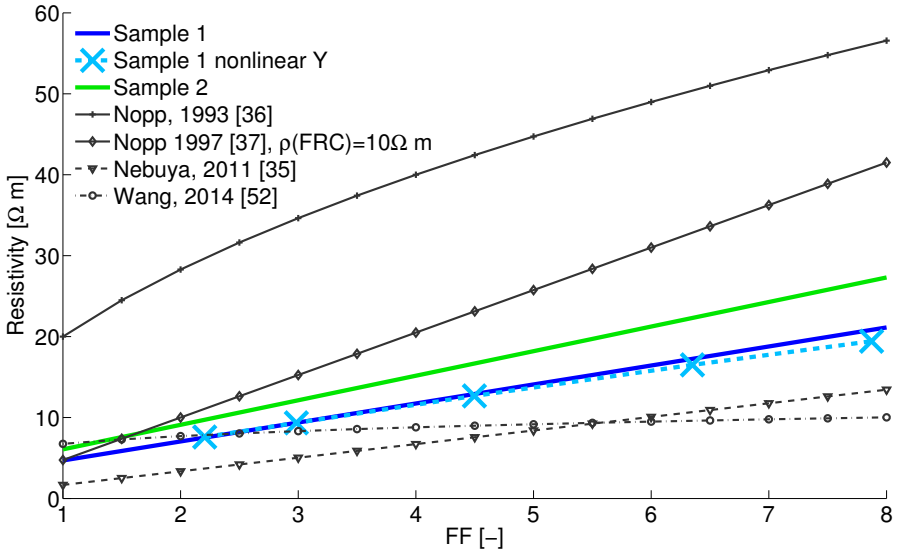

Figure 5.5.: Results for the resistivity dependence on the filling factor in the presented model and in literature. Taken from [284] with permission.

5.3.3. Non-linearity of the tortuosity

In general, the tortuosity $\tau^{\mathrm{E}}(\varepsilon_{\mathrm{V}})$ is dependent on the volume fraction ε_{V} (see Eq. (5.4)). To verify the above assumption of a constant tortuosity during stretch, the effective resistivity $\rho^{\mathrm{E}}_{\mathrm{eff}}$ is determined by Eq. (5.6) based on the deformation-dependent tortuosity $\tau^{\mathrm{E}}(\varepsilon_{\mathrm{V}})$, which is calculated by Eq. (5.9) after each increment in the structural simulation. The result is shown exemplarily for the Y-direction of sample 1 in Figure 5.5 (denoted as sample 1 nonlinear Y). It can be seen that the values for the specific resistivity almost lie on the line for the linear model and that they only start to differ slightly at very high filling factors corresponding to high values of stretch. This congruity supports the validity of the above assumption that a linear model during stretch is suitable and will be discussed in detail in Section 5.4.3. In Figure 5.6 the deformations of the homogeneous alveolar geometry at five different steps of the simulation, corresponding to the cross markers on the magenta line in Figure 5.5, are shown. Elongation and thinning of the single alveolar walls, which are the main reasons for changes in tissue resistivity, can be seen with increasing air content in the sample. Tissue volume V_{tissue} itself does not change due to incompressibility of the alveolar wall.

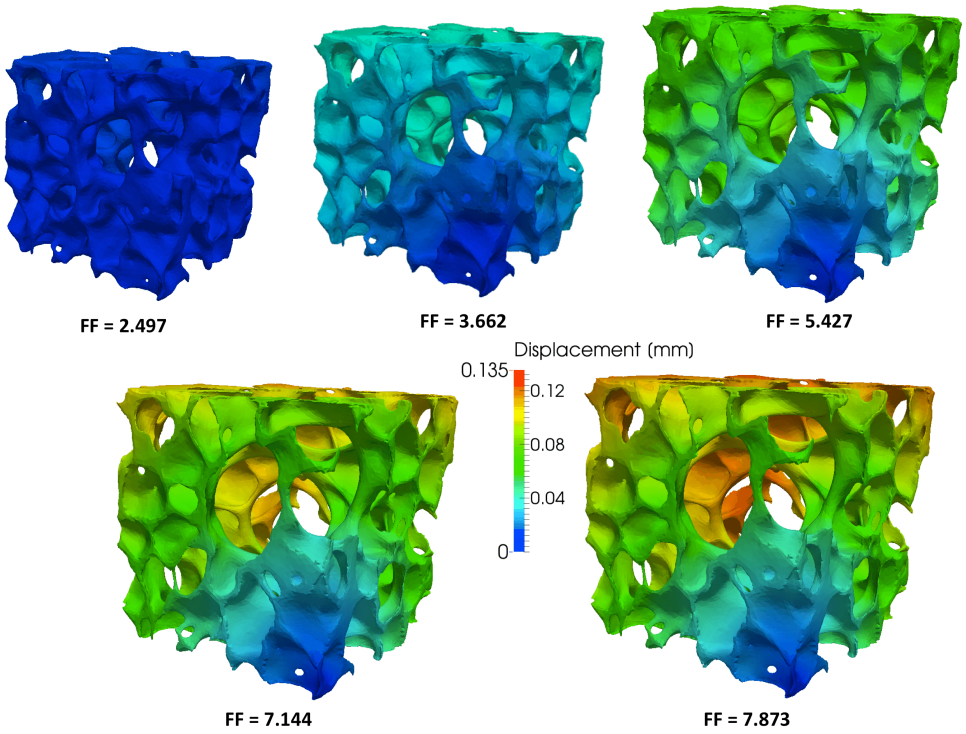

Figure 5.6.: Displacement of the homogeneous alveolar microstructure at five states. Elongation and thinning of the alveolar wall structures during stretch can be observed. Taken from [284] with permission.

5.4. Discussion

The main finding of this study is that a linear relationship for effective tissue resistivity $\rho_{\text{eff}}^{\text{E}}$ based on the filling factor FF is justified in a clinical setting. This correlation, which was also observed phenomenologically on a macroscopic scale, is now reconfirmed exploiting the physics of the parenchyma microstructure in a finite element simulation. All parameters in the relationship are physically based and can either be measured directly or are inherent in the geometry. Further enhancements to previously existing approaches have been made in this work e.g., an upper and lower bound for tissue resistivity, and will be discussed in detail in the following.

5.4.1. Correction of the filling factor

Nopp et *al.* [244] determined filling factors from two-dimensional microscopy images stating that values of FF $= 2.0$ correspond to FRC and FF $= 4.0$ to TLC. However, they already present samples with higher air content at FRC (FF > 3) in their publication. Following the observations from the three-dimensional geometries, filling factors of FF $= 2.0$ for FRC and FF $= 4.0$ for TLC seem to be quite low compared to the investigated geometries showing values of FF $= 2.1$ for the homogeneous and FF $= 3.66$ for the heterogeneous microstructure in the unstretched state. Considering the fact that a three-dimensional determination is probably more exact than a two-dimensional image slice as it averages tissue structure over a larger representative volume,

rather a filling factor of FF $= 3.0$ at FRC and FF $= 6.0$ at TLC is determined from the stretched microgeometries. This is in line with parenchyma density calculations based on a lung tissue density of $\rho^{\mathrm{S}} = 1050 kg/m^3$ [40] and a homogenised density of $\rho^{S}_{\mathrm{FRC}} = 246 kg/m^3$ [130, 238], which results in a filling factor of

$$\mathrm{FF}_{\mathrm{FRC}} = \frac{\rho^{\mathrm{S}}}{\rho^{S}_{\mathrm{FRC}}} - 1 = 3.26.$$

This also holds for the observed homogenised lung density $\rho^{S}_{\mathrm{TLC}} = 142.1 kg/m^3$ at TLC and results in a filling factor of $\mathrm{FF}_{\mathrm{TLC}} = 6.38$ [238] supporting the range of filling factors observed over a relatively large anatomical spectrum.

5.4.2. Isotropy of the electrical macroscale behaviour

Within the two alveolar microstructures possible dependencies on the direction of the applied voltage were investigated by measuring the current flow in all three directions throughout the samples. In the homogeneous geometry, no anisotropy of electrical properties of the tissue was observed, meaning that the irregular arrangement of alveoli shows an isotropic electrical behaviour on the macroscale. This result indicates that the sample can be considered as representative. Even in case of a clearly visible inhomogenity such as a small airway, reducing the tissue volume locally by around one third compared to the homogeneous structure, only small deviations of the current flow were observed depending on the direction. Furthermore, the small airways such as the one that crosses the heterogeneous sample are not located at tissue boundaries, but embedded in lung parenchyma in order to supply the surrounding alveoli with air. This surrounding tissue will further damp the influence of the inhomogeneity investigated in this study. Finally, both microgeometries do not show a respectable anisotropy in any direction of preferred current in the sample. This justifies an isotropic homogenised model for the effective resistivity of lung tissue *in vivo*.

5.4.3. Non-linear vs. linear relation

In general, the tortuosity $\tau^{\mathrm{E}}(\varepsilon_{\mathrm{V}})$ is a function of the tissue volume fraction since any deformation of the sample leads to a change in the characteristics of the microstructure. However, the results of the finite element simulations show that the approximation by a linear law is justified within the physiological range of stretch, which implies that the tortuosity remains almost constant in this range. The reason is that the uniform deformation in all spatial directions does not change the ratio between the current paths length and the edge length of the deformed sample significantly. Only at relatively high stretches beyond the physiological range (FF > 6.0) the alveolar walls start aligning in direction of the current, which shortens the way of the current relatively to the edge length of the deformed sample. This effect was already experimentally observed by Nopp et *al.* and modelled by a root function for the relation between tissue resistivity and filling factor used in [244].

5.4.4. Comparison with literature data

The linear relationship between filling factor FF and tissue resistivity $\rho_{\text{eff}}^{\text{E}}$ described in this study shows good agreement with previously published models [238, 244, 245, 354] as shown in Figure 5.5. All presented models except for the first one by Nopp (Nopp, 1993) [244] exhibit almost the same initial resistivity value at FF $= 1.0$. However, Nopp et *al.* mention local hyperinflation as one possible limitation in their experiments [244] leading to higher overall values of resistivity at a reasonable slope. The idea of local hyperinflation is supported by the noticeable non-linearity in their measurements, which are also observed in the presented geometry at high filling factors corresponding to hyperinflation. The second model by Nopp et *al.* (1997) [245] is based on a model of single cubical-shaped alveoli representing the electrical conductivity of the alveolar walls. While the initial value shows good agreement, the gradient of the curve is higher than those observed in other studies. This might be due to the simplification of single alveoli as thin-walled cubes. As already proposed by Mead et *al.* [228] and apparent in the scanned geometries, the alveolar ensembles are rather irregular and might be better approximated using tetrakaidecahedra. Nebuya et *al.* (2011) [238] adopt the thin-walled cube alveoli model by Nopp [245] and vary the conductivity of the walls obtaining a lower slope and a slightly lower initial value than presented in the original study. In the work by Wang et *al.* (Wang, 2014) [354], the resistivity remains almost constant throughout the complete range of filling factors. Assuming that this curve would show fairly small variation of tissue resistivity dependent on the filling factor, it should become rather difficult to reconstruct EIT images during respiration [1]. Finally, the presented model provides a reasonable range for the effective resistivity at different lung aeration states compliant with previously published data tightening the widely varying values in literature. The upper and lower bounds provided by our model correspond to a homogeneous microstructure in the respiratory zone and to an inhomogeneous microstructure with embedded airways that can be found in the conducting zone of the respiratory system.

5.4.5. Impact of this study and further work

This study provides a correlation between regional lung ventilation coming e.g., from a computational lung model and lung tissue bioimpedance measured via EIT. Therefore, this chapter marks an important step in computational lung model validation with EIT measurements.

One major perspective of the method described in this study lies in EIT examination of pathophysiological states e.g., if the lung of a patient is filled with water such as in lung oedema. In these cases, it is not assured that the current solely flows through the alveolar cells but can also be conducted by the liquid medium. While other methods might not be fully able to capture this effect, it can easily be included in the presented approach. One can simply ”fill” the air spaces, which are currently assumed to contain insulating air, with a liquid medium such as extracellular fluid, blood or mucus and assign the corresponding conductivities as described in Section 5.2. The calculated current will then directly take the combination of alveolar wall, air content and liquid medium into account. This can be used to investigate tissue resistivity in case of pulmonary oedema, infarction or mucus accumulation in the future. Similar research potential lies in a scenario when alveoli collapse as in lung atelectasis and, consequently, the characteristic of the microstructure changes. In these cases the linear link between alveolar ventilation and regional tissue resistivity might no longer be valid due to emerging shunts. Further

investigations are required to study these phenomena. These pathophysiological scenarios are extremely interesting in a clinicial setting as they severely damage the parenchyma [336]. They offer undeveloped potential for the extension of the method described in this chapter.

5.5. Conclusion

In this chapter, finite element simulations on lung parenchyma microgeometries are used to prove that a linear approximation between alveolar air content and effective tissue resistivity $\rho^{\mathrm{E}}_{\mathrm{eff}}$ is justified as quantitative link between lung tissue bioimpedance and the amplitude of alveolar ventilation. All parameters included in the relationship are physically based. The conductivity of the alveolar wall $\sigma^{\mathrm{E}}_{\mathrm{Alv}}$ can be measured experimentally and the mean tortuosity $\bar{\tau}^{\mathrm{E}}$ is a pure geometrical property of the alveolar microstructure. Based on simulations of real alveolar wall geometries, an upper and lower bound for tissue resistivities spanning various states of lung aeration are determined in this study. While the values reported in literature exhibit high variability, the presented method grounded on true lung anatomy can be expected to render more precise data.

In conclusion, this work presents a direct link between EIT-measured tissue impedance and regional air content resulting from finite element simulations. With this knowledge a sound validation of computational lung modelling with EIT measurements is possible on a regional basis as presented in the next chapter.

6. Predicting patient-specific ventilatory response

Providing optimal personalised mechanical ventilation for patients with acute or chronic respiratory failure is still a challenge within a clinical setting for each case anew. In this chapter knowledge from previous investigations in respiratory modelling and EIT monitoring is combined towards a powerful patient-specific computational lung model, creating an approach for personalising protective ventilatory treatment.

The coupled *0D/0D* computational lung model has been identified as most suitable approach to adequately represent the underlying physics of the lung with high reliability and efficiency. Personalisation of the model is proposed for the first time based on a single computed tomography scan and airway pressure and flow data recorded during one breath. After personalisation, the model is able to compute global airflow quantities as well as local tissue aeration and strains throughout the lung for any ventilation manoeuvre.

For validation, a novel "virtual EIT" module is integrated into the *0D/0D* computational lung model to simulate the EIT image acquisition process based on the results of numerically predicted tissue aeration and the patient's individual thorax geometry. Clinically measured EIT voltages and images are available for five minutes of mechanical ventilation but not used to calibrate the computational model. Thus, they provide an independent method to validate the computational predictions at high temporal resolution and reliability.

The performance of this coupling approach has been tested in an example patient with ARDS. The method shows good agreement between computationally predicted and clinically measured airflow data and EIT images. These results imply that the proposed framework can be used for numerical prediction of patient-specific responses to certain therapeutic measures before applying them to an actual patient.

This chapter is primarily based on a previous publication by the author [285], which is re-used here with permission.

6.1. Introduction

Mechanical ventilation is a standard therapeutic procedure required in a variety of medical scenarios. However, mechanical ventilation is not only a life-saving treatment but also a potential cause of further damage to the patient's lung (see Section 1.2.1 and e.g., [94, 312]). In recent years, efforts have been made to develop protective ventilation strategies (see Section 1.2.2). Strikingly, variations in a single ventilation parameter have shown reduced lung damage and improved patient outcome in several studies [9, 14, 88, 229]. These observations lead to one key question: If changes of only one parameter - e.g., tidal volume [14] or ventilation frequency [88]

- have such a significant effect on patient outcome, how good can a patient-tailored ventilation protocol, taking multiple parameters into account, be in case of respiratory disease?

The determination of such an optimal set of parameters is obviously an extremely challenging task. This becomes even more true as recent studies have shown that regional quantities such as lung heterogeneity [75] and regional mechanical strain [242] are directly linked to disease severity and mortality but cannot be measured with classical monitoring at the proximal end of the endotracheal tube or any other mean *in vivo*. Computational respiratory models, which are both fast to compute and reliable in their quality of clinical prediction, seem to be the perfect approach to deliver such patient-specific regional quantities and to meet the challenge of optimising ventilation. The *0D/0D* model presented in Section 3.2.4 based on underlying physics of the lung and careful diagnostics from a single CT scan is actually capable of delivering regional tissue strain and aeration data in addition to pressure and airflow at the opening of the endotracheal tube in a predictive manner. For applicability in a clinical setting, the possibility of a comprehensive validation against measurements must be ensured for all data generated numerically. In this work, such a validation is presented for a patient diagnosed with a regional atelectasis in the left lower lung lobe.

As outlined in Section 1.1.3 and in Chapter 5, one possible imaging method which can be used for real-time verification of local lung ventilation in a clinical setting is EIT [107]. In brief, EIT is a non-invasive, radiation-free imaging modality that allows the assessment of regional ventilation distribution at the bedside based on electrical impedance measurements. For more details, the reader is referred to Section 1.1.3, Chapter 5 and [107].

In this chapter, a powerful patient-specific *0D/0D* computational lung model [176, 283] is enhanced by a "virtual EIT" module to continuously calculate EIT voltages and images from the predictive tissue aeration results of the computational respiratory model. In this novel approach, patient EIT measurements are neither used for model generation nor for result computation, but rather for a pure and honest validation of the model-based predicted EIT voltages and images with real patient measurements. This approach has three important advantages over conventional EIT imaging: (i) an absolute strain level can be computed with the computational lung model while EIT only provides a strain difference between the inspired and expired states; (ii) regional strain levels for the entire lung can be obtained at high spatial resolution while EIT is limited to the plane where the electrode belt is attached (usually the 5th intercostal space); (iii) the model allows prediction of what *would* happen in a patient at different ventilatory settings while EIT only allows to monitor what *is* happening for the current setting. These predictive capabilities of the model save the patient from trial-and-error approaches in finding an adequate ventilator setting. In the long run, they might enable the selection of patient-specific ventilation protocols guided by computational modelling. It is, however, important to note that the computational model is no replacement of EIT imaging. EIT is rather used for rapid validation of the computed model results in a clinically well-known format.

In addition to the proposal of this novel EIT-model-coupling approach its successful application to an example patient with ARDS is demonstrated over a wide range of ventilation manoeuvres. Reference clinical data available for the same patient and the conducted ventilatory manoeuvres are used for comprehensive verification of the simulated data and allow a detailed retrospective study on this patient.

6.2. Material and Methods

To link EIT imaging and the predictive capabilities of the *0D/0D* reduced-dimensional lung model, a three-step approach is conducted as presented in Figure 6.1. First, the required clinical data are collected (Section 6.2.1) and the patient-specific computational lung model is built based on these data (Section 6.2.2). It is then possible to apply any arbitrary ventilation profile to the model and to predict global flow parameters and local tissue aeration over time. Further, EIT voltages are computed using a "virtual EIT" module based on the numerical results of local tissue aeration (Section 6.2.3). Finally, EIT images can be reconstructed (Section 6.2.4) for visualisation, validation and further clinical application of the model described in detail in the following sections.

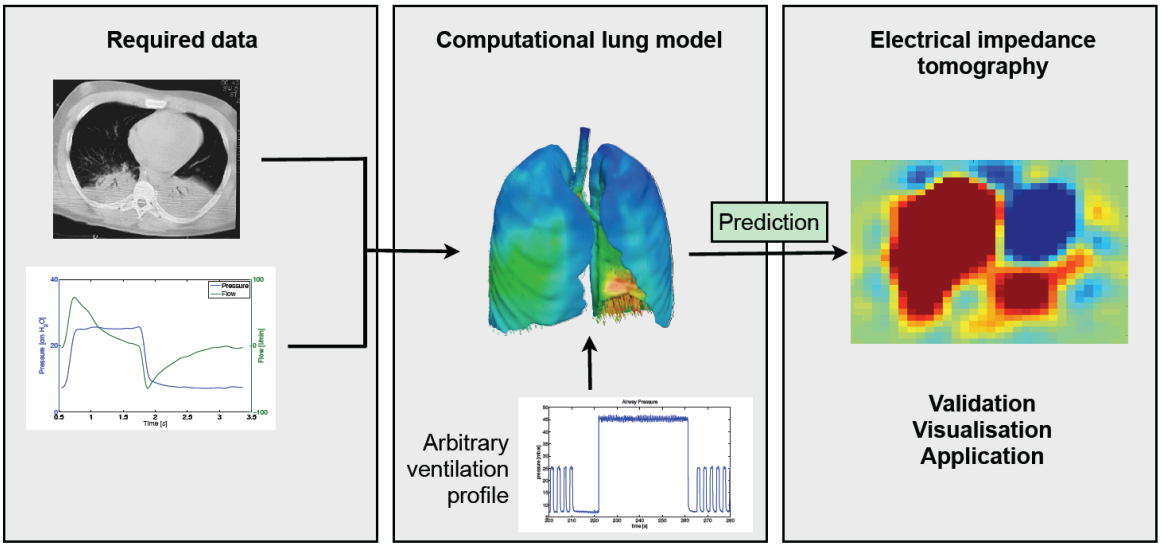

Figure 6.1.: Three-step approach for coupling of EIT with a computational lung model to numerically predict EIT images for a specific patient and ventilation profile. Taken from [285] with permission.

6.2.1. Required medical data

A single CT scan obtained in a patient at a pre-defined PEEP corresponding to EELV is provided by the Department of Anesthesiology and Intensive Care Medicine, Christian Albrechts University, Kiel and used as a basis for model creation (Figure 6.2, left). Ethical approval was obtained from the ethics committee of the Medical Faculty in Kiel and the study is carried out in accordance with the Helsinki declaration. From this scan (pixel size and slice thickness: $0.822 \times 0.822 \times 2.0$ mm) the single lung lobes, the larger airways beginning with the trachea and ending at the entry into the lobes and the utilised tracheal cannula are segmented using the software package Mimics (Materialise, Leuven, Belgium; see Figure 6.2, middle). Further, the thorax geometry is segmented from the same scan and the position of the EIT electrodes is set in the derived model.

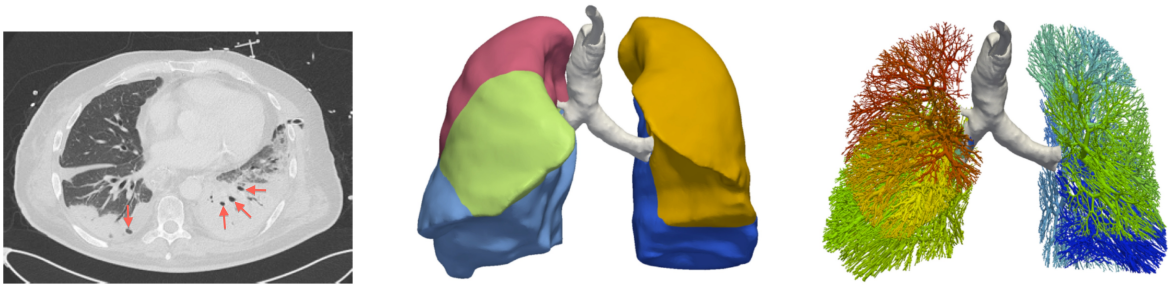

Figure 6.2.: CT scan at EELV (left), segmented lung lobes, larger airways and tracheal cannula (middle), and the fully grown 17-generation airway tree (right). Larger open airways in the atelectatic region are marked by red arrows in the CT scan (left). Taken from [285] with permission.

6.2.2. Reduced-dimensional lung model

Following the approaches in [176, 283] and [328], the *0D/0D* computational lung model (see Section 3.2.4) is created from the segmented geometry (see Section 6.2.1) by growing an airway tree into the hull of the single lobes and connecting it to the centerline of the trachea and the endotracheal tube (see Figure 6.2, right). Tree growth starts where the airways enter the single lobes and the next generation of daughter airways bifurcates relative to the direction of the lobar bronchi segmented from the CT scan. The airway tree is then recursively generated by splitting a parent airway into two daughters following morphological length and diameter ratios by [166, 216, 356]. The tree growing is terminated if a branch length is smaller than $l_{\text{min}} = 1.2$ mm, or its diameter is smaller than $d_{\text{min}} = 0.4$ mm, or the generation number of $n_{\text{max}} = 17$ is exceeded, or if it touches the hull geometry of the segmented lobes. The termination criteria for l_{min} and d_{min} are consistent with the values reported for terminal bronchioles [144, 356] and all smaller airway structures are respected in the model of the pulmonary acinus [86, 176]. Lengths and branching angles from the tree growing process are valid for healthy and diseased regions of the lung assuming that an atelectatic region was healthy during lung growth and thus follows the morphological laws in [166, 216, 356]. However, as the atelectases lead to the closure of smaller lung structures this effect is accounted for by derecruiting (i.e., fully closing) all airways in the atelectatic region defined by a Hounsfield unit of HU $= -300$ or higher in the CT scan [219] (see Figure 6.2 left).

In our patient, this tree-growth procedure resulted in $63,951$ airways which are modelled via a reduced-dimensional flow model. The model derived in detail in Section 2.1.2 has been shown to reproduce the behaviour of fully resolved three-dimensional airways in [176]. The underlying mathematics are briefly recalled. Each airway is represented by a non-linear resistance ($R = R_{\mu} + R_{\text{conv}}$), capacitance ($C$), and inductance ($I$, see Section 2.1.2). The pressure drop $\Delta P = P_1 - P_2$ between the airway inlet and the outlet are then linked with the flow rate Q_1 entering and Q_2 leaving the airway via Eq. (2.47) and Eq. (2.48). In addition to the flow through the airway, the expansion of an airway is regulated via a visco-elastic resistance R_{visc} and the external pressure of an airway $\tilde{P}_{\text{ext}}$. Further mathematical details of the respiratory model are presented in Section 2.1.2.

At the terminal ends of the airway tree, a previously described reduced model for the lung acinus [176] is attached, described in detail in Section 2.2.2. The linear parameters $B = 32.85 \cdot 10^3$ mbar s mL^{-1}, $B_a = 1.88 \cdot 10^3$ mbar s mL^{-1}, and $E_2 = 0.53 \cdot 10^5$mbar mL^{-1} are taken from literature [176] while the non-linear (E_1) sigmoidal material behaviour of lung tissue is included via an Ogden like material law [251] that has been shown to perform well in experiments on lung tissue [29, 273]. The resulting relationship between pressure difference across an acinus P_{ac}, initial volume $V_{ac,0}$ of an acinus (at the stress free state) and its current volume as V_{ac} is given in Eq. (2.80). The initial volume $V_{ac,0}$ of an acinus i is given as $V_{ac,0} = V^{lb} \cdot A_i^{lb}/A^{lb}$ where A_i^{lb} is the outlet area of the conducting airway supplying the current acinus i and A^{lb} is the sum of all outlet areas of peripheral airways in the current lobe. The variable V^{lb} denotes the volume of the current lobe at end-expiration.

The important phenomenon of interdependence and volume competition between neighbouring acini in heterogeneous lungs [228] is included via the inter-acinar linker approach presented in [283] and in detail described in Section 2.2.2. Thereto, $P_{ac} = P_{alv} - P_{Pl/intr}$ denotes the difference between alveolar pressure P_{alv} and the pressure surrounding an acinus $P_{Pl/intr}$. In case the current acinus is connected to the pleura, pleural pressure P_{Pl} is directly applied. Otherwise, pleural pressure is propagated to the current acinus based on an equilibrium of forces between neighbouring acini as described in [228, 283]. This balance of forces for the current acinus i is given in Eq. (2.89)

Local pleural pressure P_{Pl} is difficult to determine in vivo without additional measurements such as esophageal pressure. Therefore, a mean pleural pressure of -5.3 mbar is taken from literature [147] and following [359] a linear gradient of pleural pressure is added reading

$$P_{Pl} = -5.3\text{mbar} + \frac{2(x - x_0)}{L_{sp}} \Delta P_{Pl} \tag{6.1}$$

to respect the variations in pleural pressure in supine position. Here, the centre point of the lung is located at $x_0 = -155$ mm measured from the CT scan and all points in the lung are referenced as x. The corresponding pleural pressure difference $\Delta P_{Pl} = -2.75$ mbar is taken from [359] and the lung height in supine position is measured from the CT scan as $L_{sp} = 187$ mm. It should be noted that also other variations in pleural pressure could be realised with this modelling approach, e.g., those observed in prone positioning [140].

Following the law in Eq. (2.80) a shape determining parameter β and a slope determining parameter κ uniquely define the relationship between pressure and current volume for each acinus. To fine-tune the general, experimentally determined material behaviour of lung tissue [29, 273] for this specific patient, tracheal pressure and tidal volume data are recorded during a single calibration breath. The parameters β and κ are then identified using the two quasi-static points of the single calibration breath at EELV and at the end of inspiration.

As previous investigations (e.g., [346]) showed that P-V curves of atelectatic lungs retain their sigmoidal shape, the shape determining parameter β is assumed to be equal for healthy and diseased acini. To account for collapsed areas or fluid accumulation, indicated by brighter grey values in the CT scan (see Figure 6.2, left), the slope determining parameter κ is set as a relative acinus stiffness based on the Hounsfield units of the corresponding lung region. Using this approach, the phenomenological stiffer behaviour of incompressible water contained in small

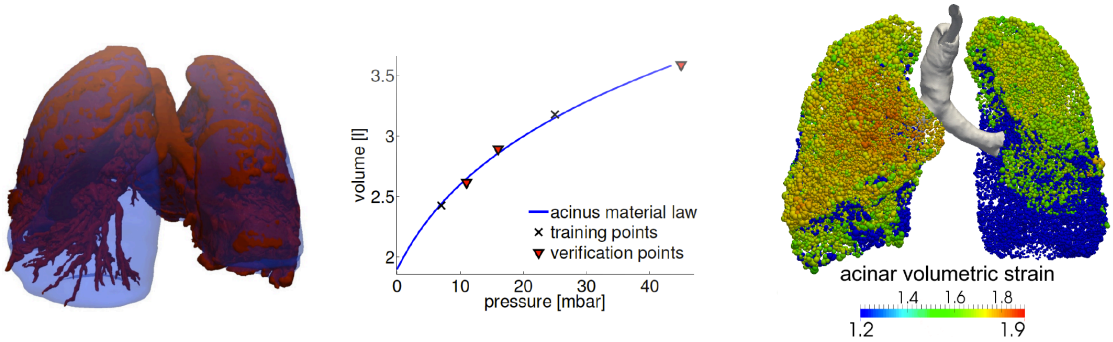

Figure 6.3.: Three-dimensional reconstruction of collapsed lung regions based on Hounsfield units showing an atelectasis (blue) in the left bottom lobe (left), pressure-volume curve of an acinus calibrated to two training points (middle), and visualisation of regional acinar strain at all acini (right). The three-dimensional representations (left and right) show the same lung geometry from different camera angles to illustrate the dimensions of the atelectasis. Taken from [285] with permission.

alveolar structures is respected following the law

$$\kappa = \kappa_0 \cdot (1 - \frac{\mathrm{HU}}{\mathrm{HU}_{avg}}) \tag{6.2}$$

where κ_0 is the baseline stiffness, HU the Houndsfield unit of the voxel corresponding to the current acinus and $\mathrm{HU}_{\mathrm{avg}} = -597$ the average HU of lung tissue in this scan. In the current ARDS patient the Hounsfield units of the lung range from -900 to -200 with an average value of -597 in good accordance with previously reported values for ARDS lungs [219, 270]. It is annotated that Eq. (6.2) is only one possible way to include the stiffness changes dependent on tissue density. However, it appears to be a reasonable choice for the stiffening situation with preserved sigmoidal shape of the P-V relationship (see Figure 6.4 and [346]).

Inserting Eq. (6.2) in Eq. (2.80) and summing over all acini allows the calculation of the material parameters β and the baseline stiffness κ_0 from two known training points of the quasi-static P-V curve of the whole lung (Figure 6.3, middle). In the present case, this results in $\beta = -4.0$ and $\kappa_0 = 20$ mbar.

With this fully coupled *0D/0D* model of the conducting and respiratory part of the patient's lung, it is possible to computationally predict local tissue aeration in terms of acinar volumetric strain $\varepsilon_{\mathrm{vol}} = \frac{V}{V_0}$ for any selected ventilation protocol prescribed at the cannula inlet. In this study, standard pressure-controlled ventilation with a PEEP of 7 mbar and a tidal volume of 6 ml kg^{-1} predicted body weight of the patient are used. Tracheal pressure, flow and tidal volume data, as well as measured EIT voltages are recorded. This recording is obtained for five minutes at a temporal resolution of 50 Hz using the PulmoVista® 500 tomograph (Dräger medical, Lübeck, Germany). The 16 electrode belt is placed around the patient's chest at the level of the fifth intercostal space. Within two minutes of the recorded time, several modifications of the ventilation protocol are carried out shown in Figure 6.5 including a decrease in plateau pressure and a recruitment manoeuvre. The pressure curve during these two minutes is applied to the reduced-

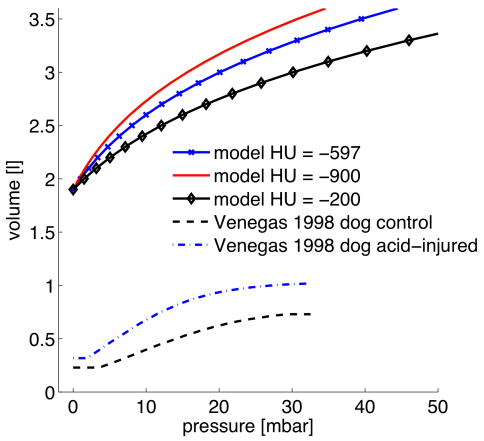

Figure 6.4.: P-V curves for different Hounsfield units are shown in the graph compared to previously reported curves for healthy and atelectatic dog lungs [346]. Both in literature and in the used scaling law (see Eq. 6.2) the shape of the curves is similar in healthy regions (HU = -900) and in maximally diseased regions (HU = -200) while the diseased curves are downscaled on the volume axis. Taken from [285] with permission.

dimensional computational lung model and computed acinar strain is handed over to the EIT part of the model described in the next section.

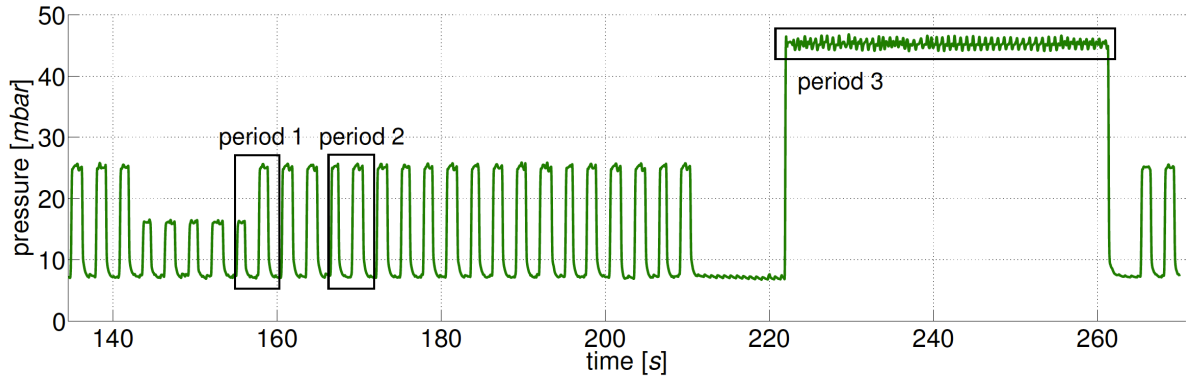

Figure 6.5.: Applied ventilation pressure during two minutes of EIT monitoring including several modifications of the ventilation protocol. The intervals marked as “period 1-3” are used for further investigation described in Section 6.3.1. Taken from [285] with permission.

6.2.3. Virtual EIT module

The principle of EIT imaging is based on the measurement of the changes in electrical tissue resistivities resulting from the variation of alveolar volume during respiration (see Section 1.1.3 and Chapter 5). Here, this effect is used in a simulation of EIT voltages for known conductivities (also known as EIT forward problem) for a three-dimensional thorax model based on the segmented patient geometry as presented in Figure 6.6.

Local tissue aeration in terms of acinar volumetric strain $\varepsilon_{\text{vol}} = \frac{V}{V_0}$ is transformed into local resistivity $\rho_{\text{eff}}^{\text{E}}$ using the linear law in Eq. (5.10) derived in Chapter 5 and similarly observed in several experiments [238, 244, 245]. A mean tortuosity of $\bar{\tau}^{\text{E}} = 1.71$, an alveolar conductivity of $\sigma_{\text{alv}}^{\text{E}} = 0.7284\ \Omega^{-1}\text{m}^{-1}$ are used and the volumetric strain is converted to the filling factor $\text{FF} = V_{\text{air}}/V_{\text{tissue}}$ via $\text{FF} = 5.0 \cdot \varepsilon_{\text{vol}} - 5.0$, which comes from the assumption that the filling factor is $\text{FF} = 3.0$ at FRC and $\text{FF} = 6.0$ at TLC [284]. The resulting local resistivity is mapped to the three-dimensional thorax model gained from the segmentation (Section 6.2.1) via linear interpolation from acini centres in the airway tree to the element centres of the 3D thorax mesh. The thorax mesh consists of $208,859$ tetrahedral elements with a background resistivity of $4\ \Omega\text{m}$ for all non-lung elements [48] and is refined at the position of the electrodes [139] with a characteristic mesh size of 1.0 mm. 16 electrodes with a diameter of $d_{\text{elec}} = 30$ mm are used and their exact positioning is determined from the imaging data.

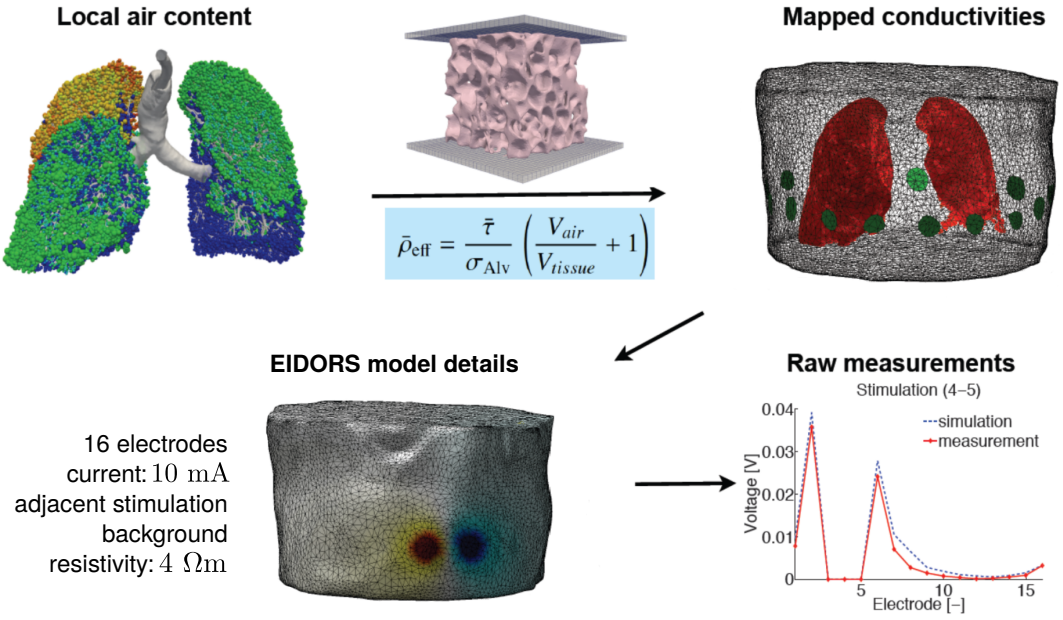

Figure 6.6.: Overview of the coupling between the computational lung model and EIT. Taken from [285] with permission.

The Laplace equation is solved using EIDORS [1] for an adjacent stimulation pattern at an imaging frequency of 50 Hz and a current of 10 mA similar to the measurements described in Section 6.2.1. Computed voltages are stored in the VIASYS data format with zero entries at the

stimulating electrodes and can directly be compared to clinically measured voltages at each time step. Further, these voltages can be used for EIT image reconstruction as presented in the next section.

6.2.4. Image reconstruction

As single voltage patterns are hard to interpret in a clinical setting, an image reconstruction method is used to visualise changes in regional resistivity of the lung tissue as a two-dimensional image in the plane of the electrode belt. In this study, functional EIT imaging is performed with the end-expiration point of the last breath taken as reference point for reconstruction in the current step. For reconstruction, a coarse version ($70,853$ elements) of the mesh utilised in the forward problem and the GREIT algorithm [2] is used. The reconstruction algorithm is trained with 965 circular training points with uniform distribution and a diameter of $d_{\text{tp}} = 0.02$ mm. The noise figure NF is set to NF $= 0.5$, which corresponds to values recommended by [129]. An image with 32×32 px is reconstructed resulting in a resolution of approximately 12.5 mm px^{-1} with the same temporal frame rate as in the measurements (50 Hz). Finally, the image is interpolated to a resolution of 64×64 px for smooth visualisation. This reconstruction is performed for the entire time of EIT monitoring and for both the measured and the computed EIT voltages to allow a consistent comparison over time.

6.3. Results

6.3.1. Global flow-derived quantities

In Figure 6.7 (top), computationally predicted and clinically measured tidal volumes are shown over time for the simulated part of the 2 minutes of monitored ventilation with the applied corresponding pressure profile (see Figure 6.5). Figure 6.7 (bottom) presents a more detailed view into the tidal volume waveforms at the transition from lower to higher plateau pressure (period 1, left), the standard breathing protocol (period 2, middle) and the conducted recruitment manoeuvre (period 3, right). The simulated and the clinically measured tidal volumes match well over the full time span and in the detailed views. The only slight difference is a small constant time shift of approximately 0.1 s and a larger decrease in the simulated volume right before and after the recruitment manoeuvre. The small deflections in the measured volume at the end of each breath resulted from automatic zero-setting of tidal volume by the ventilator.

The quasi-static points of measured volume at end-inspiration at lower plateau pressure ($t = 156$ s) and at the end of the recruitment manoeuvre ($t = 261$ s) are additionally marked as verification points in Figure 6.3 (middle). These points lie on a non-linear curve representing the mechanical behaviour of lung tissue calibrated for this patient. The decreasing slope in the upper part of the curve is similar to the upper part of sigmoidal P-V curves reported in e.g., [346]. The good agreement between the measured and simulated tissue behaviour underlines the fact that the model is able to capture the upper part of the sigmoidal pressure-volume curve in this patient.

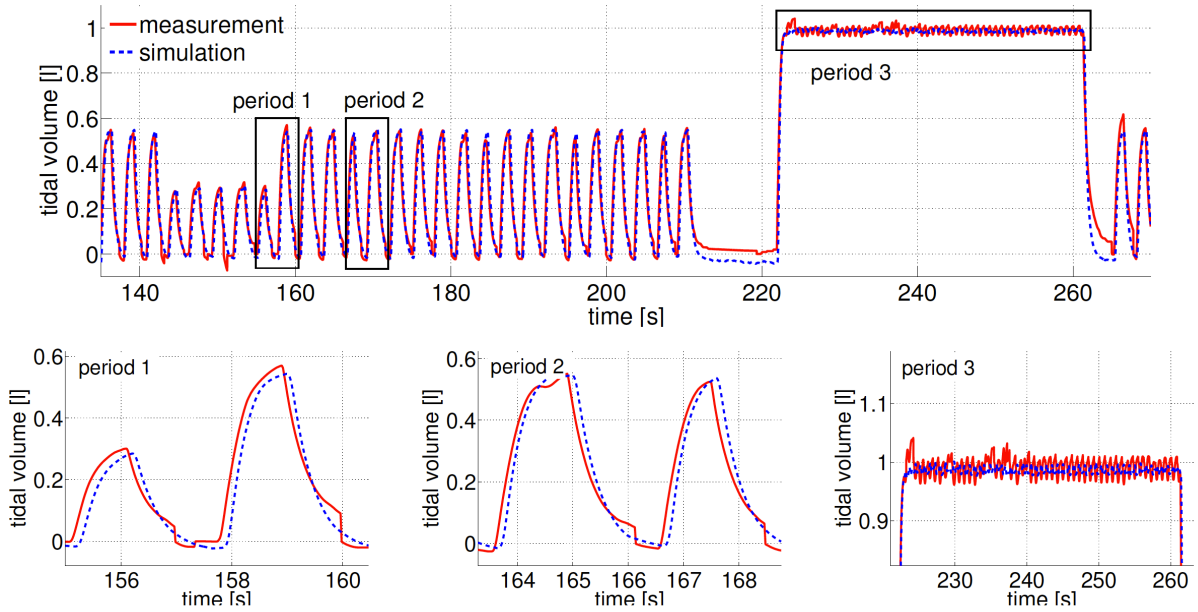

Figure 6.7.: Comparison of computed and clinically measured tidal volumes for the same applied pressure profile shown in Figure 6.5. Taken from [285] with permission.

6.3.2. Regional acinar strain

Local tissue aeration in terms of acinar strain ε_{vol} is presented in Figure 6.8 for a standard breath at different time points indicated as filled circles in the pressure-time curve. It can be seen that in the present patient, the ventral part of the right middle lobe is distended more during breathing than the remaining lung parenchyma. Moreover, this right middle part has a faster filling profile. The left top part is ventilated with less air which enters the region slightly later and the left bottom part shows almost no ventilation throughout the full cycle due to the consolidated atelectasis.

Scaling of the acinar strain images is chosen in such a way that values above 1.9 are coloured red corresponding to regions at risk of overdistension of $1.5 - 2.0$ according to [267]. Additionally, an averaged global strain $\varepsilon_{\text{glob}}$, which is calculated as the ratio between current lung volume and an FRC of 2.93 l determined from the CT scan, is marked in red in the scaling bar at each time point. This clearly shows the difference between global and regional strains especially in ARDS. In this patient 33.3% of the total lung volume, mainly the left bottom lobe are atelectatic. The maximum regional strain $\varepsilon_{\text{vol}}^{\text{max}}$ can be estimated from global strain $\varepsilon_{\text{glob}}$ derived from the flow measurement at the endotracheal tube using the relationship

$$\varepsilon_{\text{vol}}^{\text{max}} = 1.46 \cdot \varepsilon_{\text{glob}} - 0.31 \tag{6.3}$$

in the entire pressure-volume range of mechanical ventilation for this patient. This relationship reveals that maximum regional strain is at least 15% higher than global strain and that regional strain rises 46% faster than global strain.

During the recruitment manoeuvre ($t = 240$ s) where a global strain threshold of 1.66 is reached (Figure 6.8, bottom right) approximately 37% of the entire lung and 55% of the remain-

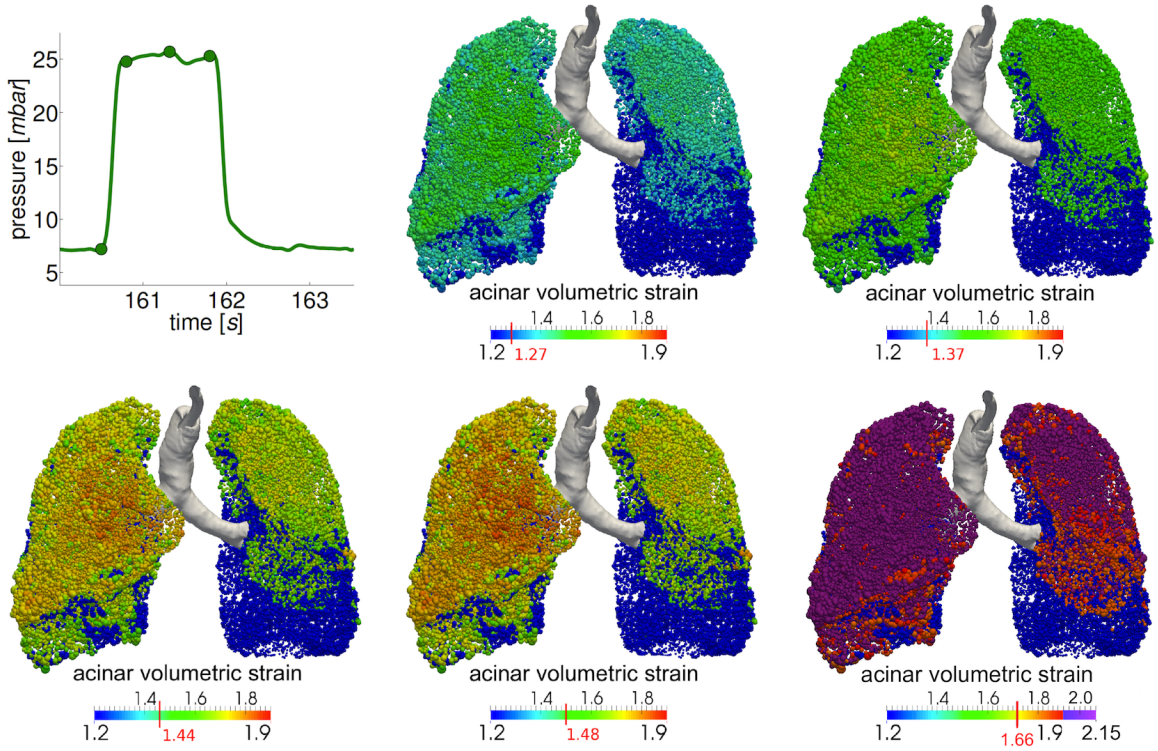

Figure 6.8.: Pressure-time curve of a standard breath with four marked time points (filled circles) for which regional acinar strain ε_{vol} is visualised (from left top to mid bottom). The last image (right bottom) visualises regional strain for the recruitment manoeuvre ($t = 240$ s). Additionally, global strain is shown in red in the colourbar at each measurement point. Taken from [285] with permission.

ing healthy lung tissue shows regional strains higher than 2.0 indicated by purple colour in the image. The maximum regional strain value in this case is 2.15 implying that a single acinus is stretched more than two times in volume compared to EELV in this short time interval. It is annotated that, at all times, except for the recruitment manoeuvre, regional acinar strain is less than the critical value of 2.0 indicating an acceptable ventilation setting for this specific patient.

6.3.3. EIT voltages

A comparison of simulated and computationally predicted EIT voltages at EELV is visualised in Figure 6.9 (top, middle and right) for two example stimulation patterns indicated in Figure 6.9 (top, left). The computed voltages lie in the same range as the measured ones and show good agreement over a wide range of stimulation patterns. In Figure 6.9 (bottom, middle and right) the voltage differences between the current and reference states are shown over time for simulated and measured EIT voltages at two representative electrodes 7 and 14 (Figure 6.8, bottom, left). These voltage differences between the current and baseline states are used for EIT image reconstruction in f-EIT as presented in the next section. Again, the computed voltage difference values are quite similar to the measured ones and smaller deviations can be attributed to cardiac

activity and inhomogeneous background conductivity encountered under in-vivo conditions (see Section 6.4.3).

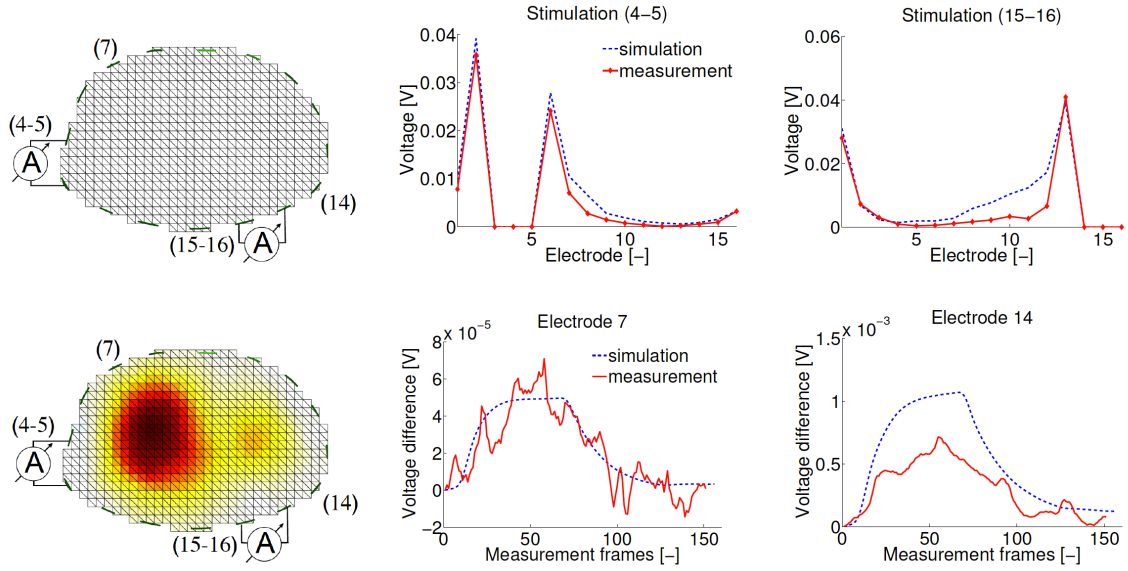

Figure 6.9.: Computed EIT voltages compared to measured voltages at bedside for adjacent current drive between electrodes 4 and 5 (4-5), and 15 and 16 (15-16) schematically visualised in the thorax geometry (left). The top panels show the reference voltages at EELV. The bottom panels correspond to the temporal difference against baseline for two representative electrodes and a breath with maximum inspiration at a pressure of 25 mbar. Possible differences between computed and measured voltages resulted from the inhomogeneity of the background conductivity caused by cardiac activity and the presence of bone tissue in the spine and ribs (see Section 6.4.3). Taken from [285] with permission.

6.3.4. Reconstructed images

Figure 6.10 compares the reconstructed changes of clinically measured (left) and simulated (right) tissue resistivity $\rho_{\text{eff}}^{\text{E}}$ in our patient. The top images correspond to EELV at the set PEEP and the bottom images to maximum inspiration at a pressure of 25 mbar.

Both images are reconstructed using the same algorithm (see Section 6.4.2) and the image values of the cardiac region are mapped from the patient measured to the computationally predicted images for better comparability. All other regions remain unaffected from this mapping. The two reference images at EELV show close to zero values of resistivity as expected. The images at end-inspiration show good agreement between local ventilation patterns in measurement and simulation and clearly indicate a larger ventilation in the right ventral lung region compared to the left lung region, which is poorly ventilated due to the atelectasis.

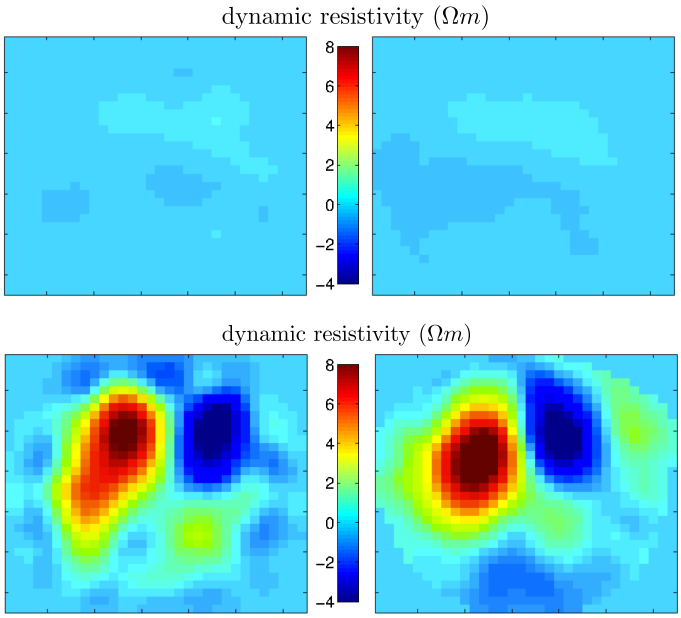

Figure 6.10.: Functional EIT images reconstructed from clinically measured (left) and simulated voltages (right). The top images show the reference at EELV while the bottom images correspond to maximum inspiration at a pressure of 25 mbar. A common colour scale is used for comparison of the clinically measured and simulated images. Taken from [285] with permission.

6.4. Discussion

The main finding of this chapter is that the *0D/0D* respiratory model allows to computationally predict global and local ventilatory quantities for an example patient suffering from ARDS. Important methodological aspects in this context are the generation of a mechanically sound and predictive reduced-dimensional lung model for an individual ARDS patient. This model is able to deliver clinically familiar data such as tidal volume, airflow and airway pressures that can be validated with actual measurements on a global level. Further, the model provides a new insight into lung physiology and tissue straining during different ventilatory manoeuvres. Finally, a novel "virtual EIT" module is proposed that mimics the EIT procedure and allows to present the simulation results as "virtual EIT" voltages and in the format of reconstructed EIT images. EIT measurements are not used for model parametrisation, and thus they can be used for comprehensive validation of computationally predicted regional ventilation as presented in the following sections.

6.4.1. Quality of the global quantities

Global quantities e.g., tracheal flow and tidal volume can be adequately predicted for the present patient for given transpulmonary pressures similar to widely used single compartment lung models (see Section 3.1 and [23, 24, 260, 346]). However, in this case it is not due to pure fitting of

resistance and compliance parameters to a huge amount of clinical data, but by modelling the respiratory system as it behaves in reality. The conducting airway tree is reconstructed [328] from medical imaging data and coupled to an experimentally determined material law for lung tissue [29, 273]. In the presented model a single calibration step based on an easy to perform measurement of one breath is sufficient to reach an almost perfect prediction of global flow data for a specific patient over a wide range of clinically relevant ventilation parameter settings including variations in plateau pressure and an unsuccessful recruitment manoeuvre. It is noted that due to the unsuccessful reopening manoeuvre, reopening dynamics presented in Section 2.2.2 are omitted in this study. However, the inclusion of reopening dynamics proposed e.g., in [22, 211, 222] is possible in the *0D/0D* model.

6.4.2. Impact of local quantities

One quantity which is often mentioned together with lung damage is regional strain in terms of heterogeneity in ventilation distribution [75, 224] or hyperdistension [73, 91, 221, 355]. Regional acinar strain basically stems from the load that is seen by the acinus and can result in even higher stresses at hotspots e.g., for an individual alveolar wall [272]. As inflammation does not affect the lung uniformly but rather in single hotspots with overdistension [312], globally monitored strain might under-estimate the real strain situation. Thus, global strain is not a fully reliable quantity for evaluating safe ventilation settings.

One suitable quantity for assessing local cellular loading is absolute regional strain. Absolute regional strain, however, cannot be measured in long time monitoring without radiation-based imaging methods and therefore, global strain thresholds from endotracheal flow monitoring are used as safety factors in mechanical ventilation [267]. Global and maximal regional acinar strains only conditionally correlate and single lung regions may already be overdistended even if the global strain threshold [267] is not exceeded. This is especially important in ARDS and impressively shown in the presented patient: While the atelectatic region is not inflated with the clinically applied ventilator settings, the right ventral regions are strained by a factor of about 1.9, already close to the critical threshold defined by [267]. Maximum regional strain in heterogeneous lungs is always higher and rises faster than global strain measured from the conventional monitoring at the endotracheal tube opening. Regional strain can, however, be estimated from global strain using a patient-specific correction factor resulting from detailed analysis in this study (see Section 6.3.2). The derived relationship reveals that the maximum regional strain is at least 15% higher and raises 46% faster than the global strain. This difference may become even more pronounced with increasing severity of ARDS and for different patients, different correction factors may be necessary depending on the degree of lung collapse. In this context, the *0D/0D* model can provide an important additional insight into the lung (patho-)physiology by predicting regional strain for different patients and ventilatory settings.

6.4.3. Virtual EIT module

Many respiratory models have been described in literature, but only a few of them can actually be verified in a clinical setting. The benefit of EIT use in this scenario is apparent: Voltages can be measured easily at bedside and also be computed, once the conductivity is known. Furthermore, this can be realised over a long time, i.e., in the course of the ventilatory therapy with different

manoeuvres without imposing any harm to the patient by radiation or invasive measurements (see Section 1.1.3 and [3, 107]). The EIT forward problem is relatively robust and uses only the known geometry, the set stimulation current and varying resistivity - a material property which has been extensively reviewed in Chapter 5 and in literature [110, 111, 244, 245, 284].

Both in the computationally predicted and in the clinically measured EIT images, single pixel values stand for local increase/decrease in bioimpedance and thus for an increase or decrease of regional air content during respiration. If calculated and actually measured EIT images show a similar behaviour, this means that computationally predicted local tissue aeration can actually be verified against real patient measurements using real EIT measurements and the new "virtual EIT" monitoring module. This promising first step of verification paves the way for further clinical studies involving larger patient cohorts and various clinical scenarios.

There are still minor differences between computed and measured voltages possibly due to the impedance changes of the heart during filling with electrically conductive blood and emptying and presence of larger bone structures, which are not yet taken into account in the forward problem. This has, however, been done in literature for single parts of the human body [41] and can be used as further extension of the current work.

The fact that EIT is not used for model parametrisation enables a detailed clinical validation of the computationally predicted results. Even if EIT exhibits relatively low spatial resolution, its advantage is the high temporal resolution which allows the dynamic behaviour of the respiratory system to be captured in real time. The proposed coupling between EIT and computational lung model provides additional information beyond those obtained from conventional EIT monitoring in three important aspects covered in this pilot study: (i) an absolute strain level can be computed compared to the relative strain differences between inspiration and expiration in simple EIT; (ii) the entire lung can be modelled in contrast to a single plane with EIT alone; (iii) the computational lung model allows prediction of patient behaviour for several different scenarios where EIT only allows monitoring of the current scenario. Still, the presented approach is not meant to be a replacement of EIT imaging. EIT is rather used for temporally highly resolved validation of computed model results in a clinically well-known format.

6.4.4. Image reconstruction

Image reconstruction is an own field of research providing efficient and robust algorithms for the ill-posed mathematical reconstruction problem of EIT [204]. In this work, we use the consensus GREIT approach [2] that has been shown to perform well in respiratory imaging and is widely used within that community. Also in the present case, it is able to reconstruct images that are very similar to the ones originating from measured data, even if the underlying voltage values differ slightly in some cases. This underlines that GREIT is robust enough to be used in the coupling between the computational lung model and EIT and does not tend to overmodulation in case of smaller voltage deviations. It is, however, annotated that there is no restriction in the usage of a specific reconstruction algorithm in this framework. Having the patient's real thorax geometry available is definitely a benefit [139] but there are also other algorithms possible, e.g., those provided by the EIT manufacturers with underlying reconstruction matrices for certain body-mass indices or other patient data. For the current choice, EIT image reconstruction is a fast operation, which can be performed in real-time with the computation providing the clinician with an immediate feedback when applying ventilatory changes to the respiratory model.

6.4.5. Limitations and future directions

The coupling between EIT and computational lung modelling developed in this chapter has been applied to a first ARDS patient in the presented pilot study. Respecting individual patient needs, not all effects that are interesting in respiratory modelling have been observed in this case. Up to now, the proposed methods are shown for a patient suffering from a regional consolidated atelectasis in an otherwise normal lung. Other sources of lung heterogeneity are conceivable such as lung derecruitment with surfactant depletion, interstitial or alveolar oedema, among others. For the specific pathologies different mechanical properties might apply which could specifically result in different realisations of Eq. (6.2). Further, a full closure of all lung structures in the atelectatic region has been assumed as all recruitment manoeuvres were unsuccessful in this patient. For cases where reopening plays a role, an adequate description of recruitment/derecruitment dynamics (see Section 2.1.2 and [211, 222]) can be included in the lung model.

Also, no direct validation against radiation-based assessment of regional ventilation is performed in this work due to research ethics guidelines. Instead, EIT imaging is used which has been shown to perform comparably well to radiation-based methods [92, 105, 278, 348] for validation. This means that validation of the model is only possible with the given spatial resolution of the EIT image. However, as no information from the EIT measurement has been used for prediction of the "virtual EIT", the observed close correlation between these measured and computed data impressively shows the applicability of the proposed methods.

6.5. Conclusion

In this chapter, a reduced-dimensional computational lung model is coupled to EIT to prove that it is possible to numerically predict important ventilatory quantities for a specific patient. The *0D/0D* model is created based on medical imaging data, airway pressure and airflow data of a single calibration breath. The model is fast and efficient in evaluation and it can increase the information obtained from classical medical imaging by providing actual flow quantities. These quantities convincingly match actual clinical measurements. Moreover, the computational model provides a deeper insight into lung physiology indicating potential sites of overdistension of lung parenchyma and dynamic heterogeneity during ventilation. These data can be represented as regional tissue strains, raw EIT voltages or reconstructed EIT images and allow a rapid validation of computed and clinically measured data. In conclusion, this work provides the clinician with important information for setting ventilation parameters in addition to those provided by conventional EIT alone. It allows an evaluation of possible treatment options for a specific patient and thus presents an important step towards individualised respiratory care in close interaction with clinical monitoring.

7. Gas exchange mechanisms in neonatal ventilation

Virtually all babies born premature and in need of mechanical ventilation are administered to high frequency oscillatory ventilation (HFOV). Despite the reported success of this method in clinical practice, the exact underlying mechanisms of gas exchange promoting this technique are still unknown.

In this chapter, spatially and temporally highly resolved computational fluid and transport dynamics modelling is used to elucidate why gas exchange in HFOV is so efficient specifically in preterm infants. The newly developed *0D/3D* computational methods are validated against available reference data and are applied to an imaging-based case of mechanical ventilation in the preterm infant under representative conditions. The results support and, for the first time, localise six mechanisms of gas exchange proposed in literature. This detailed insight into pulmonary airflow advances general knowledge on the clinically highly important HFOV-technique by detecting gas transport phenomena that have never been seen or measured before. Conducted investigations can be seen as a further learning step in understanding gas transport in HFOV. They might ultimately reveal the key components for improved oxygen delivery in preterm infants during their first breaths in life.

This chapter is primarily based on a previous publication by the author [289], which is re-used here with permission.

7.1. Introduction

Currently, approximately 11% of live births worldwide can be categorised as premature, i.e., born before 37 completed weeks of gestation [338]. Among these births, those occurring very preterm (28-31 weeks) or extremely preterm ($<$ 28 weeks) constitute a substantial share and are especially exposed to short- and long-term complications. The lungs of these infants are not fully developed at this early stage and thus they require assistance via mechanical ventilation. Even worse, these immature lungs are extremely vulnerable and sub-optimal ventilation in their first breaths can lead to consequences for a lifetime [158].

Therefore, a ventilation technique combining a continuous positive airway pressure (CPAP) with HFOV, which superimposes oscillations of very low tidal volumes (TV) at high frequencies (f), is used in clinical practice. This method has been shown to result in superior scores of short-term oxygenation [173] and long-term lung function [379] compared to conventional therapy. Still, the underlying mechanisms of this ventilation technique have not been fully understood since its invention more than three decades ago [37, 309]. Previously, experts in the field proposed eight gas exchange mechanisms among which six are based on convective transport and related to the question of how oxygen can actually be transported to the terminal lung

regions even though tidal volume is much smaller than respiratory dead volume [311]. Due to ethical limitations on measurements in the vulnerable lungs of preterm infants, none of these mechanisms has been observed clinically and their proposal remains an elaborate guess until today.

Next to experimental animal studies (see e.g., [180]), computational methods have been used to simulate airflow and gas transport during HFOV in order to disclose the secret behind the efficiency of HFOV in oxygen and CO_2 transport [8, 26, 60, 154]. Providing important first steps, the computational methods have not yet been able to fully capture the real situation during HFOV in the preterm infant. The main reason is that none of these studies used a real infantile lung for their analysis. Herrmann et *al.* investigated gas transport during HFOV in the canine lung [154], the work by Bauer et *al.* [26] is limited to an artificial geometry that mimics an adult bronchial tree, while the approaches by Choi et *al.* [60] and Alzahrany et *al.* [8] are conducted on imaging-based adult airway tree geometries. A second major reason is that none of the previously reported approaches could model real exhalation determined by the mechanics of the respiratory system. In reality, exhalation is a passive process triggered by elastic recoil forces of the compliant lung tissue and thoracic cage. Recoil forces create a pressure gradient opposite to the applied CPAP during the expiration phase and initiate a related airflow. Instead of modelling this effect, all previously reported computational approaches prescribed a negative sinusoidal outflow rate at the tracheal inlet, thereby neglecting real physiology resulting from the dynamics of lung tissue, the thoracic cage and associated respiratory muscles. Finally, even the most realistic fluid dynamics model by Choi et *al.* [60] did not account for tube leakage which is peculiar in neonatal ventilation as usually non-blocked tubes are used. Neither does the work in [60] incorporate a real gas transport model, but uses a so-called stretch rate analysis of the flow field as a surrogate for gas transport and mixing with limited significance on convective-diffusive processes.

In the present work, the outlined limitations of previous approaches are overcome and a powerful computational lung model is used to reveal the important convective and convective-diffusive gas transport mechanisms in HFOV. Further, the highly resolved model allows to exactly localise single mechanisms in the anatomy of the preterm infant for further understanding, teaching and optimisation. To ensure correctness of the presented simulation methods, an available experimental benchmark test is set up and simulations are verified against available literature data for this case. Then, an exemplary patient-specific lung model for the preterm infant is extracted from medical imaging data and associated lung compliance and resistance are obtained from lung function measurements of the same patient. Using these data, a representative case of mechanical ventilation is computed and impressively shows six proposed mechanisms behind efficient gas transport in the infantile lung during HFOV [311]. In the following, a detailed description of available patient data, the developed lung model, computed results and their detailed discussion will be presented with a strong focus on the provided methods from a clinical perspective.

7.2. Material and Methods

7.2.1. Patient recruitment and pulmonary function test

A preterm infant enrolled in the AIRR study was chosen as exemplary patient for all investigations presented in this work. This study was approved by the ethics committee of the Ludwig-

Maximilians-University (LMU Munich, Germany) and informed consent of mothers/parents was obtained.

The preterm infant had an age of 3 months, and a body weight of 3.34 kg at the time of examination. According to the standard study protocol, the patient underwent pulmonary lung function testing using a baby-bodyplethysmograph (Jäger, Germany). The lung function test revealed a FRC of 54.2 ml, a respiratory system resistance of $R_{\text{rs}} = 2.79$ kPa s l^{-1}, a respiratory system compliance of $C_{\text{rs}} = 23.65$ ml kPa^{-1} and a tidal volume of 13.7 ml during spontaneous breathing after treatment with Salbutamol.

7.2.2. Medical imaging

Three-dimensional MRI of the preterm infant has been performed using a 3.0 Tesla Magnetom Skyra scanner (Siemens Healthcare, Erlangen, Germany) and several sequences were acquired. For lung geometry extraction in this chapter, the T1-weighted magnetisation-prepared rapid gradient-echo (MP-RAGE) sequence with an image size of $256 \times 256 \times 144$ px^3 and a resolution of 1 mm px^{-1} was chosen. In this scan, the upper airways, the first generations of the lower airways, and the lung hull contour were visible. The images of the preterm infant served as a starting point for lung model generation described in the next section.

7.2.3. Lung model generation

For modelling fully resolved airflow in the upper airways and the first generations of the lower airways with realistic boundary conditions, a *0D/3D* model is used (see Section 3.2.2). The upper airways, the first generations of the lower airways and the contours of the single lung lobes were directly segmented from the previously described MR images using the software package Mimics (Materialise, Leuven, Belgium). Further, a non-blocked endotracheal tube with an inner diameter of 3.0 mm was placed in the trachea according to clinical guidelines. To respect further generations of the bronchial tree beyond those that are directly segmentable from the MR images, a recursive tree growing algorithm proposed for human adults [176, 328] has been adopted to mimic preterm infant anatomy. Tree growth started at the last fully segmentable airways and the next airway generation bifurcates relative to the direction given by the last segmentable airway. A tree was then grown by recursively splitting a parent airway into two daughters according to morphological length and diameter ratios reported in [216, 230]. Tree growth was terminated if a minimal airway length of $l_{\text{min}} = 0.36$ mm, or a minimal airway diameter of $d_{\text{min}} = 0.049$ mm were reached, if the maximum generation number of $n_{\text{max}} = 17$ was exceeded, or if an airway touched the segmented hull geometry of the lobes. The termination criteria for minimal length and diameter agreed to the values reported for terminal bronchioles in the preterm infant [230]. The resulting airway tree morphometry is visualised in Figure 7.1 and corresponds well to previously reported data for preterm infants at this age [230]. Also, the total number of $24,880$ generated terminal airways supplying the pulmonary acini is in line with reported values in literature [168]. The entire airway tree had a respiratory dead space of 2.2 ml kg^{-1} per kilogram body weight corresponding to previously reported clinical measurements of 2.51 ± 0.61 ml kg^{-1} [240].

The first seven generations including the endotracheal tube were modelled as a fully resolved three-dimensional domain with 128 outlets (see Figure 7.2). The geometry was meshed with

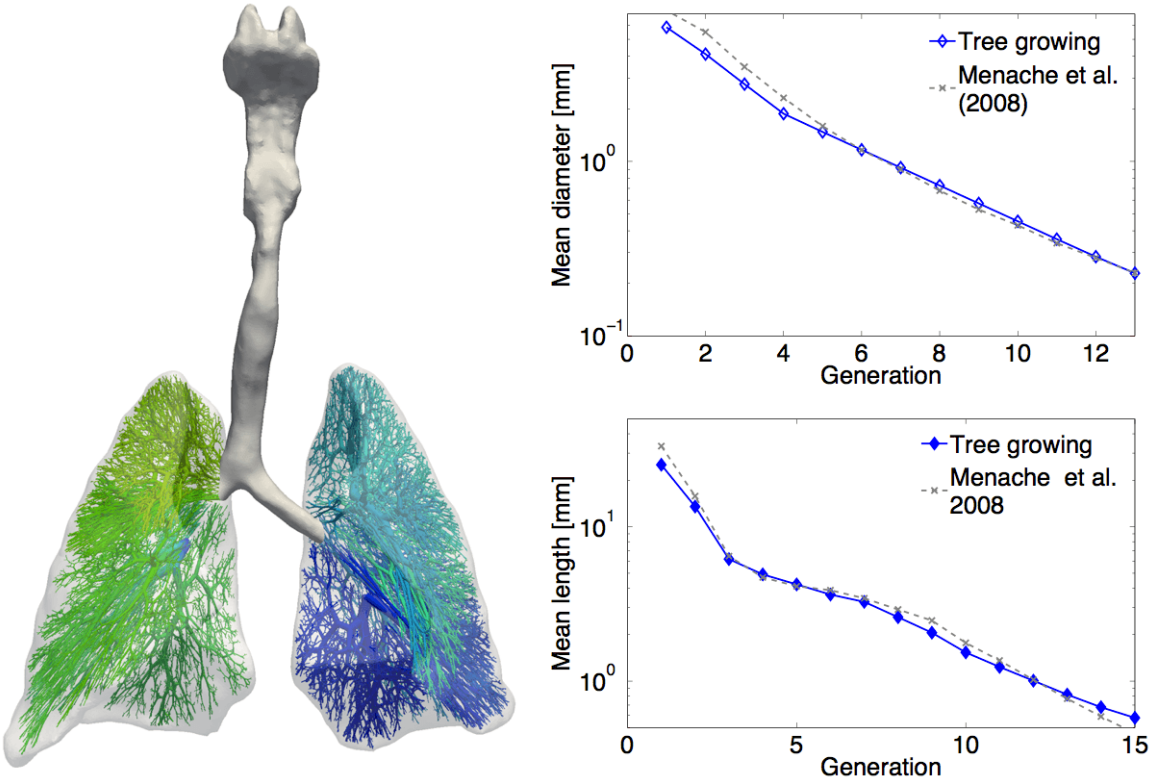

Figure 7.1.: Figure 7.1 (left) shows the segmented upper airways, parts of the lower airways and the hull geometry of the left and right lung marked in light grey. The coloured higher generations of the airway tree are generated using a tree-growing algorithm described above. Different colours refer to the single lung lobes of the preterm infant. The resulting mean lengths and diameters of the recursively grown airway tree correspond well to previously reported measurements as indicated in Figure 7.1 (right). Taken from [289] with permission.

a resolution of 0.01 mm using Gmsh (version 2.9.3; [125]) resulting in $5,109,584$ tetrahedral elements. This mesh resolution is approximately three times higher than in [26] and similar to the resolution provided in [60]. All airways located downstream to one of the 128 outlets in generation 8-16 were combined to an equivalent resistance R^i_{eq} that is computed from the arrangement of the single airways within the tree and their individual airway resistance $R^j = R_\mu + R_{\text{conv}}$. Individual airway resistance R^j is based on the model by van Ertbruggen et *al.* [93] and specified in Eq. (2.44). The dynamic viscosity $\mu^{\text{F}} = 2.04 \cdot 10^{-5}$ kg m^{-1} s^{-1}, the density of air $\rho^{\text{F}} = 1.27$ kg m^{-3} are physical flow quantities. The generation-dependent prefactor γ is taken from [93] and given in Table 2.1. It is noted that the resistance model in [93] is only valid during inspiration and generally airway compliance would have to be considered e.g., as proposed in [285]. However, during HFOV, the pressure variations are so small that no significant changes of the airway diameter occur and the model reported in [93] remains valid for both inspiration and expiration.

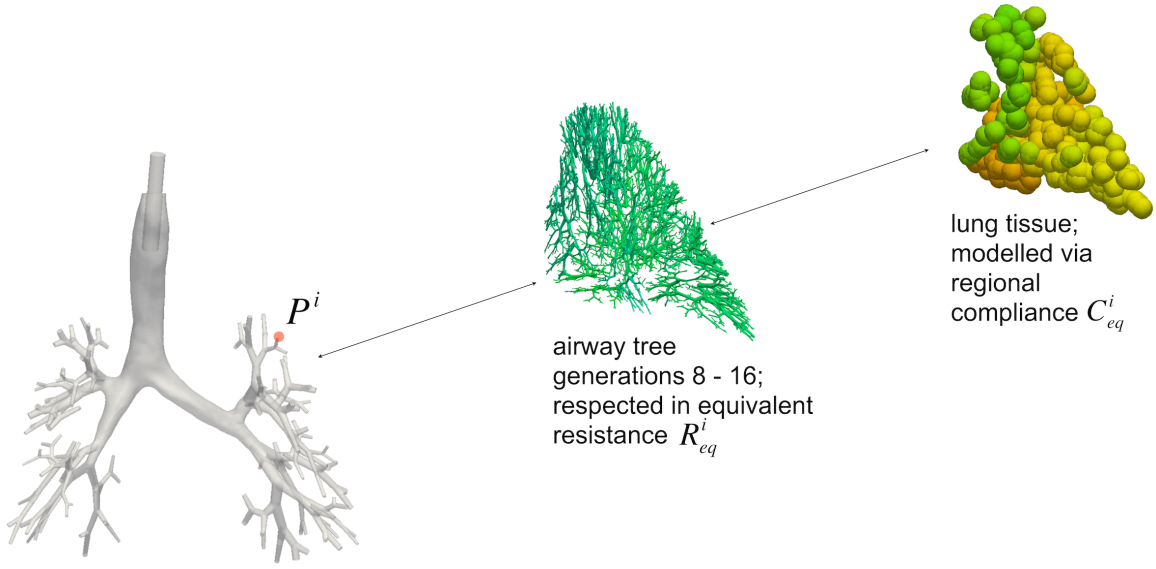

Figure 7.2.: Fully resolved bronchial tree of the first seven generations with 128 outlets (left). Starting at one exemplary outlet (marked in red), the associated further downstream generations (8-16) are visualised in green (mid). The resistance of the airway generations 8-16 at this outlet is respected via their equivalent resistance R^i_{eq}. The compliance C^i_{eq} of the lung region corresponding to the exemplary (red) outlet is obtained from Eq. (7.2) and the average pixel grey value of the MR image in this location. Taken from [289] with permission.

Similar to the resistance of an individual airway, an equivalent resistance of the larynx/pharynx with the placed endotracheal tube is computed. Thereto, the cross-sectional area of the leak between the pharynx and the tube is extracted from the imaging data. The resulting resistance $R^{\text{tl}}_{\text{eq}} = 100\ \text{cmH}_2\text{O}\,\text{l}^{-1}\,\text{s}$ is attached to the three-dimensional flow model at the cut upper end of the trachea (see Figure 7.2) to respect tube leakage in the preterm infant.

Each of the 128 tree outlets defined above supplies one region of lung tissue with an approximate diameter of 10 mm. For each part, a regional compliance C^i_{eq} is computed to represent the mechanics of lung tissue. Regional compliance is assumed to be constant due to (i) sufficiently small pressure variations in HFOV (in the current case approximately $\pm 2.5\ \text{cmH}_2\text{O}$), and (ii) the CPAP which ensures that the lung is kept within the linear part of the pressure-volume curve. Following the derivation by Ma and Bates [211], the measured total compliance of the respiratory system C_{rs} (see Section 7.2.1) is equally distributed to

$$C^*_{\text{eq}} = \frac{1}{N} C_{\text{rs}}, \tag{7.1}$$

where N denotes the number of lung regions, i.e., in the current case $N = 128$. To additionally account for the variation in regional compliance caused by the Bronchopulmonary Dysplasia (BPD), a prefactor c is introduced depending on the average pixel grey value of each tissue region in the MR image. Grey values in the MR image of the preterm infants lung range from 0 to 695. This variation is transferred towards a variation of regional compliances from 0.13

to 0.26 ml kPa^{-1} (i.e., 30% variation from the mean value $C^*_{\text{eq}} = 0.1847$ ml kPa^{-1}). With this prefactor, Eq. (7.1) reads

$$C^i_{\text{eq}} = c \cdot C^*_{\text{eq}} \tag{7.2}$$

and the regional compliance can be computed. Finally, at each of the 128 outlets of the fully resolved bronchial tree the regional resistance and compliance of the further downstream regions are respected via the *0D/3D* model equation Eq. (3.17) reading locally

$$P^i = R^i_{\text{eq}} \cdot Q^i + \frac{\Delta V^i}{C^i_{\text{eq}}}, \tag{7.3}$$

where the superscript i denotes the single regions and the volume change ΔV^i results from integration of the flow Q^i into this region over time. Using this formulation, (i) the correct dynamic pressure at each of the outlets can be computed and (ii) the volume of air entering the single tissue regions can be stored for consistent modelling of expiration based on the real mechanics of the lung.

7.2.4. HFOV settings

To drive HFOV in the model, first, a CPAP of 8 cmH_2O is prescribed at the proximal end of the endotracheal tube constant in time. Further, a flow rate is superimposed in time during the inflow phase with a frequency of $f = 10$ Hz, a tidal volume of TV $= 2.0$ ml per kilo body weight of the preterm infant and an inspiratory/expiratory ratio of $I : E = 1 : 2$. It is emphasised that there is no flow rate prescribed during the expiration phase and flow is allowed to freely develop depending on regional lung mechanics and the applied CPAP. According to clinical guidelines, a volume fraction of inspired oxygen of $FiO_2 = 0.35$ is used for the current study in the preterm infant. The simulation is run for six cycles (i.e., 600 ms) with a temporal resolution of 0.01 ms to resolve all turbulence phenomena highly in space and time. Convergence of the fluid dynamical problem is achieved if the non-linear residual in each time step is smaller than 10^{-6}.

7.2.5. Governing equations for fluid and transport dynamics

Airflow in the fully resolved three-dimensional bronchial tree is governed by the incompressible Navier-Stokes Equations Eq. (2.1) and Eq. (2.2). The formulation does not account for FSI effects as pressure variations are so small during HFOV that no significant deformation of the tree is induced. In good approximation, air is seen as Newtonian fluid with a dynamic viscosity of $\mu^{\text{F}} = 2.04 \cdot 10^{-5}$kg m^{-1} s^{-1} and a density of $\rho^{\text{F}} = 1.27$ kg m^{-3} as mentioned above. For a detailed description of the *0D/3D* model, the reader is referred to Section 3.2.2.

Gas transport in the model is governed by the convection-diffusion equation for a scalar concentration field Φ - in this case the concentration of oxygen. The equation is given as Eq. (2.112) and the diffusion coefficient for oxygen in air is $D = 0.219$ cm^2 s^{-1}.

Both equations are solved via stabilised finite elements [133, 172] in BACI [353], which has been used successfully in several biomedical flow and transport applications [72, 134, 371]. Airflow velocity and scalar transport are one-way coupled, which means that the flow solution influences the solution of scalar transport but not vice versa, which is reasonable in the present

case of convective-diffusive scalar transport [71, 371]. It is further important that all Neumann boundary terms are included in the weak finite element formulation of the fluid dynamics equations, following the formulation in [134]. Otherwise, a mathematically incomplete formulation would introduce flow instabilities during the expiration phase when no (unphysiological) flow velocity is prescribed at the inlet and expiratory flow is rather driven by the elastic recoil of the lung (see also Section 2.1.1).

7.2.6. Validation setup

For validation of the computational methods derived in this chapter, an example from literature is chosen for which an analytic reference solution is available. Following the example by Choi et *al*. [60] a straight three-dimensional tube with a radius of $a = 4.6$ mm and a length of $10a$ is created. The tube is meshed with hexahedral elements specifying a spatial resolution of 0.30 mm.

In order to set up a case where an analytical solution is available, oscillatory flow with a single frequency is simulated. Therefore, the inlet of the tube (i.e., the left cross-sectional area) is subjected to an oscillatory inflow velocity u_a in axial direction according to the analytical Womersley solution reading

$$u_a(r,t) = Re\left\{\frac{U_0}{\rho^{\mathrm{F}}}\frac{1}{i\omega}\left(1 - \frac{J_0\left(\alpha \cdot r/a \cdot i^{3/2}\right)}{J_0\left(\alpha \cdot i^{3/2}\right)}\right)e^{i\omega t}\right\}. \tag{7.4}$$

Here, U_0 denotes the amplitude and $\omega = 2\pi/T$ the angular frequency of the harmonic velocity oscillation with the period T. The variable α denotes the Womersley number defined as $\alpha = a\sqrt{\omega/\nu}$, r the radial coordinate in the tube with $-a \leq r \leq a$, i the imaginary unit and J_0 the 0-th Bessel function of the first kind. Being a physical quantity, only the real part of the velocity is used indicated by the formulation $Re\{\cdot\}$ in Eq. (7.4). In accordance with [60], a Womersley number of $\alpha = 7$ and velocity amplitude of $U_0 = 0.1848$ m s^{-1} (Reynolds number $\mathrm{Re} = U_0 \cdot 2a/\nu = 100$) is used. At the outflow (i.e., the right cross-sectional area) a zero-pressure boundary condition is applied.

As airways can be approximated as almost straight compliant tubes in a first sense, this benchmark setup is deemed suitable to quantify the accuracy of the used computational fluid dynamics methods for high-frequency oscillatory pulmonary flows.

7.3. Results

7.3.1. Model validation

Figure 7.3 shows the results of fluid flow for the validation setup described in Section 7.2.6. In Figure 7.3 (top), the velocity profile is visualised over a complete oscillation cycle. The profile is constant throughout the axial direction of the tube and the different visualised cross sections refer to different points in time of the oscillation cycle. In Figure 7.3 (bottom), the velocity profile computed in this study is compared to the results reported by Choi et *al.* [60]. It becomes visible that both solutions agree well and that the Womersley solution inside the straight tube is propagated correctly from the inflow throughout the domain both in the inspiratory phase

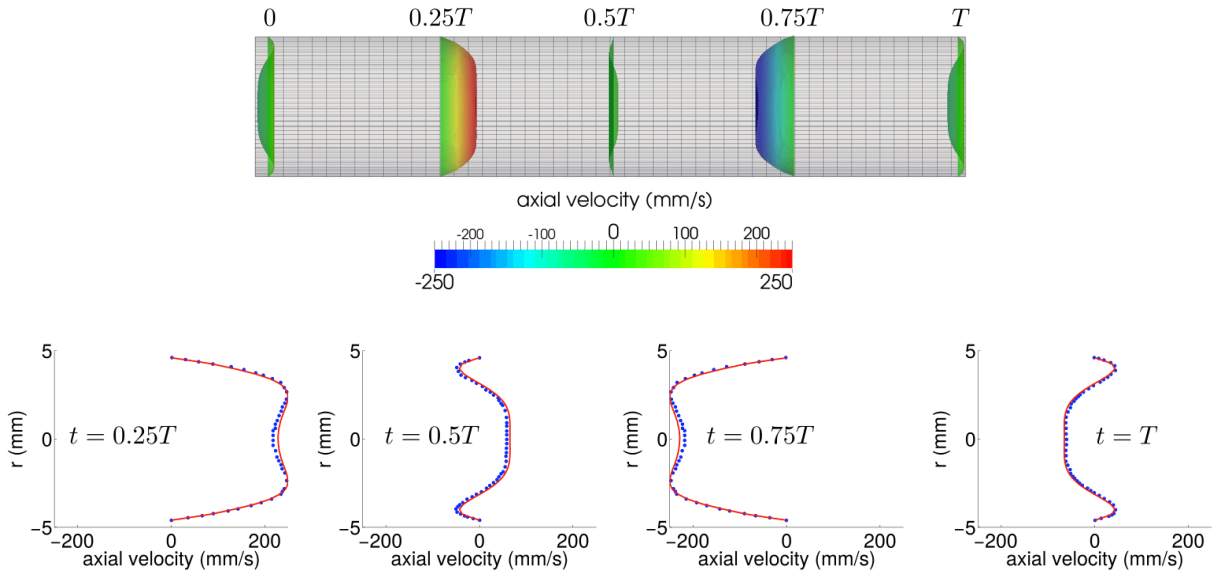

Figure 7.3.: Verification setup consisting of a straight tube with an imposed Womersley profile ($\alpha = 7$, Re $= 100$) at the inlet (left). Figure 7.3 (top) shows axial velocity profiles throughout the tube at different points in time. Figure 7.3 (bottom) compares velocity profiles computed in this study (solid red line) with the reference solution by Choi et *al.* [60] (blue dotted line). Taken from [289] with permission.

($0 \leq t \leq 0.5 \cdot T$; first two profiles) and the expiratory phase ($0.5 \cdot T \leq t \leq T$; last two profiles). At the points of flow reversal ($t \approx 0$, $t \approx 0.5 \cdot T$ and $t \approx T$), backflow (i.e., negative velocities at positive net flow) is correctly represented. The high accuracy of the solution indicates that the methods presented in this work are suitable for the investigation of HFOV dynamics as they can reproduce the reference solution for this generic scenario.

It is further annotated that the transport dynamics incorporated in the presented computational lung model have been validated previously in several setups in [371].

7.3.2. Equilibrium state conditions in HFOV

The lung model of the preterm infant developed in Section 7.2.3 is computed for the HFOV settings described in Section 7.2.4 and reveals several important effects that are also observed in clinical monitoring. Flow monitoring at the proximal end of the endotracheal tube (see point (a) in Figure 7.2) is visualised in Figure 7.4 (top) over six breathing cycles. Flow during the inspiration phase is sinusoidal as prescribed by the HFOV flow curve (see Section 7.2.4). However, in the outflow phase, when no explicit flow values are prescribed and air can stream out freely against the applied CPAP, flow is not sinusoidal but shows increased values at the beginning and decay towards the end of the expiration phase. Further, there is still a small outflow detected before the next forced inflow breath starts (see e.g., $t = 100$ ms).

Integrating this flow curve in time yields the volume curve visualised in Figure 7.4 (bottom). This curve indicates that during the first three breaths, absolute lung volume still increases and

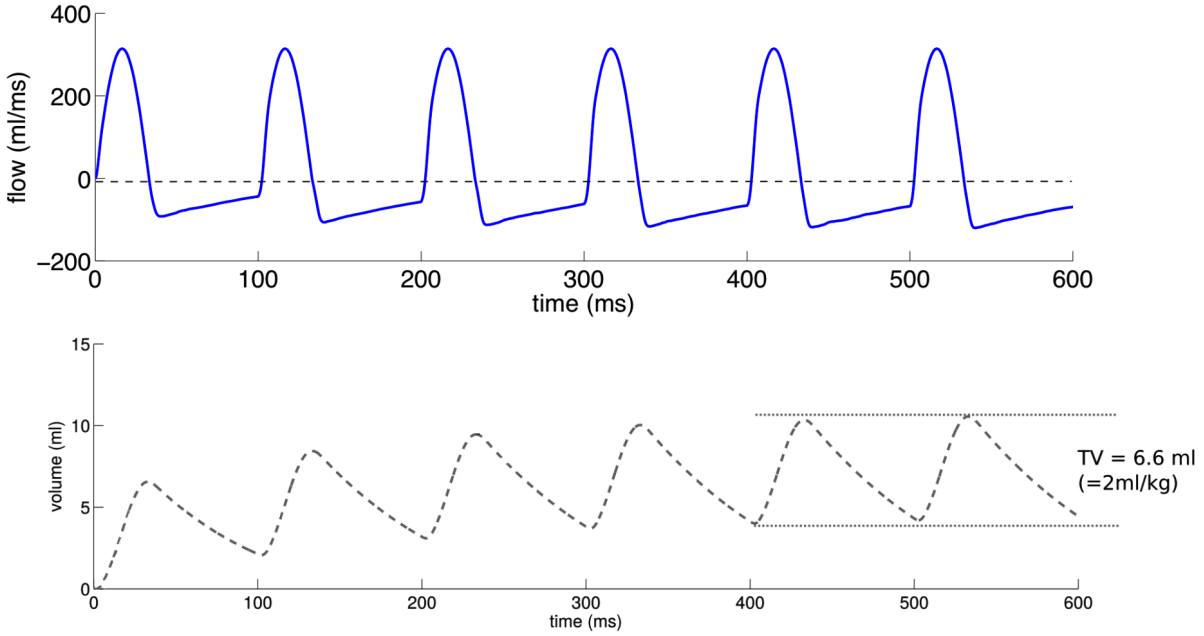

Figure 7.4.: Figure 7.4 (top) shows the monitored airflow at the proximal end of the endotracheal tube over six breathing cycles. During the inflow phase ($(n \cdot 100)$ ms $\leq t(n \cdot 100 + 33)$ ms), the prescribed sinusoidal flow is correctly represented. During the outflow phase ($(n \cdot 100 + 33)$ ms $\leq t((n+1) \cdot 100)$ ms) flow is non-sinusoidal and determined by the mechanics of the lung. Figure 7.4 (bottom) shows the volume curve resulting from integration of the flow curve over time. Lung volume increases during the first four breaths ($t \leq 400$ ms) due to a tube leakage of 16% and remains almost constant afterwards indicated by the two horizontal lines in the graph. Taken from [289] with permission.

that after the fourth breath, a dynamic equilibrium state between the mechanics of the respiratory system and the ventilator in HFOV mode is achieved. These start-up effects are also observed in clinical settings at the start of HFOV.

Finally, it can be observed that tube leakage generally reduces over-inflation of the lung as it allows airflow to pass by the endotracheal tube and to be exhaled via the gap between tube and trachea/larynx and pharynx. In the current case, a leakage of approximately 16% of the supplied tidal volume is observed in line with [215]. Therefore, tube leakage notably alters lung volume and has to be considered specifically in ventilating neonates/preterm infants. Generally, the global monitoring of simulated airflow and lung volume indicates that several cycles of HFOV have to be computed to eliminate start-up effects and to obtain a dynamic equilibrium state of ventilation which can be used for further investigations.

7.3.3. Gas exchange mechanisms

Observing the computation of HFOV at an equilibrium state after the fourth cycle, six particular flow and gas transport mechanisms are observed and visualised in Figure 7.5. Strikingly, these six mechanisms have been theoretically proposed in clinical literature [311] in similar shape and location. The single mechanisms will be described in detail in the following.

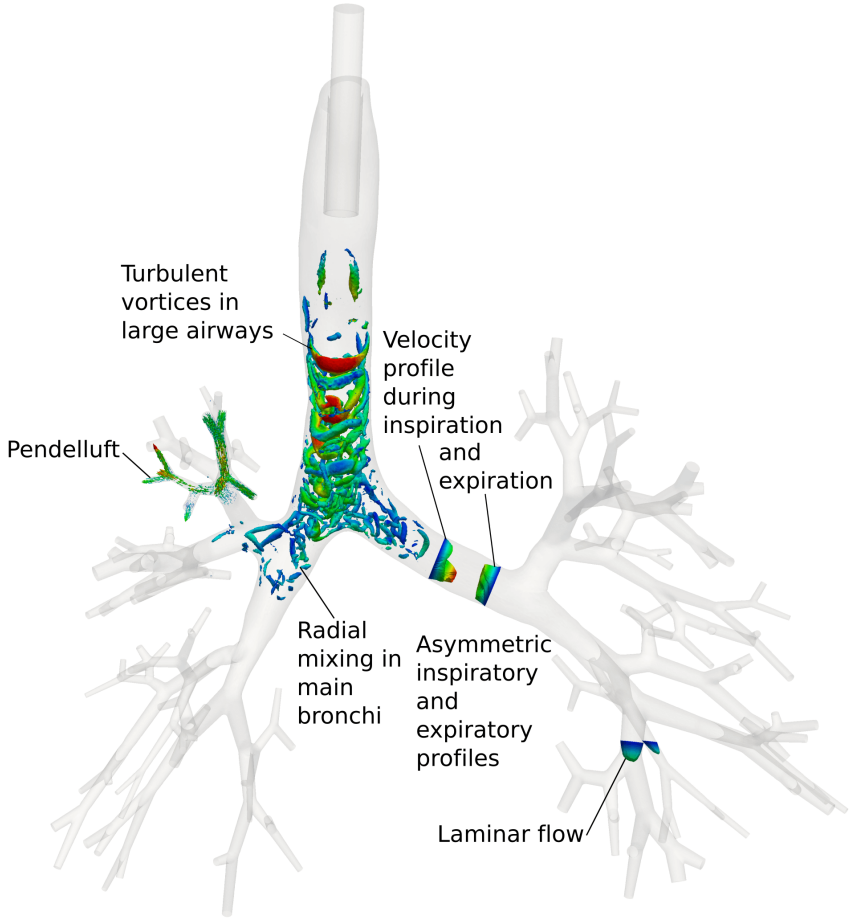

Figure 7.5.: Gas exchange mechanisms detected by the computational lung model and their location in the anatomy of the preterm infant. Taken from [289] with permission.

Turbulent vortices in large airways. One major aspect that is non-intuitive in HFOV is the fact that oxygen can be transferred towards the respiratory zone of the lung even though tidal volume is much smaller than airway tree (dead) volume. Here, turbulence plays the decisive role in transporting oxygen rapidly through the large airways especially throughout the trachea and main bronchi. To illustrate this, λ_2 iso-surfaces as a widely used criterion for turbulence are visualised in Figure 7.5. These surfaces show that during the inspiratory phase a vortex develops that allows oxygen to travel faster on the vortex surface than average flow speed of air. By this vortex, the dead volume in the major airways and especially of the trachea is easily overcome. The phenomenon of turbulence decays in higher generations and has almost vanished until the 5th to 6th

tree generation. Also, during the expiratory phase, no turbulence is observed in the large airways.

Asymmetric inspiratory/expiratory profiles. A further aspect on efficient gas transport observed in this study is the asymmetry between inspiratory and expiratory profiles. During the inspiration phase, the velocity profile shows elevated velocity values for oxygen-rich air in the lower part of the airway cross-section (see Figure 7.5). During the expiratory phase, the velocity profile indicates slightly higher values in the upper part of the cross-section and smaller values in the lower part. Due to this asymmetry, oxygen-rich air is transported faster in the lower part of the airway cross-section and low-oxygen air is rather conducted in the upper part of the cross-section. The airway then behaves as it would be subdivided by a thin membrane separating oxygen-rich and oxygen-poor air, but there is no membrane and the flow itself accounts for the separation. This subdivision forms a circulatory pattern in the main bronchi and ensures that not the same air that has just entered the bronchus is instantly transported out during the following expiration phase. Further, CO_2 is efficiently cleared during expiration through the upper part of the airway cross-section.

Laminar flow in higher generations. Laminar flow is observed in higher generations of the bronchial tree, mainly in those airways at a generation number higher than six. This means, flow is laminar at least one generation before the cut off point for full resolution in this model. Downstream of these regions, airflow is decelerated for optimal diffusive transport of oxygen from the air into the respiratory lung tissue. Therefore, this effect is no mechanism itself but rather an indication that flow becomes laminar in higher generation and secondary flow structures decay in higher generations. The respiratory zone recognises mainly diffusive phenomena and only the way down the bronchial tree is characterised by highly turbulent flows while classical laminar mixture and diffusion takes place in the higher generations of the lung. However, in contrast to conventional mechanical ventilation, these diffusive processes can take place at smaller pressure amplitudes throughout the entire bronchial tree and lung tissue.

Radial mixing in main bronchi. A prominent location where turbulent flow and radial mixing promote efficient gas exchange in HFOV is the right main bronchus. As visualised in Figure 7.5, the emerging turbulence introduces a secondary "stirring" motion into the fluid flow. This flow pattern leads to an efficient radial mixing of oxygen within the airflow introduced by the flow. One can imagine this as if a mixer would cause radial mixing of the airflow, however, there is no mixer necessary as the "stirring" motion is introduced by the fluid flow itself. During the expiratory phase, this radial mixing decays and ensures that CO_2 is removed efficiently from the main bronchus.

Pendelluft. As proposed by Greenblatt et *al.* [135], different compliances between healthy lung segments and those affected by BPD lead to regional differences in dynamic pressure and induce an airflow between these regions known as pendelluft. As visualised in Figure 7.6, one example location for such pendelluft flows in this preterm infant is the right superior lobe. The different regional compliances of lung tissue downstream of the outlets (a) to (e) lead to an airflow from regions (a) and (b) to the regions (c), (d), and (e) just before the end of the inspiration phase at $t = 32$ ms. Greenblatt et *al.* [135] suggest that pendelluft especially occurs in case of non-sinusoidal flows, as observed in this study, and that pendelluft 'may be an important phe-

nomena contributing to regional gas exchange, irreversible mixing [...] inside poorly ventilated regions of the lung" [135]. This supports current observations where pendelluft occurs in a less ventilated, BPD-affected region of the lung.

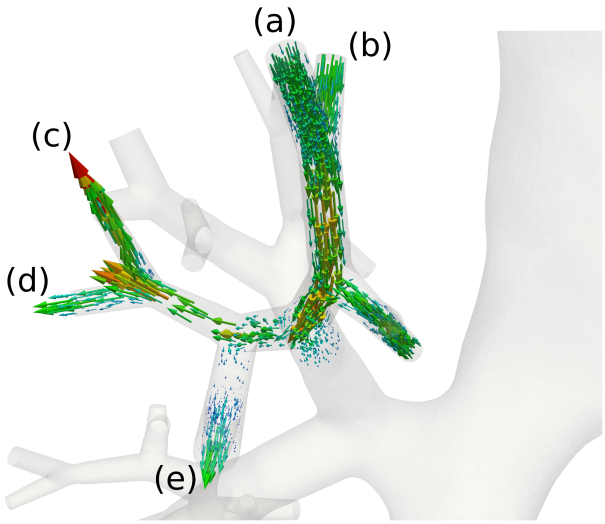

Figure 7.6.: Pendelluft flows occurring at five airway branches in the bronchial tree of the investigated preterm infant shortly before the end of the inspiration phase ($t = 32$ ms). The arrows represent airflow velocity and indicate a flow from the regions (a) and (b) into the regions (c), (d), and (e). Taken from [289] with permission.

Direct ventilation of close alveoli. So far, all mechanisms were focused on phenomena occurring in the airflow, however, no gas transport has been observed, yet. Now, Figure 7.7 shows the stream of fresh inflowing air at three points in time of the inhalation cycle. It can be seen that lung regions that are located close to the major airways become directly ventilated, especially in the right superior lobe, while other locations do not have direct contact with oxygen in the first breath. In these regions, oxygen is transported further downwards with the subsequent cycles of ventilation and is mixed in the outflow period by diffusive processes.

7.4. Discussion

The main finding of this work is that important gas exchange mechanisms proposed in clinical literature can actually be observed in the anatomy of the preterm infant under representative conditions of HFOV (TV $= 2$ ml kg^{-1}, $f = 10$ Hz). This observaton is not possible via measurements but using accurate computational modelling of respiratory mechanics based on medical imaging data and lung function measurements of the same patient and will be discussed in detail in the following.

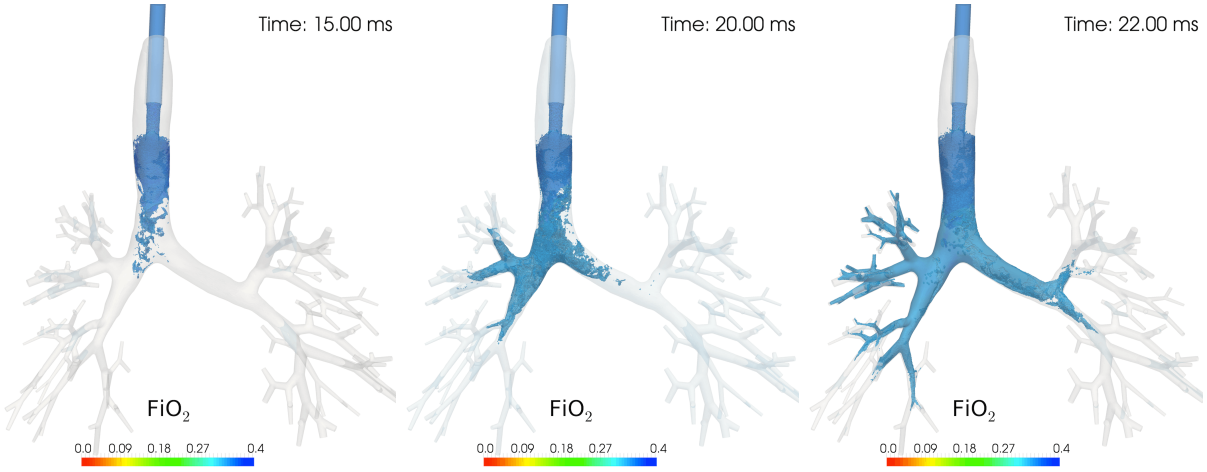

Figure 7.7.: Temporal evolution of oxygen transfer in a single HFOV cycle. The visualisation refers to the fourth ventilation cycle and annotated time starts at the beginning of the fourth cycle. The region marked in blue shows the fraction of inspired oxygen larger than 0.25 and is coloured according to the visualised scale. The distribution shows that regions close to the major airways (e.g., the right superior lobe) become directly ventilated while others such as the left inferior lobe become only ventilated within the next ventilation cycle with oxygen partly delivered throughout the tree in the current breath. It is noted that the effects of turbulence on oxygen transport can be clearly seen in Figure 7.7 (left) and of asymmetry in the inspiratory velocity profile in the left main bronchus in Figure 7.7 (middle). Taken from [289] with permission.

7.4.1. Model physiology

One important question to be asked for all investigations using experimental or computational models of HFOV is the quality of representing real physiology of the model. In this case, the computational lung model is derived from medical imaging and lung function test data of a preterm infant and therefore more accurate than generic or downscaled adult bronchial tree geometries. Further, it is the first model of HFOV that is able to model real exhalation based on the previously inspired lung volume and the mechanics of lung tissue. The feature of free exhalation against the applied CPAP requires additional inclusion of all Neumann boundary terms into the finite element formulation of the fluid problem. Without such a formulation, flow would become unstable during the exhalation phase following the argumentation in [134].

To respect the BPD of the patient, medium variations of regional compliance of up to 30% of the mean regional compliance are introduced into the model based on the regional grey value of the MR image. It is annotated that this is only one possibility to account for heterogeneous lung mechanics and that variations in regional compliance might be larger in BPD patients depending on the severity of the disease. In the presented approach the grey values are scaled in such a way that the difference between the lowest/highest grey value compared to the mean grey value lead to a difference in regional compliance of 30% compared to the averaged regional compliance.

These variations are sufficient to discover pendelluft phenomena in poorly ventilated regions of the tissue (see Section 3.3).

A final important point in the presented study is the inclusion of tube leakage for the first time in a patient-specific computational fluid dynamics model of HFOV in the preterm infant. As outlined above, tube leakage leads to a loss of approximately 16% of the supplied tidal volume which is in line with previously reported values in literature [215]. Therefore, tube leakage reduces over-inflation of the preterm infants lung - a phenomenon which is also observed clinically.

Together, these properties of the computational fluid dynamics model lead to an increase in lung volume during the first four breaths of HFOV. After this start-up time, a dynamic equilibrium in the flow and the gas transport is observed. This corresponds to real clinical behaviour, where respiratory response to the HFOV settings requires some small time in the preterm infant.

Incorporating all these aspects into the presented computational fluid dynamics model results in probably the most realistic approach for investigating HFOV in the preterm infant known today. Also, previous experimental settings, mainly using particle image velocimetry (PIV) [26], suffer from a lack of modelling (i) real exhalation, (ii) realistic incorporation of smaller airways and lung tissue, as well as (iii) the tube leakage in real infantile anatomy. Therefore, the model presented in this chapter is physiologically more realistic than the previously described experimental setups.

7.4.2. Additional insight into pulmonary physiology

This study confirms six convective and convective-diffusive gas transport mechanisms that have been proposed for ventilation of a preterm infant in HFOV mode [311]. Further, the exact location of the single phenomena, namely (i) turbulence; (ii) asymmetric inspiratory/expiratory velocity profiles; (iii) laminar flow and radial mixing; (iv) turbulent flow and radial mixing; (v) pendelluft and (vi) direct ventilation of proximal regions of the lung, are detected and strikingly match descriptions that were assumed theoretically. Each mechanism takes place at its specific location and time in the breathing cycle to optimally supply oxygen to the respiratory region and to efficiently clear CO_2 from the infantile lung.

The quality of the computed results significantly advances insight into pulmonary physiology during ventilation with high frequency. Now, knowledge on HFOV is no longer solely based on measurements from clinical studies, but also the underlying physics of airflow, convective, and convective-diffusive transport have been revealed. The discovered mechanisms have been unconfirmed for almost three decades and only been hypothesised theoretically by experts in the field of HFOV [311]. Further, no measurements have been possible inside the lung to detect specific vortex structures and flow patterns that ultimately make HFOV so efficient in neonates. Therefore, computational modelling is a valuable tool to increase understanding in highly relevant respiratory care.

The detailed knowledge about the underlying gas transport mechanisms is, however, only a first step in advancing respiratory therapy. The understanding of single phenomena and their development under certain physiological conditions might allow to specifically trigger certain effects for improved oxygen transport and CO_2 clearance. In this respect, computational modelling might be able to advance respiratory therapy by computing several parameter settings of HFOV. If e.g., improvement of gas transport at a certain frequency or CPAP is observed *in silico*,

equivalent parameters may be used in reality. For such computer-assisted treatment, rigorous validation in retrospective studies (see Chapter 6) is, however, indispensable.

Further work in this context might also be related to the question whether these mechanisms also exist in the adult, and if yes, under which conditions. Current computational models of HFOV have only observed adult patients and downscaled adult geometries. However, a child is not a downscaled adult, but shows different anatomy and morphometry of the lung. Therefore, dimensionless flow quantities such as the Reynolds and Womersley number are different in the child and might support the success of HFOV in neonates while it has not been beneficial in adult patients [95].

7.4.3. Limitations

The observations in this chapter are limited in a few clinical and methodological aspects that are worth mentioning. First, the medical imaging data used in this chapter are obtained from a preterm infant at the age of 3 months and might underestimate the flow situation in an extremely preterm neonate that is subjected to HFOV. Further, usually no MRI scan is available for a neonate in the first few hours. The only imaging data available at this early stage are X-ray images due to ethical concerns and interference with other necessary life-saving treatment. Therefore, one future goal in bringing the presented methods into clinical practice is, if possible, the build-up of a generic lung model for a neonatal subgroup where imaging is available for other diagnostic reasons. This generic model can then be personalised with available X-ray images of the current neonate using e.g., the basic methods of image registration [218, 337] and be used for optimising ventilation according to the principles of this work.

Further, in the current approach, oxygen is assumed to be fully lost if it leaves the outlet after the 7th generation of the bronchial tree. This aspect makes the model a conservative estimation of real gas exchange, as oxygen would be partly stored in the lower airways and could re-enter the domain in the next breath from the outlets for mixture with further oxygen-rich air.

Finally, this chapter is limited to the observation of convective and convective-diffusive mechanisms, which comprises six out of eight phenomena proposed in the article by Slutsky and Drazen [311]. The remaining two mechanisms might be detectable in combination with detailed models of the respiratory zone. Filoche et *al.* [96] and Hofemeier et *al.* [162] have provided important steps towards tracking diffusion processes in lung tissue which can be adopted to study the remaining diffusion and collateral ventilation on the alveolar scale. However, as the majority of gas transport phenomena proposed in [311] are conditional to efficient convective and convective-diffusive transport, this work is restricted to these effects.

7.5. Conclusion

In this chapter, evidence is submitted for six efficient mechanisms of gas exchange during high-frequency oscillatory ventilation (HFOV), namely: (i) turbulence; (ii) asymmetric inspiratory/expiratory velocity profiles; (iii) laminar flow and radial mixing; (iv) turbulent flow and radial mixing; (v) pendelluft and (vi) direct ventilation of proximal regions of the lung. Limitations on measurements and sequential medical imaging especially in the preterm infant are overcome via using an advanced computational lung model based on anatomy and physiology

of the infantile lung. The model is verified against available literature data and for the first time localises six mechanisms of gas exchange that have been proposed in clinical literature. This detailed insight into HFOV promotes a better understanding of this successful ventilation technique in theory and provides a further step towards its optimisation via targeting single mechanisms in individual patients. Finally, deeper understanding is the basis of optimal ventilatory assistance to the immature and vulnerable lung during its first breaths in life.

8. Summary and Outlook

In this work, computational modelling in respiratory biomechanics has made a further step towards clinical applicability providing methods with high physiological relevance and thorough validation against patient measurements.

In Part I, the state of the art in modelling respiratory mechanics is summarised in a way that gives an unbiased overview over available models of the entire respiratory system or parts thereof. This overview should guide a reader, new to this field, towards the best approach for a given clinical or research question.

Further, it has been revealed that physically based modelling approaches are more powerful and predictive than pure fitting of parameters to clinical measurements or observation of medical imaging data. Especially, the interaction between airflow dynamics and lung tissue mechanics has been identified as essential component for realistic description of lung behaviour during respiration. Based on this knowledge, modelling approaches, partly reported previously, have been extended towards four novel coupled models in respiratory biomechanics. Coupled models are (i) based on the underlying physics of airflow dynamics and lung tissue mechanics, and (ii) able to tackle the interaction between these two physical fields. The four approaches consist of fully resolved and dimensionally reduced descriptions of airflow dynamics and lung tissue mechanics and are equipped with all necessary properties to simulate lung behaviour in a physiologically extremely realistic manner. They further contain the first pure reduced-dimensional method that includes lung interdependence, parenchymal tethering and the dynamics of recruitment/derecruitment validated against published data. From this complexity it has become apparent that there cannot be one approach in modelling respiratory biomechanics, but a variety of different concepts to solve the current problem at hand. Introducing these concepts along with recommendations for adequate usage has been the core of Part I in this work.

In Part II of this work, three patient-specific examples have been presented, representative for important clinical scenarios in respiratory care to evaluate the applicability of the proposed methods in a clinical setting.

Fully resolved modelling, supported by a variety of medical imaging data, gives a deep insight into pulmonary airflow and lung tissue inflation both during active breathing and mechanical ventilation. Conducted investigations show, how active breathing is triggered by the movement of the respiratory muscles and the diaphragm, and how regional inflation occurs in reaction to this motion. The computed results provide additional information to available medical imaging and can transfer knowledge to situations where less imaging data are available. Further, the fully resolved models provide an important reference solution for dimensionally reduced models.

Extensive thoughts on rigorous validation of computed results, especially in terms of regional tissue aeration have also been given. Limitations in terms of radiation and patient transport preclude the usage of computed tomography (CT) and pave the way for using a novel imaging modality, namely electrical impedance tomography (EIT). As EIT measures tissue bioimpedance rather than ventilation directly, a quantitative link between regional air content and lung tissue

bioimpedance has been derived based on the exact microstructure of the lung. The obtained relationship is linear in the physiologically relevant range and in line with available experimental data. This correlation between computed lung tissue aeration and regional bioimpedance now enables regional validation of computed quantities with EIT measurements.

Using this knowledge, an efficient and reliable reduced-dimensional lung model has been personalised for an ARDS patient and validated via EIT measurements. Conducted investigations show that availability of a single CT scan and airway pressure and flow monitoring during a single breath is sufficient to personalise a lung model that is suitable for clinical prediction. Additionally, a novel "virtual EIT" module mimics the EIT imaging process and delivers data for rigorous validation of the model. Good agreement between computationally predicted and actually measured data prepare the first steps from this pilot study towards larger clinical trials.

Finally, previous knowledge in modelling respiratory biomechanics is transferred towards a case where no detailed insight has been available, yet. High-frequency oscillatory ventilation (HFOV) is by far the most popular method in ventilating neonates. However, detailed understanding in involved gas transport mechanisms has been lacking for approximately 30 years. In this work, computational lung modelling has provided an insight that would never have been possible on the basis of measurements in such vulnerable lungs. Clinically hypothesised gas transport mechanisms are confirmed and for the first time localised in the bronchial tree of the preterm infant. These mechanisms help to understand why HFOV is so successful especially in the preterm infant.

Even though this work has provided important further insight into respiratory modelling in general and into specific applications in more detail, several directions can be sketched for further application and clinical validation of the models derived in this work. It is noted that the number of patients ($n = 3$) in this work is still low and that there may be numerous phenomena in respiratory biomechanics that are not yet captured.

To begin with, the reduced-dimensional models are still lacking an individualised mechanical representation of the thorax. A detailed representation of the thoracic wall is, however, a necessity in two aspects. First, the mechanical properties of the thorax are crucial as they determine pleural pressure and consequently transpulmonary and trans-alveolar pressures. Second an exact thorax geometry of a patient and specification of bioimpedances for anatomical details are superior to homogeneous background conductivities in both solving the EIT forward problem and for EIT image reconstruction. Therefore individualisation of the thorax geometry is an important aspect for further work in close validation with esophageal pressure measurements and EIT imaging.

Equally important, the current realisation of recruitment/derecruitment dynamics has not yet been applied in a patient-specific setting as none of the available patients has shown recruitment while being ventilated. Therefore, the model presented in Chapter 6 may be applied to a case where a patient exhibits significant recruitment behaviour. Additionally, EIT-based validation should be performed for such a case to confirm that the model is able to predict the clinically important phenomena of recruitment/derecruitment in a patient-specific setting.

Finally, to increase trust in the proposed modelling and virtual monitoring techniques their validation with actual measurements in a small retrospective clinical study is proposed. A retrospective analysis might answer the question how good the respiratory model can actually predict patient behaviour in a larger study cohort without any involved risk in clinical care. In such a study, potential sources of disagreement between model an reality can be identified and outline

further perspectives on continuous model development in respiratory biomechanics. So far, this work provides an important step towards patient-specific computationally predicted protective mechanical ventilation and serves as a basis for further optimisation of treatment strategies *in silico* hopefully improving long-term outcome.

A. Mathematical derivation of the *0D* fluid dynamics equations

A.1. Derivation from *1D* fluid dynamics equations

In this appendix, the derivation of the *0D* flow model starting from the well-known *1D* formulation (see e.g., [101, 305, 306]) is performed. This includes all mathematical details that are required to follow the single steps for integration of the fluid velocity in axial direction. Integrating the continuity equation Eq. (2.20) (e.g., from [101, 305, 306]) in axial direction reads

$$\begin{aligned}
&\int_{x_1}^{x_2} \left(\frac{\partial A}{\partial t} + \frac{\partial Q}{\partial x} \right) dx = 0 \\
\Rightarrow &\int_{x_1}^{x_2} \frac{\partial A}{\partial t} dx + \int_{x_1}^{x_2} \frac{\partial Q}{\partial x} dx = 0 \\
\Rightarrow &\, l \frac{\partial}{\partial t} \left(\frac{1}{l} \int_{x_1}^{x_2} A dx \right) + Q \Big|_{x_1}^{x_2} = 0 \\
\Rightarrow &\, l \frac{d\hat{A}}{dt} + Q(x_2, t) - Q(x_1, t) = 0.
\end{aligned} \tag{A.1}$$

Integrating the momentum equation Eq. (2.21) yields

$$\begin{aligned}
&\int_{x_1}^{x_2} \left(\frac{\partial Q}{\partial t} + \frac{\partial}{\partial x} \left(\alpha \frac{Q^2}{A} \right) + \frac{A}{\rho} \left(\frac{\partial p}{\partial x} \right) + K_{\mathrm{R}} \frac{Q}{A} \right) dx = 0 \\
\Rightarrow &\int_{x_1}^{x_2} \frac{\partial Q}{\partial t} dx + \int_{x_1}^{x_2} \frac{\partial}{\partial x} \left(\alpha \frac{Q^2}{A} \right) dx + \int_{x_1}^{x_2} \frac{A}{\rho} \left(\frac{\partial p}{\partial x} \right) dx + \int_{x_1}^{x_2} K_{\mathrm{R}} \frac{Q}{A} dx = 0 \\
\Rightarrow &\, l \frac{\partial}{\partial t} \left(\frac{1}{l} \int_{x_1}^{x_2} Q dx \right) + \frac{\alpha}{A} Q^2 \Big|_{x_1}^{x_2} + \frac{A}{\rho} p \Big|_{x_1}^{x_2} + \frac{K_R l}{A} \frac{1}{l} \int_{x_1}^{x_2} Q dx = 0 \\
\Rightarrow &\, l \frac{d\hat{Q}}{dt} + \frac{\alpha}{A} \left(Q^2(x_2) - Q^2(x_1) \right) + \frac{A}{\rho} \left(p(x_2) - p(x_1) \right) + \frac{K_R l}{A} \hat{Q} = 0 \\
\Rightarrow &\, l \frac{d\hat{Q}}{dt} + \frac{\alpha}{A} \left(Q(x_2) - Q(x_1) \right) \left(Q(x_2) + Q(x_1) \right) + \frac{A}{\rho} \left(p(x_2) - p(x_1) \right) + \frac{K_R l}{A} \hat{Q} = 0
\end{aligned}$$

with the assumption that $Q(x_2) + Q(x_1) = 2Q(x_2)$

$$\begin{aligned}
\Rightarrow &\underbrace{\frac{\rho l}{A}}_{I} \frac{d\hat{Q}}{dt} + \underbrace{\frac{2\alpha\rho}{A^2} \left(Q(x_2) - Q(x_1) \right)}_{R_{\mathrm{conv}}} Q(x_2) + p(x_2) - p(x_1) + \underbrace{\frac{K_R l \rho}{A^2}}_{R_\mu} \hat{Q} = 0 \\
\Rightarrow &\, I \frac{d\hat{Q}}{dt} + R_{\mathrm{conv}} Q(x_2) + p(x_2) - p(x_1) + R_\mu \hat{Q} = 0.
\end{aligned} \tag{A.2}$$

Integrating the wall mechanics equation Eq. (2.22) finally reads

$$\begin{aligned}
&\int_{x_1}^{x_2} \frac{\partial p}{\partial t} dx = \int_{x_1}^{x_2} \frac{\partial}{\partial t} \left(p_{\text{ext}} + \beta_{\text{w}}(\sqrt{A} - \sqrt{A_0}) + \frac{\gamma_{\text{w}}}{A\sqrt{A}} \frac{\partial A}{\partial t} \right) \\
\Rightarrow &\int_{x_1}^{x_2} \frac{\partial p}{\partial t} dx = \int_{x_1}^{x_2} \frac{\partial p_{\text{ext}}}{\partial t} dx + \int_{x_1}^{x_2} \frac{\partial}{\partial t} \left(\beta_{\text{w}}(\sqrt{A} - \sqrt{A_0}) \right) dx + \int_{x_1}^{x_2} \frac{\partial}{\partial t} \left(\frac{\gamma_{\text{w}}}{A\sqrt{A}} \frac{\partial A}{\partial t} \right) dx \\
&\Rightarrow \frac{d\hat{p}}{dt} = \frac{d\hat{p}_{\text{ext}}}{dt} + \frac{\beta_{\text{w}}}{2\sqrt{A}} \frac{d\hat{A}}{dt} + \frac{\gamma_{\text{w}}}{A\sqrt{A}} \frac{d}{dt} \left(\frac{d\hat{A}}{dt} \right)
\end{aligned}$$

Including the integrated form of the continuity equation Eq (2.32) in rearranged from

$$\begin{aligned}
l\frac{d\hat{A}}{dt} + Q(x_2, t) - Q(x_1, t) &= 0 \\
\Leftrightarrow \frac{d\hat{A}}{dt} &= \frac{1}{l} \left(Q(x_1, t) - Q(x_2, t) \right)
\end{aligned}$$

the term $\frac{d\hat{A}}{dt}$ can be replaced which leads to

$$\begin{aligned}
&\frac{d\hat{p}}{dt} = \frac{d\hat{p}_{\text{ext}}}{dt} + \frac{\beta_{\text{w}}}{2\sqrt{Al}} \left(Q(x_1) - Q(x_2) \right) + \frac{\gamma_{\text{w}}}{A\sqrt{Al}} \frac{d}{dt} \left((Q(x_1) - Q(x_2)) \right) \\
\Rightarrow &\frac{2\sqrt{Al}}{\beta_{\text{w}}} \frac{d\hat{p}}{dt} = \frac{2\sqrt{Al}}{\beta_{\text{w}}} \frac{d\hat{p}_{\text{ext}}}{dt} + Q(x_1) - Q(x_2) + \frac{2\sqrt{Al}}{\beta_{\text{w}}} \frac{\gamma_{\text{w}}}{A\sqrt{Al}} \left(\frac{dQ(x_1)}{dt} - \frac{dQ(x_2)}{dt} \right) \\
\Rightarrow &\underbrace{\frac{2\sqrt{Al}}{\beta_{\text{w}}}}_{C} \left(\frac{d\hat{p}}{dt} - \frac{d\hat{p}_{\text{ext}}}{dt} \right) + Q(x_2) - Q(x_1) + \underbrace{\frac{2\sqrt{Al}}{\beta_{\text{w}}}}_{C} \underbrace{\frac{\gamma_{\text{w}}}{A\sqrt{Al}}}_{R_{\text{visc}}} \left(\frac{dQ(x_2)}{dt} - \frac{dQ(x_1)}{dt} \right) = 0
\end{aligned} \tag{A.3}$$

A.2. Linearisation of the *0D* fluid equations

This derivation is partly based on the work in [177] and recalled here for completeness. Discretisation of Eq. (2.47) and Eq. (2.48) in time using a backward Euler scheme results in

$$\begin{aligned}
&C\frac{\left(P_1^{n+1} - P_1^n\right)}{\Delta t} - C\frac{\left(P_{\text{ext}}^{n+1} - P_{\text{ext}}^n\right)}{\Delta t} + Q_2^{n+1} - Q_1^n + \\
&\quad + C \cdot R_{\text{visc}} \frac{\left(Q_2^{n+1} - Q_2^n\right)}{\Delta t} - C \cdot R_{\text{visc}} \frac{\left(Q_1^{n+1} - Q_1^n\right)}{\Delta t} = 0, \qquad \text{(A.4)} \\
&I\frac{Q_2^{n+1} - Q_2^n}{\Delta t} + (R_\mu + R_{\text{conv}}) \cdot Q_2^{n+1} + P_2^{n+1} - P_1^{n+1} = 0. \qquad \text{(A.5)}
\end{aligned}$$

where the superscript $n+1$ denotes the current and n the previous step and Δt the time step. Reformulation in matrix notation the leads to the following airway element matrix

$$\begin{bmatrix} -\frac{1}{K_{\text{I}}} - \frac{C}{K_{\text{vis}}} & \frac{1}{K_{\text{I}}} \\ \frac{1}{K_{\text{I}}} & -\frac{1}{K_{\text{I}}} \end{bmatrix} \begin{bmatrix} P_1^{n+1} \\ P_2^{n+1} \end{bmatrix} = \begin{bmatrix} -Q_1^{n+1} - RHS_1^n \\ Q_2^{n+1} + RHS_2^n \end{bmatrix} \tag{A.6}$$

with

$$K_{\mathrm{I}} = \frac{I}{\Delta t} + R_{\mu}, \tag{A.7}$$

$$K_{\mathrm{vis}} = 1 + \frac{CR_{\mathrm{vis}}}{\Delta t}, \tag{A.8}$$

$$RHS_1^n = -Q_1^{n+1} + Q_2^n \left(\frac{-CR_{\mathrm{vis}}}{\Delta t K_{\mathrm{vis}}} + \frac{I}{\Delta t K_{\mathrm{I}}} \right) + Q_1^n \left(\frac{CR_{\mathrm{vis}}}{\Delta t K_{\mathrm{I}}} \right) - \frac{C}{K_{\mathrm{vis}}} \frac{\left(P_{\mathrm{ext}}^{n+1} - P_{\mathrm{ext}}^n \right)}{\Delta t} + P_1^n \left(\frac{-C}{\Delta t K_{\mathrm{vis}}} \right), \tag{A.9}$$

$$RHS_2^n = Q_2^{n+1} - Q_2^n \left(\frac{I}{\Delta t K_{\mathrm{I}}} \right) \tag{A.10}$$

A.3. Validation of the *0D* recruitment/derecruitment dynamics

For validation of the *0D* recruitment/derecruitment dynamics two example setups from [22] are chosen (see also [276]).

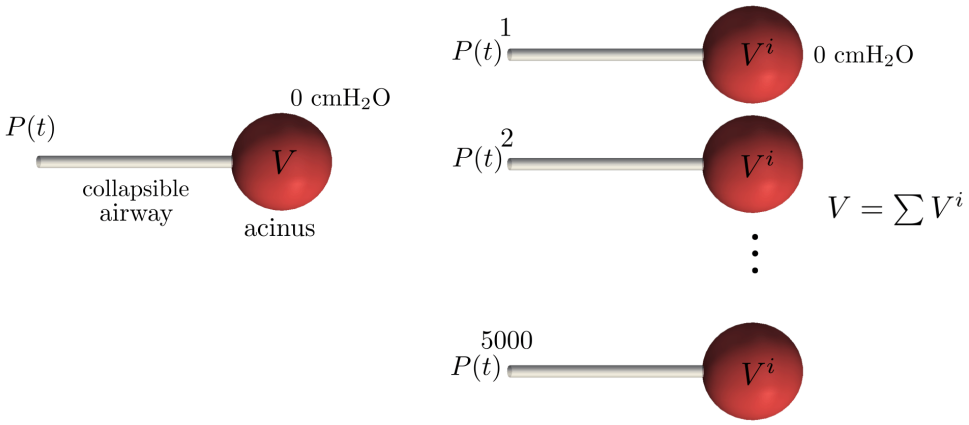

Figure A.1.: Simulation setup for single collapsible airway-acinus compartment (left) and for 5000 parallel compartments (right). For detailed description see text.

The first example is visualised in Fig. A.1 (left) and consists of a single collapsible airway with a resistance of $R_{\mu} = 10\ \mathrm{cmH_2O \cdot s \cdot mm^{-3}}$ (length of $l = 10$ mm, cross-section area $A = 1$ mm, dynamic viscosity of the fluid $\nu = 0.04\ \mathrm{cmH_2O \cdot s}$). At the distant end of the airway a single acinar unit is attached originally modelled via the Salazer-Knowles relationship ($V = A - B \cdot e^{(-K \cdot P)}$, from [294]; A, B arbitrary units, $K = 0.14\ \mathrm{cmH_2O^{-1}}$) in [22]. This behaviour of the acinar unit is approximated via the acinar model presented in Section 2.2.2, Eq. (2.74). The stiffness E_1, Eq. (2.75) - (2.77) is fit to a Salazer-Knowles relationship with $A = 2\ \mathrm{mm^3}$, $B = 1\ \mathrm{mm^3}$, and $K = 0.14\ \mathrm{cmH_2O^{-1}}$ resulting in $E_1^o = 8$, $b = 1$, $\kappa^{\mathrm{u}} = 0.022$ and $\tau^{\mathrm{u}} = 7$. The initial volume of the acinar unit is chosen as $V_0 = 1\ \mathrm{mm^3}$.

Reopening parameters are chosen as $s_o = s_c = 0.05\ \mathrm{s}^{-1} \cdot \mathrm{cmH_2O}^{-1}$ and $P_o = P_c = 5\ \mathrm{cmH_2O}$. At the proximal end of the airway (point A), a sinusoidal pressure waveform is applied reading

$$P(t) = 15\ \mathrm{cmH_2O} \left(1 - \cos\left(\frac{2\pi \cdot t}{100\mathrm{s}}\right)\right) \tag{A.11}$$

and the pressure at the outside of the acinar unit is set to zero for all times. The simulation is performed for $T = 100$ s with a time step of $\Delta t = 0.01s$.

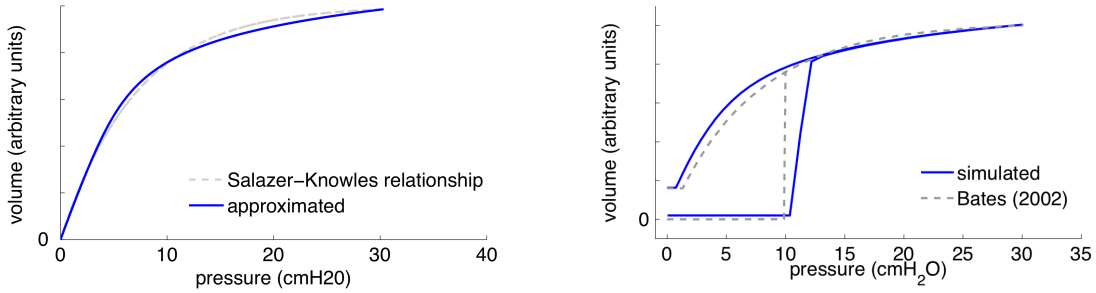

Figure A.2.: Pressure-volume curve for Salazer-Knowles relationship [294] and the fit exponential acinar unit used in this example (left); Comparison for reopening behaviour between the published results from [22] and the current approach (right).

The behaviour of the acinar unit and the P-V curve for the reopening scenario are visualised compared to the results from [22] in Fig. A.2. It can be seen that the reopening behaviour can be reproduced well and that differences between the present approach and [22] can be attributed to the approximation of the Salazer-Knowles relationship for the acinar unit. Reopening dynamics are, however, well recovered. It is noted that the non-vertical line at the point of reopening results from the usage of a finite resistance in the current approach in order to avoid instabilities at infinite flow rates.

The second validation example is now extended connecting 5000 of such airway-acinar units in parallel (see Fig. A.1, right). Each airway is modelled with a resistance of $R_\mu = 10\ \mathrm{cmH_2O} \cdot \mathrm{s} \cdot \mathrm{mm}^{-3}$ (length of $l = 10$ mm, cross-section area $A = 1$ mm, dynamic viscosity of the fluid $\nu = 0.04\ \mathrm{cmH_2O} \cdot \mathrm{s}$) similar to the previous example. Also, the acinus model is chosen as in the previous example and the sum of individual acini volumes results in overall lung volume.

For each airway an individual set of reopening parameters s_o, s_c, P_o, P_c is chosen. The critical reopening/closing pressures are assumed to follow a Gaussian distribution with a mean of $\mu_P = 5\ \mathrm{cmH_2O}$ and a standard deviation of $\sigma_P = 3\ \mathrm{cmH_2O}$. The reopening and closing parameters s_o and s_c are distributed quasihyperbolically with

$$s_o \in \frac{S_o}{\xi}, \quad \text{and} \quad s_c \in \frac{S_c}{\xi} \tag{A.12}$$

with ξ being a uniformly distributed random variable in the interval $[0, 1]$ and $S_o = S_c = 0.005\ \mathrm{s}^{-1}\ \mathrm{cmH_2O}^{-1}$.

Initially, all airways are closed and the virtual trajectory variables x are set to zero. Similar to the previous example, the pressure at the airway inlets is cycled sinusoidally between 0 and

30 cmH_2O with a period of 100 s (see Eq. (A.11)) for two cycles. The simulation is performed for 200 s with a time step of 0.01 s. The pressure outside all acini is set to 0 cmH_2O.

The resulting P-V curve is visualised in Figure A.3. It can be seen that the results correspond well to previous reported literature [22] and that the slight deviation is again attributable to the difference in material behaviour mentioned previously (see Figure A.2).

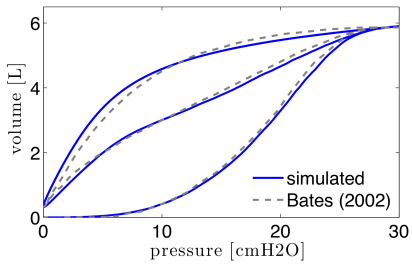

Figure A.3.: Pressure-volume curve for first and second cycle of the 5000 compartment setup. Simulated results are compared to [22].

Finally, following the work in [22] four variations in reopening parameters are realised with the setup of 5000 parallel airway-acini compartments indicated in Figure A.4. The computed results again match those reported in literature with slight deviations due to the differences in the used material model. Therefore it is concluded that reopening behaviour proposed by Bates and Irvin [22] is recovered in this work.

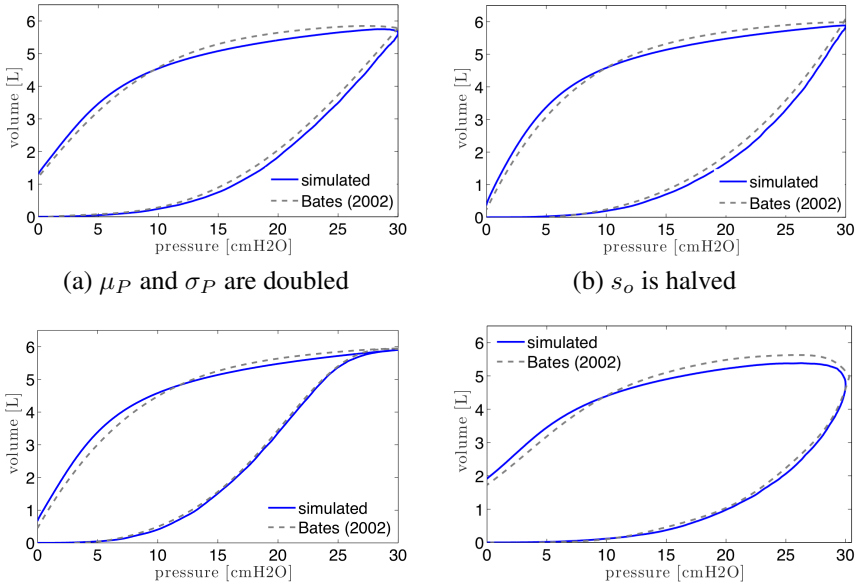

(a) μ_P and σ_P are doubled

(b) s_o is halved

(c) s_c is doubled

(d) all parameter changes realised together

Figure A.4.: Pressure-volume loops for reopening parameter variations according to [22].

B. Mathematical derivation of the *0D* lung tissue mechanics equations

B.1. *0D* Ogden acinus

In this appendix, the derivation of the *0D* tissue model coming from the Ogden strain energy function [251] (last summand in Eq. (2.74)) is given. The *0D* model assumes pure volumetric expansion for a single acinus/alveolar duct. The strain energy function reads

$$\Psi_{\text{vol,Ogden}} = \frac{\kappa}{\beta^2}\left(\beta \cdot lnJ + J^{-\beta} - 1\right). \tag{B.1}$$

Following [164] (p. 216) the second Piola-Kirchhoff stresses read

$$\mathbf{S} = 2\frac{\partial \Psi(\mathbf{C})}{\partial \mathbf{C}} = J\frac{\partial \Psi(\mathbf{C})}{\partial J}\mathbf{C}^{-1} \tag{B.2}$$

$$= J\frac{\kappa}{\beta}\left(\beta\frac{1}{J} + (-\beta)J^{-\beta}\right)\mathbf{C}^{-1} \tag{B.3}$$

$$= \frac{\kappa}{\beta}\left(1 - J^{-\beta}\right). \tag{B.4}$$

Transferring towards Cauchy stresses is done via

$$\sigma = \frac{1}{J}\mathbf{F}\mathbf{S}\mathbf{F}^T \tag{B.5}$$

and then Eq. (B.4) reads in terms of Cauchy stresses

$$\sigma = \frac{1}{J}\mathbf{F}\frac{\kappa}{\beta}\left(1 - J^{-\beta}\right)\mathbf{C}^{-1}\mathbf{F}^T. \tag{B.6}$$

Considering pure volumetric expansion by λ the deformation gradient reads

$$\mathbf{F} = \begin{bmatrix} \lambda & 0 & 0 \\ 0 & \lambda & 0 \\ 0 & 0 & \lambda \end{bmatrix} \tag{B.7}$$

and the right Cauchy-Green tensor and its inverse read

$$\mathbf{C} = \begin{bmatrix} \lambda^2 & 0 & 0 \\ 0 & \lambda^2 & 0 \\ 0 & 0 & \lambda^2 \end{bmatrix}, \quad \mathbf{C}^{-1} = \begin{bmatrix} \lambda^{-2} & 0 & 0 \\ 0 & \lambda^{-2} & 0 \\ 0 & 0 & \lambda^{-2} \end{bmatrix}, \quad \text{and} \quad J = \lambda^3. \tag{B.8}$$

The Cauchy stresses then become

$$\begin{bmatrix} \sigma_{11} & 0 & 0 \\ 0 & \sigma_{22} & 0 \\ 0 & 0 & \sigma_{33} \end{bmatrix} = \frac{1}{\lambda^3} \begin{bmatrix} \lambda & 0 & 0 \\ 0 & \lambda & 0 \\ 0 & 0 & \lambda \end{bmatrix} \frac{\kappa}{\beta} \left(1 - \left(\lambda^3\right)^{-\beta}\right) \mathbf{C}^{-1} \begin{bmatrix} \lambda & 0 & 0 \\ 0 & \lambda & 0 \\ 0 & 0 & \lambda \end{bmatrix} \tag{B.9}$$

$$\begin{bmatrix} \sigma_{11} & 0 & 0 \\ 0 & \sigma_{22} & 0 \\ 0 & 0 & \sigma_{33} \end{bmatrix} = \frac{1}{\lambda^3} \frac{\kappa}{\beta} \left(1 - \lambda^{-3\beta}\right) \begin{bmatrix} 1 & 0 & 0 \\ 0 & 1 & 0 \\ 0 & 0 & 1 \end{bmatrix} \tag{B.10}$$

Extracting pure hydrostatic pressure $P = \sigma_{11} = \sigma_{22} = \sigma_{33}$ yields

$$P = \frac{1}{\lambda^3} \frac{\kappa}{\beta} \left(1 - \lambda^{-3\beta}\right) \tag{B.11}$$

and with

$$\lambda^3 = \frac{V_i}{V_i^o} \tag{B.12}$$

being the ratio between current volume V_i and initial volume V_i^o of an alveolar duct, the hydrostatic pressure reads

$$P = \frac{V_i^o}{V_i} \frac{\kappa}{\beta} \left(1 - \left(\frac{V_i^o}{V_i}\right)^{\beta}\right). \tag{B.13}$$

B.2. Linearisation of the *0D* tissue equations

This derivation is partly based on the work in [177] and recalled here for completeness. For brevity, the subscript $(\cdot)_{\text{ac}}$ is omitted. Derivation starts with the non-linear acinar model Eq. (2.83)

$$\begin{aligned} N_{\text{ad}} P + N_{\text{ad}} \frac{B}{E_2} \left(\frac{dP}{dt}\right) = &\left(\frac{B B_a}{E_2}\right) \left(\frac{d^2 V}{dt^2}\right) + (B_a + B) \left(\frac{dV}{dt}\right) \\ &+ N_{\text{ad}} \frac{B}{E_2} \left(\frac{dP_{E1}}{dt}\right) + N_{\text{ad}} P_{E1}. \end{aligned} \tag{B.14}$$

Replacing the volume by the integral of the flow gives

$$\begin{aligned} N_{\text{ad}} P + N_{\text{ad}} \frac{B}{E_2} \left(\frac{dP}{dt}\right) = &\left(\frac{B B_a}{E_2}\right) \left(\frac{dQ}{dt}\right) + (B_a + B) \cdot Q \\ &+ N_{\text{ad}} \frac{B}{E_2} \left(\frac{dP_{E1}}{dt}\right) + N_{\text{ad}} P_{E1}. \end{aligned} \tag{B.15}$$

and discretisation of Eq. (B.15) in time using a Backward Euler scheme yields

$$N_{\text{ad}}P^{n+1} + N_{\text{ad}}\frac{B}{E_2}\left(\frac{P^{n+1}-P^n}{\Delta t}\right) = \left(\frac{BB_a}{E_2}\right)\left(\frac{Q^{n+1}-Q^n}{\Delta t}\right) + (B_a+B)\cdot Q^{n+1} \\ \underbrace{+N_{\text{ad}}\frac{B}{E_2}\left(\frac{dP_{E1}}{dt}\right) + N_{\text{ad}}P_{E1}}_{P_{\text{nonlin}}(V)}. \tag{B.16}$$

where the contribution of the non-linear spring E_1 is summarised as P_{nonlin}. Collocating all terms with quantities in the current/last time step n yields

$$\underbrace{N_{\text{ad}}\left(1+\frac{B}{E_2\Delta t}\right)}_{K_p^{n+1}}P^{n+1} + \underbrace{N_{\text{ad}}\left(-\frac{B}{E_2\Delta t}\right)}_{K_p^{n}}P^n = \underbrace{\left(\frac{BB_a}{E_2\Delta t}+B+B_a\right)}_{K_q^{n+1}}Q^{n+1}+ \\ \underbrace{\left(-\frac{BB_a}{E_2\Delta t}\right)}_{K_q^{n}}Q^n + P_{\text{nonlin}}(V) \tag{B.17}$$

with the "stiffness" matrices for pressure and flow (K_p^{n+1}, K_p^n, K_q^{n+1}, K_q^n). The pressure $P_{\text{nonlin}}(V)$ reads

$$P_{\text{nonlin}}(V) = N_{\text{ad}}\frac{B}{E_2}\dot{P}_{E1}^{n+1} + N_{\text{ad}}P_{E1}^{n+1} \tag{B.18}$$

is still non-linear dependent on V via P_{E1} and $\dot{P}_{E1} = dP_{E1}/dt$. These two terms are linearised via

$$P_{E1,j+1}^{n+1} = P_{E1,j}^{n+1} + \frac{\partial P_{E1,j}^{n+1}}{\partial V}\left(V_{j+1}^{n+1} - V_j^{n+1}\right) \tag{B.19}$$

$$\dot{P}_{E1,j+1}^{n+1} = \dot{P}_{E1,j}^{n+1} + \frac{\partial \dot{P}_{E1,j}^{n+1}}{\partial V}\left(V_{j+1}^{n+1} - V_j^{n+1}\right) \tag{B.20}$$

where the subscript j indicates the linear iteration. Inserting Eq. (B.19) and Eq. (B.20) in the non-linear pressure equation Eq. (B.18) it becomes

$$P_{\text{nonlin}}(V) = N_{\text{ad}}\frac{B}{E_2}\left(\dot{P}_{E1,j}^{n+1} + \frac{\partial \dot{P}_{E1,j}^{n+1}}{\partial V}\left(V_{j+1}^{n+1} - V_j^{n+1}\right)\right) \\ +N_{\text{ad}}\left(P_{E1,j}^{n+1} + \frac{\partial P_{E1,j}^{n+1}}{\partial V}\left(V_{j+1}^{n+1} - V_j^{n+1}\right)\right) \tag{B.21}$$

or re-arranged

$$P_{\text{nonlin}}(V) = N_{\text{ad}}\frac{B}{E_2}\dot{P}_{E1,j}^{n+1} + N_{\text{ad}}P_{E1,j}^{n+1} + \\ \left(\frac{B}{E_2}\frac{\partial \dot{P}_{E1,j}^{n+1}}{\partial V} + \frac{\partial P_{E1,j}^{n+1}}{\partial V}\right)\left(V_{j+1}^{n+1} - V_j^{n+1}\right) \tag{B.22}$$

The volume of an alveolar duct is obtained from the flow via

$$V_{j+1}^{n+1} = V^n + \frac{Q_{j+1}^{n+1} + Q^n}{2}\Delta t \tag{B.23}$$

and thus the last summand in Eq. (B.22) is re-formulated towards

$$\left(\frac{B}{E_2}\frac{\partial \dot{P}_{E1,j}^{n+1}}{\partial V} + \frac{\partial P_{E1,j}^{n+1}}{\partial V}\right)\left(\frac{Q_{j+1}^{n+1}}{2}\Delta t + \frac{Q^n}{2}\Delta t + V^n - V_j^{n+1}\right) \tag{B.24}$$

and the term containing Q_{j+1}^{n+1} creates an additional linearised "stiffness" matrix K_{lin}^{n+1} while the rest remains as linearised pressure P_{lin}^{n+1}. The two entries read

$$K_{\text{lin}}^{n+1} = \left(\frac{B}{E_2}\frac{\partial \dot{P}_{E1,j}^{n+1}}{\partial V} + \frac{\partial P_{E1,j}^{n+1}}{\partial V}\right)\frac{\Delta t}{2} \tag{B.25}$$

$$P_{\text{lin}}^{n+1} = N_{\text{ad}}\frac{B}{E_2}\dot{P}_{E1,j}^{n+1} + N_{\text{ad}}P_{E1,j}^{n+1} + \left(\frac{B}{E_2}\frac{\partial \dot{P}_{E1,j}^{n+1}}{\partial V} + \frac{\partial P_{E1,j}^{n+1}}{\partial V}\right)\left(\frac{Q^n}{2}\Delta t + V^n - V_j^{n+1}\right) \tag{B.26}$$

and the non-linear acinus equation Eq. (B.17) finally becomes

$$N_{\text{ad}}K_p^{n+1}\cdot P^{n+1} + N_{\text{ad}}K_p^n \cdot P^n = \left(K_q^{n+1} + K_{\text{lin}}^{n+1}\right)\cdot Q^{n+1} + K_q^n \cdot Q^n + N_{\text{ad}}P_{\text{lin}}. \tag{B.27}$$

Written in a matrix formulation Eq. (B.27) reads

$$\begin{bmatrix} -K_{ac} & K_{ac} \\ K_{ac} & -K_{ac} \end{bmatrix}\begin{bmatrix} P_a^{n+1} \\ P_{\text{pl/intr}}^{n+1} \end{bmatrix} = \begin{bmatrix} -Q^{n+1} - LHS^n \\ Q^{n+1} + LHS^n \end{bmatrix}. \tag{B.28}$$

with the following abbreviations

$$K_{\text{ac}} = \frac{N_{\text{ad}}K_p^{n+1}}{K_q^{n+1} + K_{\text{lin}}^{n+1}}, \tag{B.29}$$

$$P = P_{\text{alv}} - P_{\text{pl/intr}}, \tag{B.30}$$

$$LHS^n = -\frac{N_{\text{ad}}K_p^n}{K_q^{n+1} + K_{\text{lin}}^{n+1}}P^n + \frac{K_q^n}{K_q^{n+1} + K_{\text{lin}}^{n+1}}Q^n + \frac{N_{\text{ad}}}{K_q^{n+1} + K_{\text{lin}}^{n+1}}P_{\text{lin}} \tag{B.31}$$

C. Material identification of the lower airway tree

The mammalian airway tree is a complex network of branching tubes with different geometrical and mechanical properties exactly designed to optimally fulfil its function during respiration. Unphysiological loading with high pressures in mechanical ventilation can, however, induce changes in airway structure and trigger severe respiratory dysfunction. In this appendix, the underlying mechanical properties of airway walls are investigated at different dimensions and locations in the bronchial tree. A continuum-mechanics based, diameter-dependent material law for the entire lower bronchial tree is derived from more than 150 samples excised from ten healthy porcine lungs. All samples are dynamically loaded in uniaxial tensile tests and stress-strain measurements are combined with high-speed motion tracking to fit all constitutive parameters of a novel airway strain-energy potential in an inverse analysis process. Results show that a combination of a linear and an exponential strain-energy function accurately represents airway behaviour over a wide range of scales and that stiffness decreases with diameter. These insights help to further investigate situations involving large airway deformations that cannot be described by existing linear material models, e.g., airway collapse or hyperinflation. Further, knowledge about an exact stiffness of the walls at various diameters allows a quantification of contraction forces that are exerted on airways during allergic reaction tests and provides important information for drug design and efficacy studies.

This appendix is primarily based on a publication by the author in preparation [290], which is re-used here with permission.

C.1. Introduction

Airways are designed mainly for one specific task - to efficiently conduct air throughout the bronchial tree down to the respiratory bronchioli and the alveoli where gas exchange takes place. To fulfil this task at its best, airways are equipped with different mechanical properties depending on their location in the bronchial tree. The trachea, e.g., is composed of smooth muscle cells, membranes and cartilage rings [332]. The stiff cartilage rings prevent dynamic collapse of the main conducting airway during coughing or forced manoeuvres when air is inspired at high flow rates. The fraction of cartilage decreases with higher generation numbers and there is virtually no cartilage present in higher airway generations [320]. This softening of the airways enables the tree to easily follow motion during respiration and to deform accordingly to the surrounding parenchyma requiring low additional breathing effort.

However, when leaving the healthy loading regime in a setting of non-natural, mechanical ventilation, airways over-distend due to applied high pressures or tidal volumes and a part of the air pushed into a patient will solely expand the bronchial tree not even reaching the respiratory

zone and take part in the gas exchange [217]. Even worse, large deformations of the airway wall cause elevated tissue strains and lead to lung injury triggered by the ventilator (see Section 1.2.1). Another important phenomenon that is strongly dependent on airway wall stiffness and highly dangerous in mechanical ventilation is cyclic closure and reopening of small airways e.g., reported e.g., in [32, 148, 149, 151].

To study these and other effects, several investigations on the mechanical behaviour of airways have been conducted experimentally [16, 65, 66, 118, 170, 198, 199, 234, 252, 265, 279, 308, 332, 335, 339] and numerically [148, 149, 151]. Yet, the material law used in the numerical studies has been linear and is not valid in such a large deformation regime as it occurs in overdistension or closure and reopening. Moreover, only three experimental studies [198, 265, 339] use a consistent continuum-mechanics based description of the non-linear constitutive law in form of a strain-SEF while the remaining ones only report phenomenological stress-strain curves. The work in [339] is focused on the trachea, which is anatomically different to smaller airways, and thus not all findings are applicable to the entire tree. The studies in [198, 265] investigate a larger part of the bronchial tree, however, a stiff rubber stop used to seal the end of the airways during testing with inner pressure will have a significant influence on wall movement, especially in small airways, where the distance between measurement location and the stop is only approximately 1.0 mm.

In this appendix, a novel experimental and computational protocol is presented to overcome the main limitations from previous studies in the following aspects: (i) a non-linear hyperelastic constitutive law is derived based on an exponential strain-energy function capable of representing airway material behaviour; (ii) large to small-size airways (diameter $2 - 16$ mm) at different positions in the bronchial tree are included in the study; (iii) measurements include uniaxial tensile tests of ring-shaped samples as well as high-speed motion tracking during the full testing cycle; (iv) a virtual replication of the tensile test allows computational fitting of diameter-dependent material parameters in an inverse analysis process; (v) an adequate number of samples permits statistically relevant statements for the large animal and provides a well-established testing protocol for human samples.

The remainder of this appendix is subdivided into five parts: In Section C.2, sample preparation techniques and the experimental setup and protocol are introduced. Section C.3 covers the theoretical background of the underlying computational framework and the used strain-energy functions. In Section C.4, the resulting material parameters are presented. A conclusion of the presented work is drawn in Section C.5.

C.2. Sample Material and Experimental Methods

The experiments conducted in this study are enhancements of existing methods developed for lung parenchyma tested as plane tissue strips [29, 272]. However, as circumferential fibres and radial prestress would be destroyed by cutting airway strips, the experimental setup and protocol [365] are enhanced in several aspects to test whole airway segments close to *in vivo* loading conditions.

C.2.1. Sample Preparation

Ten healthy adult pig lungs including the upper and lower airways are freshly harvested from the local slaughterhouse. The handling of the animals and slaughtering follows the regulatories of the European Communities Council directive concerning animal welfare during commercial slaughtering process (86/609/ECC) and is constantly monitored by local authorities.

Samples are prepared by dissecting the bronchial tree in a diameter range of $d = 2 - 16$ mm (see Figure C.1). Within this tree, rings are cut such that each airway diameter in the group $d = \{2, 4, 6, 8, 10, 16\}$ mm is represented in the samples and that each ring has a sufficient distance ($1.5 \times d$) to the previous and the next bifurcation. The airway rings are sorted according to lumen diameter and stored in Earle's Balanced Salt Solution (Sigma-Aldrich, St. Louis, USA) at 4°C until being tested (see Figure C.1).

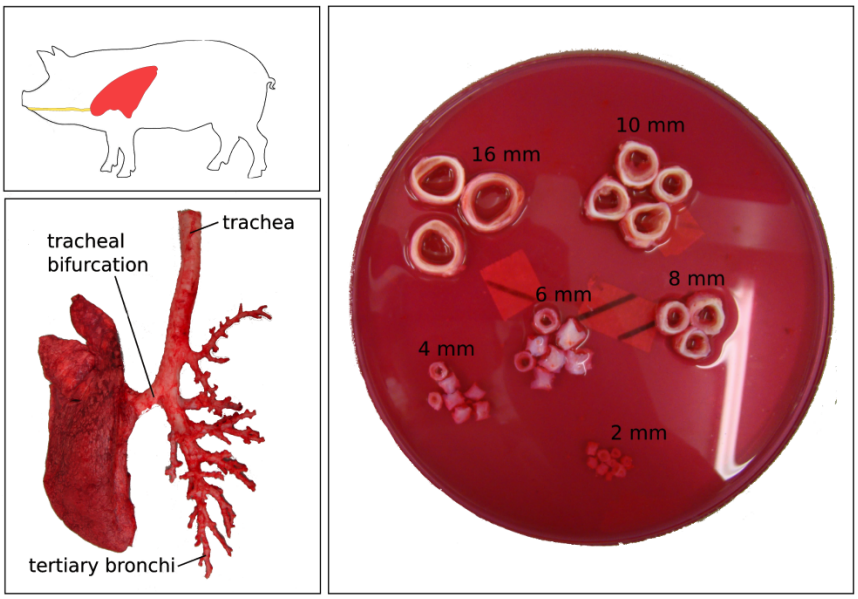

Figure C.1.: Dissected bronchial tree in diameter range of $d = 2 - 16$mm (left), and prepared ring-like samples sorted according to inner diameter (right).

All tests are completed within 12 h after death and previous studies [66, 198] show that freshly tested airway tissue retains its *in vivo* properties. Due to inaccuracies in motion recording (blurred images, no exactly orthogonal camera position), not all samples can be completely included in the analysis resulting in a baseline characteristics for the number of successfully tested samples per diameter (see Table C.1). In total, 166 samples have been tested successfully.

Table C.1.: Baseline characteristics for number of successfully tested samples per diameter. A diameter of $d = 16$ mm refers to tracheal samples.

Lumen diameter d [mm]	2	4	6	8	16
Number of samples	48	42	42	24	10

C.2.2. Experimental setup

Tests are performed on a Bose ElectroForce 3100 uniaxial tensile testing machine (Bose Corporation, Eden Prairie, USA, see Figure C.2). All test are conducted in displacement-controlled mode with a maximum amplitude of ± 2.5 mm (resolution 12.5 μm) induced via the moving right clamp connected to the internal displacement sensor of the machine. The left clamp is mounted on a force sensor with a range of ± 2.5 N (resolution 2.5 mN) and both displacement and force are recorded at a acquisition rate of 100 Hz.

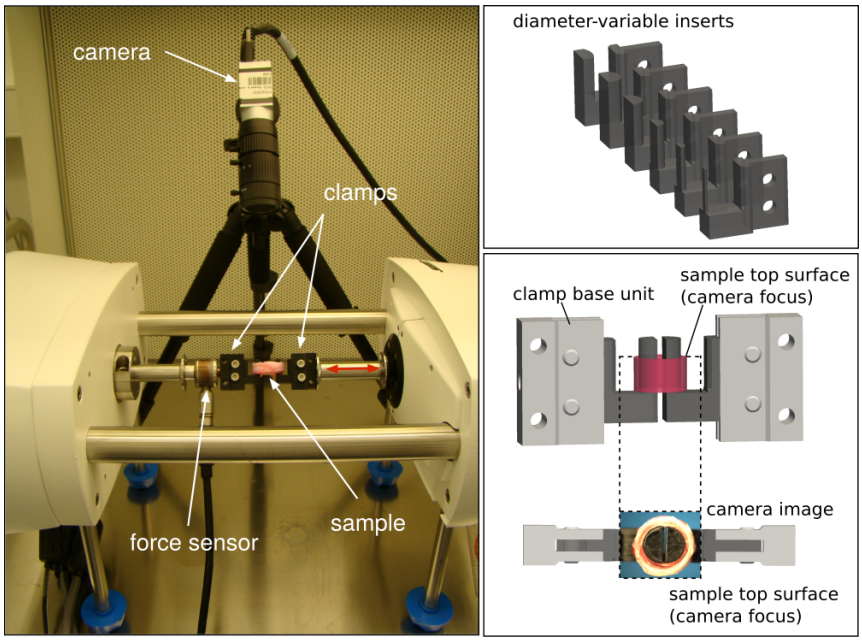

Figure C.2.: Experimental setup with Bose ElectroForce 3100 machine, clamps and placed sample. The high-speed camera system is placed perpendicular to the sample. The red double arrow indicates clamp movement in the tensile axis. Clamps consist of a base unit and diameter-variable inserts. The ring-like upper cross-sectional area of the sample is focused for the camera image in motion tracking.

The clamps are specifically designed for airway testing and consist of a base unit and several half-cylindrical inserts with variable diameter $d = 2 - 16$ mm (see Figure C.2). The modular clamp design allows quick and easy exchanges of the half-cylindrical inserts to optimally fit the airway inner diameter. Insert changes can be performed without unmounting the force sensor. The clamps are mounted such that the centre point of the semi-circular clamp surface is exactly on the interface between the two half cylinders. This means that clamps with a diameter of $2, 4, 6,$ and 8 mm are mounted with direct contact. Clamps with a diameter of 10 and 16 mm are mounted with a defined initial distance of 4 and 8 mm respectively. After exchanging the inserts at the correct distance a simple tare of force and displacement sensors is sufficient to continue testing.

A high-speed camera (Basler acA2000-340kc, Basler, Germany) with macro lens (0.3-1.0x, Computar, Japan) is aligned perpendicular to the clamps and recording the testing cycle at a resolution of 1008×800 px^2 and a frame rate of 100 fps (see Figure C.2). The recorded images

allow high-speed motion tracking of the entire ring-like upper cross-sectional area of the sample over the full testing cycle. Tracking of each pixel of the image over time relies on the natural contrast between the black clamps and background and the brighter sample. More details on extraction of a motion field from the images have been given in Section 4.2.4.

C.2.3. Testing protocol

C.2.3.1. Sample dimensions

As a first step in the testing protocol, the diameter d and axial length l of a sample are measured from two photographs taken from top and frontal views on underlying millimetre paper. The sample dimensions are used for exact geometry generation (see Section C.3.1) and for assignment of a suitable clamp diameter for testing.

C.2.3.2. Sample placement

After measurement, the sample is slipped on the clamps using a pair of tweezers. As airway diameter usually does not exactly match clamp diameter, sample placement results in a small tension force recorded with the force sensor which is always smaller than 0.01 N. If the initial force is higher, the sample is tested on the next smaller diameter. The advantage of this small initial tension is, that the sample will always be subjected to a small positive tension force resulting in a clean mechanical loading state without buckling during dynamic testing. This so-called prestressing force can consistently be respected in the numerical identification method [120] as described in Section C.3.1. If sample placement is correct and the measured initial tension force is sufficiently small, the camera system is focused on the top surface of the ringlike sample before continuing the testing protocol.

C.2.3.3. Preconditioning phase

Before the actual test, the tissue is preconditioned to stabilise the residual strain of an airway segment [29, 272]. Therefore, the maximum displacement of 2.5 mm is prescribed in five steps with a velocity of 0.5 mm/s and held for 10 s at each step. Afterwards the tissue is relaxed to a displacement of 0.2 mm (see Figure C.3). This additional displacement of 0.2 mm in addition to the initial clamp distance (see Section C.2.2) ensures a prestressing tension force in samples that exactly fit their clamp diameter and prevents buckling which has lead to numerical difficulties in [29].

C.2.3.4. Testing phase

As breathing is a periodic process in nature with a breathing frequency of $0.25 - 0.5$ Hz in the pig, the hysteresis loop due to the visco-elasticity of the tissue is additionally stabilised. Therefore, nine sinusoidal loading cycles are performed with a displacement between $+0.2$ mm and $+2.5$ mm at a frequency of 0.5 Hz. The 10th cycle is filmed for motion tracking and used for post processing of the experimental raw data described in Section C.2.4. The results show that nine cycles are sufficient to stabilise the dynamic behaviour of the sample (see Section C.4.1).

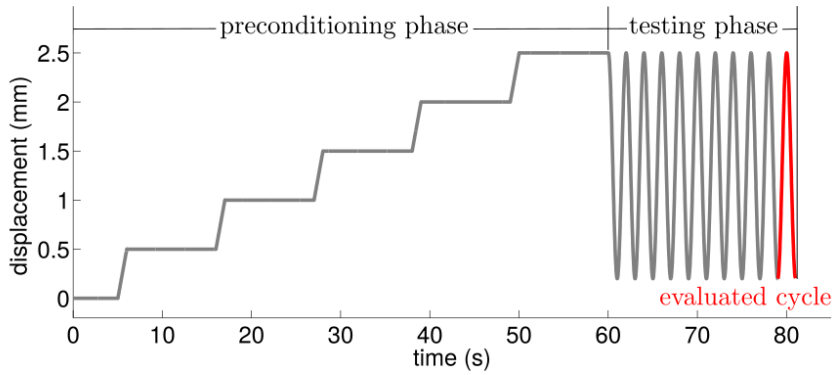

Figure C.3.: Prescribed clamp displacement over time for the preconditioning and the testing phase in the experimental protocol. The analysed 10th cycle is marked in red.

A pure tensile loading state is achieved during testing by an initial clamp distance of $d_0 = 0.2$ mm after the prestressing phase (see Section C.2.3). The state at $d_0 = 0.2$ mm is defined as reference state (time t_0) with the corresponding force measurement F_0 and camera image I_0 for motion tracking.

C.2.3.5. After the test

After the test, the sample is removed from the machine, cut in length direction and photographed again from top view to measure the opening angle due to circumferential residual strains. This opening angle is important to accurately define the mechanical loading in the reference state and the required prestress for each sample individually. Further, the thickness of the sample is measured with a micrometre (accuracy 10 μm) and used for geometry generation in the numerical test (see Section C.3.2).

C.2.4. Analysis of experimental raw data

C.2.4.1. Extraction of the force-displacement curve

To fit a non-linear hyperelastic constitutive law for airway walls, the ascending part of the 10th cycle of the measured force-displacement curve is extracted (see Figure C.3). By definition of the testing protocol, the displacement ranges from $d_0 = 0.2$ mm to a maximum displacement of $d_{max} = 2.5$ mm in a sinusoidal profile with a frequency of 0.5 Hz. For better comparability between samples of different size, applied displacement and measured force are converted to strain and stress in the sample. The strain in the airway wall is computed via

$$\varepsilon = \frac{2(d(t) - d_0)}{\pi d_{\text{clamp}}}, \tag{C.1}$$

where $d(t)$ is the current displacement and d_{clamp} denotes the clamp diameter which is equal to the airway diameter. Stresses in the airway wall are evaluated via

$$\sigma = \frac{F}{2h_{\text{sample}} t_{\text{sample}}}, \tag{C.2}$$

with F being the measured force, h_{sample} the geometric height of the sample and t_{sample} being the airway wall thickness. Representative stress-strain curves for airway walls are presented in Section C.4.1.

C.2.4.2. Displacement field from high-speed motion tracking

The displacement of the entire sample in the experiment is monitored from top view focusing the ring-like upper cross-sectional area of the sample using the camera system described in Section C.2.2.

The process of motion-tracking is based on an image registration algorithm similar to [29] and in detail explained in Section 4.2.4. The algorithm used here is similar, also using a SSD metric and a diffusive regulariser with a prefactor of $\alpha^{\mathcal{T}} = 0.03$ (see Eq. (4.3)).

The registration process is performed sequentially between all images reflecting the ascending part of the testing cycle (approximately 50 images). Registration between two images is repeated iteratively until the solution is converged with a relative $L2$-residual error smaller than 10^{-12}. Representative results for the registered displacements and relative $L2$-residual error for the multiresolution approach are presented in Figure C.4. Computing a solution with the required accuracy of 10^{-12} requires approximately 100, 35, 200, 115, and 75 iterations from coarsest to finest level.

Finally, the displacements at specific points of the sample (i.e., the nodes of the finite element mesh generated in Section C.3.2) are linearly interpolated from the entire displacement field over time. These interpolated displacements are later used for comparison between experimentally measured and simulated displacements of the sample (see Section C.3.3).

C.3. Numerical Framework

C.3.1. Computational model including prestressing and contact

The numerical identification is based on a simulation of the experimental test setup presented in Section C.2.3 and a replication of the sample displacements with the experimentally measured force. To exactly mimic the experimental scenario, the sample is modelled via the equations of non-linear elastodynamics in the structural domain Ω^S (Eq. (2.53)). To realise the frictionless contact between clamps and sample, an additional contact constraint is introduced between the cylinder surface of the clamp (slave) and the inner surface of the sample (master) [264] reading

$$g_n(\mathbf{d}, t) \geq 0 \tag{C.3}$$

$$p_n(\mathbf{d}, t) = 0 \tag{C.4}$$

with the gap g_n between clamps and sample and the tangential component p_n of the contact stress. Finally, to respect the small initial prestress due to sample placement and initial clamp distance, a modified updated Lagrangian formulation [120] is used, which performs well for biological cylindrical tissues. The sample is prestressed to the current stress $\sigma_0 = F_0/(2h_{\text{sample}}t_{\text{sample}})$. For more details on the used prestressig method, the reader is referred to [120]. After the prestressing, the identification procedure starts (see Section C.3.3).

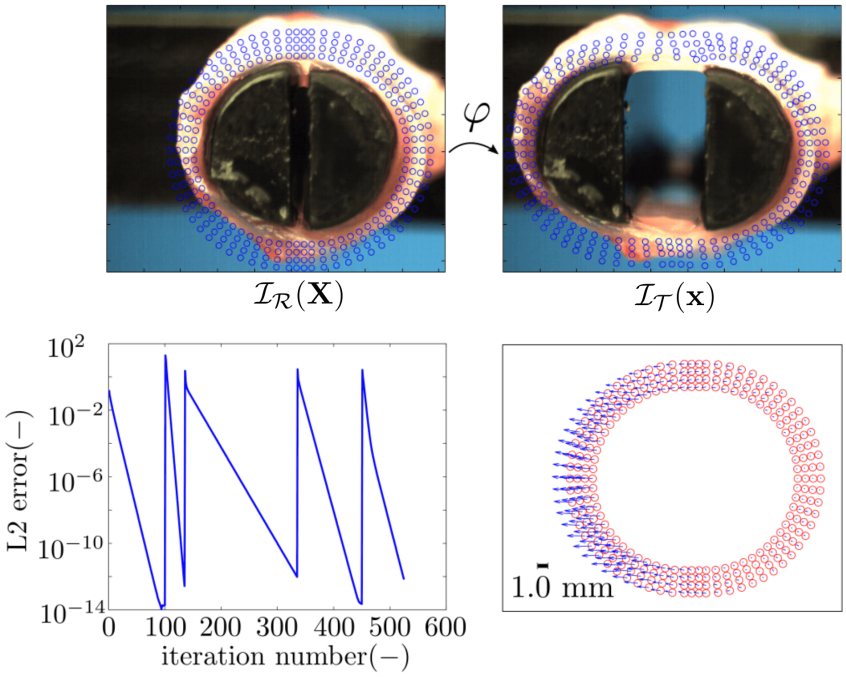

Figure C.4.: Reference ($\mathcal{I}_{\mathcal{R}}$) and target ($\mathcal{I}_{\mathcal{T}}$) image for image registration showing the initial state (top, left) and the state of maximum clamp displacement (top, right). Registration is usually performed in 50 equidistant steps for this motion. The $L2$ error and the displacement field for one such step is shown in the bottom row of the image.

C.3.1.1. Geometry generation from images

Geometry generation is performed with the software package Cubit (Sandia National Laboratories, NM, USA). The sample geometry for the simulation is extracted from the camera image I_0 at the initial state t_0. The sample consists of two half-cylindrical segments with inner radius $r_i = d/2$ of the corresponding clamp and the measured wall thickness t. The segments are connected via two compatible cuboids with the length of the current clamp distance d_0 obtained from the image. As the geometry is assumed to be symmetric in axial direction, a fraction with unit height $h = 1.0$ mm is computed.

Both clamps are modelled as rigid half cylinders with equal diameters d and unit height h. Sample and clamps are meshed with hexahedral elements with a spacing of 30 elements over the radius r_i and 3 elements across cuboid length d_0. The unit height h is represented by 3 elements.

C.3.2. Airway constitutive law

The goal of this work is to identify a constitutive law which is able to represent airway behaviour in the entire bronchial tree and and over a wide range of deformation states. In this study, airways are modelled as isotropic as a first guess, as little is known about fibre families and angles throughout the bronchial tree and thus airways are frequently modelled as isotropic in larger FSI studies [148, 149, 151, 352, 372]. It is, however, noted that the proposed methods can be used

for anisotropic constitutive laws and that the derived isotropic parameters provide a good initial guess for more advanced models.

Several polynomial and exponential strain energy functions have been tested for material characterisation in this study. However, for brevity, only the best material law will be described in the rest of this appendix. The exponential law

$$\Psi_{exp} = \underbrace{c_1 \left(\bar{\mathrm{I}}_1 - 3\right)}_{1} + \underbrace{\frac{k_1}{2k_2}(\mathrm{e}^{k_2(\bar{\mathrm{I}}_1-3)^4} - 1)}_{2} + \underbrace{\frac{\kappa}{4}\left(-2\ln J + J^2 - 1 \right)}_{3} \tag{C.5}$$

consists of a linear contribution (1), an exponential part (2), and an Ogden like material law [251]. The linear part describes sample behaviour well in the linear loading regime, while the exponential part recovers the non-linear material behaviour for large deformations. The Ogden like part accounts for incompressibility of the sample as airway walls mainly consist of water and thus can be seen as incompressible. The parameters c_1, k_1, k_2 marked in blue are fit in the inverse analysis procedure (see Section C.3.3). The volumetric parameter κ is chosen as $\kappa = 1$ MPa ensuring that volume changes of the sample are less that 2%.

C.3.3. Inverse Analysis Procedure

The core process of material parameter identification is basically a optimisation problem mimicking the tensile test computationally. It is noted that the real experiment is displacement driven and forces are measured (see Section C.2.3). In the computational case, the test is driven by this force and displacements are computed. This way, the the error between experimentally determined and simulated displacements can be compared for the entire ringlike sample surface in each time step. If the displacements agree between motion tracking and simulation, it is assumed that the material behaviour is recovered.

To drive the simulation, a traction is prescribed on the inner surface of the moving clamp corresponding to the measured force in the experiment. The non-moving clamp is fixed by a Dirichlet boundary condition.The simulation is computed with a time step of $\Delta t = 0.01$ s which exactly matches the experimental time span between two image frames.

Minimisation follows a Levenberg-Martquardt algorithm described in detail in [29]. In this work, the inverse analysis is converged if the gradient of the error is smaller than 10^{-7}. The maximum number of optimisation steps is 15 and the perturbation parameters are $a = 0.0$ and $b = 0.01$. The initial regularisation factor is given as $\mu = 0.1$. A nested parallelisation implemented in BACI [353] allows for the computation of these simulations in parallel, each simulation being itself also computed in parallel and the identification is usually converged after nine optimisation steps.

C.4. Results

C.4.1. Force-displacement curves

Measured force is plotted versus displacement for the 10 cycles of sinusoidal loading in Figure C.5 for a 8 mm diameter sample. The hysteresis stabilises over the first cycles and can bee seen

as stationary on the last cycle, which is used for material identification. The ascending part of the force-displacement curve is visualised including the tangent modulus E_t for the hyperelastic behaviour of the sample in the small displacement case.

It is visible that airways behaviour is linear-elastic over a for a small strain range $(0.0 - 0.12)$ but becomes increasingly non-linear with higher strains. This is important to consider in extreme deformation states such as collapse and reopening, or overdistension. In the following, the material behaviour will be identified for the entire strain range. The values for the tangent modulus E_t determined from the stress-strain curve are used as initial guess for material identification of linear law c_1.

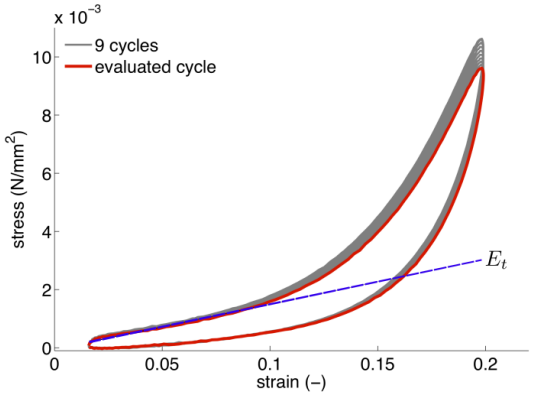

Figure C.5.: Stress-strain curve for an airway with 8 mm inner diameter. The tangent modulus indicates that material behaviour is linear for small strains and becomes increasingly non-linear for higher strain values.

C.4.2. Material identification for tracheal samples

To evaluate the quality of the inverse analysis procedure the material behaviour of tracheal samples is investigated and compared to the results in [66]. The resulting material parameters in this work are $c_1 = 66.2$ kPa, $k_1 = 58$ Pa, and $k_2 = 2435$. In case of small strains, the parameter c_1 can be seen as equivalent to the tangent modulus. Thus the results in this study match well with previously reported values of $E_t = 53$ kPa [66] for an average tangent modulus of pig trachea. Therefore, it is assumed that the experimental setup and the identification procedure are well suited to recover the material behaviour of airway walls.

C.4.3. Material identification for the entire bronchial tree

In the following, results are presented for smaller airways with a diameter of $\{2, 4, 6, 8\}$ mm. In Figure C.6 the displacements for the point that lies on the inner diameter of the sample and on the tensile axis (i.e., the point with highest displacement) are compared between motion tracking and simulation for two airways. The curves show that the motion is equal between experiment and simulation for a given force curve and thus that the quality of the fit is appropriate.

In Figure C.7, the resulting material parameters c_1, k_1, and k_2 are presented for the single diameters. It can be seen that the linear parameter c_1 is similar across the diameters with approx-

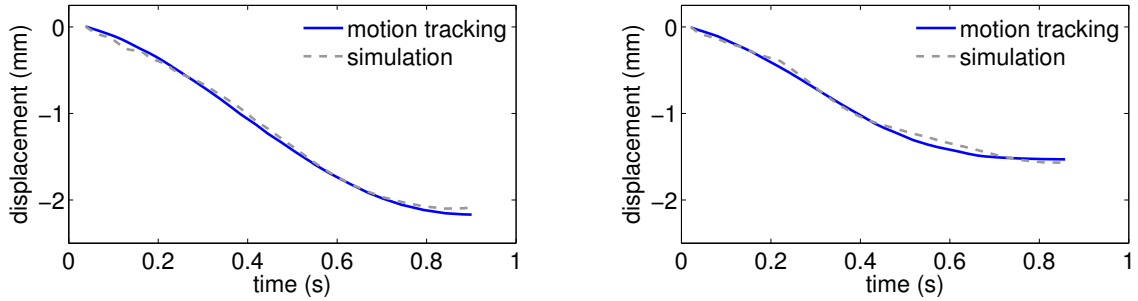

Figure C.6.: Comparison between motion-tracked and simulated displacement for the point of maximum displacement in an $d = 8$ mm (left) and an $d = 2$ mm airway.

imately $c_1 = 2$ kPa. This value is in line with previous observations on bronchi with an tangent modulus of $1.5 - 3.0$ kPa [198]. Further, a dependency of airway stiffness on diameter is visible in the parameter k_1. Airways become significantly stiffer with increasing diameter providing additional strength against collapse and hyperinflation. This knowledge can now be used in FSI simulations of airway closure/reopening to quantify critical stresses and strains. Further, this non-linear relationship could be included as non-linear compliance of *0D* airways to correctly represent bronchial tree expansion in the *0D/0D* lung model.

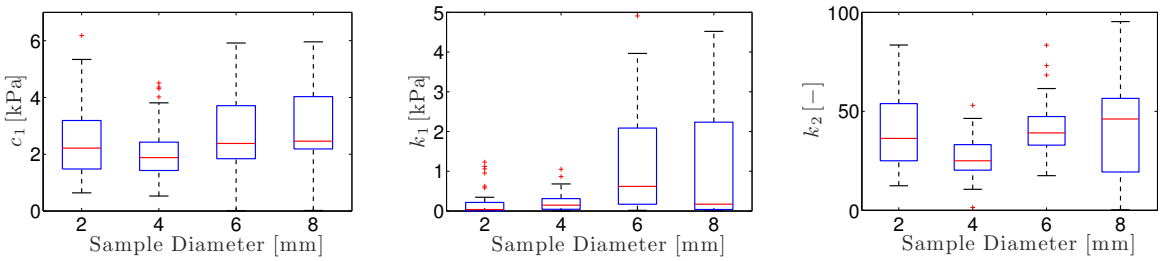

Figure C.7.: Box plot showing identified material parameters c_1, k_1, k_2 for airways with different diameters.

C.5. Discussion and Conclusion

In this appendix, a novel uniaxial tensile test protocol is developed for cylindrical samples and successfully applied to airways with different diameters existent in the bronchial tree. The cylindrical geometry remains intact and circumferential fibres and residual strains are preserved during testing. The results show, that airways become softer with decreasing diameter and a constitutive law consisting of a linear and an exponential part fits airway behaviour well over a wide diameter and deformation range. All parameters included in the material law are presented, compared to, and convincingly match available literature values for tracheal samples and scattered bronchial data. Finally, the presented experimental protocol is also suitable in other applications involving cylindrical samples and fibres such as in arteries, veins or stenting scaffolds. It

is concluded that this protocol is easy to realise with standard equipment and yet powerful in the case of airway walls at various diameters. The derived material parameters can be included into advanced fluid-structure interaction models to investigate airway overdistension during mechanical ventilation or collapse and reopening scenarios with realistic highly non-linear material behaviour.

D. A model for lung tissue microstructure

As outlined in the main part of this work, mammalian lungs mainly consist of a sponge-like microstructure containing several millions of alveoli which are essential for gas exchange. The physiological and mechanical properties of this microstructure are crucial for respiration and influence the macroscopic behaviour of the entire organ in health and disease. Hence, if computational models are sought to gain more insight into lung behaviour, predict lung states in certain scenarios or suggest better treatment options in early stages of respiratory dysfunction, an adequate representation of this microstructure is essential. However, investigating the real microstructural architecture requires complex medical-imaging methods and would be computationally extremely expensive. Even worse, there is currently no way of obtaining the real patient-specific microstructure *in vivo*. Hence, a fast and easy to compute parametrised model of lung microstructures is presented based on tetrakaidecahedra which can represent both physiolocial and mechanical properties of the parenchyma. It is shown that gas transport pathways and stress and strain distributions are comparable to real alveolar microstructures and even capable of capturing variations present in biology. Inclusion of this parametrised microgeometries into macroscopic clinical or computational lung models would allow quantification of critical stresses and strains during mechanical ventilation on the level of the alveolar wall - an insight that has not been provided so far.

This appendix section is primarily based on a submitted publication by the author [288], which is re-used here with permission.

D.1. Introduction

Recently, several observations in the occurrence of VILI have been related to high stress and strain in parts of the lungs [34, 76, 116, 242, 269, 319] and investigations strive for a reliable strain safety threshold in the course of mechanical ventilation [267–269, 280]. The reason why such a limit may be hard to find lies in the microstructural architecture of the lung. On the microscopic scale, the lung is no uniformly stressed continuum but rather characterised by a dense packing of alveoli to maximise surface area for an efficient gas exchange. Overstraining potentially starts at the weakest alveolar walls and spreads from these stress raisers even if a global stress limit is not reached or overcome [74, 114, 228, 268, 272]. Further, the gas exchange process [96] and the distribution of hazardous particles and curative aerosols are governed by the microscopic structure of the lung [152, 304, 324, 325]. Consequently, more detailed information on the microstructural shape would be desirable for better understanding of structural functional coherence [323], the release of proinflammatory cytokines as a result of mechanical stimulation

of tissue [344] and for proposing better treatment options in the course of aerosol transport or mechanical ventilation [115].

One reason why there is little information available on lung behaviour on the alveolar level is the lack of easily accessible imaging data. Currently, existing information on the lungs microstructure rely predominantly on reconstructions of two-dimensional microscopic images as described by [43], [55], or [231]. More recent imaging methods have extended the geometrical information to three dimensions by applying synchrotron-based X-ray tomography methods [143, 298] to excised lung tissue. However, these reconstructions are extremely costly, complex and not applicable to visualise the alveolar structure *in vivo* due to the need for tissue dissection and/or lethal radiation doses.

Therefore, attempts to artificially generate alveolar geometries have been made in the past [50, 78, 84, 109, 184, 185, 189, 190, 324]. Such artificial alveolar geometries consist of two components: a base cell geometry and an approach to connect the single cells for gas exchange. The acinar model introduced by [184] was based on cubic cells representing alveolar ducts and alveoli. The cubes were interconnected via a labyrinthine algorithm under the assumption of minimal path lengths for oxygen exchange. Although the model did provide good correlation to experimental data, cubic acinar geometries are fairly unrealistic in their regularity and especially in the number of septal junctions per alveolus [228]. This problem remains in a newer study using quadrangular prisms [185]. A more authentic shape in terms of the number of and angle between septal junctions for a single alveolus is the so-called tetrakaidecahedron. This 14-sided polyhedron has been used for single alveolus studies including pressure-volume relationships [78] or the role of surface tension [190]. Fixed arrangements of tetrakaidecahedra have been proposed by [84] to mimic the morphology of an alveolar duct. The interconnection between single cells in the work by [84] was realised by an annealing algorithm which optimises a random initial connection of cells. This approach has been able to connect large ensembles of tetrakaidecahedra, however, it creates a solution which may be dependent on the initial distribution and created gas transport pathways may not necessarily be optimal due to local minima during the optimisation process. Further space-filling assemblies by [109] have shown to correlate well to morphological measurements and [324] have used a space-filling arrangement of tetrakaidecahedra to simulate alveolar particle deposition. Recently, [189] have created heterogeneous acinar structures based on Voronoi tesselation and were able to reproduce morphological information of the rat acinus.

To make these morphologically realistic artificial alveolar ensemble geometries suitable for investigations in the context of VILI, they need to be capable of mimicking realistic mechanical properties of the real lung microstructure - a feature that has not been provided so far. Hence, the aim of this work is twofold. First, the best interconnection algorithm, i.e., cell connection based on the assumption of optimal gas exchange pathways [184] is extended, towards the most realistic tetrakaidecahedral alveolar cells respecting irregularities. The cell ensembles can be created in arbitrary size and for any desired species and be used for previously mentioned applications such as the simulation of gas exchange, particle deposition, or mechanical loading. Second, the focus lies on the simulation of mechanical stresses and strains in the course of VILI. Therefore, all ensemble parameters, i.e., the number of contained alveoli, their characteristic cell size, and the alveolar wall thickness are calibrated such that a mechanical behaviour identical to real imaging-based alveolar microstructures [272, 284] is obtained. The such calibrated novel parametrised microgeometries can then be used in clinical trials as well as in numerical studies

to close the gap between macroscopic lung inflation and microscopic stresses and strains for better understanding the mechanisms behind VILI.

D.2. Material and Methods

To determine a physiologically and mechanically realistic lung microstructure model, several ensembles of tetrakaidecaherda are constructed, interconnected for gas transport by an enhanced labyrinthine algorithm and investigated in their mechanical behaviour to derive all relevant parameters required for a realistic mechanical behaviour on the microscale.

D.2.1. Ensembles of tetrakaidecahedra

Ensemble creation starts from a single tetrakaidecahedron, which itself is a truncated octahedron with a side length of L. This base cell is converted to a hollow body with wall thickness h. At the quadratic sides of this base cell, further tetrakaidecahedra are added until ensembles of arbitrary size and an ensemble edge length s are created. In order to respect variations present in biology, the wall thickness h is allowed to vary between neighbouring cells. The characteristic cell length L is constant within an ensemble to assure face-connectivity, but can be varied for different ensembles.

As the created ensembles, similar to the real microstructure samples, are only a part of the structure excised from a larger tissue region, the outer layer of cells is cut open at a distance of $0.25\sqrt{2}L$ from the quadratic boundary to respect cut cells in real samples. For further consideration of biological irregularity, all cells that are completely located inside the ensemble are varied in the position of their vertex coordinates with random values from the interval $[0; 0.15L]$ in x, y and z direction relative to the characteristic cell length L (see also [42]). This finally results in an internally closed, thin-walled irregular ensemble of tetrakaidecahedra handed over to the labyrinthine algorithm presented in the next section. An exemplary visualisation of an ensemble of nine tetrakaidecahedral cells including its characteristic geometrical parameters can be found in in Figure D.1.

D.2.2. Enhanced labyrinthine algorithm

In general, a labyrinthine algorithm enables the creation of a network of interconnected cells for an *a priori* defined assemblage of identical initially closed cells. By successively opening faces, connections of all cells to a given starting cell are established. Assuming that the design of peripheral air spaces is guided by effective gas transport, the generated cell connections should have minimal length.

In [184], a labyrinthine algorithm for square and cubic cells was introduced using priority directions. Thereby, directions pointing from the starting cell to the centre of the assemblage are prioritised. If there are several priority cells available to be connected, one of them can be chosen randomly. If, otherwise, priority directions are lacking, then a cell is selected randomly from non-priority directions. In assemblages of square and cubic base cells, the pathway from one cell to each of its neighbours is of equal length.

For tetrakaidecahedral cells, however, two kinds of connections have to be distinguished as a consequence of the more complicated geometry. Cells affiliated via square faces are connected with a path length of $2\sqrt{2}L$ between cell centres. This connection is subsequently referred to as straight. By contrast, cells sharing a hexagonal face are linked with a path length of $\sqrt{6}L$. This connection is denoted as diagonal in the following.

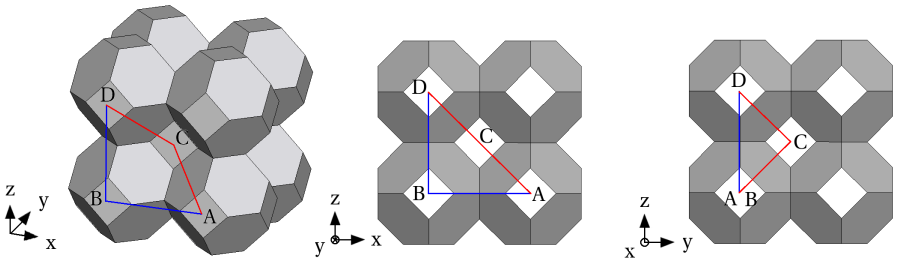

Figure D.1.: Comparison of different pathways through an ensemble of nine tetrakaidecahedra. The connection between A and D via C marked in red is shorter than the straight one via B marked in blue. Figure adapted from [363] with permission.

Without violating the concept of priority directions, different pathways are conceivable connecting two given cells. An illustrative example is provided in Figure D.1. Here, the path connecting A and D via C is shorter than the straight connection via B, even if the concept of priority directions is partially violated due to the change in one coordinate direction.

As a remedy, a novel connection rule based on an explicit check for the optimality of the created paths is proposed. All cells affiliated in the course of labyrinth creation are stored in a queue. In each step, the cell ranked first in the queue is set active and can create a connection to a new cell N by randomly choosing one of its neighbours that is not yet passed. The connection of the new cell N to the active cell A is admissible if no pathway to N via another queue cell is shorter. The path length p^N to N via the currently active cell A is

$$p^N = p^A + \begin{cases} 2\sqrt{2}L & \text{for straight connection} \\ \sqrt{6}L & \text{for diagonal connection} \end{cases} \tag{D.1}$$

with p^A denoting the path length from the start to the currently active cell. The remaining cells in the queue are not necessarily direct neighbours of N. In this case the shortest path to N via a queue cell C includes as many diagonal connections as possible. To determine the numbers of connections in straight (n_{straight}) and diagonal (n_{diag}) directions along the optimal path between C and N, a special coordinate system is introduced. In this coordinate system the determination of the optimal number of straight and diagonal connections can be calculated based on simple algebraic operations. Using these definitions, the optimal overall path length to N via C then reads

$$\tilde{p}^N = p^C + 2\sqrt{2}L \cdot n_{\text{straight}} + \sqrt{6}L \cdot n_{\text{diag}}. \tag{D.2}$$

If none of the alternative path lengths $\tilde{p}^N$ is smaller than p_N from Equation (D.1), then the new cell N can be connected to the currently active cell A and both the active cell and the just affiliated new cell are moved to the end of the queue. Otherwise another cell has to be selected from the range of neighbours. In case that either no other adjacent cell is at hand or can be

affiliated optimally, the current active cell A is deleted from the queue and its successor is set active. This process is repeated until the queue is empty.

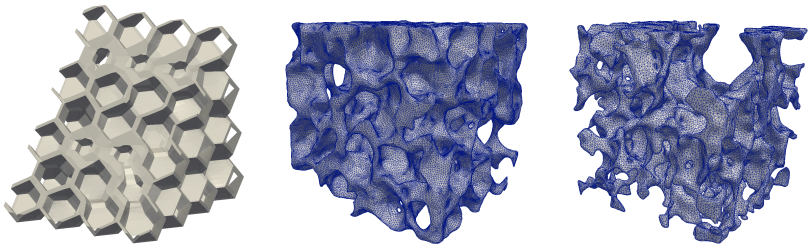

Figure D.2.: Clipped view of an exemplary parametrised ensemble with 91 tetrakaidecahedral cells connected by the novel labyrinthine algorithm (left) and imaging-based alveolar microstructures taken from [272] (middle) and [284] (right). Figure taken from [288] with permission.

Finally, all face-connections along the calculated optimal path are cut open creating an internally connected geometry (see Figure D.2, left). This geometry can be used in several applications including the previously mentioned simulation of gas exchange and particle deposition in the pulmonary acinus. Further, surface tension terms [254] can be applied to the generated surface and thus respect the influence of surfactant, which significantly changes pulmonary mechanics [81].

D.2.3. Calibration of representative parametrised lung microgeometries for structural mechanics simulations

The current focus lies in the investigation of structural mechanics of the alveolar microstructure and in determination of local stress and strain distributions on the alveolar scale. The aim of this appendix is to replicate the mechanical behaviour of the complex imaging-based microstructures with geometrically simpler, still physiologically realistic, parametrised microgeometries. Therefore, two imaging-based microstructures representing two relatively extreme cases of lung tissue are used for comparison: Microstructure A (Figure D.2, middle) is taken from a very dense and homogeneous region of lung tissue; Microstructure B (Figure D.2, right) is crossed by a small airway on the top surface which influences its mechanical stiffness.

For comparison of their mechanical behaviour, both the imaging-based microstructures and the parametrised lung microgeometries are deformed in structural mechanics simulations following the laws of non-linear elastodynamics (Eq. (2.53)). The material model for a single wall is described by a Neo-Hookean like strain energy function [35]. The Young's modulus is taken from previous experimental studies as $E = 6.75\,\mathrm{kPa}$ [272] and the Poisson's ratio is set to $\nu = 0.49$ to respect the low compressibility of the alveolar wall mainly consisting of water. Alveolar wall density is chosen as $\rho^S = 10^3\,\mathrm{kg\,m^{-3}}$ accordingly. The computations are by no means limited to Neo-Hookean like strain energy functions and can be conducted analogously for various material types. In this work, a Neo-Hookean like constitutive law to ensure comparability to previous studies on imaging-based microstructures is used [272, 284].

Deformation is driven by pure Dirichlet boundary conditions fixing the bottom surface and moving the top up to a purely uniaxial elongation of $\varepsilon_{zz} = \Delta z/L_0 = 75\%$ and pure shear deformation of $\gamma_{xy} = \Delta x/L_0 = 75\%$ as visualised in Figure D.3. A dynamic equilibrium state is computed every $\Delta\varepsilon_{zz} = \Delta\gamma_{xy} = 0.25\%$ of prescribed strain until the maximum deformation is reached. With these two rather extreme deformation states it is possible to cover most of the physiologically relevant deformation, which is basically a combination of the two previously mentioned cases. Moreover, for these material parameters and deformation states highly resolved results from realistic alveolar microstructures are available in literature and can be used for comparison of the mechanical properties of the parametrised models.

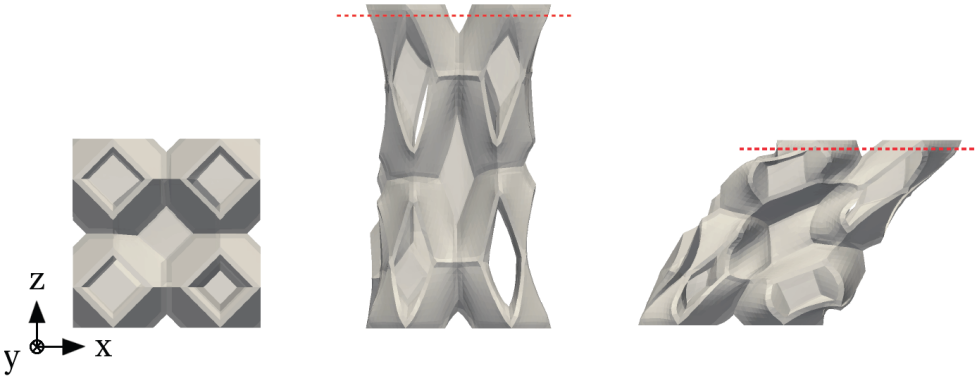

Figure D.3.: Illustration of pre-defined deformation states for an ensemble of nine tetrakaidecahedra: initial geometry (left), uniaxial tension with $\varepsilon_{zz} = 75\%$ (middle) and shear deformation with $\gamma_{xy} = 75\%$, (right). The cutting plane for evaluation of mean stress is marked in red. Figure taken from [288] with permission.

The aim of this study is to calibrate all geometrical quantities of the parametrised microgeometries, i.e., ensemble edge length s, the number of cells N, the characteristic cell length L and wall thickness h until the parametrised geometries show similar stress distributions as the imaging-based microstructures do. This calibration process is performed for ensemble sizes between nine and 91 combined cells. All governing parameters are chosen from realistic values in the range defined by the microstructures A and B (see Table D.1). Previous studies [272] have shown that the imaging-based microstructures with the chosen ensemble edge length $s = 175 - 200$ μm can be seen as representative element volume for lung tissue. Therefore, the ensemble edge length s is chosen in the range of the imaging-based microstructures. Variations in the number of contained cells N are realised via changes in the characteristic cell size L. The two resulting parametrised topologies consist of nine larger or 91 smaller tetrakaidecahedral cells and are denotes as “large cell” and “small cell” geometries in the following.

Mechanical behaviour is evaluated for various geometrical parameter combinations via measuring the mean uniaxial stress ($\sigma_{zz,m}$) under maximum uniaxial tension and the mean shear ($\tau_{xy,m}$) stress under maximum shear deformation at a distance of one element layer below the top surface (see Figure D.3). As for this comparison, stresses as a derived quantity are investigated, mesh size is chosen carefully to obtain a spatially converged solution. If mean uniaxial and shear stresses match the values given from the imaging-based microstructures, stress-volume fraction histograms are created to match detailed stress distributions of the parametrised microgeometries with stress distributions in the imaging-based microstructures.

Table D.1.: Parameter ranges used for ensemble calibration compared to measurements in microstructures A and B. Values for wall thickness are presented as mean ± standard deviation (SD). The mean alveolar diameter for the artificial geometries is calculated as $D = \sqrt{6}L$.

	lower parameter limit	upper parameter limit	microstructure A	microstructure B
Ensemble edge length s [μm]	175	200	200	175
Number of contained alveoli N	9	91	14	11
Characteristic cell size L [μm]	16.5	40.4	n/a	n/a
Mean alveolar diameter D [μm]	40.4	98.9	82	103
Alveolar wall thickness h [μm]	6.0 ± 1.0	12.4 ± 5.6	10.5 ± 4.6	14.3 ± 6.6

After successful calibration, the parametrised microgeometries mimic two essential properties observed in real lung tissue: (i) minimal mean pathlengths for gas transport and (ii) realistic mechanical behaviour on the alveolar scale.

D.3. Results

D.3.1. Distribution of gas transport pathway lengths

An important geometrical property for pulmonary acinar structures is the gas transport pathway lengths from a defined starting cell to the individual alveolar sacs within an ensemble of fixed size. The resulting distribution of individual pathway lengths for an ensemble with the dimensions of $20\sqrt{2}L \times 20\sqrt{2}L \times 23\sqrt{2}L$ and a characteristic length of $L = 26.96$ μm reported by [84] is shown in Figure D.4. The enhanced labyrinthine algorithm meets both the values computed by Denny and Schroter (1996) and the experimental results by Mercer and Crapo (1987). A slight tendency towards medium-length pathways and a slightly smaller average path length of $1,015$ μm is observed compared to $1,244$ μm and $1,287$ μm in the previous studies. However, an overall good accordance with previously reported experimental and numerical data can be observed.

D.3.2. Calibrated mechanical behaviour and resulting optimal parameter values

In a first calibration step of mechanical properties, exemplary realisations of "large cell" and "small cell" ensembles are investigated under $\varepsilon_{zz} = 75\%$ uniaxial tension.

The characteristic cell length is $L_{\text{large cell}} = s/(3.5\sqrt{2})$ in case of the "large cell" ensembles. This means that the cell diameter $D = \sqrt{6}L_{\text{large cell}} = 92.8$ μm of the "large cell" ensembles is similar to the mean alveolar diameter $\bar{D}_{meas} = 100.2 \pm 3.5$ μm measured from the imaging-based microstructures.

Computed values for mean uniaxial stress $\sigma_{zz,m}$ in the "large cell" ensembles are presented in Table D.2. It can be seen that mean uniaxial stress increases with ensemble edge length for a

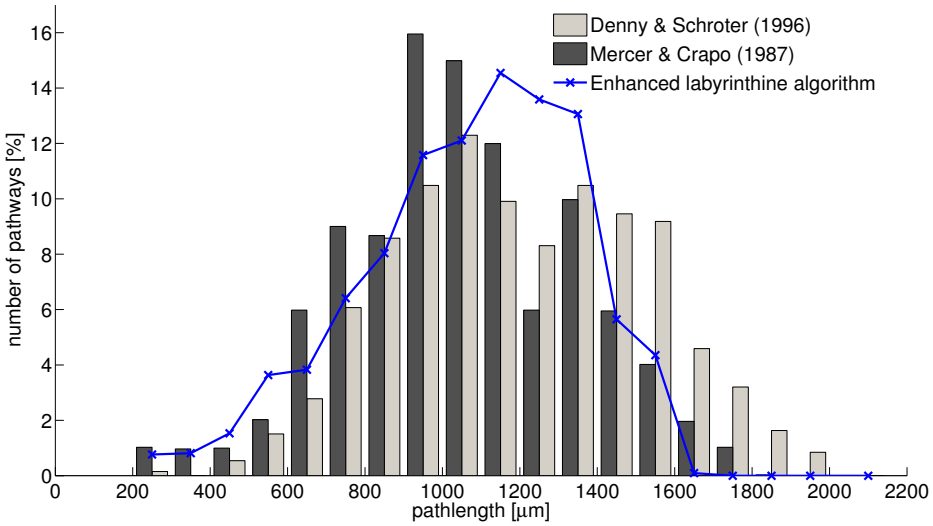

Figure D.4.: Distribution of path lengths for gas exchange from a starting cell to the single alveolar sacs in a $20\sqrt{2}L \times 20\sqrt{2}L \times 23\sqrt{2}L$ ensemble obtained using the proposed enhanced labyrinthine algorithm. Values are compared to previous computational and experimental results taken from [84] and [231]. Figure taken from [288] with permission.

given wall thickness of $h = 12.4 \pm 5.6$ μm defined as mean $\pm$ standard deviation (SD). Variations in wall thickness allow further fine-tuning of mean uniaxial stress. For an ensemble edge length of $s = 187.5$ μm, which is actually the mean value of the sizes of microstructures A and B, a wall thickness of 9.0 ± 1.2 μm results in an uniaxial stress of $\sigma_{zz,m} = 1.9$ kPa. This is exactly the mean value of the stresses observed in microstructures A and B.

The mean shear stress value $\tau_{xy,m}$ for this "large cell" ensemble realisation with $s = 187.5$ μm and $h = 9.0 \pm 1.2$ μm is $\tau_{xy,m} = 0.33$ kPa and lies only 10% above the value of microstructure A (see Table D.4).

Table D.2.: Chosen parameters and computed mean uniaxial stress for exemplary parametrised"large cell" realisations under $\varepsilon_{zz} = 75\%$ uniaxial tension. Values for wall thickness are presented as mean $\pm$ SD.

Ensemble edge length s [μm]	175	187.5	187.5	187.5	200
Characteristic cell size L [μm]	35.4	37.9	37.9	37.9	40.4
Alveolar wall thickness h [μm]	12.4 ± 5.6	6.0 ± 1.6	9.0 ± 1.2	12.4 ± 5.6	12.4 ± 5.6
Mean uniaxial stress $\sigma_{zz,m}$ [kPa]	2.2	1.8	1.9	2.4	2.8

In Table D.3, the properties of "small cell" ensembles with 91 cells are presented for the listed parameter combinations.

The characteristic cell size reduces towards $L_{\text{small cell}} = s/(7.5\sqrt{2})$ in case of the "small cell" ensembles. The corresponding cell diameter $D = \sqrt{6}L_{\text{small cell}} = 43.4$ μm of the "small cell"

ensembles is much smaller than the mean alveolar diameter measured from the imaging-based microstructures (see Table D.1).

The values for mean uniaxial stress range from 2.7 to 4.1 kPa and are much higher than mean uniaxial stress in the "large cell" ensembles and the imaging based microstructures. This is already observed for realistic ensemble edge lengths of $s = 187.5$ μm and relatively thin walls ($h = 8.0 \pm 1.0$ μm). This difference would even increase for larger ensemble edge lengths s or wall thickness h. Consequently, the "small cell" ensembles are less suitable for exact micromechanical calibration under the given assumption of equal ensemble edge length s.

Table D.3.: Chosen parameters and computed mean uniaxial stress for exemplary parametrised "small cell" realisations under $\varepsilon_{zz} = 75\%$ uniaxial tension. Values for wall thickness are presented as mean $\pm$ SD.

Ensemble edge length s [μm]	187.5	187.5	187.5
Characteristic cell size L [μm]	17.7	17.7	17.7
Alveolar wall thickness h [μm]	6.0 ± 1.0	8.0 ± 1.0	10.0 ± 1.0
Mean uniaxial stress $\sigma_{zz,m}$ [kPa]	2.7	3.4	4.1

The best calibration parameters and respective values for mean uniaxial and shear stress are summarised in Table D.4, compared to the real microstructures A and B.

Table D.4.: Comparison of mechanical properties in best calibrated "large cell" and "small cell" ensemble geometries with real alveolar microstructures A and B under tension and shear deformation. Values for wall thickness are presented as mean $\pm$ SD.

	"large cell"	"small cell"	microstructure A	microstructure B
Ensemble edge length s [μm]	187.5	187.5	200	175
Mean alveolar diameter D [μm]	93.8	43.4	82	103
Alveolar wall thickness h [μm]	9.0 ± 1.2	8.0 ± 1.0	10.5 ± 4.6	14.3 ± 6.6
Mean uniaxial stress $\sigma_{zz,m}$ [kPa]	1.9	3.4	2.1	1.6
Computation time for $\varepsilon_{zz} = 75\%$ [min]	60	70	870	760
Mean shear stress $\tau_{xy,m}$ [kPa]	0.31	1.0	0.27	0.17
Computation time for $\gamma_{xy} = 75\%$ [min]	500	390	910	790

For detailed comparison of stress distributions in real and parametrised artificial alveolar geometries, stress-volume histograms are shown in Figure D.5 indicating the percentage of the tissue subjected to a certain stress. One can see that the stress distribution in the best calibrated "large cell" geometry fits those in microstructures A and B well, both under uniaxial tension and under shear deformation. The best calibrated "small cell" geometry shows a similar behaviour in the case of shear deformation but exhibits greater variations under uniaxial tension.

Computation time for uniaxial tension of the best calibrated "large cell" ensemble is approximately 10 times less as compared to uniaxial tension of the imaging-based microstructures. The remarkable savings in computation time are due to the simpler geometry of the parametrised microgeometries compared to the imaging-based microstructures. This simpler geometry comes

along with a less complex mesh topology and a reduced number of finite elements that have to be evaluated in the computational simulation of the parametrised microgeometries.

The best calibrated "large cell" and "small cell" ensembles are provided in the supplementary material (see S.1 and S.2) for easy access and further use.

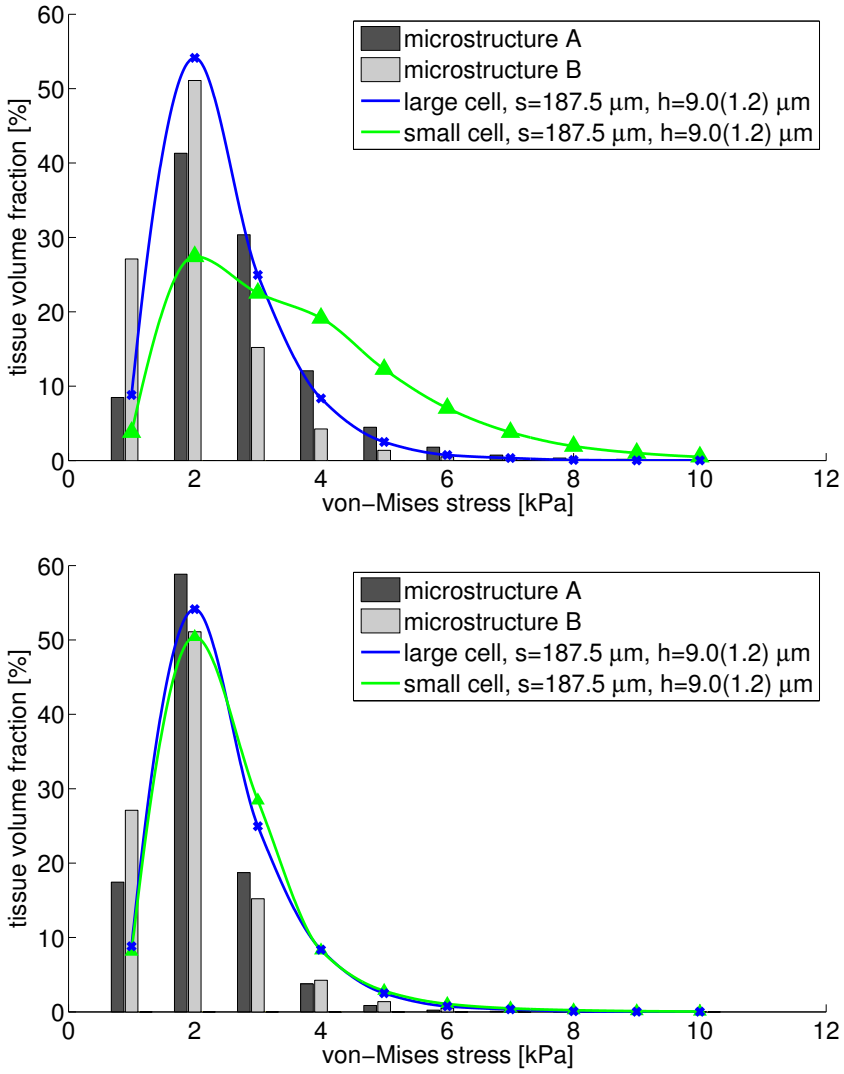

Figure D.5.: Stress-volume histogram for real microstructures and best "large cell" and "small cell" ensembles under $\varepsilon_{zz} = 75\%$ uniaxial strain (top) and under $\gamma_{xy} = 75\%$ shear deformation (bottom). Figure taken from [288] with permission.

D.4. Discussion

The main finding of this appendix is that a relatively simple parametrised model of lung microstructure is able to represent both the physiological property of minimal mean gas transport pathways and the mechanical behaviour observed in imaging-based microstructures. The de-

rived model consists of nine tetrakaidecahedra combined to a cell ensemble and can be seen as realistic representation for lung tissue under uniaxial tension and shear deformation up to $\varepsilon_{zz} = \gamma_{xy} = 75\%$. All model parameters resulting from calibration of the mechanical properties (ensemble edge length $s = 187.5$ μm, characteristic cell size $L = 37.9$ μm, and alveolar wall thickness $h = 9.0 \pm 1.2$ μm) are geometrically motivated and correspond to real measurements and literature data. The single features of the approach proposed in Section D.2 will be discussed in detail in the following.

D.4.1. Geometry generation and enhanced labyrinthine algorithm

Essentially, all artificially generated alveolar microstructures available in literature consist of two components: a base cell geometry and an approach to interconnect the single cells for gas exchange. In this appendix, the tetrakaidecahedron as most realistic alveolar base cell is combined with an enhanced labyrinthine interconnection algorithm to ensure minimal mean path lengths for gas exchange within the ensembles.

All parameters involved in ensemble creation are physically motivated and correlate well with experimental studies such as the seminal work by Mercer & Crapo (1987). Their measured mean alveolar diameter of 100 ± 16 μm is comparable to the diameter $\bar{D}_{meas} = 100.2 \pm 3.5$ μm measured in the imaging-based microstructures. This value is similar to the mean alveolar diameter in case of the best calibrated "large cell" ensemble of $\bar{D}_{\text{large cell}} = 93.75$ μm. Alveolar wall thickness h is measured at various locations in the microstructures A and B with values of $h_A = 10.5 \pm 4.6$ μm and $h_B = 14.6 \pm 6.6$ μm in line with values of $h = 4.0 - 10.7$ μm reported in literature [343]. These values are also reached by the best calibrated "large cell" ensembles with a wall thickness of $h_{\text{large cell}} = 9.0 \pm 1.2$ μm. Another important quantity for gas exchange and surface tension studies is a correct surface to volume ratio S/V. In case of the investigated "large cell" ensemble one obtains $(S/V)_{\text{large cell}} = 580$ cm^{-1} matching the range given by [342] of $S/V = 432 - 649$ cm^{-1}.

One possible approach for ensemble interconnection is the annealing algorithm by [84]. One prerequisite in their case is an initial random pathway tree which is then optimised by simulated annealing. Being a very elegant approach, this algorithm naturally requires several cycles and dependent on the initial tree local minima might influence the solution process. The labyrinthine approach by [184, 185], extended in this work towards irregular tetrakaidecahedra, requires no initial tree and creates an optimal pathway in the first run that is not influenced by local minima. Therefore, it can be seen as the method of choice to create a fast and robust interconnection through irregular tetrakaidecahedral ensembles.

In case of the reported example of approximately 2300 tetrakaidecahedra in [84] the enhanced labyrinthine algorithm provides similar results to those reported in [84] which also agree with the experimental path lengths measured by Mercer & Crapo (1987) (see Figure D.4).

The resulting cell dimensions and mean pathway lengths in line with literature data support the fact that the enhanced labyrinthine algorithm is capable of creating a physiologically realistic alveolar structure. This structure can be used for gas transport, particle deposition and dispersive aerosol drug transport investigations in the lung on a microscopic level.

D.4.2. Realistic mechanical behaviour on the microscale

In the course of determination of a strain safety threshold in mechanical ventilation, the parametrised alveolar geometries provide efficient structures mimicking the mechanical loading of real micro-level geometries under the assumption that the real imaging-based samples provided a representative element volume. Governing ensemble parameters are calibrated to represent two relatively extreme regions in the lung being very homogeneous (microstructure A) and crossed by a small airway weakening structural mechanical properties (microstructure B). The mean stress values $\sigma_{zz,m}$ and $\tau_{xy,m}$ and the stress-volume histogram for shear deformation (see Figure D.5) almost exactly match results from real imaging-based microstructures with slightly higher values for tissue regions with higher stress. This analogously holds for uniaxial tension where the parametrised "large cell" ensemble provides closest values compared to the real imaging-based microstructures A and B.

The fact that the "small cell" ensembles do not perform better than the "large cell" geometries although they contain a larger number of cells can be explained with properties of the real samples. For ensemble side lengths between 175 and 200 μm the real geometries contain approximately $11 - 14$ alveoli with a mean diameter of $\bar{D}_{meas} = 100.2$ μm. If ensemble side length s is *a priori* fixed by the fact that $s = 175 - 200$ μm is the edge length of a representative element volume in the imaging-based microstructures, an increase in cell number requires the characteristic cell length L to decrease below a realistic alveolar diameter. Consequently, the number of alveolar walls in the ensemble increases and the ensembles become stiffer in case of mechanical loading. This also explains, why no larger cell numbers were chosen for the structural mechanics calibration. It is, however, important to note, that in case representative element volumes may be larger for different species or loading scenarios, the presented mechanical calibration can analogously be performed for larger ensemble sizes and cell numbers.

The parametrised microstructures presented in this work finally mimic stress and strain distributions of the real lung microstructure. They are much easier accessible (see supplementary to [288]) and require approximately 10 times less computational resources for mechanical simulation than imaging-based microstructures for the same global deformation state.

D.4.3. Possible extensions

The long term goal of this appendix is not only to simulate mechanical loading of isolated lung microgeometries but also of superalveolar structures such as whole tissue samples or even the entire lung during inflation. This can e.g., be realised in computational studies using an advanced multi-scale analysis [361] to quantify strain hotspots on the alveolar wall for different states of lung inflation.

On the experimental side, a so-called bioreactor proposed by [80] allows to observe inflammation reactions in lung tissue samples for realistic global strain states. Together with the calibrated microgeometries, these experimentally or other clinically measured strain data [34, 76, 116, 242, 269, 319] would for the first time provide a relationship between global strain, alveolar stress/strain and inflammation. This interlinkage could lead to more precise strain-based safety values for mechanical ventilation preventing inflammation and potentially lead to more protective mechanical ventilation techniques in future.

For physiologically relevant investigations in lung microstructures and the onset of VILI *in vivo*, surfactant is an important factor that has neither been considered in the real microstructures nor in the parametrised models, yet. However, corresponding approaches to consider the influence of surface tension on the mechanical behaviour of alveolar structures have already been developed previously [254, 362]. These surface tension factors can be utilised in the current model in a straightforward manner, particularly since the surface-to-volume ratio S/V is in a physiologically realistic range. The change in surface area during deformation will then automatically respect the correct surface tension due to surfactant. Hence, investigations of VILI close to *in vivo* conditions and surfactant related pathologies become possible on the microscopic scale.

In fact there is a substantial number of respiratory diseases apart from VILI that originate in pathological changes on the alveolar scale including e.g., oedema, emphysema, and fibrosis. The involved changes in thickness and architecture of the alveolar wall, have recently become visible *in vivo* using dark-field radiography [345, 368]. This novel imaging technique requires similar radiation doses as conventional CT scans and does not resolve single alveolar walls. However, the number of alveolar walls per unit volume can be estimated regionally from the dark-field radiograph. This wall density information can be included in microgeometry generation, e.g., via changing the characteristic cell size L regionally. Using such personalised microgeometries in strain threshold determination is a further step towards patient-tailored ventilation guided by microstructural needs.

D.5. Conclusion

In this appendix, an enhanced labyrinthine algorithm is proposed and applied to parametrised ensembles of tetrakaidecahedral cells to create lung microstructures ensuring minimal mean path lengths for oxygen transport. The resulting geometries are subjected to various deformation states and their characteristic geometrical parameters are calibrated to mimic the mechanical behaviour observed in imaging-based three-dimensional alveolar structures. Furthermore, the resulting characteristic parameters for cell size and wall thickness correspond to measurements and include variability present in biology. The created parametrised microstructure geometries are used to compute local stress distributions in single alveolar walls, a quantity that is not obtainable by imaging techniques at clinical site. Compared to real alveolar microstructures obtained from synchrotron-based X-ray tomography scans the parametrised model requires only 10 per cent of the computational time for computing the same strain state. This means that the parametrised models can provide the same stress information 10 times faster, or 10 times more information on various strain levels throughout the lung in the same time. Using this parametrised models, stress elevations in single alveolar walls can be investigated in health and disease and help to derive a stress-based safety limit for mechanical ventilation protocols in future.

Bibliography

[1] Adler A, Lionheart WRB. Uses and abuses of EIDORS: An extensible software base for EIT. *Physiol Meas* **27**: 25-42, 2006.

[2] Adler A, Arnold JH, Bayford R, Borsic A, Brown B, Dixon P, Feas TJC, Frerichs I, Gagnon H, Gärber Y, Grychtol B, Hahn G, Lionheart WRB, Malik A, Patterson RP, Stocks J, Tizzard A, Weiler N, Wolf GK. GREIT: a unified approach to 2D linear EIT reconstruction of lung images. *Physiol Meas* **30**: 35-55, 2009.

[3] Adler A, Amato MB, Arnold JH, Bayford R, Bodenstein M, Bohm SH, Brown BH, Frerichs I, Stenqvist O, Weiler N, Wolf GK. Whither lung EIT: where are we, where do we want to go and what do we need to get there? *Physiol Meas* **33**: 679-694, 2012.

[4] Agostoni E, Hyatt RE. Static Behavior of the Respiratory System. *Compr Physiol*, Supplement 12: Handbook of Physiology, The Respiratory System, Mechanics of Breathing: 113-130, 1986.

[5] Alastruey J. Numerical modelling of pulse wave propagation in the cardiovascular system: development, validation and clinical applications. *PhD thesis, Imperial College London, London, England*, 2006.

[6] Alastruey J, Khir AW, Matthys KS, Segers P, Sherwin SJ, Verdonck PR , Parker KH, Peiro J. Pulse wave propagation in a model human arterial network: Assessment of 1-D visco-elastic simulations against in vitro measurements. *J Biomech* **44**: 2250-2258, 2011.

[7] Albert SP, DiRocco J, Allen GB, Bates JHT, Lafollette R, Kubiak BD, Fischer J, Maroney S, Nieman GF. The role of time and pressure on alveolar recruitment. *J Appl Physiol* **106**: 757-765, 2009.

[8] Alzahrany M, Banerjee A. A biomechanical model of pendelluft induced lung injury. *J Biomech* **48**: 1804-1810, 2015.

[9] Amato MBP, Barbas CSV, Medeiros DM, Magaldi RB, Schettino GP, Lorenzi-Filho G, Kairalla RA, Deheinzelin D, Munoz C, Oliveira R, Takagaki TY, Carvalho CRR. Effect of a Protective-Ventilation Strategy on Mortality in the Acute Respiratory Distress Syndrome. *N Engl J Med* **338**: 347-354, 1998.

[10] Amato MBP, Meade MO, Slutsky AS, Brochard L, Costa ELV, Schoenfeld DA, Stewart TE, Briel M, Talmor D, Mercat A, Richard JCM, Carvalho CRR, Brower RG. Driving Pressure and Survival in the Acute Respiratory Distress Syndrome. *N Engl J Med* **372**: 747-755, 2015.

[11] Amelon R, Cao K, Ding K, Christensen GE, Reinhardt JM, Raghavan ML. Three dimensional characterization of regional lung deformation. *J Biomech* **44**: 2489-2495, 2011.

[12] Amini R, Kaczka DW. Impact of ventilation frequency and parenchymal stiffness on flow and pressure distribution in a canine lung model. *Ann Biomed Eng* **41**: 2699-2711, 2013.

[13] Amini R, Herrmann J, Kaczka DW. Intratidal Overdistention and Derecruitment in the Injured Lung: A Simulation Study. *IEEE Trans Biomed Eng* **99**, 2016.

[14] The Acute Respiratory Distress Syndrome Network. Ventilation with Lower Tidal Volumes as compared with traditional tidal volumes for acute lung injury and the acute respiratory distress syndrome. *N Engl J Med* **342**: 1301-1308, 2000.

[15] Baffico L, Grandmont C, Maury B. Multiscale modelling of the respiratory tract. *Mathematical Models and Methods in Applied Sciences, World Scientific Publishing*, 2010.

[16] Bagnoli P, Cozzi B, Zaffora A, Acocella F, Fumero R, Costantino ML. Experimental and computational biomechanical characterisation of the tracheo-bronchial tree of the bottlenose dolphin (*Tursiops truncatus*) during diving. *J Biomech* **44**: 1040-1045, 2011.

[17] Balzani D. Polyconvex anisotropic energies and modeling of damage applied to arterial walls. *PhD thesis, Technische Universität Darmstadt, Darmstadt, Germany*, 2006.

[18] Barkow U, Strohmaier A. CT images. *Provided by medical office Diagnostische Radiologie, Stuttgart, Germany*, 2007.

[19] Bates AJ, Doorly DJ, Cetto R, Calmet H, Gambaruto AM, Tolley NS, Houzeaux G, Schroter RC. Dynamics of airflow in a short inhalation. *J R Soc Interface* **12**: 20140880, 2014.

[20] Bates AJ, Comerford A, Cetto R, Schroter RC, Tolley NS, Doorly DJ. Power loss mechanisms in pathological tracheas. *J Biomech* **S0021-9290**: 00675-2, 2015.

[21] Bates AJ, Cetto R, Doorly DJ, Schroter RC, Tolley NS, Comerford A. The effects of curvature and constriction on airflow and energy loss in pathological tracheas. *Respir Physiol Neurobiol* **234**: 69-78, 2016.

[22] Bates JHT, Irvin CG. Time dependence of recruitment and derecruitment in the lung: a theoretical model. *J Appl Physiol* **93**: 705-713, 2002.

[23] Bates JHT, Suki B. Assessment of peripheral lung mechanics. *Respir Physiol Neurobiol* **163**: 54-63, 2008.

[24] Bates JHT. Lung Mechanics An inverse modeling approach. *Cambridge University Press, Cambridge, England*, 2009.

[25] Bates JHT, Smith BJ, Allen GB. Computational Models of Ventilator Induced Lung Injury and Surfactant Dysfunction. *Drug Discov Today Dis Models* **15**: 17-22, 2015.

[26] Bauer K, Brücker C. The Influence of Airway Tree Geometry and Ventilation Frequency on Airflow Distribution. *J Biomech Eng* **137**: 081001, 2015.

[27] Bayford R, Kantartzis P, Tizzard A, Yerworth R, Liatsis P, Demosthenous A. Development of a neonate lung reconstruction algorithm using a wavelet AMG and estimated boundary form. *Med Phys* **29**: 125-138, 2008.

[28] Bear J, Bachmat Y. Introduction to Modeling of Transport Phenomena in Porous Media. *Springer, Netherlands*, 1990.

[29] Bel-Brunon A, Kehl S, Martin C, Uhlig S, Wall WA. Numerical identification method for the non-linear viscoelastic compressible behavior of soft tissue using uniaxial tensile tests and image registration - application to rat lung parenchyma. *J Mech Behav Biomed Mater* **29**: 360-374, 2014.

[30] Berger LU, Bordas R, Burrowes K, Brightling CE, Hartley R, Kay D. A poroelastic model coupled to a fluid network with applications in lung modelling. *Int J Numer Meth Biomed Engng*, 2016.

[31] Bertoglio C, Caiazzo A. A tangential regularization method for backflow stabilization in hemodynamics. *J Comput Phys* **261**: 162-171, 2014.

[32] Bertram CD, Gaver DP. Biofluid mechanics of the pulmonary system. *Ann Biomed Eng* **33**: 1681-1688, 2005.

[33] Bilek AM, Dee KC, Gaver DP 3rd. Mechanisms of surface-tension-induced epithelial cell damage in a model of pulmonary airway reopening. *J Appl Physiol* **94**: 770-783, 2003.

[34] Blankman P, Hasan D, Bikker IG, Gommers D. Lung stress and strain calculations in mechanically ventilated patients in the intensive care unit. *Acta Anaesthesiol Scand* **60**: 69-78, 2016.

[35] Blatz PJ, Ko WL. Application of finite elastic theory to the deformation of rubbery materials. *Trans Soc Rheol* **6**: 223-251, 1962.

[36] Bodenstein M, David M, Markstaller K. Principles of electrical impedance tomography and its clinical application. *Crit Care Med* **37**: 713-724, 2009.

[37] Bohn DJ, Miyasaka K, Marchak BE, Thompson WK, Froese AB, Bryan AC. Ventilation by high frequency oscillation. *J Appl Physiol* **48**: 710-716, 1980.

[38] Boldea V, Sharp GC, Jiang SB, Sarrut D. 4D-CT lung motion estimation with deformable registration: Quantification of motion nonlinearity and hysteresis. *Med Phys* **35**: 1008-1018, 2008.

[39] Boudin L, Grandmont C, Lorz A, Moussa A. Modelling and numerics for respiratory aerosols. *Commun Comput Phys* **18**: 723-756, 2015.

[40] Boyd E. Growth, Including Reproduction and Morphological Development Biological Handbooks. ed Altmann P and Dittmer DS, *Washington, DC: Federation of American Societies for Experimental Biology*, 346-348, 1962.

[41] Braun F, Proenca M, Rapin M, Lemay M, Adler A, Grychtol B, Sola J, Thiran JP. Aortic blood pressure measured via EIT: investigation of different measurement settings. *Physiol Meas* **36**: 1147-1159, 2015.

[42] Bräu F. Erstellung einer parametrisierten Mikroskalen-Lungengeometrie. *Bachelor thesis, Technische Universität München, München, Germany*, 2013.

[43] Brewer KK, Sakai H, Alencar AM, Majumdar A, Arold SP, Lutchen KR, Ingenito EP, Suki B. Lung and alveolar wall elastic and hysteretic behaviour in rats: effects of elastase treatment. *J Appl Physiol* **95**: 1926-1936, 2003.

[44] Brooks AN, Hughes TJR. Streamline Upwind/Petrov-Galerkin formulations for convection dominated flows with particular emphasis on the incompressible Navier-Stokes equations. *Comput Method Appl M* **32**: 199-259, 1982.

[45] Brower RG, Lanken PN, MacIntyre N, Matthay MA, Morris A, Ancukiewicz M, Schoenfeld D, Thompson BT. Higher versus Lower Positive End-Expiratory Pressures in Patients with the Acute Respiratory Distress Syndrome. *N Eng J Med* **351**: 327-336, 2004.

[46] Brown BH, Barber DC. Electrical impedance tomography; the construction and application to physiological measurement of electrical impedance images. *Med Prog Technol* **13**: 69-75, 1987.

[47] Brown BH, Barber DC, Morice AH, Leathard AD. Cardiac and Respiratory Related Electrical Impedance Changes in the Human Thorax. *IEEE Trans Biomed Eng* **41**: 729-734, 194.

[48] Brown BH. Electrical Impedance Tomography (EIT) - A Review. *J Med Eng Technol* **27**: 97-108, 2003.

[49] Burrowes KS, Hunter PJ, Tawhai MH. Anatomically based finite element models of the human pulmonary arterial and venous trees including supernumerary vessels. *J Appl Physiol* **99**: 731-738, 2005.

[50] Burrowes KS. An anatomically-based mathematical model of the human pulmonary circulation. *PhD thesis, University of Auckland*, 2005.

[51] Calmet H, Gambaruto AM, Bates AJ, Vazquez M, Houzeaux G, Doorly DJ. Large-scale CFD simulations of the transitional and turbulent regime for the large human airways during rapid inhalation. *Comput Biol Med* **69**: 166-180, 2016.

[52] Caretto LS, Gosman AD, Patankar SV, Spalding DB. Two calculation procedures for steady, three-dimensional flows with recirculation. *Proceedings of the Third International Conference on Numerical Methods in Fluid Mechanics* **19**: 60-68, 1973.

[53] Cassidy KJ, Gavriely N, Grotberg JB. Liquid plug flow in straight and bifurcating tubes. *J Biomech Eng* **123**: 580-589, 2001.

[54] Castillo E, Castillo R, Martinez J, Shenoy M, Guerrero T. Four-dimensional deformable image registration using trajectory modeling. *Phys Med Biol* **55**: 305-327, 2009.

[55] Cavalcante FSA, Ito S, Brewer KK, Sakai H, Alencar AM, Almeida MP, Anrade JS, Majumdar A, Ingenito EP, Suki B. Mechanical interactions between collagen and proteoglycans: implications for the stability of lung tissue. *J Appl Physiol* **98**: 672-679, 2005.

[56] Cazeaux P, Grandmont C. Homogenization of a multiscale viscoelastic model with nonlocal damping, application to the human lungs. *Math Mod Meth Appl Sci* **25**: 1125, 2015.

[57] Charpail E. Analyse du comportement mecanique des côtes humaines en dynamique. *Thèse à l'École Nationale Supérieure d'Arts et Métiers, Paris, France*, 2006.

[58] Chiumello D, Carlesso E, Cadringher P, Caironi P, Valenza F, Polli F, Tallarini F, Cozzi P, Cressoni M, Colombo A, Marini JJ, Gattinoni L. Lung stress and strain during mechanical ventilation for acute respiratory distress syndrome. *Am J Respir Crit Care Med* **178**: 346-455, 2008.

[59] Chiumello D, Marino A, Brioni M, Menga F, Cigada I, Lazzerini M, Andrisani MC, Biondetti P, Cesana B, Gattinoni L. Visual anatomical lung CT scan assessment of lung recruitability. *Intensive Care Med* **39**: 66-73, 2013.

[60] Choi J, Xia G, Tawhai MH, Hoffman EA, Lin CL. Numerical study of high-frequency oscillatory air flow and convective mixing in a CT-based human airway model. *Ann Biomed Eng* **38**: 3550-3571, 2010.

[61] Choi S, Hoffman EA, Wenzel SE, Tawhai MH, Yin Y, Castro M, Lin CL. Registration-based assessment of regional lung function via volumetric CT images of normal subjects vs. severe asthmatics. *J Appl Physiol* **115**: 730-742, 2013.

[62] Choi S, Hoffman EA, Wenzel SE, Castro M, Fain SB, Jarjour NN, Schiebler ML, Chen K, Lin CL. Quantitative assessment of multiscale structural and functional alterations in asthmatic populations. *J Appl Physiol* **118**: 1286-1298, 2015.

[63] Christensen GE, Song JH, Lu W, Naqa IE, Low DA. Tracking lung tissue motion and expansion/compression with inverse consistent image registration and spirometry. *Med Phys* **34**: 2155-2163, 2007.

[64] Chung J, Hulbert GM. A time integration algorithm for structural dynamics with improved numerical dissipation: the generalised-α method. *J Appl Math* **60**: 371-375, 1993.

[65] Codd SL, Lambert RK, Alley MR, Pack RJ. Tensile stiffness of the ovine tracheal wall. *J Appl Physiol* **76**: 2627-2635, 1994.

[66] Cozzi B, Bagnoli P, Acocella F, Costantino ML. Structure and Biomechanical Properties of the Trachea of the Striped Dolphin *Stenella coeruleoalba*: Evidence for Evolutionary Adaptions to Diving. *Anat Rec A Discov Mol Cell Evol Biol* **284**: 500-510, 2005.

[67] Cignoni P, Corsini M, Ranzuglia G. MeshLab: an Open-Source 3D Mesh Processing System. *ERCIM News* **73**, 2008.

[68] Clennell MB. Tortuosity: a guide through the maze. *Geological Society, London, Special Publications* **122**: 299-344, 1997.

[69] Colletti AA, Amini R, Kaczka DW. Simulating ventilation distribution in heterogenous lung injury using a binary tree data structure. *Comput Biol Med* **41**: 936-945, 2011.

[70] Comerford A, Bauer G, Wall WA. Nanoparticle transport in a realistic model of the tracheobronchial region. *Int J Numer Meth Biomed Engng* **26**: 904-914, 2010.

[71] Comerford A, Förster C, Wall WA. Structured tree impedance outflow boundary conditions for 3d lung simulations. *J Biomech Eng* **132**: (10 pages), 2010.

[72] Comerford A, Gravemeier V, Wall WA. An algebraic variational multiscale-multigrid method for large-eddy simulation of turbulent pulsatile flows in complex geometries with detailed insight into pulmonary airway flow. *Int J Numer Meth Fluids* **71**: 1207-1225, 2012.

[73] Costa E, Borges JB, Melo A, Suarez-Sipmann F, Toufen C Jr., Böhm SH, Amato MBP. Bedside estimation of recruitable alveolar collapse and hyperdistension by electrical impedance tomography. *J Intensive Care Med* **35**: 1132-1137, 2009.

[74] Cressoni M, Amini M, Cadringher P, Chiurazzi C, Febres D, Gallazzi E, Marino A, Brioni M, Menga F, Cigada I, Carlesso E, Chiumello D, Gattinoni L. Quantification of stress raisers in ARDS. *Crit Care* **17**: P105, 2013.

[75] Cressoni M, Cadringher P, Chiurazzi C, Amini M, Gallazzi E, Marino A, Brioni M, Carlesso E, Chiumello D, Quintel M, Budego G, Gattinoni L. Lung inhomogeneity in patients with acute respiratory distress syndrome. *Am J Respir Crit Care Med* **189**: 149-158, 2014.

[76] Cressoni M, Chiurazzi C, Gotti M, Amini M, Brioni M, Algieri I, Cammaroto A, Rovati C, Massari D, di Castiglione CB, Nikolla K, Montaruli C, Lazzerini M, Dondossola D, Colombo A, Gatti S, Valerio V, Gagliano N, Carlesso E, Gattinoni L. Lung inhomogeneities and time course of ventilator-induced mechanical injuries. *Anesthesiology* **123**: 618-627, 2015.

[77] Cyr EC, Shadid JN, Tuminaro RS. Stabilization and scalable block preconditioning for the NavierStokes equations. *J Comput Phys* **231**: 345-363, 2012.

[78] Dale PJ, Matthews FL, Schroter RC. Finite element analysis of lung alveolus. *J Biomech* **13**: 865-873, 1980.

[79] Darquenne C, van Ertbruggen C, Prisk GK. Convective flow dominates aerosol delivery to the lung segments. *J Appl Physiol* **111**: 48-54, 2011.

[80] Dassow C, Wiechert L, Martin C, Schumann S, Müller-Newen G, Pack O, Guttmann J, Wall WA, Uhlig S. Biaxial distension of precision-cut lung slices. *J Appl Physiol* **108**: 713-721, 2010.

[81] Davis JM, Veness-Meehan K, Notter RH, Bhutani VK, Kendig JW, Shapiro DL. Changes in pulmonary mechanics after the administration of surfactant to infants with respiratory distress syndrome. *N Engl J Med* **319**: 476-479, 1988.

[82] Denai MA, Mahfouf M, Mohamad-Samuri S, Panoutsos G, Brown BH, Mills GH. Absolute electrical impedance tomography (aEIT) guided ventilation therapy in critical care patients: simulations and future trends. *IEEE Trans Inf Technol Biomed* **14**: 641-649, 2010.

[83] Denny E, Schroter R. The mechanical behavior of mammalian lung alveolar duct model. *J Biomech Eng* **117**: 254-261, 1995.

[84] Denny E, Schroter RC. A Mathematical model for the morphology of the pulmonary acinus. *J Biomech Eng* **118**: 210-215, 1996.

[85] Denny E, Schroter R. Relationships between alveolar size and fiber distribution in a mammalian lung alveolar duct model. *J Biomech Eng* **119**: 289-297, 1997.

[86] Denny E, Schroter RC. Viscoelastic behavior of a lung alveolar duct model. *J Biomech Eng* **122**: 143-151, 2000.

[87] Denny E, Schroter RC. A model of non-uniform lung parenchyma distortion. *J Biomech* **39**: 652-663, 2006.

[88] Derdak S, Mehta S, Stewart TE, Smith T, Rogers M, Buchman TG, Carlin B, Lowson S, Granton J, The Multicenter Oscillatory Ventilation for Acute Respiratory Distress Syndrome Trial (MOAT) Study Investigators. High-frequency oscillatory ventilation for acute respiratory distress syndrome in adults. *Am J Respir Crit Care Med* **166**: 801-808, 2002.

[89] De Backer JW, Vos WG, Vinchurkar SC, Claes R, Drollmann A, Wulfrank D, Parizel PM, Germonpre P, De Backer W. Validation of computational fluid dynamics in CT-based airway models with SPECT/CT. *Radiology* **257**: 854-862, 2008.

[90] Donea J, Huerta A. Finite element methods for flow problems. *John Wiley & Sons Ltd., Chichester, England*, 2003.

[91] Dreyfuss D, Soler P, Basset G, High SG. High inflation pressure pulmonary edema: respective effects of high airway pressure, high tidal volume, and positive end-expiratory pressure. *Am Rev Respir Dis* **137**: 1159-1164, 1988.

[92] Elke G, Fuld MK, Halaweish AF, Grychtol B, Weiler N, Hoffman EA, Frerichs I. Quantification of ventilation distribution in regional lung injury by electrical impedance tomography and xenon computed tomography. *Physiol Meas* **34**: 1303-1318, 2013.

[93] van Ertbruggen C, Hirsch C, Paiva M. Anatomically based three-dimensional model of airways to simulate flow and particle transport using computational fluid dynamics. *J Appl Physiol* **98**: 970-980, 2005.

[94] Esteban A, Anzueto A, Frutos F, Ala I, Brochard L, Stewart TE, Benito S, Epstein SK, Apezteguia C, Nightingale P, Arroliga AC, Tobin MJ for the Mechanical Ventilation International Study Group. Characteristics and outcomes in adult patients receiving mechanical ventilation: A 28-day international study. *JAMA* **287**: 345-355, 2002.

[95] Ferguson ND, Cook DJ, Guyatt GH, Mehta S, Hand L, Austin P, Zhou Q, Matte A, Walter SD, Lamontagne F, Granton JT, Arabi YM, Arroliga AC, Stewart TE, Slutsky AS, Meade MO, for the OSCILLATE Trial Investigators and the Canadian Critical Care Trials Group. High-frequency oscillation in early acute respiratory distress syndrome. *N Engl J Med* **368**: 795-805, 2013.

[96] Filoche M, Moreira AA, Andrade Jr JS, Sapoval B. Quantitative analysis of the oxygen transfer in the human acinus. *Adv Exp Med Biol* **605**: 167-172, 2008.

[97] Filoche M, Tai CF, Grotberg JB. Three-dimensional model of surfactant replacement therapy. *Proc Natl Acad Sci U S A* **112**: 9287-9292, 2015.

[98] Fischer B, Modersitzki J. Ill-posed medicine - an introduction to image registration. *Inverse Probl* **24**: 16pp, 2008.

[99] Florens M, Sapoval B, Filoche M. An anatomical and functional model of the human tracheobronchial tree. *J Appl Physiol* **110**: 756-763, 2011.

[100] Florens M, Sapoval B, Filoche M. The optimal branching asymmetry of a bidirectional distribution tree. *Comput Phys Commun* **182**: 1932-1936, 2011.

[101] Formaggia L, Quateroni A, Veneziani A. Cardiovascular Methamatics Modeling and simulation of the circulatory system. *Springer-Verlag Italia, Milano*, 2009.

[102] Formaggia L, Lamponi D, Quarteroni A. One-dimensional models for blood flow in arteries. *J Eng Math* **47**: 251-276, 2003.

[103] Frerichs I. Electrical impedance tomography (EIT) in applications related to lung and ventilation: a review of experimental and clinical activities. *Physiol Meas* **21**: R1-21, 2000.

[104] Frerichs I, Dudykevych T, Hinz J, Bodenstein M, Hahn G, Hellige G. Gravity effects on regional lung ventilation determined by functional EIT during parabolic flights. *J Appl Physiol* **91**: 39-50, 2001.

[105] Frerichs I, Hinz J, Herrmann P, Weisser G, Hahn G, Dudykevych T, Quintel M, Hellige G. Detection of local lung air content by electrical impedance tomography compared with electron beam CT. *J Appl Physiol* **93**: 660-666, 2002.

[106] Frerichs I, Becher T, Weiler N. Electrical impedance tomography imaging of the cardiopulmonary system. *Curr Opin Crit Care* **20**: 323-332, 2014.

[107] Frerichs I, Amato MB, van Kaam AH, Tingay DG, Zhao Z, Grychtol B, Bodenstein M, Gagnon H, Böhm SH, Teschner E, Stenqvist O, Mauri T, Torsani V, Camporota L, Schibler A, Wolf GK, Gommers D, Leonhardt S, Adler A, TREND study group. Chest electrical

impedance tomography examination, data analysis, terminology, clinical use and recommendations: consensus statement of the TRanslational EIT developmeNt stuDy group. *Thorax*, 2016.

[108] Fuld MK, Easley RB, Saba OI, Chon D, Reinhardt JM, Hoffman EA, Simon BA. CT-measured regional specific volume change reflects regional ventilation in supine sheep. *J Appl Physiol* **104**: 1177-1184, 2008.

[109] Fung YC. A model of the lung structure and its validation. *J Appl Physiol* **64**: 2132-2141, 1988.

[110] Gabriel C, Gabriel S, Corthout E. The dielectric properties of biological tissues: I. Literature survey. *Med Phys Biol* **41**: 22312249, 1996.

[111] Gabriel S, Lau R, Gabriel C. The dielectric properties of biological tissues: II. Measurements in the frequency range 10 Hz to 20 GHz. *Med Phys Biol* **41**: 22512269, 1996.

[112] Gattinoni L, Caironi P, Pelosi P, Goodman LR. What has computed tomography taught us about the acute respiratory distress syndrome? *Am J Respir Crit Care Med* **164**: 1701-1711, 2001.

[113] Gattinoni L, Caironi P, Cressoni M, Chiumello D, Ranieri VM, Quintel M, Russo S, Patroniti N, Cornejo R, Bugedo G. Lung recruitment in patients with the acute respiratory distress syndrome. *N Engl J Med* **354**: 1175-1186, 2006.

[114] Gattinoni L, Carlesso E, Caironi P. Stress and strain within the lung. *Curr Opin Crit Care* **18**: 42-47, 2012.

[115] Gattinoni L, Carlesso E, Langer T. Towards ultraprotective mechanical ventilation. *Curr Opin Anaesthesiol* **25**: 141-147, 2012.

[116] Gattinoni L, Marini JJ, Pesenti A, Quintel M, Mancebo J, Brochard L. The ”baby lung” became an adult. *Intensive Care Med* **42**: 663-673, 2016.

[117] Gaudenzi F, Avolio AP. Conf Proc IEEE Eng Med Biol Soc. *Intensive Care Med* **2013**: 473-476, 2013.

[118] Gauthier SP, Wolfson MR, Deoras KS, Shaffer TH. Structure-function of airway generations 0 to 4 in the preterm lamb. *Pediatr Res* **31**: 157-162, 1992.

[119] Gaver DP 3rd, Samsel RW, Solway J. Effects of surface tension and viscosity on airway reopening. *J Appl Physiol* **69**: 74-85, 1990.

[120] Gee MW, Förster Ch, Wall WA. A computational strategy for prestressing patient-specific biomechanical problems under finite deformation. *Int J Numer Meth Biomed Engng* **26**: 52-72, 2010.

[121] Gee MW, Küttler U, Wall WA. Truly monolithic algebraic multigrid for fluid-structure interaction. *Int J Numer Meth Engng* **85**: 987-1016, 2011.

[122] Geitner C. Simulation der Atembewegung mittels 4D-CT Daten der Lunge. *Bachelor thesis, Technische Universität München, München, Germany*, 2016.

[123] Gerbeau JF, Vidrascu M, Frey P. Fluidstructure interaction in blood flows on geometries coming from medical imaging. *Comput Struct* **83**: 155-165, 2005.

[124] van Genderingen HR, van Vught AJ, Jansen JR. Estimation of regional lung volume changes by electrical impedance pressures tomography during a pressure-volume maneuver. *Intensive Care Med* **29**: 233-240, 2003.

[125] Geuzaine C, Remacle JF. Gmsh: a three-dimensional finite element mesh generator with built-in pre- and post-processing facilities. *Int J Numer Methods Eng* **79**: 1309-1331, 2009.

[126] Ghadiali SN, Gaver DP. Biomechanics of liquid-epithelium interactions in pulmonary airways. *Respir Physiol Neurobiol* **163**: 232-243, 2008.

[127] Ghadiali SN, Huang. Role of airway recruitment and derecruitment in lung injury. *Crit Rev Biomed Eng* **39**: 297-317, 2011.

[128] Goligher EC, Ferguson ND, Brochard LJ. Clinical challenges in mechanical ventilation. *Lancet* **387**: 1856-1866, 2016.

[129] Graham B, Adler A. Objective selection of hyperparameter for EIT. *Physiol Meas* **27**: S65, 2013.

[130] de la Grandmaison GL, Clairand I, Durigon M. Organ weight in 684 adult autopsies: new tables for a Caucasoid population. *Forensic Sci Int* **119**: 149-154, 2001.

[131] Grandmont C, Maury B, Meunier N. A viscoelastic model with non-local damping: Application to the human lungs. *ESAIM M2AN* **40**: 201-224, 2006.

[132] Grandmont C, Maury B, Soualah A. Multiscale modelling of the respiratory track: a theoretical framework. *ESAIM Proc* **23**: 10-29, 2008.

[133] Gravemeier V, Gee MW, Kronbichler M, Wall WA. An algebraic variational multiscale-multigrid method for large eddy simulation of turbulent flow. *Comput Methods Appl Mech Engrg* **199**:853-864, 2010.

[134] Gravemeier V, Comerford A, Yoshihara L, Ismail M, Wall WA. A novel formulation for Neumann inflow boundary conditions in biomechanics. *Int J Numer Meth Biomed Engng* **28**:560-573, 2012.

[135] Greenblatt EE, Butler JP, Venegas JG, Winkler T. Pendelluft in the bronchial tree. *J Appl Physiol* **117**:979-988, 2014.

[136] Gresho PM, Sani RL. Incompressible flow and the finite element method volume two: isothermal flow. *John Wiley & Sons Ltd., Chichester, England*, 2000.

[137] Grotberg JB. Respiratory fluid mechanics and transport processes. *Annu Rev Biomed Eng* **3**: 421-457, 2001.

[138] Grotberg JB. Respiratory fluid mechanics. *Phys Fluids* **23**: 021301, 2011.

[139] Grychtol B, Adler A. FEM electrode refinement for electrical impedance tomography. *Conf Proc IEEE Eng Med Biol Soc* 2013: 6429-6432, 2013.

[140] Guerin C, Reignier J, Richard J-C, Beuret P, Gacouin A, Boulain T, Mercier E, Badet M, Mercat A, Baudin O, Clavel M, Chatellier D, Jaber S, Rosselli S, Mancebo J, Sirodot M, Hilbert G, Bengler C, Richecoeur J, Gainnier M, Bayle F, Bourdin G, Leray V, Girard R, Baboi L, Ayzac L, for the PROSEVA Study Group. Prone Positioning in Severe Acute Respiratory Distress Syndrome. *N Engl J Med* **368**: 2159-2168, 2013.

[141] Guyton AC, Hall JE. Textbook of Medical Physiology, Eleventh Edition. *Elsevier, Saunders, Philadelphia, PA*, 2006.

[142] Haber E, Modersitzki J. A multilevel method for image registration. *SIAM J Sci Comput* **27**: 1594-1607, 2006.

[143] Haberthur D, Barre SF, Tschanz SA, Yao E, Stampanoni M, Schittny JC. Visualization and stereological characterization of individual rat lung acini by high-resolution X-ray tomographic microscopy. *J Appl Physiol* **115**: 1379-1387, 2013.

[144] Haefeli-Bleuer B, Weibel ER. Morphometry of the human pulmonary acinus. *Anat Rec* **220**: 401-414, 1988.

[145] Hamlington KL, Smith BJ, Allen GB, Bates JHT. Predicting ventilator-induced lung injury using a lung injury cost function. *J Appl Physiol* **121**: 106-114, 2016.

[146] Handels H. Medizinische Bildverarbeitung - Bildanalyse, Mustererkennung und Visualisierung für die computergestützte ärztliche Diagnostik und Therapie. *Vieweg+Teubner, Wiesbaden, Germany*, 2009.

[147] Harris RS. Pressure-volume curves of the respiratory system. *Respir Care* **50**: 78-98, 2005.

[148] Hazel AL, Heil M. Three-dimensional airway reopening: the steady propagation of a semi-infinite bubble into a buckled elastic tube. *J Fluid Mech* **478**: 47-70, 2003.

[149] Hazel AL, Heil M. Finite-Reynolds-number effects in steady, three-dimensional airway reopening. *J Biomech Eng* **128**: 573-578, 2005.

[150] Heil M. An efficient solver for the fully coupled solution of large-displacement fluidstructure interaction problems. *Comput Method Appl M* **193**: 1-23, 2004.

[151] Heil M, Hazel AL, Boyle J. Solvers for large-displacement fluidstructure interaction problems: segregated versus monolithic approaches. *Comput Mech* **43**: 91-101, 2008.

[152] Henry FS, Tsuda A. Onset of alveolar recirculation in the developing lungs and its consequence on nanoparticle deposition in the pulmonary acinus. *J Appl Physiol* **120**: 38-54, 2016.

[153] Heroux MA, Bartlett RA, Howle VE, Hoekstra RJ, Hu JJ, Kolda TG, Lehoucq RB, Long KR, Pawlowski RP, Phipps ET, Salinger AG, Thornquist HK, Tuminaro RS, Willenbring JM, Williams A, Stanley KS. An overview of the Trilinos project. *ACM Trans Math Softw* **31**: 397-423, 2005.

[154] Herrmann J, Tawhai MH, Kaczka DW. Regional gas transport in the heterogeneous lung during oscillatory ventilation. *J Appl Physiol*, 2016.

[155] Hickling KG. The pressure-volume curve is greatly modified by recruitment A mathematical model of ARDS lungs. *Am J Respir Crit Care Med* **158**: 194-202, 1998.

[156] High KC, Ultman JS, Karl SR. Mechanically induced pendelluft flow in a model airway bifurcation during high frequency oscillation. *J Biomech Eng* **113**: 342-347, 1991.

[157] Higuita-Castro N, Mihai C, Hansford DJ, Ghadiali SN. Influence of airway wall compliance on epithelial cell injury and adhesion during interfacial flows. *J Appl Physiol* **117**: 1231-1242, 2014.

[158] Hilgendorff A, OReilly MA. Bronchopulmonary dysplasia early changes leading to long-term consequences. *Front Med* **2**: 2, 2015.

[159] Hofemeier P, Sznitman J. Role of alveolar topology on acinar flows and convective mixing. *J Biomech Eng* **136**: 061007, 2014.

[160] Hofemeier P, Sznitman J. Revisiting pulmonary acinar particle transport: convection, sedimentation, diffusion, and their interplay. *J Appl Physiol* **118**: 1375-1385, 2015.

[161] Hofemeier P, Sznitman J. The role of anisotropic expansion for pulmonary acinar aerosol deposition. *J Biomech* **49**: 3543-3548, 2016.

[162] Hofemeier P, Shachar-Berman L, Tenenbaum-Katan J, Filoche M, Sznitman J. Unsteady diffusional screening in 3D pulmonary acinar structures: from infancy to adulthood. *J Biomech* **49**: 2193-2200, 2016.

[163] Holder DS. Electrical Impedance Tomography. Methods, History and Applications, Part 1 Algorithms. *Institute of Physics: Bristol and Philadelphia*, 2005.

[164] Holzapfel GA. Nonlinear Solid Mechanics: A Continuum Approach for Engineering. *John Wiley & Sons Ltd., Chichester, England*, 2000.

[165] Holzer L, Wiedenmann D, Münch B, Keller L, Prestat M, Gasser Ph, Robertson I, Grobety B. The influence of constrictivity on the effective transport properties of porous layers in electrolysis and fuel cells. *J Mater Sci* **48**: 2934-2952, 2013.

[166] Horsfield K, Dart G, Olson DE, Filley GF, Cumming G. Models of the human bronchial tree. *J Appl Physiol* **31**: 207-217, 1971.

[167] Horsfield K. Morphometry of airways. *Compr Physiol*, Supplement 12: Handbook of Physiology, The Respiratory System, Mechanics of Breathing: 75-88, 1986.

[168] Horsfield K, Gordon WI, Kemp W, Phillips S. Growth of the bronchial tree in man. *Thorax* **42**: 383-388, 1987.

[169] Hu Y, Bian S, Grotberg J, Filoche M, White J, Takayama S, Grotberg JB. A microfluidic model to study fluid dynamics of mucus plug rupture in small lung airways. *Biomicrofluidics* **9**: 044119, 2015.

[170] Hughes JMB, Hoppin FG, Mead J. Effect of lung inflation on bronchial length and diameter in excised lungs. *J Appl Physiol* **32**: 25-35, 1972.

[171] Hughes TJR, Franca LP, Balestra M. A new finite element formulation for computational fluid dynamics: V. Circumventing the Babuska-Brezzi condition: a stable Petrov-Galerkin formulation of the Stokes problem accommodating equal-order interpolation. *Comput Method Appl M* **59**: 85-99, 1986.

[172] Hughes TJR, Scovazzi G, Franca LP. Multiscale and stabilized methods. Encyclopedia of Computational Mechanics, eds Stein E, de Borst R, Hughes TJR, *John Wiley & Sons Ltd., Chichester, England*, pp. 5-59.

[173] Imay Y, Slutsky AS. High-frequency oscillatory ventilation and ventilator-induced lung injury. *Crit Care Med* **33**: S129-133, 2005.

[174] Ingenito EP, Mark L, Morris J, Espinosa FF, Kamm RD, Johnson M. Biophysical characterization and modeling of lung surfactant components. *J Appl Physiol* **86**: 1702-1714, 1999.

[175] Irons B, Tuck RC. A version of the Aitken accelerator for computer implementation. *Int J Numer Methods Eng* **1**: 275-277, 1969.

[176] Ismail M, Comerford A, Wall WA. Coupled and reduced dimensional modeling of respiratory mechanics during spontaneous breathing. *Int J Numer Meth Biomed Engng* **29**: 1285-1305, 2013.

[177] Ismail M. Reduced dimensional modeling of the entire human lung. *PhD thesis, Technische Universität München, München, Germany*, 2014.

[178] Jahani N, Yin Y, Hoffman EA, Lin CL. Assessment of regional non-linear tissue deformation and air volume change of human lungs via image registration. *J Biomech* **47**: 1626-1633, 2014.

[179] Jahani N, Choi XS, Choi J, Iyer K, Hoffman EA, Lin CL. Assessment of regional ventilation and deformation using 4D-CT imaging for healthy human lungs during tidal breathing. *J Appl Physiol* **119**: 1064-1074, 2015.

[180] Kaczka DW, Herrmann J, Zonneveld CE, Tingay DG, Lavizzari A, Noble PB, Pillow JJ. Multifrequency oscillatory ventilation in the premature lung: Effects on gas exchange, mechanics, and ventilation distribution. *Anesthesiology* **123**: 1394-1403, 2015.

[181] Kamm RD, Schroter RC. Is airway closure caused by a liquid film instability? *Respir Physiol* **75**: 141-156, 1989.

[182] Kay SS, Bilek AM, Dee KC, Gaver DP 3rd. Pressure gradient, not exposure duration, determines the extent of epithelial cell damage in a model of pulmonary airway reopening. *J Appl Physiol* **97**: 269-276, 2004.

[183] Khangure SR, Noble PB, Sharma A, Chia PY, McFawn PK, Mitchell HW. Cyclical elongation regulates contractile responses of isolated airways. *J Appl Physiol* **97**: 913-919, 2004.

[184] Kitaoka H, Tamura S, Takaki R. A three-dimensional model of the human pulmonary acinus. *J Appl Physiol* **88**: 2260-2268, 2000.

[185] Kitaoka H, Nieman GF, Fujino Y, Carney D, DiRocco J, Kawase I. A 4-dimensional model of the alveolar structure. *J Physiol Sci* **57**: 175-185, 2007.

[186] Kleinstreuer C, Zhang Z, Donohue J. Targeted drug-aerosol delivery in the human respiratory system. *Annu Rev Biomed Eng* **10**: 195-220, 2008.

[187] Kleinstreuer C, Zhang Z. Airflow and particle transport in the human respiratory system. *Annu Rev Fluid Mech* **42**: 301-334, 2010.

[188] Kleinstreuer C, Feng Y. Computational analysis of non-spherical particle transport and deposition in shear flow with application to lung aerosol dynamics - a review. *J Biomech Eng* **135**: 021008, 2013.

[189] Koshiyama K, Wada S. Mathematical model of a heterogeneous pulmonary acinus structure. *Comput Biol Med* **62**: 25-32, 2015.

[190] Kowe R, Schroter RC, Matthews FL, Hitchings D. Analysis of elastic and surface tension effects in the lung alveolus using finite element methods. *J Biomech* **19**: 541-549, 2000.

[191] Küttler U, Wall WA. Fixed-point fluid-structure interaction solvers with dynamic relaxation. *Comput Mech* **43**: 61-72, 2008.

[192] Küttler U. Effiziente Lösungsverfahren für Fluid-Struktur-Interaktions Probleme. *PhD thesis, Technische Universität,München, München, Germany*, 2009.

[193] Küttler U, Gee M, Förster C, Comerford A, Wall WA. Coupling strategies for biomedical fluid-structure interaction problems. *Int J Numer Meth Biomed Engng* **26**: 305-321, 2010.

[194] Kumar H, Vasilescu DM, Yin Y, Hoffman EA, Tawhai MH, Lin CL. Multiscale imaging and registration-driven model for pulmonary acinar mechanics in the mouse. *J Appl Physiol* **114**: 971-978, 2013.

[195] Lachmann B. Open up the lung and keep the lung open. *Intensive Care Med* **18**: 319-321, 1992.

[196] Lambert RK, Wilson TA, Hyatt RE, Rodarte JR. A computational model for expiratory flow. *J Appl Physiol* **52**: 44-56, 1982.

[197] Lambert AR, O'Shaughnessy P, Tawhai MH, Hoffman EA, Lin CL. Regional deposition of particles in an image-based airway model: Large-eddy simulation and left-right lung ventilation asymmetry. *Aerosol Sci Technol* **45**: 11-25, 2011.

[198] LaPrad, Lutchen KR, Suki B. A Mechanical Design Principle for Tissue Structure and Function in the Airway Tree. *PLoS Comput Biol* **9**: e1003083, 2013.

[199] Ley S, Mayer D, Brook BS, van Beek EJR, Heussel CP, Rinck D, Hose R, Markstaller K, Kauczor HU. Radiological imaging as the basis for a simulation software of ventilation in the tracheo-bronchial tree. *Eur Radiol* **12**: 2218-2228, 2002.

[200] Levy MM. PEEP in ARDS - How Much Is Enough? *N Engl J Med* **351**: 389-391, 2004.

[201] Levy R, Hill DB, Forest MG, Grotberg JB. Pulmonary fluid flow challenges for experimental and mathematical modeling. *Integr Comp Biol* **54**: 985-1000, 2014.

[202] Le Rolle V, Samson N, Praud JP, Hernandez AI. Mathematical modeling of respiratory system mechanics in the newborn lamb. *Acta Biotheor* **61**: 91-107, 2013.

[203] Lester H, Arridge SR. A survey of hierarchical non-linear medical image registration. *Pattern Recognit* **32**: 129-149, 1999.

[204] Lionheart WRB. EIT reconstruction algorithms: pitfalls, challenges and recent developments. *Physiol Meas* **25**: 125, 2004.

[205] Lin CL, Tawhai MH, McLennan G, Hoffman EA. Characteristics of the turbulent laryngeal jet and its effect on airflow in the human intra-thoracic airways. *Respir Physiol Neurobiol* **157**: 295-309, 2007.

[206] Lin CL, Tawhai MH, Hoffman EA. Multiscale image-based modeling and simulation of gas flow and particle transport in the human lungs. *Wiley Interdiscip Rev Syst Biol Med* **5**: 643-655, 2013.

[207] Longest P, Tian G, Walenga R, Hindle M. Comparing MDI and DPI aerosol deposition using in vitro experiments and a new stochastic individual path (SIP) model of the conducting airways. *Pharm Res* **29**: 1670-1688, 2012.

[208] Lupton-Smith AR, Argent AC, Rimensberger PC, Morrow BM. Challenging a paradigm: Positional changes in ventilation distribution are highly variable in healthy infants and children. *Pediatr Pulmonol* **49**: 764-771, 2014.

[209] Ma B, Lutchen KR. An anatomically based hybrid computational model of the human lung and its application to low frequency oscillatory mechanics. *Ann Biomed Eng* **14**: 1691-1704, 2006.

[210] Ma B, Lutchen K. CFD simulation of aerosol deposition in an anatomically based human large-medium airway model. *Ann Biomed Eng* **37**: 271-285, 2009.

[211] Ma B, Bates JHT. Modeling the complex dynamics of derecruitment in the lung. *Ann Biomed Eng* **38**: 3466-3477, 2010.

[212] Ma B, Sanderson M, Bates JH. Airway-parenchymal interdependence in the lung slice. *Respir Physiol Neurobiol* **185**: 211-216, 2013.

[213] Ma B, Bates JHT. Mechanical interactions between adjacent airways in the lung. *J Appl Physiol* **116**: 628-634, 2014.

[214] Magnussen JS, Chicco P, Palmer AW, Van der Wall H, Vu DH. Creation of a three-dimensional model of human segmental lung anatomy. *AJR Am J Roentgenol* **174**: 1333-1336, 2000.

[215] Mahmoud RA, Proquitte H, Hadhood SE, Schmalisch G. Effect of endotracheal tube leakage on respiratory function monitoring: Comparison of three neonatal ventilators. *J Pediatr Intensive Care* **2**: 61-69, 2012.

[216] Majumdar A, Alencar AM, Buldyrev SV, Hantos Z, Lutchen KR, Stanley H, Suki B. Relating airway diameter distributions to regular branching asymmetry in the lung. *Phys Rev Lett* **95**: 168101, 2005.

[217] Malve M, del Palomar AP, Trabelsi O, Lopez-Villalobos JL, Ginel A, Doblare M. Modeling of the fluid structure interaction of a human trachea under different ventilation conditions. *Int Commun Heat Mass* **38**: 10-15, 2011.

[218] Markelj P, Tomazevic D, Pernus F, Likar BT. Robust gradient-based 3-D/2-D registration of CT and MR to X-ray images. *IEEE Trans Med Imaging* **27**: 1704-1714, 2008.

[219] Markstaller K, Kauczor H-U, Weiler N, Karmrodt J, Doebrich M, Ferrante M, Thelen M, Eberle B. Lung density distribution in dynamic CT correlates with oxygenation in ventilated pigs with lavage ARDS. *Br J Anaesth* **91**: 699-708, 2003.

[220] Martin S, Maury B. Modeling of the oxygen transfer in the respiratory process. *ESAIM Math Model Numer Anal* **47**, 2012.

[221] Mascheroni D, Kolobow T, Fumagalli R, Moretti MP, Chen V, Buckhold D. Acute respiratory failure following pharmacologically induced hyperventilation: an experimental animal study. *J Intensive Care Med* **15**: 8-14, 1988.

[222] Massa CB, Allen GB, Bates JHT. Modeling the dynamics of recruitment and derecruitment in mice with acute lung injury. *J Appl Physiol* **105**: 1813-1821, 2008.

[223] Matthay MA, Bhattacharya S, Gaver D, Ware LB, Lim LH, Syrkina O, Eyal F, Hubmayr R. Ventilator-induced lung injury: in vivo and in vitro mechanisms. *Am J Physiol Lung Cell Mol Physiol* **283**: L678-682, 2002.

[224] Mauri T, Bellani G, Confalonieri A, Tagliabue P, Turella M, Coppadoro A, Citerio G, Patroniti N, Pesenti A. Topographic distribution of tidal ventilation in acute respiratory distress syndrome: effects of positive end-expiratory pressure and pressure support. *Crit Care Med* **41**: 1664-1673, 2013.

[225] Maury B. The Respiratory System in Equations. Modeling, Simulation and Applications 7, *Springer-Verlag, Italia*, 2013.

[226] Mauroy B, Filoche M, Andrade JS Jr, Sapoval B. Interplay between geometry and flow distribution in an airway tree. *Phys Rev Lett* **90**: 148101, 2003.

[227] Mauroy B, Filoche M, Weibel ER, Sapoval B. An optimal bronchial tree may be dangerous. *Nature* **427**: 633-636, 2004.

[228] Mead J, Takishima T, Leith D. Stress distribution in lungs: a model of pulmonary elasticity. *J Appl Physiol* **28**: 596-608, 1970.

[229] Meade MO, Cook DJ, Guyatt GH, Slutsky AS, Arabi YM, Cooper DJ, Davies AR, Hand LE, Zhou Q, Thabane L, Austin P, Lapinsky S, Baxter A, Russel J, Skrobik Y, Ronco JJ, Stewart TE. Ventilation Strategy Using Low Tidal Volumes, Recruitment Maneuvers, and High Positive End-Expiratory Pressure for Acute Lung Injury and Acute Respiratory Distress Syndrome: A Randomized Controlled Trial. *JAMA* **299**: 637-645, 2008.

[230] Menache MG, Hofmann W, Ashgarian B, Miller FJ. Airway Geometry Models of Children's Lungs for Use in Dosimetry Modeling. *Inhal Toxicol* **20**: 101-126, 2008.

[231] Mercer RR, Crapo JD. Three dimensional reconstruction of the rat acinus. *J Appl Physiol* **63**: 785-794, 1987.

[232] Metzger RJ, Klein OD, Martin GR, Krasnow MA. The branching programme of mouse lung development. *Nature* **453**: 745-750, 2008.

[233] Miedema M, de Jongh FH, Frerichs I, van Veenendaal MB, van Kaam AH. The effect of airway pressure and oscillation amplitude on ventilation in pre-term infants. *Eur Respir J* **40**: 479-484, 2012.

[234] Miller TL, Altmann AR, Tsuda T, Shaffer TH. An ultrasound imaging method for in vivi tracheal bulk and Young's muduli of elasticity. *J Biomech* **40**: 1615-1621, 2006.

[235] Miyawaki S, Tawhai MH, Hoffman EA, Lin CL. Effect of carrier gas properties on aerosol distribution in a CT-based human airway numerical model. *Ann Biomed Eng* **40**: 1495-1507, 2012.

[236] Montaudon M, Desbarats P, Berger P, de Dietrich G, Marthan R, Laurent F. Assessment of bronchial wall thickness and lumen diameter in human adults using multidetector computed tomography: comparison with theoretical models. *J Anat* **211**: 579-588, 2007.

[237] Naureckas ET, Dawson CA, Gerber BS, Gaver DP 3rd, Gerber HL, Linehan JH, Solway J, Samsel RW. Airway reopening pressure in isolated rat lungs. *J Appl Physiol* **76**: 1372-1377, 1994.

[238] Nebuya S, Mills GH, Milnes P, Brown BH. Indirect measurement of lung density and air volume from electrical impedance tomography (EIT) data. *Physiol Meas* **32**: 1953-1967, 2011.

[239] Netter FH. Atlas of Human Anatomy. Sixth Edition, *Elsevier, Saunders, Philadelphia, PA*, 2014.

[240] Neumann RP, Pillow JJ, Thamrin C, Larcombe AN, Hall GL, Schulzke SM. Influence of gestational age on dead space and alveolar ventilation in preterm infants ventilated with volume guarantee. *Neonatology* **107**: 43-49, 2015.

[241] Nguyen DT, Jin C, Thiagalingam A, McEwan AL. A review on electrical impedance tomography for pulmonary perfusion imaging. *Physiol Meas* **33**: 695-706, 2012.

[242] Nieman GF, Gatto LA, Habashi NM. Impact of mechanical ventilation on the pathophysiology of progressive acute lung injury. *J Appl Physiol* **119**: 1245-1261, 2015.

[243] Noel CE, Parikh PJ. Effect of mid-scan breathing changes on quality of 4DCT using a commercial phase-based sorting algorithm. *Med Phys* **38**: 2430-2438, 2011.

[244] Nopp P, Rapp E, Pfützner H, Nakesch H, Ruhsam Ch. Dielectric properties of lung tissue as a function of air content. *Phys Med Biol* **38**: 699-716, 1993.

[245] Nopp P, Harris ND, Zhao TX, Brown BH. Model for the dielectric properties of human lung tissue against frequency and air content. *Med Biol Eng Comput* **35**: 695-702, 1997.

[246] Oakes JM, Marsden AL, Grandmont C, Shadden SC, Darquenne C, Vignon-Clementel IE. Airflow and Particle Deposition Simulations in Health and Emphysema: From In Vivo to In Silico Animal Experiments. *Ann Biomed Eng* **42**: 899-914, 2014.

[247] Oakes JM, Marsden AL, Grandmont C, Darquenne C, Vignon-Clementel IE. Distribution of aerosolized particles in healthy and emphysematous rat lungs: Comparison between experimental and numerical studies. *J Biomech* **48**: 1147-1157, 2015.

[248] Oakes JM, Hofemeier P, Vignon-Clementel IE, Sznitman J. Aerosols in healthy and emphysematous in silico pulmonary acinar rat models. *J Biomech* **49**: 2213-2220, 2016.

[249] Ochs M, Nyengaard JR, Jung A, Knudsen L, Voigt M, Wahlers T, Richter J, Gundersen HJ. The number of alveoli in the human lung. *Am J Respir Crit Care Med* **169**: 120-124, 2004.

[250] Oertel H jr. Prandtl - Essentials of Fluid Mechanics. *3rd Edition, Springer, New York, United States*, 2010.

[251] Ogden RW. Large deformation isotropic elasticity - on the correlation of theory and experiment for incompressible rubberlike solids. *P Roy Soc Lond A Mat* **326**: 565-584, 1972.

[252] Okazawa M, Pare PD, Lambert RK. Compliance of peripheral airways deduced from morphometry. *J Appl Physiol* **89**: 2373-2381, 2000.

[253] Ostrovski Y, Hofemeier P, Sznitman J. Augmenting regional and targeted delivery in the pulmonary acinus using magnetic particles. *Int J Nanomedicine* **11**: 3385-3395, 2016.

[254] Otis DR, Ingenito EP, Kamm RD, Johnson M. Dynamic surface tension of surfactant TA: experiments and theory. *J Appl Physiol* **77**: 2681-2688, 1994.

[255] Papadakos PJ, Lachmann B. The open lung concept of mechanical ventilation: the role of recruitment and stabilization. *Crit Care Clin* **23**: 241-250, 2007.

[256] Pare PD, Mitzner W. Airway-parenchymal interdependence. *Compr Physiol* **2**: 1921-1935, 2012.

[257] Patroniti N, Foti G, Cortinovis B, Maggioni E, Bigatello LM, Cereda M, Pesenti M. Sigh improves gas exchange and lung volume in patients with acute respiratory distress syndrome undergoing pressure support ventilation. *Anesthesiology* **96**: 788-794, 2002.

[258] Pedley T, Schroter R, Sudlow M. The prediction of pressure drop and variation of resistance within the human bronchial airways. *Respir Physiol* **9**: 387-405, 1970.

[259] Pedley TJ. Pulmonary fluid dynamics. *Ann Rev Fluid Mech* **9**: 229-274, 1977.

[260] Pelosi P, Goldner M, McKibben A, Adams A, Eccher G, Caironi P, Losappio S, Gattinoni L, Marini JJ. Recruitment and derecruitment during acute respiratory failure: an experimental study. *Am J Respir Crit Care Med* **164**: 122-130, 2001.

[261] Perun MD, Gaver DP 3rd. Interaction between airway lining fluid forces and parenchymal tethering during pulmonary airway reopening. *J Appl Physiol* **79**: 1717-1728, 1995.

[262] Polydorides N, Lionheart WRB. A Matlab toolkit for three-dimensional electrical impedance tomography: a contribution to the Electrical Impedance and Diffuse Optical Reconstruction Software project. *Meas Sci Technol* **13**: 1871-1883, 2002.

[263] Pope SB. Turbulent Flows. *Cambridge University Press, Cambridge, England*, 2000.

[264] Popp A, Gitterle M, Gee MW, Wall WA. A dual mortar approach for 3D finite deformation contact with consistent linearization. *Int J Numer Meth Eng* **11**: 1428-1465, 2010.

[265] Powell WR. Static Mechanical Properties of the Trachea and Bronchial Tree. *J Biomech* **8**: 111-117, 1975.

[266] Prange HD. Laplace's law and the alveolus: a misconception of anatomy and a misapplication of physics. *Adv Physiol Educ* **27**: 34-40, 2003.

[267] Protti A, Cressoni M, Santini A, Langer T, Mietto C, Febres D, Chierichetti M, Coppola S, Conte G, Gatti S, Leopardi O, Masson S, Lombardi L, Lazzerini M, Rampoldi E, Cadringher P, Gattinoni L. Lung stress and strain during mechanical ventilation: any safe threshold? *Am J Respir Crit Care Med* **183**: 1354-1362, 2011.

[268] Protti A, Votta E, Gattinoni L. Which is the most important strain in the pathogenesis of ventilator-induced lung injury: dynamic or static? *Curr Opin Crit Care* **20**: 33-38, 2014.

[269] Protti A, Andreis DT, Milesi M, Lapichino GE, Monti M, Comini B, Pugni P, Melis V, Santini A, Dondossola D, Gatti S, Lombardi L, Votta E, Carlesso E, Gattinoni L. Lung anatomy, energy load, and ventilator-induced lung injury. *Intensive Care Med Exp* **3**: 34, 2015.

[270] Quintel M, Pelosi P, Caironi P, Meinhardt JP, Luecke T, Herrmann P, Taccone P, Rylander C, Valenza F, Carlesso E, Gattinoni L. An increase of abdominal pressure increases pulmonary edema in oleic acidinduced lung injury. *Am J Respir Crit Care Med* **169**: 534-541, 2004.

[271] Ranieri VM, Rubenfeld GD, Thompson BT, Ferguson ND, Caldwell E, Fan E, Camporota L, Slutsky AS. Acute respiratory distress syndrome: The Berlin definition. *JAMA* **307**: 2526-2533, 2012.

[272] Rausch SMK, Haberthür D, Stampanoni M, Schittny JC, Wall WA. Local strain distribution in real three-dimensional alveolar geometries. *Ann Biomed Eng* **39**: 2835-2843, 2011.

[273] Rausch SMK, Martin C, Bornemann PB, Uhlig S, Wall WA. Material model of lung parenchyma based on living precision-cut lung slice testing. *J Mech Behav Biomed Mater* **4**: 583-592, 2011.

[274] Reifferscheid F, Elke G, Pulletz S, Gawelczyk B, Lautenschlager I, Steinfath M, Weiler N, Frerichs I. Regional ventilation distribution determined by electrical impedance tomography: reproducibility and effects of posture and chest plane. *Respirology* **16**: 523-531, 2011.

[275] Reinhardt JM, Ding K, Cao K, Christensen GE, Hoffman EA, Bodas SV. Registration-based estimates of local lung tissue expansion compared to xenon CT measures of specific ventilation. *Med Image Anal* **12**: 752-763, 2008.

[276] Rettinger AK. Respiratory flow simulation with dynamic airway reopening. *Bachelor thesis, Technische Universität München, München, Germany*, 2016.

[277] Reynolds D, Lee J. Modeling study of the pressure-flow relationship of the bronchial tree (abstract). *FASEB J* **38**: 1444, 1979.

[278] Richard JC, Pouzot C, Gros A, Tourevieille C, Lebars D, Lavenne F, Frerichs I, Guerin C. Electrical impedance tomography compared to positron emission tomography for the measurement of regional lung ventilation: an experimental study. *Crit Care* **13**: R83, 2009.

[279] Robertson C, Lee SW, Anh YC, Mahon S, Chen Z, Brenner M, George SC. Investigating *in vivo* airway wall mechanics during tidal breathing with optical coherence tomography. *J Biomed Opt* **16**: 106011, 2011.

[280] Rocco PR, Dos Santos C, Pelosi P. Pathophysiology of ventilator-associated lung injury. *Curr Opin Anaesthesiol* **25**: 123-130, 2012.

[281] Rodarte JR, Rehder K. Dynamics of Respiration. *Compr Physiol*, Supplement 12: Handbook of Physiology, The Respiratory System, Mechanics of Breathing: 131-144, 1986.

[282] Rohrer F. Flow resistance in human air passages and the effect of irregular branching of the bronchial system on the respiratory process in various regions of the lungs. *Arch Ges Physiol* **162**: 225-299, 1915.

[283] Roth CJ, Ismail M, Yoshihara L, Wall WA. A comprehensive computational human lung model incorporating interacinar dependencies: Application to spontaneous breathing and mechanical ventilation. *Int J Numer Meth Biomed Engng*, 2016.

[284] Roth CJ, Ehrl A, Becher T, Frerichs I, Schittny JC, Weiler N, Wall WA. Correlation between alveolar ventilation and electrical properties of lung parenchyma. *Physiol Meas* **36**: 1211-1226, 2015.

[285] Roth CJ, Becher T, Frerichs I, Weiler N, Wall WA. Coupling of EIT with a computational lung model for predicting patient-specific ventilatory response. *J Appl Physiol* **122**: 855-867, 2017.

[286] Roth CJ, Yoshihara L, Ismail M, Wall WA. Computational modelling of the respiratory system: discussion of coupled modelling approaches and two recent extensions. *Comput Method Appl M* **314**: 473-493, 2017.

[287] Roth CJ, Yoshihara L, Wall WA. Modelling and simulation of the respiratory system. *Encyclopedia of Biomechanics*, 2016.

[288] Roth CJ, Yoshihara L, Wall WA. A simplified parametrised model for lung microstructures capable of mimicking realistic physiological and mechanical properties. *Comput Biol Med* **89**: 104-114, 2017.

[289] Roth CJ, Förster KM, Hilgendorff A, Ertl-Wagner B, Flemmer AW, Wall WA. Gas exchange mechanisms in HFOV - a computational approach. *Eur Respir J*, in preparation, 2016.

[290] Roth CJ, Wirthl B, Wall WA. Material identification of the lower airway tree: an experimental and numerical study. *J Mech Behav Biomed Mater*, in preparation, 2016.

[291] Roth M. Simulation of a fully resolved three dimensional lung model with volumetric coupling. *Semester thesis, Technische Universität München, München, Germany*, 2015.

[292] Rush S, Abildskov JA, McFee R. Resistivity of body tissues at low frequencies. *Circulation* **22**: 40-50, 1963.

[293] Ryans J, Fujioka H, Halpern D, Gaver DP. Reduced-Dimension Modeling Approach for Simulating Recruitment/De-recruitment Dynamics in the Lung. *Ann Biomed Eng* **44**: 3619-3631, 2016.

[294] Salazar E, Knowles JH. An analysis of pressure-volume characteristics of the lungs. *J Appl Physiol* **19**: 97-104, 1964.

[295] Sampsonas F, Kontoyiannis DP, Dickey BF, Evans SE. Performance of a standardized bronchoalveolar lavage protocol in a comprehensive cancer center: a prospective 2-year study. *Cancer* **117**: 3424-3433, 2011.

[296] Sapoval B, Filoche M, Weibel ER. Smaller is better-but not too small: a physical scale for the design of the mammalian pulmonary acinus. *Proc Natl Acad Sci U S A* **99**: 10411-10416, 2002.

[297] Saxer T, Zumbuehl A, Müller B. The use of shear stress for targeted drug delivery. *Cardiovasc Res* **99**: 328-333, 2013.

[298] Schittny JC, Mund SI, Stampanoni M. Evidence and structural mechanism for late lung alveolarization. *Am J Physiol Lung Cell Mol Physiol* **294**: 246-254, 2008.

[299] Schloegel K, Karypis G, Kumar V. Parallel static and dynamic multi-constraint graph partitioning. *Concurrency Computat: Pract Exper* **14**: 219-240, 2002.

[300] Schmidt RF, Lang F, Heckmann M. Physiologie des Menschen. *Springer. Berlin, Germany*, 2010.

[301] Schranz C, Knöbel C, Kretschmer J, Zhao Z, Möller K. Hierarchical parameter identification in models of respiratory mechanics. *IEEE Trans Biomed Eng* **58**: 3234-3241, 2011.

[302] Schranz C, Becher T, Schädler D, Weiler N, Möller K. Model-based setting of inspiratory pressure and respiratory rate in pressure-controlled ventilation. *Physiol Meas* **35**: 383-397, 2014.

[303] Schwan HP, Kay CF. Specific resistance of body tissues. *Circ Res* **4**: 664-670, 1956.

[304] Sera T, Uesugi K, Yagi N, Yokota H. Numerical simulation of airflow and microparticle deposition in a synchrotron micro-CT-based pulmonary acinus model. *Comput Methods Biomech Biomed Engin* **18**: 1427-1435, 2015.

[305] Sherwin SJ, Franke V, Peiro J, Parker K. One-dimensional modelling of a vascular network in space-time variables. *J Eng Math* **47**:217-250, 2003.

[306] Sherwin SJ, Formaggia L, Peiro J, Franke V. Computational modelling of 1D blood flow with variable mechanical properties and its application to the simulation of wave propagation in the human arterial system. *Int J Numer Meth Fluids* **43**: 673-700, 2003.

[307] Simon BA, Kaczka DW, Bankier AA, Parraga G. What can computed tomography and magnetic resonance imaging tell us about ventilation? *J Appl Physiol* **113**:647-657, 2012.

[308] Sinclair SE, Molthen RC, Harworth ST, Dawson CA, Waters CM. Airway strain during mechanical ventilation in an intact animal model. *Am J Respir Crit Care Med* **176**: 786-794, 2007.

[309] Slutsky AS, Drazen FM, Ingram RH Jr, Kamm RD, Shapiro AH, Fredberg JJ, Loring SH, Lehr J. Effective pulmonary ventilation with small-volume oscillations at high frequency. *Science* **209**: 609-671, 1980.

[310] Slutsky AS, Tremblay LN. Multiple system organ failure. Is mechanical ventilation a contributing factor? *Am J Respir Crit Care Med* **157**: 1721-1725, 1998.

[311] Slutsky AS, Drazen JM. Ventilation with small tidal volumes. *N Engl J Med* **347**: 630-631, 2002.

[312] Slutsky AS, Ranieri VM. Ventilator-induced lung injury. *N Engl J Med* **369**: 2126-2136, 2013.

[313] Smith BJ, Gaver DP. The pulsatile propagation of a finger of air within a fluid-occluded cylindrical tube. *J Fluid Mech* **601**: 1-23, 2008.

[314] Smith BJ, Bates JHT. Assessing the progression of ventilator-induced lung injury in mice. *IEEE Trans Biomed Eng* **60**: 3449-3457, 2013.

[315] Smith BJ, Grant KA, Bates JH. Linking the development of ventilator-induced injury to mechanical function in the lung. *Ann Biomed Eng* **41**: 527-536, 2013.

[316] Smith BJ, Bates JHT. Variable ventilation as a diagnostic tool for the injured lung. *IEEE Trans Biomed Eng* **62**: 2106-2113, 2015.

[317] Smith BJ, Lundblad LK, Kollisch-Singule M, Satalin J, Nieman G, Habashi N, Bates JH. Predicting the response of the injured lung to the mechanical breath profile. *J Appj Physiol* **118**: 932-940, 2015.

[318] Spieth PM, Güldner A, Huhle R, Beda A, Bluth T, Schreiter D, Ragaller M, Gottschlich B, Kiss T, Jaber S, Pelosi P, Koch T, Gama de Abreu M. Short-term effects of noisy pressure support ventilation in patients with acute hypoxemic respiratory failure. *Crit Care* **17**: R261, 2013.

[319] Spieth PM, Bluth T, Gama De Abreu M, Bacelis A, Goetz AE, Kiefmann R. Mechanotransduction in the lungs. *Minerva Anestesiol* **80**: 933-941, 2014.

[320] Standring S. Gray's Anatomy, 40th Edition: The Anatomical Basis of Clinical Practice, Expert Consult. *Elsevier, New York, USA*, 2009.

[321] Suki B, Barabasi AL, Hantos Z, Petak F, Stanley HE. Avalanches and power-law behaviour in lung inflation. *Nature* **368**: 615-618, 1994.

[322] Suki B, Lutchen KR, Ingenito EP. On the progressive nature of emphysema: roles of proteases, inflammation, and mechanical forces. *Am J Respir Crit Care Med* **168**: 516-521, 2003.

[323] Szabari MV, Tolnai J, Maar BA, Parameswaran H, Bartolak-Suki E, Suki B, Hantos Z. Lung structure and function in elastase-treated rats: A follow-up study. *Respir Physiol Neurobiol* **215**: 13-19, 2015.

[324] Sznitman J, Heimsch T, Wildhaber JH, Tsuda A, Rösgen T. Respiratory flow phenomena and gravitational deposition in a three-dimensional space-filling model of the pulmonary acinar tree. *J Biomech Eng* **131**: 031010-1-16, 2009.

[325] Sznitman J. Respiratory microflows in the pulmonary acinus. *J Biomech* **46**: 284-298, 2013.

[326] Talmor D, Sarge T, Malhotra A, O'Donnell CR, Ritz R, Lisbon A, Novack V, Loring SH. Mechanical ventilation guided by esophageal pressure in acute lung injury. *N Engl J Med* **359**: 2095-2104, 2008.

[327] Tavana H, Zamankhan P, Christensen PJ, Grotberg JB, Takayama S. Epithelium damage and protection during reopening of occluded airways in a physiologic microfluidic pulmonary airway model. *Biomed Microdevices* **13**: 731-742, 2011.

[328] Tawhai MH, Pullan AH, Hunter PJ. Generation of an anatomically based three-dimensional model of the conducting airways. *Ann Biomed Eng* **28**: 793-802, 2000.

[329] Tawhai MH, Hoffman EA, Lin CL. The lung physiome: merging imaging-based measures with predictive computational models. *Wiley Interdiscip Rev Syst Biol Med* **1**: 61-72, 2009.

[330] Tawhai MH, Lin CL. Image-based modeling of lung structure and function. *J Magn Reson Imaging* **32**: 1421-1431, 2010.

[331] Tawhai MH, Bates JHT. Multi-scale lung modeling. *J Appl Physiol* **110**: 1466-1472, 2011.

[332] Teng Z, Trabelsi O, Ochoa I, He J, Gillard JH, Doblare M. Anisotropic material behaviours of soft tissues in human trachea: an experimental study. *J Biomech* **45**: 1717-23, 2012.

[333] Tezduyar TE, Sathe S, Cragin T, Nanna B, Conklin BS, Pausewang J, Schwaab M. Modelling of fluidstructure interactions with the spacetime finite elements: Arterial fluid mechanics. *Int J Numer Meth Fluids* **54**: 901-9222, 2007.

[334] Tian G, Longest PW, Su G, Hindle M. Characterization of respiratory drug delivery with enhanced condensational growth using an individual path model of the entire tracheobronchial airways. *Ann Biomed Eng* **39**: 1136-1153, 2011.

[335] Tiddens HA, Hofhuis W, Bogaard JM, Hop WC, de Bruin H, Willems LN, de Jongste JC. Compliance, hysteresis and collapsibility of human small airways. *Am J Respir Crit Care Med* **160**: 1110-1118, 1999.

[336] Tobin MJ. Advances in mechanical ventilation. *N Engl J Med* **344**: 1986-1996, 2001.

[337] Tomazevic D, Likar B, Slivnik T, Pernus F. 3-D/2-D registration of CT and MR to X-ray images. *IEEE Trans Med Imaging* **22**: 1407-1412, 2003.

[338] Torchin H, Ancel PY. Epidemiology and risk factors of preterm birth. *J Gynecol Obstet Biol Reprod*, 2016.

[339] Trabelsi O, del Palomar AP, Lopez-Villalobos JL, Ginel A, Doblare M. Experimental characterization and constitutive modeling of the mechanical behavior of the human trachea. *Med Eng Phys* **32**: 76-82, 2010.

[340] Tremblay L, Valenza F, Ribeiro SP, Li J, Slutsky AS. Injurious ventilatory strategies increase cytokines and c-fos m-RNA expression in an isolated rat lung model. *J Clin Invest* **99**: 944-952, 1997.

[341] Tschanz SA, Makanya AN, Haenni B, Burri PH. Effects of neonatal high-dose short-term glucocorticoid treatment on the lung: a morphologic and morphometric study in the rat. *Pediatr Res* **53**: 72-80, 2003.

[342] Tschumperlin DS, Margulies SS. Alveolar epithelial surface area-volume relationship in isolated rat lungs. *J Appl Physiol* **86**: 2026-2033, 1999.

[343] Tsunoda S, Fukaya H, Sugihara H, Martin CJ, Hildebrandt CJ. Lung volume, thickness of alveolar walls and microscopic anisotropy of expansion. *Respir Physiol* **22**: 285-296, 1974.

[344] Uhlig S, Uhlig U. Molecular mechanisms of pro-inflammatory responses in overventilated lungs. *Recent Res Devel Resp Critical Care Med* **1**: 49-58, 2001.

[345] Velroyen A, Yaroshenko A, Hahn D, Fehringer A, Tapfer A, Müller M, Noel PB, Pauwels B, Sasov A, Yildirim AÖ, Eickelberg O, Hellbach K, Auweter SD, Meinel FG, Reiser M, Bech M, Pfeiffer F. Grating-based X-ray dark-field computed tomography of living mice. *EBioMedicine* **2**: 1500-1506, 2015.

[346] Venegas JG, Harris RS, Simon BA. A comprehensive equation for the pulmonary pressure-volume curve. *J Appl Physiol* **84**: 389-395, 1998.

[347] Verdugo F, Roth CJ, Yoshihara L, Wall WA. Efficient solvers for coupled models in respiratory mechanics. *Int J Numer Meth Biomed Engng*, 2016.

[348] Victorino JA, Borges JB, Okamoto VN, Matos GF, Tucci MR, Caramez MP, Tanaka H, Sipmann FS, Santos DC, Barbas CS, Carvalho CR, Amato MB. Imbalances in regional lung ventilation: a validation study on electrical impedance tomography. *Am J Respir Crit Care Med* **169**: 791-800, 2004.

[349] Villar J, Kacmarek RM, Perez-Mendez L, Aguirre-Jaime A. A high positive end-expiratory pressure, low tidal volume ventilatory strategy improves outcome in persistent acute respiratory distress syndrome: a randomized, controlled trial. *Crit Care Med* **34**: 1311-1318, 2006.

[350] Vogt B, Pulletz S, Elke G, Zhao Z, Zabel P, Weiler N, Frerichs I. Spatial and temporal heterogeneity of regional lung ventilation determined by electrical impedance tomography during pulmonary function testing. *J Appl Physiol* **113**: 1154-1161, 2012.

[351] Vuong AT, Yoshihara L, Wall WA. A general approach for modeling interacting flow through porous media under finite deformations. *Comput Method in Appl M* **283**: 1240-1259, 2015.

[352] Wall WA, Rabczuk T. Fluid-structure interaction in lower airways of ct-based lung geometries. *Int J Numer Meth Fluids* **57**: 653-675, 2008.

[353] Wall WA, BACI: A parallel multiphysics simulation environment. Technical Report, Institute for Computational Mechanics, Technische Universtät München, 2016.

[354] Wang JR, Sun BY, Wang HX, Pang S, Xu X, Sun Q. Experimental study of dielectric properties on human lung tissue in vitro. *Med Biol Eng Comput* **34**: 598-604, 2014.

[355] Webb HH, Tierney DF. Experimental pulmonary edema due to intermittent positive pressure ventilation with high inflation pressures: protection by positive end-expiratory pressure. *Am Rev Respir Dis* **110**: 556-565, 1974.

[356] Weibel ER. Morphometry of the human lung. *Springer. Berlin, Germany*, 1963.

[357] Weibel ER. The pathway for oxygen. *Harvard University Press. Cambridge, MA and London, England*, 1984.

[358] Weibel ER, Sapoval B, Filoche M. Design of peripheral airways for efficient gas exchange. *Respir Physiol Neurobiol* **148**: 3-21, 2005.

[359] West J. Respiratory Physiology: The Essentials. *Lippincott Williams and Wilkins, Philadelphia, United States*, 2008.

[360] Wellman TJ, Winkler T, Costa ELV, Musch G, Harris RS, Venegas JG, Melo MFV. Measurement of regional specific lung volume change using respiratory-gated PET of inhaled ^{13}N-nirtogen. *J Nucl Med* **51**: 646-653, 2010.

[361] Wiechert L, Wall WA. A nested dynamic multi-scale approach for 3d problems accounting for micro-scale multi-physics. *Comput Method Appl M* **199**: 1342-1351, 2010.

[362] Wiechert L, Metzke R, Wall WA. Modeling the mechanical behavior of lung tissue at the micro-level. *J Eng Mech* **135**: 434-438, 2009.

[363] Wiechert L. Computational modeling of multi-field and multi-scale phenomena in respiratory mechanics. *PhD thesis, Technische Universität München, München, Germany*, 2011.

[364] Wiedenmann D, Keller L, Holzer L, Stojadinovic J, Münch B, Suarez L, Fumey B, Hagendorfer H, Brönnimann R, Modregger P, Gorbar M, Vogt UF, Züttel A, La Mantia F, Wepf R, Grobety B. Three-dimensional pore structure and ion conductivity of porous ceramic diaphragms. *AIChE J* **59**: 1446-1457, 2013.

[365] Wirthl B. Experimentelle und numerische Ermittlung eines Materialgesetzes für Atemwege. *Bachelor thesis, Technische Universität München, München, Germany*, 2015.

[366] Xia G, Tawhai MH, Hoffman EA, Lin CL. Airway wall stiffening increases peak wall shear stress: A fluid-structure interaction study in rigid and compliant airways. *Ann Biomed Eng* **38**: 1836-1853, 2010.

[367] Yalcin HC, Hallow KM, Wang J, Wei MT, Ou-Yang HD, Ghadiali SN. Influence of cytoskeletal structure and mechanics on epithelial cell injury during cyclic airway reopening. *Am J Physiol Lung Cell Mol Physiol* **297**: L881-891, 2009.

[368] Yaroshenko A, Hellbach K, Yildirim AÖ, Conlon TM, Fernandez IE, Bech M, Velroyen A, Meinel FG, Auweter S, Reiser M, Eickelberg O, Pfeiffer F. Improved in vivo assessment of pulmonary fibrosis in mice using X-ray dark-field radiography. *Sci Rep* **5**: 17492, 2010.

[369] Yin Y, Choi J, Hoffman AH, Tawhai MH, Lin CL. Simulation of pulmonary airflow with a subject-specific boundary condition. *J Biomech* **43**: 2159-2163, 2010.

[370] Yin Y, Choi J, Hoffman EA, Tawhai MH, Lin CL. A multiscale mdct image-based breathing lung model with timevarying regional ventilation. *J Comput Phys* **244**: 168-192, 2013.

[371] Yoshihara L, Coroneo M, Comerford A, Bauer G, Klöppel T, Wall WA. A combined fluid-structure interaction and multi-field scalar transport model for simulating mass transport in biomechanics. *Int J Numer Meth Engng* **100**: 277-299, 2014.

[372] Yoshihara L, Roth CJ, Wall WA. Fluid-structure interaction including volumetric coupling with homogenised subdomains for modeling respiratory mechanics. *Int J Numer Meth Biomed Engng*, 2016.

[373] Zhang Z, Kleinstreuer C. Airflow structures and nano-particle deposition in a human upper airway model. *J Comput Phys* **198**: 178-210, 2004.

[374] Zhang J, Patterson R. Non-invasive determination of absolute lung resistivity in adults using electrical impedance tomography. *Physiol Meas* **31**: 45-56, 2010.

[375] Zheng Y, Anderson JC, Suresh V, Grotberg JB. Effect of gravity on liquid plug transport through an airway bifurcation model. *J Biomech Eng* **127**: 798-806, 2005.

[376] Zheng Y, Fujioka H, Bian S, Torisawa Y, Huh D, Takayama S, Grotberg JB. Liquid plug propagation in flexible microchannels: A small airway model. *Phys Fluids* **21**: 071903, 2009.

[377] Zienkiewicz OC, Taylor RL. The finite element method for solid and structural mechanics. *Butterworth Heinemann*, 2006.

[378] Zierenberg JR, Halpern D, Filoche M, Sapoval B, Grotberg JB. An asymptotic model of particle deposition at an airway bifurcation. *Math Med Biol* **30**: 131-156, 2013.

[379] Zivanovic S, Peacock J, Alcazar-Paris M, Lo JW, Lunt A, Marlow N, Calvert S, Greenough A. Late outcomes of a randomized trial of high-frequency oscillation in neonates. *N Engl J Med* **370**: 1121-1130, 2014.